Imagerie de nanofils uniques par diffraction cohérente des rayons X

Francesca Mastropietro

▶ **To cite this version:**

Francesca Mastropietro. Imagerie de nanofils uniques par diffraction cohérente des rayons X. Physique [physics]. Université de Grenoble, 2011. Français. NNT : 2011GRENY052 . tel-00716410

HAL Id: tel-00716410
https://theses.hal.science/tel-00716410

Submitted on 10 Jul 2012

HAL is a multi-disciplinary open access archive for the deposit and dissemination of scientific research documents, whether they are published or not. The documents may come from teaching and research institutions in France or abroad, or from public or private research centers.

L'archive ouverte pluridisciplinaire **HAL**, est destinée au dépôt et à la diffusion de documents scientifiques de niveau recherche, publiés ou non, émanant des établissements d'enseignement et de recherche français ou étrangers, des laboratoires publics ou privés.

UNIVERSITÉ DE GRENOBLE

THÈSE

Pour obtenir le grade de

DOCTEUR DE L'UNIVERSITÉ DE GRENOBLE

Spécialité : **Physique de Matière Condensée et Rayonnement**

Arrêté ministérial : 7 Août 2006

Présentée par

Francesca Mastropietro

Thèse dirigée par **Joël Eymery**
et codirigée par **Vincent Favre-Nicolin et Dina Carbone**

préparée au sein **SP2M / UMR-E CEA / UJF-Grenoble 1, INAC, Grenoble, F-38054, France**
et de **École Doctorale de Physique**

Imagerie de Nanofils Uniques par Diffraction Cohérente des Rayons X

Thèse soutenue publiquement le **4 Octobre 2011**,
devant le jury composé de :

Sylvain RAVY
Directeur de Recherche CNRS, Université Paris-Sud, Paris (France), Président

Cinzia GIANNINI
Chercheuse CNR, Bari (Italie), Rapporteur

Olivier THOMAS
Professeur IM2NP Marseille (France), Rapporteur

Joël EYMERY
Chercheur-Ingénieur CEA, Grenoble (France), Directeur de thèse

Vincent FAVRE-NICOLIN
Maitre de Conférence, UJF-Grenoble 1-CEA, Grenoble (France), Co-Directeur de thèse

Dina CARBONE
Chercheuse ESRF, Grenoble (France), Co-Directeur de thèse

Till H. METZGER
Directeur de Recherche, Max Plank Institut, Potsdam (Allemagne), Invité

Contents

Acknowledgements

Several people have contributed to the realization of my thesis. I am grateful to Dr. Vincent Favre-Nicolin, Dr. Joël Eymery and Dr. Till Metzger who offered me the possibility of joining their research groups and working in a great collaboration. I was impressed by their passion for science and their human qualities. I really appreciated their pedagogy and their patience. Thanks for everything you taught me.

I warmly acknowledge Dr. Dina Carbone, that was for me not only a continuous source of scientific knowledge and motivation but also a very kind friend. Thanks for sharing the chaos of the office with me during the last two years and for your good mood.

I also had the chance to work with Dr. Virginie Chamard. I really thank her for the interest she showed in my research and the fruitful discussions in Marseille. I want to thank also Dr. Ana Diaz for her scientific support at the beginning of my PhD and for the unforgettable nights we spent in Grenoble.

I would like to thank Dr. Cinzia Giannini, Prof. Olivier Thomas and Dr. Sylvain Ravy for the careful reading of the manuscript and for their presence in the examination jury.

I express my gratitude to the people I met at the INAC laboratory of the CEA and the staff of ID01 for their support during experiments.

My warm thanks go to all my friends and to Piero, without them life in Grenoble would not be so amazing!

I cannot forget all the people I left in Italy. A lovely thought goes my parents, Pino and Annalisa, my sister Teresa and my brother in law Nick, who always believed in me and for the unconditional love they give me every day, to my niece Nicole and to Ester and Felice...I missed all of you a lot during my stay in France.

List of Figures

List of Tables

Introduction

During the last decade, the interest in semiconductor nanostructures increased enormously, mainly due to their different applications in optical and electronic micro devices. The continuous demand of high performing functional materials gave rise to the development of engineering techniques aimed to the controlled fabrication of nano-objects getting rid of strain and defects. On the other hand, experimental evidences of the improvement of interesting physical properties was showed in the case of strained crystal with respect to the unstrained case.

In this context, the development of characterisation methods with the adequate resolution at the nanometre scale and high strain sensitivity was necessary. Among them, imaging techniques were developed to obtain surface morphology characterisation, as in the case of scanning transmission and atomic force microscopy, and internal structure investigation. In the particular case of strain determination, scattering based techniques, as transmission electron microscopy (TEM) and x-ray diffraction, are largely applied. The first has the advantage of being an imaging technique with atomic resolution and good strain sensitivity. The second provides an extremely high strain sensitivity but is based on indirect model-dependent methods. Nevertheless, x-ray diffraction represents the method of choice to circumvent some limitations of TEM in term of penetration depth and radiation damage.

The wide use of x-ray-based methods to study nanostructures has been also possible due to the development of synchrotron sources combined with the employment of dedicated focusing optics such as Fresnel zone plate to obtain high brilliant radiation with high coherent properties in a micro-sized focal spot. In particular, the use of coherent x-ray beams is at the basis of lens-less microscopy techniques as coherent diffraction imaging (CDI) that allows the model free investigation of a crystal at the nanoscale. Phase retrieval algorithms are used to retrieve at the sample position the complex

exit wavefield from the measurement of far-field coherent intensity patterns, collected in the forward direction (to get morphological information) or in Bragg geometry (that gives access also to the strain fields). In the latter, the strain fields are encoded in the phase of the reconstructed complex-valued function at the sample position. However, this phase also brings the information of the illumination function that needs, therefore, to be taken into account for the correct interpretation of the strain.

The work presented in this manuscript aims to the demonstration of the experimental feasibility of the CDI approach in Bragg condition to recover the strain in single heterogeneous or highly strained homogeneous nanowires. In addition, the characterisation of the illumination function in the particular experimental conditions is offered in order to disentangle the different contributions in the retrieved phase.

In Chapter 1, I discuss the scientific motivation of this work. I first recall some theoretical concepts to describe the stress in a crystal and then, using examples from literature, I describe how the strain can be investigated in single nanowires using coherent diffraction techniques.

In Chapter 2, the basic principles of x-ray diffraction and the coherence properties of x-rays produced in a synchrotron facility are reviewed in order to introduce the coherent x-ray diffraction imaging technique. The experimental set-up used for coherent experiments at the undulator beamline ID01 at the European Synchrotron Radiation Facility is also described.

In Chapter 3 the working principles of a Fresnel zone plate, a "perfect" diffractive optic used to focus the beam during the described experiments, are detailed. Moreover, the paraxial Fresnel free-space approximation is discussed as an essential theoretical tool to explain the propagation of x-rays with a small deviation from a central axis.

Chapter 4 is dedicated to the study of focused X-ray beam obtained from the partial illumination of a Fresnel Zone Plate: as x-rays produced in a synchrotron facility only present finite coherence lengths, the coherent part of the beam is selected by means of an opening matching the transverse coherence length of the available radiation. This partial illumination condition affects the wavefront of the focused x-ray beam with a consequent modification of the exit wavefield. Using both numerical (calculations) and experimental (*ab initio* reconstruction) approaches, I have determined the illumination function (phase and amplitude) at the focal point.

In Chapter 5, I discuss about the application of CDI technique on real

systems presenting specific experimental issues. First, I present a study of the radiation damage observed in strained silicon line, with a time-dependent experiment allowing to recover the strain field as a function of the radiation damage. Then, I demonstrate, through numerical calculations, how the illumination function influences the recovered strain field. Finally, I show that it is possible to image the strain in InSb/InP nanowires even in the presence of stacking faults, by choosing a Bragg reflection insensitive to such defects.

Chapter 6 shows the preliminary results obtained from the measurement of the displacement field in single 300 nm diameter GaAs nanowires with a single layer of InAs quantum dots or quantum well. I show that the recorded coherent diffraction data can be used to determine the thickness and the phase shift in the nanowire and localise the insertion smaller than the achievable resolution.

Chapter 1

Imaging the strain at the nanoscale

As stated in the Introduction, the aim of this work is to study the displacement field in strained nanostructures using coherent diffraction imaging technique. In this chapter, I will give a short overview to understand the structural and physical properties of materials described in this work as object of strain determination. I will first recall some theoretical concepts to describe the stress and the strain in a crystal. Then, I will describe typical imaging techniques used to characterize nanostructures. Finally, I will show some interesting example from literature concerning the investigation of the strain in single nanowires using coherent diffraction technique.

1.1 The origin of the strain

The increasing interest in semiconductor nanowires [Samuelson, 2003], nanocrystals [Wang et al., 2005] and nanotubes [Ouyang et al., 2002], during the last decade [Smith, 1979] can be first attributed to their attractive potential applications [Thelander et al., 2006]. New structures are provided to create artificial potential for charge carriers (both electrons and holes) in semiconductors at a scale comparable to the de Broglie wavelength; quantum confinement effects [Kaufmann et al., 2001] become important and the electronic and optical properties deviate substantially from those of bulk material. In addition, new combination of defect-free materials allows getting original band gap alignment. Moreover, semiconductors are nowdays an integral part in our practical lives. The challenging down-scaling of electronics and optical devices paved the way to the tremendous develop-

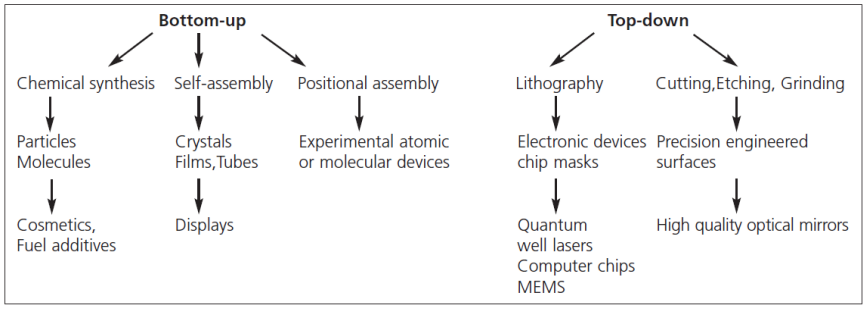

Figure 1.1: The use of bottom-up and top-down techniques in manufacturing. (http://www.nanotec.org.uk/finalReport.htm)

ment of nanostructure engineering for electronic and optoelectronic nanosemiconductors [Mokkapati and Jagadish, 2009, Thelander et al., 2006, Li et al., 2006] that could enable new applications in the future. The demand for ever more powerful systems has enhanced the controlled fabrication of nanoscale systems to obtain desired performances, as in the case of heterostructure nanowires [Caroff et al., 2009, Tomioka et al., 2008]. Concerning the growth of functional materials the main problem of crystal growers was for many years to get rid of defects and stress. However, it has been shown in some systems that the stress may not be detrimental to the physical properties (optical and electronic) of strained crystals when they are carefully controlled. Consequently the device performances may sometimes be improved with respect to the case of unstrained crystal, as shown for the mobility in transistor heterostructures [Jain and Hayes, 1991, Sander et al., 1998, Baudot et al., 2009].

1.1.1 Fabrication techniques

The techniques developed to create nanostructures can be divided in two categories : "*bottom-up*" and "*top-down*". A diagram illustrating the principle of these two approaches is shown in Fig. 1.1. Bottom-up manufacturing involves the building of structures, atom-by-atom or molecule-by-molecule, for example chemical synthesis, self-assembly or positional assembly. The latter consists of the self-assembly directional growth achieved by the presence on the substrate of catalysts (metal droplets), or patterning (holes in the substrate). An example of nanostructure grown through bottom-up method is shown in Fig. 1.2. The depicted case is the vapor-liquid-solid (VLS) deposition to grow Si nanowires from metallic catalysts with a

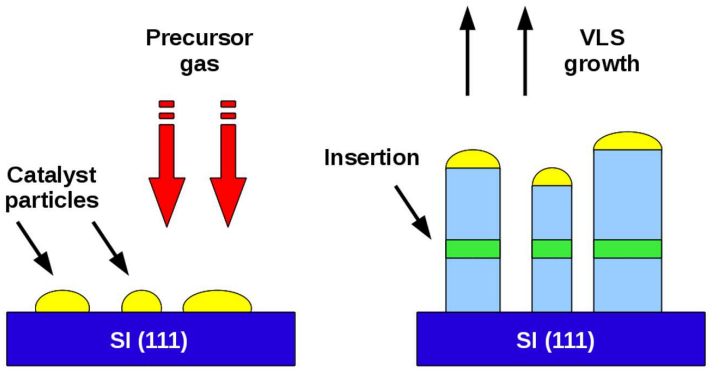

Figure 1.2: Schematics of bottom-up process to growth Si nanowires from metallic catalysts with a hetero-insertion (modified from http://fillergroup.gatech.edu/research).

hetero-insertion. Bottom-up techniques are especially suitable to grow heterostructures with one or multi heterojunctions, to obtain complex systems.

Top-down manufacturing, also known as step-wise design, creates nanostructures from a larger material through etching, milling or machining. This approach has been highly refined by the semiconductor industry over the past 30 years, in terms of high precision techniques, such as lithography. Top-down methods offer reliability and device complexity, although they are generally higher in energy usage, and produce more waste than bottom-up methods. An example of nanostructure grown through top-down method is shown in Fig. 1.3. In that case lithography is used to fabricate nano

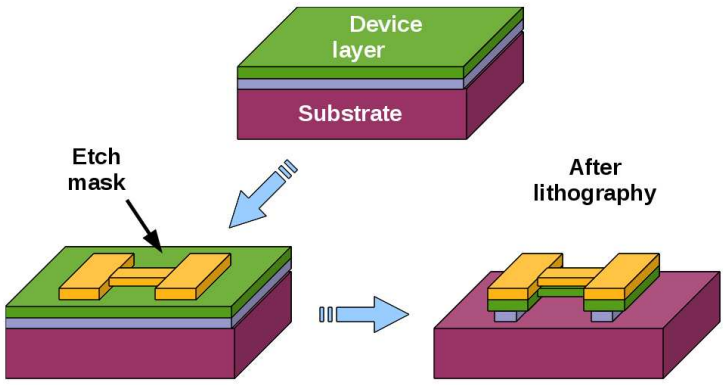

Figure 1.3: Schematics illustrating top-up (lithography) process to fabricate nano electro-mechanical systems (NEMS) (S. Afr. J. Sci. 104, 5-6, 2008).

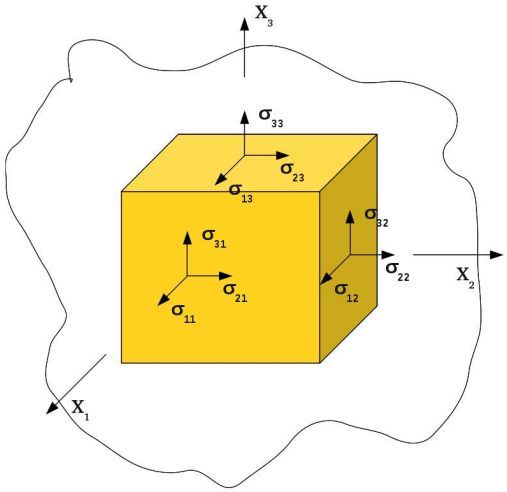

Figure 1.4: Action of the bulk stress σ_{ij} on an elementary cube. The index i refers to the direction X_i where the stress acts while j gives the direction perpendicular to the three front faces.

electro-mechanical systems (NEMS).

1.2 Linear elastic theory: Bulk strain tensor

The strain in fully coherent epitaxial heterostuctures (without extended defects) can be theoretically described through the linear elastic theory and it will be quickly introduced in the following. Let us consider a crystalline material A grown in a given well-defined orientation on a crystal surface B. The lattice parameter of the contact surface of A can be accommodated without the formation of extended defects in the case of coherent epitaxy (as in the case of thin layer). When a 2-dimensional array of extended defects is created (as in the case of misfit dislocations) we are in presence of semi-coherent epitaxy. This process is at the origin of the strain.

Let us consider now a cubic elementary crystal with the elementary volume $dV = dx_i dx_j dx_k$ centred in a stressed material. The normals x_k define the faces of the cube lying in the plane x_{ij}. These faces are submitted to a force per unit area that is defined by the stress tensor σ_{ik}, where $i = 1, 2, 3$. When $i = k$ the force is acting normally to the i^{th} face, while it is applied on the face surface when $i \neq k$. The tensor σ consists therefore of a total of 9 elements (second order matrix) [Elsevier, 1920, Landau et al., 1986]. A sketch of the stress tensor acting on a cubic crystal is shown in Fig. 1.4. The trace of the σ is invariant under the rotation axis; moreover identical forces

are applied on the opposite faces with opposite signs. This assumption is valid in the case of homogeneous stresses. In the inhomogeneous case, to which I will refer later in this chapter, forces on the back face are slightly different. For mechanical equilibrium maintained under external forces f_i applied to the crystal, not inducing torsion and/or rotation, we get the following condition

$$\frac{\partial \sigma_{ij}}{\partial x_j} = f_i \tag{1.1}$$

is satisfied. Using the Einstein's notation, the sum is performed on the repeated indices. When the stress is applied on a crystal A, the deformation is observed. In this case, the useful notation of *displacement fields* is introduced to quantify how much the distorted crystal differs from the unstressed condition [Landau et al., 1986]. In the (x,y,z) frame, $\mathbf{r}$ is the radial vector that localises each point in the volume of A. The displacement field $\mathbf{u}(\mathbf{r})$ is defined as follows:

$$\mathbf{r}' = \mathbf{r} + \mathbf{u}(\mathbf{r}) \tag{1.2}$$

where $\mathbf{r}$ is the radial vector in the case of an unstressed crystal and $\mathbf{r}'$ is vector transformed under the deformation. Hence, the strain, ϵ_{ij} can be introduce as a 2^{th} order symmetric tensor:

$$\epsilon_{ij} = \frac{1}{2}\left(\frac{\partial u_i}{\partial x_j} + \frac{\partial u_j}{\partial x_i}\right) \tag{1.3}$$

The strain defines the infinitesimal deformation related to the gradient of the displacement $\frac{\partial u_i}{\partial x_j}$. As in the case of σ_{ij}, ϵ_{ij} can be decomposed into normal (symmetric) and shear (asymmetric) components. The trace of ϵ_{ij} is invariant under rotation as it represents the expansion of the crystal. The asymmetric contribution is carried by the tensor ω_{ij}, defined as:

$$\omega_{ij} = \frac{1}{2}\left(\frac{\partial u_i}{\partial x_j} - \frac{\partial u_j}{\partial x_i}\right) \tag{1.4}$$

Strain and stress are related in the framework of the linear elasticity theory with two 4^{th} tensors C_{ikmn} and S_{ikmn}, that represent the stiffness and the compliance, respectively. They are used as coefficients in the following

transformation relationships, known as Hooke's laws [Tsao, 1992]:

$$\begin{cases} \sigma_{ij} = C_{ikmn}\epsilon_{mn} \\ \epsilon_{ij} = S_{ikmn}\sigma_{mn}. \end{cases} \tag{1.5}$$

C_{ikmn} and S_{ikmn} contain a total of 81 components but, taking into account crystal symmetries and considering that stress and strain are invariant under rotation, the number of independent parameters can be reduced. The Voigt's notation [Hearmon, 1946] is indeed preferred, and the tensors σ_{ij} and ϵ_{ij} are replaced by vectors, so that:

$$\begin{aligned} &\epsilon_i \equiv \epsilon_{ii}, \quad \epsilon_4/2 \equiv \epsilon_{23}, \quad \epsilon_5/2 \equiv \epsilon_{31} \quad \text{and} \quad \epsilon_6/2 \equiv \epsilon_{12} \\ &\sigma_i \equiv \sigma_{ii}, \quad \sigma_4 \equiv \sigma_{23} = \sigma_{32}, \quad \sigma_5 \equiv \sigma_{31} = \sigma_{13} \quad \text{and} \quad \sigma_6 \equiv \sigma_{12} = \sigma_{21}. \end{aligned} \tag{1.6}$$

Equation 1.5 can be re-written as:

$$\begin{cases} \sigma_i = C_{ik}\epsilon_k \\ \epsilon_i = S_{ik}\sigma_k. \end{cases} \tag{1.7}$$

C_{ikmn} and S_{ikmn} are represented by 6×6 matrices inverse to each other.

Let consider now the case of a cubic crystal in the reference frame ([100],[010],[001]). The quantitative description of the volumetric and distortional components of an external strain is given by the generalised Hook's law:

$$\begin{pmatrix} \sigma_x \\ \sigma_y \\ \sigma_z \\ \tau_{xy} \\ \tau_{yz} \\ \tau_{zx} \end{pmatrix} = \begin{pmatrix} C_{11} & C_{12} & C_{12} & 0 & 0 & 0 \\ C_{12} & C_{11} & C_{12} & 0 & 0 & 0 \\ C_{12} & C_{12} & C_{11} & 0 & 0 & 0 \\ 0 & 0 & 0 & C_{44} & 0 & 0 \\ 0 & 0 & 0 & 0 & C_{44} & 0 \\ 0 & 0 & 0 & 0 & 0 & C_{44} \end{pmatrix} \begin{pmatrix} \epsilon_x \\ \epsilon_y \\ \epsilon_z \\ \omega_{xy} \\ \omega_{yz} \\ \omega_{zx} \end{pmatrix}, \tag{1.8}$$

where τ_i and ω_i are the shear stresses and rotation tensors, respectively.

In the case of a isotropic biaxial strain $\sigma = (\sigma, \sigma, 0, 0, 0, 0)$ and for an epitaxial film oriented along the $\langle 111 \rangle$ cubic direction, the biaxial modulus M_{111} is given by:

$$M_{111} = \frac{6C_{44}(C_{11} + C_{12})}{C_{11} + 2C_{12} + 4C_{44}} = \frac{1}{S_{11} + S_{12}} \tag{1.9}$$

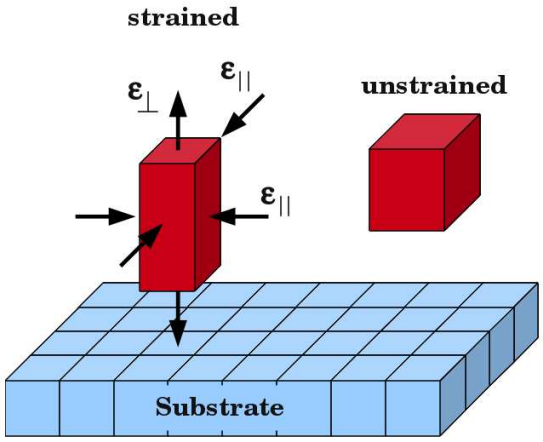

Figure 1.5: Sketch of the coherent accommodation in the hetero-epitaxial deposition of a layer with an unstrained lattice parameter a_{unstr} on a substrate with lattice parameter a_{bulk}. The lattice a_{unstr} shrinks due to the effect of the strain.(Modified from [Malachias, 2005])

For the complete mathematical derivation of C_{111} and S_{111} see [Vaxelaire, 2011], Appendix A.

1.2.1 Elastic energy

The interface between the epitaxial layer A and the bulk B and the total volume of the heterostructure store a certain amount of elastic energy responsible of the origin of strain [Elsevier, 1920, Landau et al., 1986]. In the following the growth of an epitaxial film on a substrate is discussed from the energetic point of view.

Let the lattice parameter of the film be larger than the one of the substrate. A compressive in-plane force is applied to the epitaxial layer while an equal but opposite tensile in-plane force acts on the substrate. Hence, the layer lattice parameter shrinks to accommodate the one of the substrate. The epitaxial layer is joined coherently to the substrate. In a good approximation, the substrate is considered much thicker than the layer and all the lattice accommodation mainly occurs in the thin film.

In figure 1.5 a sketch of the strain for an hetero-epitaxial layer deposition is shown. The epitaxial layer is strained in the direction parallel to the interface; consequently, it develops a parallel (in-plane) stress but also a perpendicular (out-of-plane) strain.

A detailed theoretical study of the elastic lattice deformation of a semi-

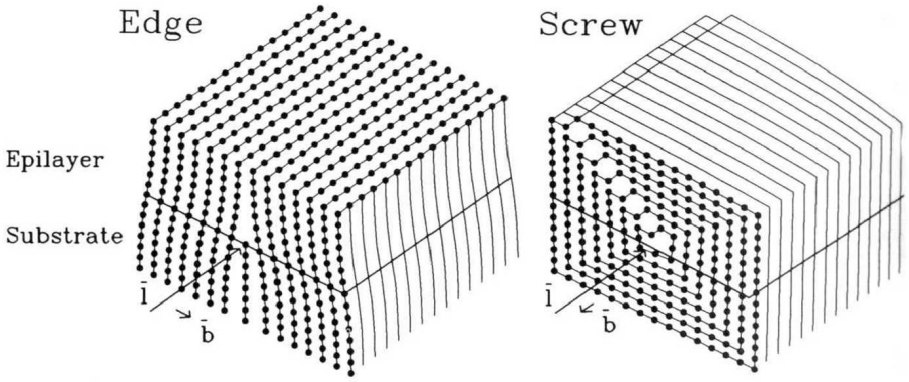

Figure 1.6: Pure edge (left) and pure screw (right) dislocations. [Tsao, 1992]

conductor heterostructure grown on an arbitrarily oriented substrate surface can be found in De Caro and Tapfer [1993]. The strain energy of the epitaxial layer in the unit volume is calculated according to the following relation:

$$E_{el} = \frac{1}{2} C_{ij} \epsilon_i \epsilon_j \tag{1.10}$$

1.2.2 Dislocations and defects

As previously discussed, the epitaxial growth of a layer on a substrate induces the accommodation of the misfit between layer and substrate surfaces. In this subsection, the particular case of epitaxial films that are semi-coherent with the substrate is discussed. In this case a misfit dislocation array occurs as the coherent registry breaks. Dislocations are therefore defects that introduce plastic deformation in a perfect crystal.

In the simplest case, a misfit dislocation consists of a vertical half missing plane, as shown in Fig. 1.6, left. As a consequence, the adjacent planes collapse to minimise the total energy stored in the film. This dislocation is known as *edge dislocation*. When the plane is displaced horizontally in the parallel direction we are in presence of a *screw dislocation*. This dislocation comprises a structure in which a helical path is traced around the defect by the atomic planes in the crystal lattice (see Fig. 1.6, right)

In order to define the atom plane displacement due to the dislocation and identify its position, the Burgers vector is introduced. The Burgers vector **b** is a vector that represents the magnitude and direction of the lattice

distortion of the planes in the crystal lattice. By definition, Burgers vector is perpendicular to the edge dislocation line while for a screw dislocation it is parallel, as shown in Fig. 1.6.

1.3 Strain in nanowires

The development of 1-dimensional semiconductors, such as single-crystal nanowires, is based on the impressive breadth of applications [Pauzauskie and Yang, 2006, Thelander et al., 2006, Cui et al., 2001, Lu et al., 2006]. These semiconductor rods usually have a diameter in the range of 20-200 nm and they can be synthesized using a wide range of semiconductor materials by means of different growth process allowing the precise control of composition, doping and interface sharpness. Most of the wires, including IV, II-VI and III-V compounds, are grown by vapour-liquid-solid mechanism (VLS), following the pioneer work of Wagner and Ellis [1964].

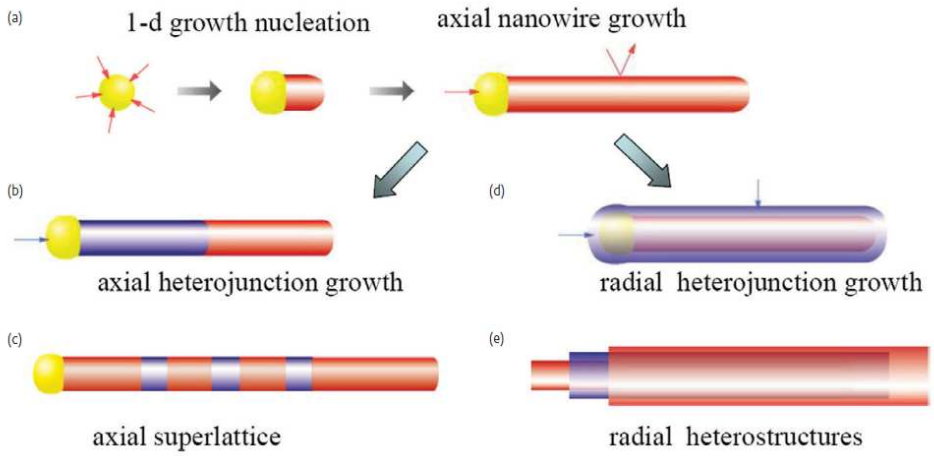

Figure 1.7: Heterogeneous nanowires. (a) Growth through catalyst-mediated axial synthesis. (b,c) Axial and radial heterojunction. (d,e) Axial superlattice and radial heterostructure (core-shell). [Hayden et al., 2008]

As an illustration, figure 1.7a shows the metal catalyst-mediated axial growth through the vapor-liquid-solid mechanism [Wu and Yang, 2001] is shown. The use of a catalyst assures the control of the nanowire lateral size, directly depending on the size of the initial metal droplet. For some application, the use of metal as catalyst may be detrimental to the physical properties. Catalyst-free methods are therefore under development.

Nanowires are mainly divided in two categories: homogeneous and heterogeneous structures. Heterogeneous nanowires are of particular interest

due to the formation of specific defect-free heterostructures that can not be obtained in 2D materials. The nanowire geometry takes the advantage of free surface elastic relaxation that is enhanced for small diameters. These structures also improve the light extraction based on guiding and polarization effects. Heterostructures can be obtained as axial or radial structures. In axial heterostructures, the wire material is varied along the wire axis, i.e. the growth direction; these materials can be combined via the elastic relaxation at the junction. Heterostructure, both radial and axial, can be achieved switching the source material during the growth, resulting in a heterostructure with one or more junction (Fig. 1.7,b and c). A conformal deposition of different materials leads to the formation of core/shell nanowires, consisting of single (Fig. 1.7d) or multi-shell structure (Fig. 1.7e).

When growing heterostructures, the band structures and energies may be directly modified by the strain. The influence of strain on the band gap has to be taken into account especially in quantum structures, where the local band gap plays an important role. As already discussed, the strain fields is directly related to the lattice mismatch between the two materials, the elastic properties and the geometry [De Caro and Tapfer, 1994, Niquet, 2006, Ertekin et al., 2005, Samuelson, 2004].

1.3.1 Strain relaxation and intermixing

The strain profile of a GaN/AlN nanowire heterostructures, reported by Camacho [2010], is discussed to highlight the strain distribution and relaxation in these heterostructures. The AlN nanowire is oriented along the c-axis and modelled as a 30 nm diameter and 150 nm long pillar. A single GaN quantum dot with a thickness of 5 nm is inserted in the middle. The strain in these nanowires can be computed with Keatings valence field model. [Keating, 1966], but using atomistic simulations.

The hydrostatic strain $dV/V = \epsilon_{xx} + \epsilon_{yy} + \epsilon_{zz}$ is plotted in a plane containing the axis of the nanowire in figure 1.8b. The hydrostatic strain is the variation of the volume of the unit cell with respect to the unstrained material. As expected, the GaN layer is compressed by the AlN majority material. The strain is however very inhomogeneous, being significant at the center of the GaN insertion, but almost completely relaxed at the surface. The GaN insertion indeed deforms the surface of the nanowire outwards to relieve the inner strain. This transfers tensile strain to the AlN nanowire, which relaxes over a few nanometers on each side of the GaN insertion.

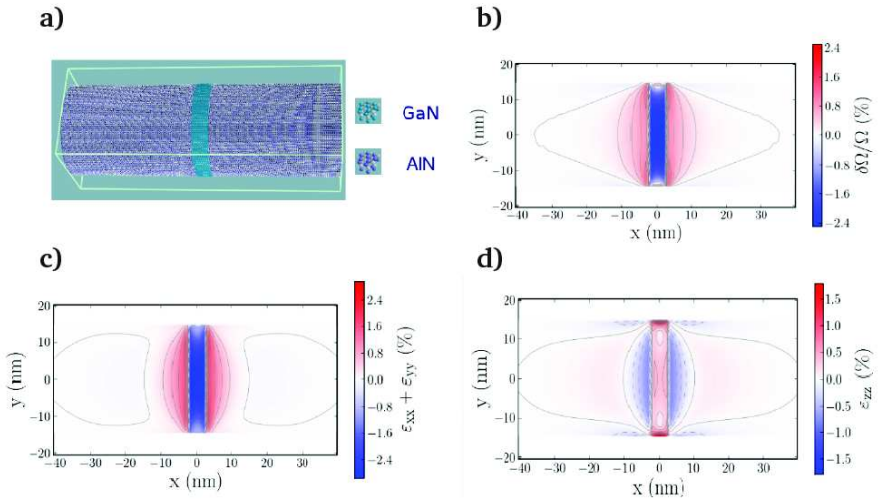

Figure 1.8: a) AlN nanowire with a 5 nm thick GaN insertion. b) Hydrostatic deformation, c) in-plain strain $\epsilon_{xx} + \epsilon_{yy}$ and d) vertical strain ϵ_{zz} in AlN/GaN nanowires. (Modified from [Camacho, 2010])

The strain field $\epsilon_{xx} + \epsilon_{yy}$ and ϵ_{zz} are also plotted separately in figures 1.8, c and d, respectively. The in-plane strain $\epsilon_{xx} + \epsilon_{yy}$ shows the same features as the hydrostatic strain. The strain ϵ_{zz} is opposite to the in-plane strains, as the material compensates the compression along x and y by a dilatation along z to mitigate volume variations (i.e., hydrostatic strains). The residual in-plane strain at the center of the GaN layer, $\epsilon_{xx} + \epsilon_{yy}$ ≈2.8% is much smaller than the lattice mismatch between GaN and AlN (≈ 4.8%), which shows that strain relaxation is very efficient.

1.4 Imaging techniques

The knowledge of structural properties of nano-objects is important to achieve the control of physical properties. Therefore, the investigation at the nanoscale, with a particular interest in the determination of displacement fields, has required the development of dedicated techniques capable of adequate spatial resolution and high strain sensitivity. The usual approach for nanostructure characterisation are imaging techniques for morphology determination (scanning tunnelling and atomic force microscopy) and internal structure investigation. The latter profits, for example, from the scattering of electrons (transmission electron microscopy) or x-rays (x-ray diffraction) beams. In the following these different techniques are illustrated along with their advantages and limitations.

1.4.1 Scanning tunnelling and atomic force microscopy

Scanning tunnelling microscopy (STM) is a technique with a high sensitivity to surface electron density and morphology. It employs a conducting probe to scan the structure. A bias voltage is applied to produce a tunnelling current flowing between the probe and the sample. In the standard operating mode, the current value is maintained while the probe is raster scanning the sample surface. If an increase or decrease of current is detected during scanning, the voltage supplied to the piezo is adjusted, maintaining a constant pre-set current. These changes in voltage are analysed to obtain the electron profile across the sample surface or it can be used to kept a contrast height, which allows accessing to the morphology. The resolution of the image is limited by the radius of curvature of the scanning tip of the STM. The limitations of STM are the need of electrically conducting samples and the necessity to work under vacuum.

The successful development of atomic force microscopy (AFM) [Binnig et al., 1986] allows the investigation of samples in both ambient air environment or in liquid. It employes a sharp probe that is positioned in proximity to the sample surface. Such probes are constructed of a tip mounted at the end of a short flexible cantilever or a tuning fork. The tip generally has a radius in the range of 5-40 nm. As with the STM, the AFM probe is raster scanned on the surface plane by means of a piezo-electric device. As the probe is translated laterally across the sample, it interacts differently through the atomic forces with the surface atoms [McPherson et al., 2004]. Due to these interactions the probe moves vertically and the response signal can be recorded and, consequently, analysed. This system is sensitive enough to detect atomic-scale movement of the tip as it scans the sample [Morris et al., 1999]. Also in this case, the resolution is limited by the radius of curvature, the aspect-ratio of the tip and the analysed structure.

1.4.2 Transmission electron microscopy

Electron-based techniques are extremely interesting as imaging tools with atomic resolution [De Wolf et al., 2003], due to the very small wavelength of employed electrons, that varies in the range of 4-0.3 pm.

An electron microscope usually consists of an electron source and an assembly of magnetic lenses in vacuum. The electrons are accelerated by a

high potential (100-500 kV). The convergence angle and, consequently, the size of the beam impinging on the specimen can be varied by means of a condenser lens system and field-limiting apertures and, recently, aberration correction systems have strongly improved the resolution. The specimen is mounted on a special holder and can be tilted, in most systems, by more than 30° around two orthogonal axes to allow crystallographic analysis.

The electron beam strongly interacts with matter due to the nature of the interaction with the atoms. In the case of crystalline specimens, the elastically diffracted electrons (Bragg diffraction) contain information on the crystal lattice parameter, the crystal structure, the specimen shape and the presence of ordering effects. The emerging electrons recombine to form an image in the plane of the objective lens. High resolution imaging [Hüe et al., 2008] has a very good spatial resolution (<1 nm) and a strain sensitivity of 1×10^{-3}, but its field of view is narrow ($100\times100\text{nm}^2$) and specimens need to be very thin and homogeneous. This preparation may alter the initial strain, which must be measured. Convergent beam electron diffraction [Armigliato et al., 2003] is another very accurate TEM technique (strain sensitivity of 1×10^{-4}). It uses the information of high indices diffracting planes and has a very fine spatial resolution (2-3 nm). However, the specimen must be tilted slightly off axis leading to structure shadowing.

As another example of TEM techniques, dark field holography [Hytch et al., 2008] appeared as a very promising method having a good spatial resolution combined to a high strain sensitivity (1×10^{-3}) and a large field of view of 250×1000 nm^2. However, its principal limitation is the need of an unstrained reference area close to the zone of interest (within 1 μm) and

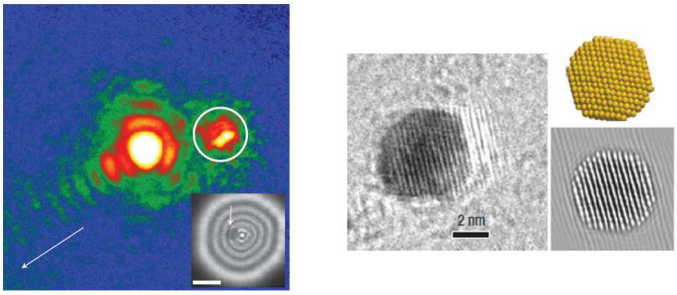

Figure 1.9: Left: Coherent electron diffraction pattern recorded from a single, faceted, Au nanocrystal (≈3.5 nm in diameter) at the (111) reflection. Right: The experimental (left) and simulated (lower right) high-resolution TEM images and the Au nanocrystal model (upper right). The scale bar is 2 nm. [Huang et al., 2008]

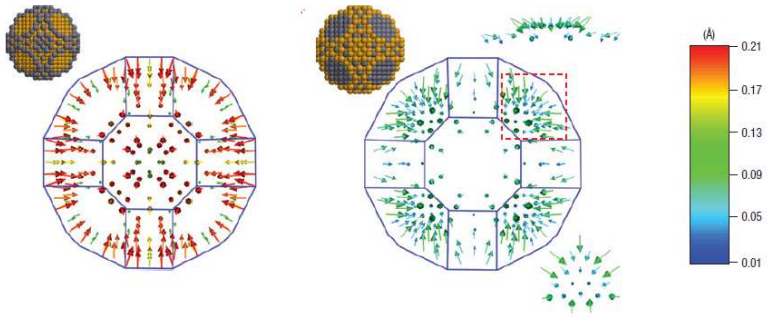

Figure 1.10: Surface atom displacements shown as vectors for atoms possessing a coordination number less than 9 (left, mostly are 100 atoms and neighbouring vicinal facet atoms) and equal to 9 (right, mostly are 111 surface atoms). Here, the magnitudes of the displacements are rendered using colours. Also directions of the surface atom displacements is represented by arrows. [Huang et al., 2008]

in a strict epitaxy. Nano beam electron diffraction (NBD or NBED) has been also quite recently applied to strain measurement. A strain precision of 6×10^{-4} using a probe size of 2.7 nm with a convergence angle of 0.5 mrad was achieved [Béché et al., 2009].

Using a 40 nm diameter coherent electron beam, Huang et al. [2008] demonstrated the possibility of reconstructing a single small Au particle ($\approx$3.5 nm in diameter) from its diffraction pattern (Fig. 1.9). The lateral coherent length of the electron beam was about 35 nm, Moreover, they imaged the atomic displacements of the surface atom as 3D vector maps (both in magnitude and direction) (Fig. 1.10). The method they proposed was recently modified by De Caro et al. [2010] to image individual TiO_2 nanocrystals with a resolution of 70 pm revealing the location of light atoms (oxygen) in the crystal lattice.

A major disadvantage of this technique is that, the higher the resolution, the smaller is the zone of the specimen one can look at. In addition, one single TEM image has no depth sensitivity and complementary techniques or theoretical models are needed for a full characterization of the specimen. The risk of beam damage increases with the accelerating voltage and in presence of very intense electron sources the sample can be destroyed. Therefore, the observation conditions must be carefully tested for each material and the possibility of sampling the specimen is reduced. Specimens for TEM observations must be homogeneous and thin enough (<50 nm) to be transparent to the electrons, having naturally limited penetration depth.

1.4.3 Imaging with X-rays

The strength of x-ray based techniques aiming to the characterisation at the nanoscale is the high penetration depth of photons that allows the imaging of buried structures, without the need of specific sample preparation. Furthermore, the extension of x-ray wavelength, from few tens to a small fraction of nanometers, offers the possibility to image objects at the corresponding spatial resolution. Finally, the associated photon energy spectrum is spread enough to make x-ray sensitivity to all elements, providing the element identification and the probing chemical bonds, simply using energies close to a given absorption edge. A detailed review on the imaging at the nanoscale using x-rays is given in [Sakdinawat and Attwood, 2010] and references therein.

Among the x-ray imaging techniques, scanning transmission x-ray microscopy (STXM) and tomography are of relevant application. In the first, the radiation is focused in a small spot on the sample and the transmitted radiation is detected. The sample is two-dimensionally raster-scanned to form an image. The spatial resolution is limited by the focal spot size. In STXM, it is also possible to change the incoming photon energy and to provide spectral information for elemental and chemical specimen.

X-ray tomographic microscopy is a projection imaging technique in which the x-rays transmitted through a sample are imaged directly onto an array detector. 3D images are then reconstructed from the 2D projection datasets. This is often performed at micrometre-scale spatial resolutions using hard x-rays, with an increasing amount of research being performed at the sub-micrometre level. This technique is particularly used with synchrotron radiation for thick and absorbing samples measured at high energy. In this case the spatial resolution is limited by the detector pixel size.

X-ray scattering techniques that are sensitive to the displacement fields in nanostructures [Thomas, 2008, Thomas et al., 2006] are based on the Bragg diffraction. Being of extreme relevance for this work, they will be the subject of a separate section.

1.5 Coherent x-ray diffraction imaging: from assemblies to single nano-objects

The use of x-rays for the study of nano-object has been made possible with the development of synchrotron source, producing radiation with high flux and brilliance and, when required, high coherent properties. This is due to the necessity to get a meaningful signal coming from the small volume of interesting materials in the investigated samples, assemblies as well as single nanostructures.

1.5.1 The European Synchrotron Radiation Facility

All the experiments described in this manuscript have been performed at the European synchrotron radiation facility in Grenoble (France) (http://www.esrf.fr). Here, high energy electrons are emitted by an electron gun and packed in bunches; then they are accelerated by a pulsed electric field to approach the speed of light. A race-track shaped booster accelerator, 300 m long, is used to make electrons reaching the final energy of 6 GeV. The booster synchrotron consists of accelerating cavities and synchronising bending magnets which force the electrons to deviate from a linear to a curved trajectory. Accelerated electrons are sent in the giant storage ring (844 m of circumference), where a current of 200 mA can be stored; here electrons travel in order to be used to generate synchrotron light. Since the opening, 43 beamlines are operating using either bending magnets (BM) or undulator/wiggler insertion devices (ID) to generate high brilliance radiation with wavelength ranging from UV light to hard x-ray. The purpose of the bending magnets is to change the direction of the beam. They are placed at a number of locations on the ring to guide the beam along the reference path. Undulators consist of two opposite rails, each equipped with a large number of magnets, with alternating polarity (Fig.1.11). Such a device can create nearly sinusoidal magnetic field of up to 1 T. Undulators can provide several orders of magnitude higher flux than a simple bending magnet. Typical brilliance of synchrotron sources are compared in Fig. 1.12 to free electron laser facilities. Recently, efforts are made to reduce the source size and increase the brilliance of the available radiation.

1.5.2 X-ray focusing optics

The extensive use of available x-ray tools has been accompanied by the development of appropriate focusing optics to improve the spatial resolution by creating brighter and smaller probes. Focused beams act as local probes allowing to investigate submicron parts of an extended sample and permit to look at single nano-objects, avoiding average information from assembly.

Kirckpatrick-Baez (KB) mirrors [Kirkpatrick and Baez, 1948] are reflective optics at near-glancing angle of incidence, largely used today with hard x-rays. They consist of crossed curved mirrors focusing in orthogonal directions (Fig. 1.13a). The resolution of reflective optics was limited to small fraction of micrometer but recently reached the world record of 7 nm in one direction at 20keV [Mimura et al., 2009].

The development of compound refractive lenses (CRL) [Snigirev et al., 1998] also demonstrated that also refractive optics can be employed to focus x-ray beams to sub-micron size (Fig. 1.13b). They are particularly suitable in the case of hard x-rays (above 2.5 keV) as, due to their high degree of absorption, cannot be used with soft x-rays (below 2.5 keV).

To focus both soft and hard x-rays, diffractive optics, such as Fresnel zone plate (FZP) [Baez, 1961, Chao et al., 2005, Di Fabrizio et al., 1999], are widely employed as their performances can be easily tuned for the specific application. The advances in nanofabrication improved the FZP manufacturing using electron beam lithography and electroplating/etching of a metal [Jefimovs et al., 2007, David et al., 2002]. Their working principle is based on interferences between diffracted radiation along its grating structure (Fig. 1.13c). Zone plates represent high-resolution optics as source imaging-forming objective. They are versatile as the spatial resolution and the efficiency are set during the construction. In particular, the spatial resolution depends linearly on the outermost zone width and on the choice of

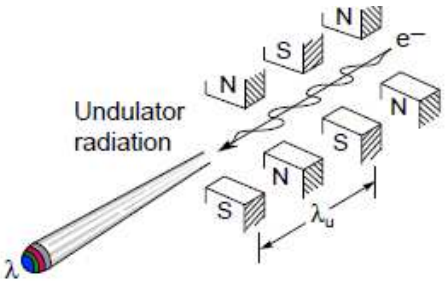

Figure 1.11: Tunable undulator radiation generated by the passage of relativistic electrons through a periodic magnet structure [Attwood et al., 1993]

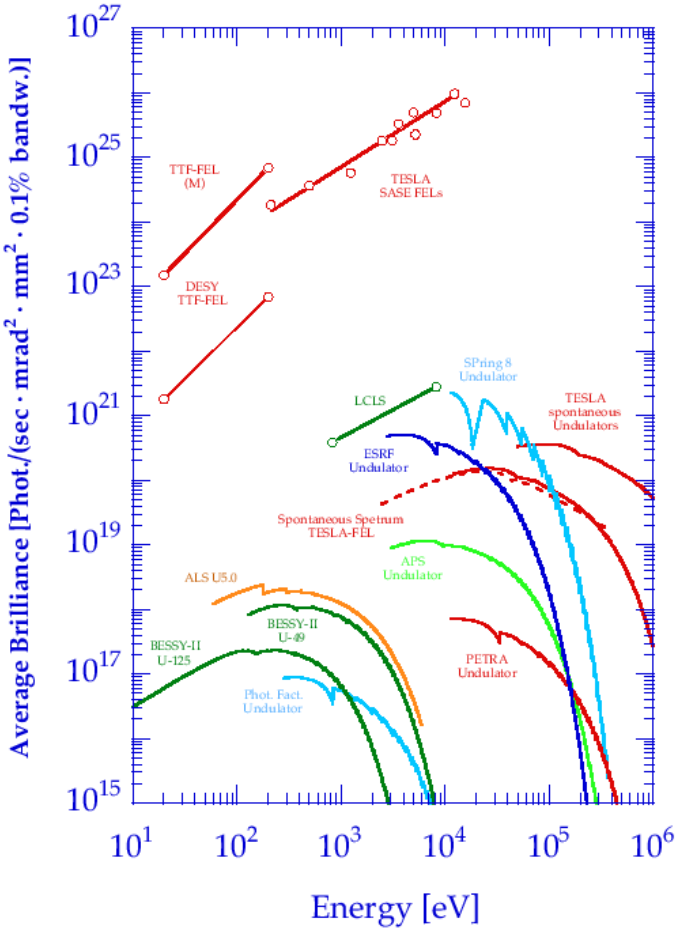

Figure 1.12: Average brilliance of third generation synchrotron radiation sources. (http://hasylab.desy.de)

material. Fresnel zone plates can be considered a "perfect" diffractive object and it has been used during the experiments performed for this work. Moreover, this lens preserves the phase relation of the wavefront after the focusing process as it is free from local aberrations. This is due to the fabrication technique or small angle scattering from surface roughness or grain structure as in the case of Beryllium compound reflective lenses and KB mirrors preventing local curvature deformation (see Chapter 3 for more details).

1.5.3 X-ray diffraction on assemblies of nanostructures

X-ray diffraction techniques, as specifically grazing incidence small angle x-ray scattering (GISAXS) and grazing incidence x-ray diffraction (GIXRD)

[Renaud et al., 2009] are useful tools to study assemblies of nanostructures and recover average information on structural properties and strain. As an example, we illustrate in the following how Eymery et al. [2007] determined with GIXRD the strain and the composition of an assembly of InAs nanowires with an InP insertion (Fig. 1.14, left). As shown in Fig. 1.14 right, the fit of in-plane measurements allows the determination of the different contributions to the measured intensity: the substrate overgrowths, the relaxed InAs segments at the bottom and the top of the nanowire, and the average InAs and InP insertions in the superlattice. The wurtzite InAs nanowire position ((200) Bragg reflection) is slightly larger than the cubic InAs substrate. It corresponds to the bottom and to the top of the nanowire. It should be relaxed due to the small diameter and the small lattice mismatch. The in-plane lattice parameter is only decreased by about $0.32\% \pm 0.03$ according to the substrate reference. For the (003) measurement (see Figure 4b), the relaxed InAs NW signal is superposed to the twinned overgrowth contribution. The fit of this composite peak gives $0.17\% \pm 0.03$, suggesting that the two last phases are very close to bulk cubic InAs. These techniques allow to separate the contributions from substrate and wire but they can only yield ensemble averaged information about crystallographic phases, epitaxial relationships (with orientation distribution) and strain.

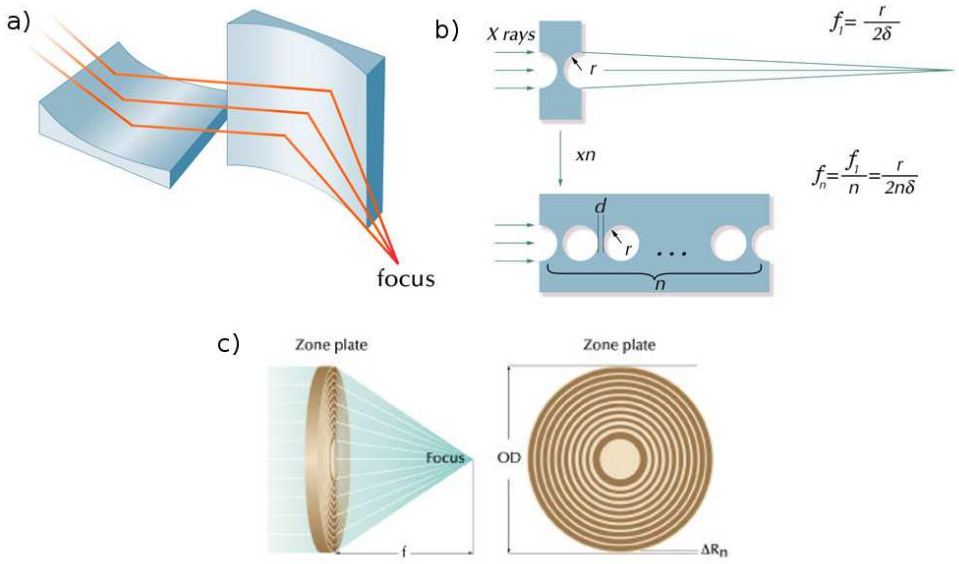

Figure 1.13: X-ray focusing optics: schematics of : a) Kirkpatrick-Baez mirrors, b) compound refractive lenses and c) Fresnel zone plate.(http://www.xradia.com/technology/basic-technology/focusing.php)

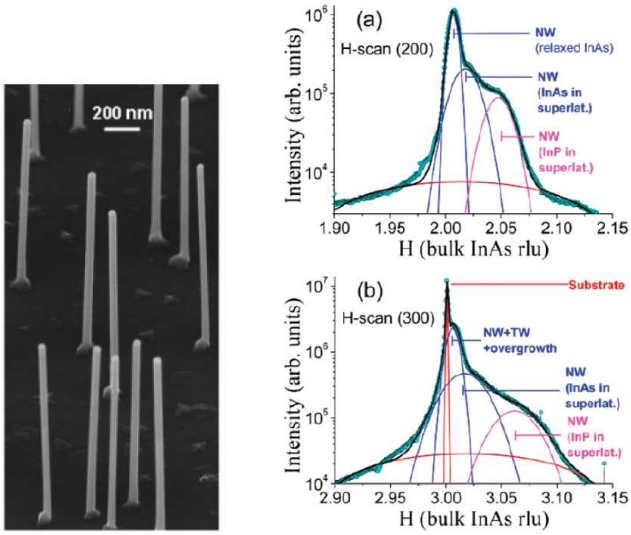

Figure 1.14: Left: Scanning electron microscopy images of CBE grown epitaxial InAs/InP nanowires. Right: In-plane measurements along h for the (a) (200) and (b) (300) reflections. [Eymery et al., 2007]

X-ray diffraction data provide a reciprocal space map that have to be treated to get information of real space. In addition, as only intensities can be measured, the phase information is lost. This reflects into the necessity of some model assumptions to overcome this loss.

Recently, the possibility of using highly coherent beams, combined with focusing optics, paved the way to the development of model-free investigation of single nano-objects. The well-defined phase relation of the coherent wavefront, which is preserved through the elastic scattering process, assures an high sensitivity to the exact position of the single scatterers. This is the basic principle of lens-less microscopy techniques as coherent diffraction imaging. Coherent diffractive imaging (CDI), applied both in small angle and Bragg geometry, is a model-free technique used to solve the classic phase problem in imaging without the help of *ab-initio* knowledge of the investigated sample. This is possible due to the high resolution achieved during the experiment. This technique is based on the measurement of far-field coherent intensity patterns; from those, numerical methods are used to retrieve at the sample position the complex exit wavefield. Adequate iterative phase retrieval algorithms (discussed in Chapter 2) have been developed to retrieve the phase of the object.

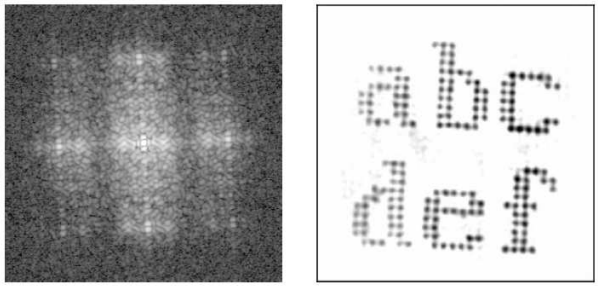

Figure 1.15: Left: A diffraction pattern of the specimen (using a logarithmic intensity scale). Right: The specimen image as reconstructed from the diffraction pattern. [Miao et al., 1999]

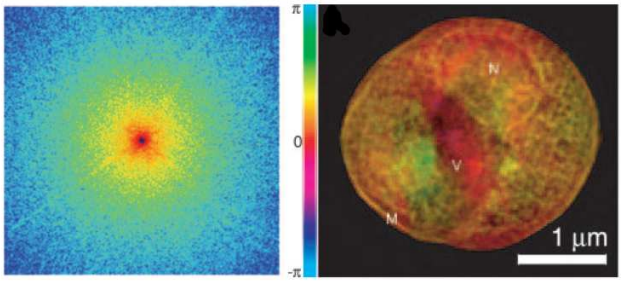

Figure 1.16: Left: Soft x-ray diffraction pattern of a freeze-dried yeast cell. Right: Images of the reconstructed freeze-dried yeast cell. [Shapiro et al., 2005])

1.5.4 Coherent x-ray imaging of non-crystalline objects

A considerable interest in using CDI techniques with short wavelength and high coherence at available synchrotron x-ray sources has been focused on non-crystalline phase [Sayre et al., 1998], or biomolecular samples. CDI provides an opportunity to determine the structure of proteins and other biological samples, which cannot be phased with the standard techniques of protein crystallography typically due to lack of crystallinity.

The first demonstration of CDI was offered by Miao et al. [1999]. They reconstructed, using adequate iterative algorithms, a specimen consisting of 100 nm diameter and 80 nm thick gold dots deposited on a silicon nitride membrane (Fig. 1.15). They also suggested that the extension from two to three dimensions requires a series of diffraction patterns recorded by rotating the specimen around an axis perpendicular to the beam.

Shapiro et al. [2005] reported the first reconstruction of the complex-

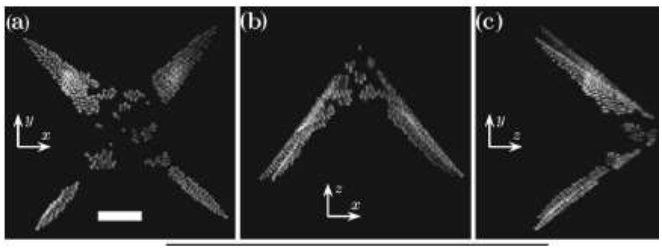

Figure 1.17: Maximum value projections along three orthogonal directions of the reconstructed 3D non-periodic object. Projections were performed along (a) z, (b) x, and (c) y directions. The scale bars are 500 nm. [Chapman et al., 2006b]

valued exit wavefront (both phase and magnitude) of a whole freeze-dried and unstained yeast cell (Fig. 1.16, right) form its diffraction pattern (Fig. 1.16, left). The images, at 30-nm resolution from multiple angular orientations of the cell, required an exposure of approximately one minute each using 750 eV x-rays. With these results, the application of 3D x-ray diffraction microscopy with the use of a coherent beam was extended to frozen-hydrated samples.

Another example can be found in Ref. [Chapman et al., 2006b]. Here, the 3D image of a nonperiodic object was directly reconstructed from coherent x-ray diffraction, exhibiting high resolution in all three dimensions (Fig. 1.17). The coherent x-ray diffraction comprised 140 views, at 1° intervals, and extended to a maximum spatial frequency of 0.068 nm^{-1}.

1.5.5 Coherent diffraction imaging of crystalline structures

The work presented in this thesis is based on the extension of CDI technique applied to nano-objects with a crystalline structure. Far-field diffraction patterns are collected for a chosen Bragg reflection, with the aim of reconstructing the amplitude and the phase of the exit field at the sample position. In these conditions, the retrieved phase gives access to the strain fields as it represents in good approximation the projection of the displacement of a crystalline lattice onto the scattering vector [Takagi, 1969]. The feasibility of CDI in Bragg geometry has been already demonstrated [Pfeiffer et al., 2006b, Robinson and Harder, 2009, Newton et al., 2010]. As an example, the phase of a 200 nm gold nanocrystal reconstructed by Robin-

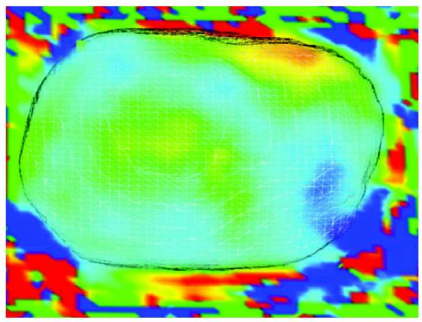

Figure 1.18: Phase map of a slice through a 200 nm Au nanocrystal obtained by hybrid inputoutput inversion of its coherent pattern measured with the (111) Bragg peak using a focused x-ray beam. [Robinson and Harder, 2009]

son and Harder [2009] from the coherent diffraction pattern collected at the (111) Bragg reflection is shown in Fig. 1.18. A slight curvature of the phase within the central region of the crystal, as stated by the authors, can be attributed to strain or be an image of the curved wavefront of the focused illuminating x-ray beam. Indeed, it is not strictly possible to separate in a single measurement the phase structures of both the sample and the probe, which are superimposed.

The most recent evidence of the possibility to reconstruct from 3-dimensional coherent diffraction patterns the strain field in single nanowires can be found in Ref. [Newton et al., 2010]. Here, for the first time, the six independent components of the strain field of the same nanorod were reconstructed. ZnO rod-shaped nanocrystals, synthesized through a chemical vapour transport and deposition, have been investigated in that work. The hexagonal-prism-shaped crystals have lengths in the range of $2-4$ μm and widths of $1-2$ μm. Measurements have been carried out at the Advanced Photon Source and diffractions have been collected from six-independent Bragg reflections. This enabled to retrieve from all three orthogonal components of the displacement vector u_i the nine components of the Eulerian strain (ϵ) tensor and rigid-body rotation (τ). In Fig. 1.19 regions of compressive (negative) strain are observed near the (100) surfaces of the crystal and at the interface with the Si substrate. A strained layer approximately 200 nm in width near the surface and along the length of the rod (y axis) is visible in all tensor components except the ϵ_{yy} component. This implies that the strain is uniform along the length of the rod.

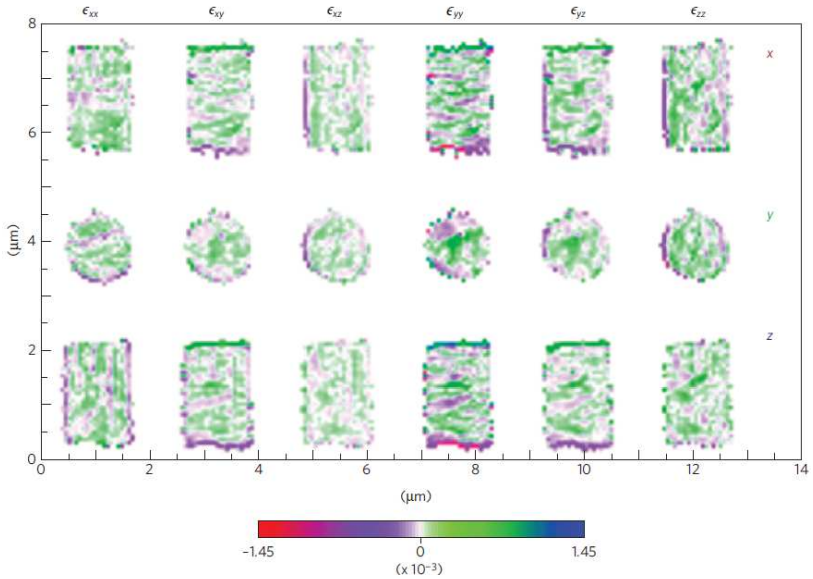

Figure 1.19: Two-dimensional slices of the six independent components of the strain tensor.[Newton et al., 2010]

The first evidence of CDI applied to heterogeneous structure is reported by Minkevich et al. [2011]. There, the strain distribution in (Ga,Mn)As/GaAs nanowires was determined by artificially separating the two different contributions of the coherent diffraction signal. The vertical components μ_z of the reconstructed displacement field is shown in Fig. 1.20, for the (004) Bragg reflection. As mentioned, this map is the result of two independent reconstructions, one considering the only contribution of (Ga,Mn)As (upper slide in Fig. 1.20a) and further isolating the signal coming from GaAs part (lower slide in Fig. 1.20a) in the reciprocal space pattern. A specific phase retrieval algorithm reported in Ref. [Minkevich et al., 2007] was developed for this specific case. The results of the reconstruction are in

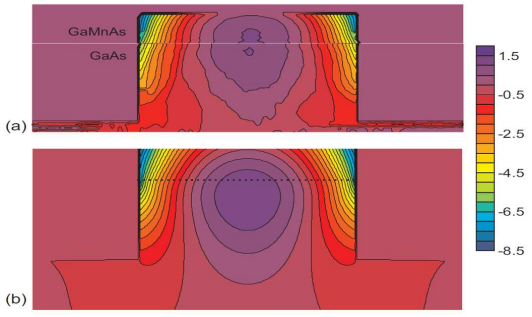

Figure 1.20: (a) Reconstructed vertical component μ_z of the dispacement field in a (Ga,Mn)As/GaAs nanowire. (b) Numerical calculation of μ_z using finite element methods. [Minkevich et al., 2011]

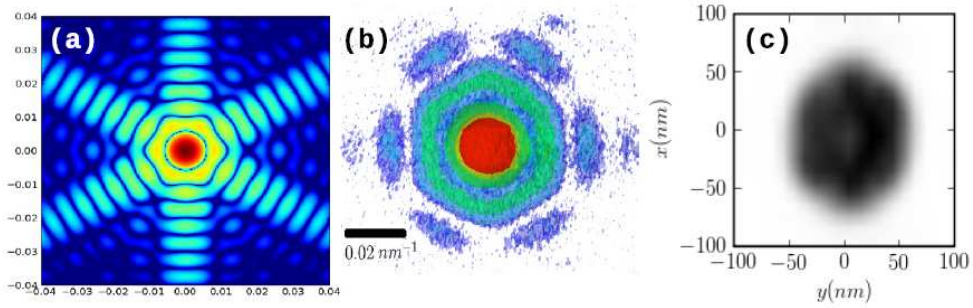

Figure 1.21: CDI of a single Si nanowire: (a) simulated 2D scattering pattern (in the plane perpendicular to the nanowire axis), (b) experimental pattern recorded on a 95 nm silicon nanowire and (c) the corresponding real-space reconstruction of the nanowire cross-section

perfect agreement with numerical calculations (Fig. 1.20b), demonstrating the validity of the method.

The following two reported examples are referred to recent results obtained from single nanowires investigated using CDI at the ID01 beamline at the ESRF, where experiments described in this work have been performed.

In reference Favre-Nicolin et al. [2009], a single homogeneous silicon nanowire was imaged using CDI. The simulated 2D scattering pattern (in the plane perpendicular to the nanowire axis) (Fig. 1.21a), is compared to the experimental pattern recorded on a homogeneous silicon nanowire (Fig. 1.21b), with a diameter of 95 nm. The experimental pattern has been used as input of an iterative phase retrieval algorithm to obtain a real-space reconstruction of the nanowire cross-section (Fig. 1.21c). In this specific case, the reconstructed nanowire didn't present any internal strain; however these results are important as a first proof of CDI feasibility on single nanowires with diameters smaller than 100 nm and with quite low scattering atoms ($Z_{Si} = 14$).

Another example is reported in reference [Diaz et al., 2009]. Here the cross section of an InAs nanowire of 150 nm diameter grown on an InP 111-oriented substrate were imaged, achieving a resolutions of about 8 nm in the x direction and 16 nm in the y direction. The reconstruction were performed using a centro-symmetrised diffraction pattern collected around the (111) InAs peak, in order to fill the region of missing data. The obtained reconstruction is shown in Fig. 1.22. The reconstructed phase is shown in Fig. 1.22b. Within the wire region, the phase shows smooth variations. Since the illuminated part of the wire was strain-free, these phase variations were attributed by the authors to artefacts in the experimental data or to

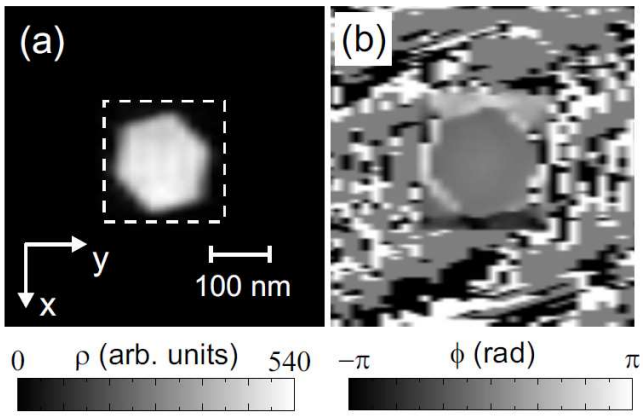

Figure 1.22: (a) Retrieved complex-valued electron density and (b) phase of the wire section. Scales in both a and b are linear. The dashed square indicates the support region used in the reconstruction algorithm. [Diaz et al., 2009]

a distorted incident wave front onto the sample.

As shown by these examples, the knowledge of the illumination function is a fundamental issue when using coherent x-ray imaging technique. Further, this represents the motivation of part of the work presented in this manuscript and developed in Chapter 4.

Chapter 2

Coherent X-ray Diffraction Imaging

The knowledge of the atomic position is achievable by means of x-ray diffraction techniques only in presence of ordered atomic array. In the case of disordered systems the exact positions of scatterers can not be measured and the accuracy relies on the goodness of theoretical models. This is due to the so-called phase problem discuss in the following. Coherent diffraction imaging offers a model-free method to overcome the phase problem and obtain the atomic structure. In this chapter the basic principles of x-ray diffraction[1] are reviewed in order to introduce the coherent x-ray diffraction Imaging technique. In the last section, the experimental set-up used for coherent experiments at the undulator beamline ID01 at the European Synchrotron Radiation Facility in Grenoble (France) is also described.

2.1 X-ray diffraction

X-rays are deeply penetrating electromagnetic radiation with wavelengths ranging from 0.1 to 6 $\mathring{A}$ (hard x-rays) and from 6 to 100 $\mathring{A}$ (soft x-rays). X-rays are employed in several domains of material science, such as crystallography, radiography and spectroscopy, to probe the electron density of studied materials through either absorption or scattering process with the aim of determining the internal atomic structure.

For the studies of relevance to this work, a monochromatic beam is employed, in the range of hard x-rays. Such a beam is produced by a synchrotron radiation source with high brilliance and (partial) coherence

[1]The term "diffraction" is often employed in the text to indicate the x-ray scattering.

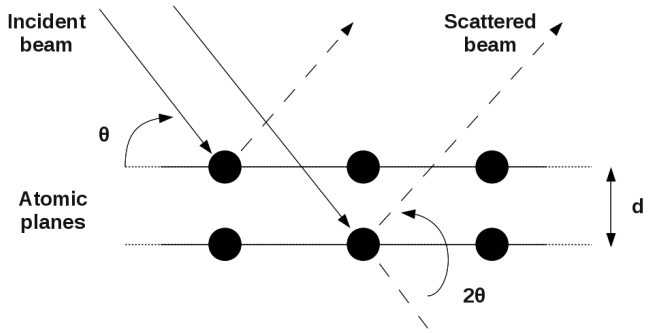

Figure 2.1: Bragg scattering geometry : the incident beam is scattered by atoms of parallel atomic planes. The length path difference between two scattered beams can be used to determine the atomic distance d of two atomic planes.

characteristics. Two assumptions can be used to describe the interaction of x-rays with matter. First, the incoming wavefield, with amplitude U and wavevector $\mathbf{k}$, is considered as a monochromatic plane wave. Second, the kinematical approximation is also assumed [Warren, 1990], i.e. the incident beam has the same magnitude all over the specimen and it is elastically scattered form single scatterers (Born approximation).

Let consider an x-ray beam, with wavelength λ and incident angle θ, that impinges on a crystal. The geometry of the considered process is depicted in Fig. 2.1, in which, for simplicity, only two parallel atomic planes are depicted. The plane wave is elastically scattered from electrons according to the Bragg's law:

$$n\lambda = 2d\sin\theta, \quad n\epsilon\mathbb{N} \tag{2.1}$$

In this relation, d is the distance between the two parallel planes and $2d\sin\theta$ represents the optical path difference between the two waves. The interference between scattered wavefronts is constructive only if it is equal to $n\lambda$. This simply means that constructive interference occurs when the phases are equal, i.e. when n is an integer. Every angle 2θ at which constructive interference can be registered is called Bragg angle.

In this discussion, phases of incident waves are considered identical. This is generally not true as the source size and beam wavelength play an important role on the determination of the phase. The distance over which phases are equivalent is called coherence length and it defines the spatial coherence of the beam. This point is of primary importance for this work and will be discussed in details further in this chapter.

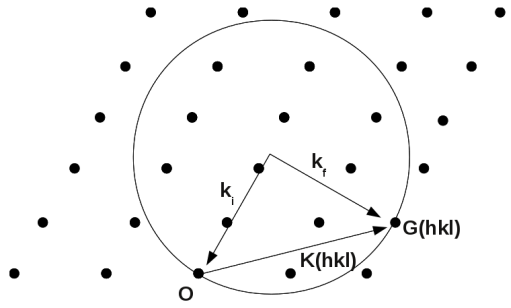

Figure 2.2: Two-dimensional Ewald sphere: Bragg condition is satisfied for any point of the circle, overlying point on the lattice in the reciprocal space S(hk)=G(hk).

Moreover, assumed the kinematical approximation, the measured intensity $I(\mathbf{s})$ is given by the following equation:

$$I(\mathbf{s}) = |\mathbf{A}(\mathbf{s})|^2 = \left| \int_V \rho(\mathbf{r}) e^{2i\pi \mathbf{s}\cdot\mathbf{r}} dV \right|^2 = |FT[\rho(\mathbf{r})]|^2 \tag{2.2}$$

$\mathbf{A}(\mathbf{s})$ is the complex function that describes the scattering, $\mathbf{s} = \mathbf{s}_f - \mathbf{s}_i$ represents the scattering vector, where $\mathbf{s}_f$ and $\mathbf{s}_i$ are the scattered and the incident wavevectors ($|\mathbf{s}_f| = |\mathbf{s}_i| = 1/\lambda$), $\rho(\mathbf{r})$ the electron density in the volume V, $\mathbf{r}$ is the vector indicating the electron position in the lattice and FT denotes the Fourier Transform operator.

The three dimensional lattice of a crystal is defined using a set of vectors $\mathbf{R_n} = x\mathbf{a} + y\mathbf{b} + z\mathbf{c}$, where (x,y,z) are integers and a, b,c the lattice parameters of the unit cell. The scattered amplitude of the unit cell is described by the structure factor $F(\mathbf{s})$, that represents the Fourier transform of the electron density into the unit cell:

$$F(\mathbf{s}) = \sum_{jj=1}^{N} f_{jj}(\mathbf{s}) e^{2\pi i \mathbf{s}\cdot\mathbf{r}_{jj}} \tag{2.3}$$

that is valid for jj atoms inside a unit cell at positions $\mathbf{r}_{jj}$ with atomic form factor $f_{jj}(\mathbf{s})$, which is the Fourier transform of the electron density of the atom. Considering that a finite crystal can be built from the lattice and assuming a perfect crystal lattice and a perfectly coherent illuminating beam, the scattered amplitude can be written as:

$$A(\mathbf{s}) = F(\mathbf{s}) \sum_{R_n}^{lattice} e^{2\pi i \mathbf{s}\cdot R_n} \tag{2.4}$$

The recorded intensity is therefore proportional to

$$I(\mathbf{s}) \propto \frac{sin^2(\pi N_1 \mathbf{s}\cdot\mathbf{a})}{sin^2(\pi \mathbf{s}\cdot\mathbf{a})} \cdot \frac{sin^2(\pi N_2 \mathbf{s}\cdot\mathbf{b})}{sin^2(\pi \mathbf{s}\cdot\mathbf{b})} \cdot \frac{sin^2(\pi N_3 \mathbf{s}\cdot\mathbf{c})}{sin^2(\pi \mathbf{s}\cdot\mathbf{c})} \tag{2.5}$$

where N_1, N_2 and N_3 are the number of unit cells along $\mathbf{a}$, $\mathbf{b}$ and $\mathbf{c}$. The intensity can be registered when

$$\mathbf{s}\cdot\mathbf{R}_n = m. \tag{2.6}$$

In the reciprocal lattice unit, Eq. 2.6 is satisfied if

$$\mathbf{a}\cdot\mathbf{a}^* = h, \quad \mathbf{b}\cdot\mathbf{b}^* = k, \quad \mathbf{c}\cdot\mathbf{c}^* = l, \tag{2.7}$$

where (hkl) are the so-called Miller indices of the structure and $\mathbf{a}^*$, $\mathbf{b}^*$ and $\mathbf{c}^*$ are the basis vector of the reciprocal space. Points in the reciprocal space are defined by the vector $\mathbf{G} = h\mathbf{a}^* + k\mathbf{b}^* + l\mathbf{c}^*$. The Bragg reflection occurs when $\mathbf{K}(hkl) = \mathbf{G}(hkl)$. The Ewald sphere, defined in reciprocal space, consists of a geometrical spherical shell of radius $1/\lambda$. For sake of simplicity in Fig 2.2 a two dimensional Ewald circle is illustrated. Using the Ewald sphere, each reciprocal lattice point defined by $\mathbf{G}(hkl)$ and lying on its surface meets the Bragg condition. All the directions (hkl) for which the Bragg condition is met, i.e. the interference is constructive, are called diffraction peaks (or Bragg peaks).

2.2 Coherence properties of a Synchrotron radiation

X-ray beams available in a Synchrotron facility with (partially) coherent characteristics and low divergence are generally obtained. The wavefront has a precise phase relation that has to be preserved during the propagation. High degree of coherence is achieved using small source size and increasing the distance between source and sample position (discussed in the following). Due to the small divergence, photons propagate at small angle with respect to the direction of the beam at the exit of the source. This characteristic, which assumes that $sin\theta \approx \theta$, where θ is the angle subtended by the direction of propagation and the axis of the beam, allows to use the paraxial approximation in a theoretical treatment (for details see Chapter

4). Moreover, a synchrotron source naturally produces polarised radiation. The polarisation direction is along the instantaneous acceleration of the electron, i.e. in the horizontal plane, as the velocity is tangential to the orbit. An observer in the vertical plane with respect to the sample is, therefore, insensitive to this polarisation. For this reason, most of the experiments at a synchrotron facility are carried out using vertical scattering plane as no loss of intensity due to the polarization factor are observed. In this condition the degree of coherence can be estimated using a scalar formalism of electromagnetic theory, neglecting effects due to the polarization.

2.2.1 Temporal and Spatial coherence

Instead of giving the complete theoretical description of the coherence properties of a complex field [Born Wolf 1999], a simple geometrical argument can be offered to get a good estimation of the degree of coherence of a radiation. From an experimental point of view, the characteristic scale used is the so-called coherence length. Two different coherence length can be distinguished: the " *spatial* or *transverse coherence length*" ϵ_T and the "*temporal* or *longitudinal coherence* " ϵ_L.

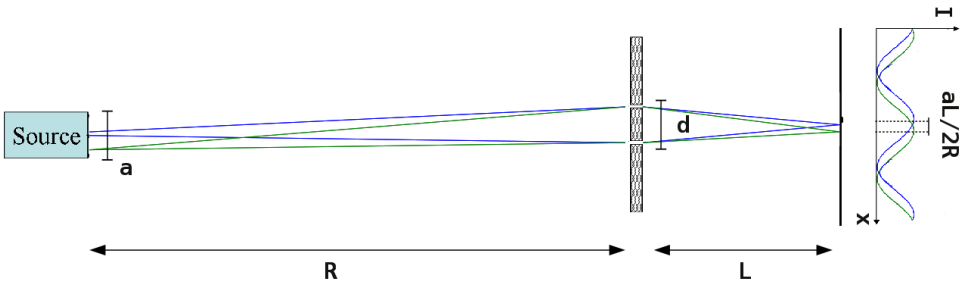

Figure 2.3: Young's Double slits experiment: the interference pattern from two slits separated by a distance d. Slits are illuminated by the central part (solid line) and the edge (dotted line) of the source a.

Spatial coherence : We consider the double slits experiment with a one-dimensional source of transverse size a. A sketch of the experiment is shown in Fig. 2.3. Each point of the source is completely incoherent. R is the distance between the source a and the slits, separated by d. At a distance L from the slits a screen is placed to collect the interference. Two

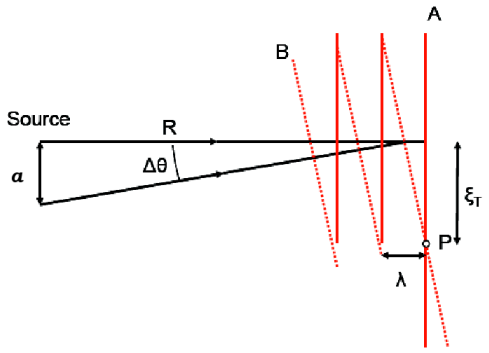

Figure 2.4: Another representation of the transverse coherent length ϵ_T. [Leake, 2010]

patterns are generated, both due to the scattering of the slits (Fig. 2.3): one is produced by the central part of the source and another shifted by an angle $a/2R$ with respect to the previous given by the scattering of an element at the edge of the source. Maxima and minima of these diffraction patterns coincide if

$$\frac{\lambda}{2d} = \frac{a}{2R} \tag{2.8}$$

The analytical expression for ϵ_T can be derived from condition 2.8, assuming that ϵ_T is represented by the distance d between the two pinhole:

$$\epsilon_T = d = \frac{\lambda R}{2a} \tag{2.9}$$

Another representation of the transverse coherence length is shown in Fig. 2.4. Two wavefronts are propagating from two points of a source, distant d. They have the same wavelength and propagate in two different directions coinciding at the point P. The propagation direction is dependent on the source size, two points at the extent of the source will have the largest divergence angle and set the limit on ϵ_T . Therefore, ϵ_T can also be interpreted as the distance travelled along the wavefront A from the point P in both directions at which destructive interference occurs .

In a more realistic case, i.e. a two dimensional source responding to a Gaussian intensity distribution, the horizontal and vertical coherence lengths can be defined as:

$$\epsilon_h = \frac{\lambda R}{2\pi\sigma_h} \qquad \epsilon_v = \frac{\lambda R}{2\pi\sigma_v} \tag{2.10}$$

σ_h and σ_v are the sigma width of the Gaussian distribution [van der Veen and Pfeiffer, 2004]. It is worth noticing that the transverse coherence length grows linearly with the distance from the source. It means that even a fully incoherent source can get coherent properties if it is measured sufficiently far. This happens in a synchrotron radiation source, consisting of incoherent emitters confined in a small source size. The degree of coherence is enhanced increasing the distance source-sample position or reducing the source size.

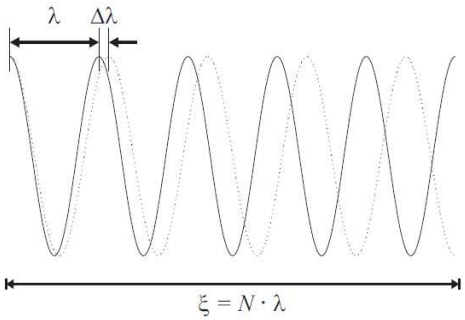

Figure 2.5: Two quasi-monochromatic waves of wavelenght λ and $\lambda + \Delta\lambda$. The difference in phase is π at the longitudinal coherence length. [Dierolf, 2007]

Longitudinal coherence : Two wavefields start from the same point but with two different wavelengths λ and $\lambda + \Delta\lambda$, respectively. The longitudinal coherence length ϵ_L defines the distance at which the difference in phase of two waves is π, as illustrated in Fig. 2.5 and it is equal to $\epsilon_L = N\lambda/2$. We suppose that after N/2 oscillations of the first wave, the second one has made only N/2-1 oscillations; in this condition waves are in anti-phase. In the limit of $N \Rightarrow \infty$

$$\frac{N}{2}\lambda = (\frac{N}{2} - 1)(\lambda + \Delta\lambda) \Rightarrow \frac{\lambda}{\Delta\lambda} = \frac{N}{2} - 1 \approx \frac{N}{2}, \quad N \gg 1 \qquad (2.11)$$

and

$$\epsilon_L = \frac{\lambda^2}{2\Delta\lambda} \qquad (2.12)$$

The longitudinal coherence is dependent on the bandwidth of the monochromator ($\Delta\lambda/\lambda$), that is attributed to the thickness of the monochromator crystal. Contrarily to the transverse coherence length , ϵ_L does not depend on the source size and neither on geometrical distances. When the optical

path length difference through the sample is smaller than ϵ_L, a sample is coherently illuminated, meeting the required conditions for CDI measurements.

For a typical synchrotron source whose size is $125_h \times 30_v$ μm^2 distant 50 m from the sample position, $\epsilon_h = 20$ μm, $\epsilon_v = 60$ μm and $\epsilon_L = 0.5$ μm for $\lambda = 1$ $\mathring{A}$ and a Si(111) bandwidth of $\approx 10^{-4}$; therefore the longitudinal coherence length is the limiting factor for successful CDI measurements. However, he coherence lengths are sufficient to investigate micro/nano-sized objects with nanometre precision.

2.2.2 Mutual coherence function and degree of coherence

A typical measure of the degree of coherence between two scattered x-ray beams is the visibility ν, defined as the contrast of fringes in a interference pattern:

$$\nu = \frac{I_{max} - I_{min}}{I_{max} + I_{min}} \tag{2.13}$$

For the coherent illumination of two point scatterers the visibility of the interference pattern is equal to 1 for all fringes, and drop to zero as the two fields are π out of phase. Theoretically, the degree of coherence can be expressed through the mutual coherence function Γ. We consider an electromagnetic radiation, with electric field $U(\rho, t)$; here ρ defines positions in three-dimensional space and t the time. Coherence properties at the sample position are defined by the mutual coherence function $\Gamma(\rho_\mathbf{1}, \rho_\mathbf{2}, \tau)$, where ρ_1 and ρ_2 are the positions at time t and $t + \tau$, respectively :

$$\Gamma(\rho_\mathbf{1}, \rho_\mathbf{2}, \tau) = \left\langle U(\rho_\mathbf{1}, t) U^*(\rho_\mathbf{2}, t + \tau) \right\rangle \tag{2.14}$$

The mutual coherence function is a complex un-normalised function, treated as an ensemble average over the field after a time τ. To date, x-ray sources of relevance to this manuscript, have essentially a thermal, i.e. Gaussian, character, so that the electric field $U(\rho, t)$ is completely defined by the first order mutual coherence function $\Gamma(\rho_\mathbf{1}, \rho_\mathbf{2}, \tau)$ [Lemieux and Durian, 1999, Nugent, 2010]. The degree of coherence is, in the simplest form, the nor-

malised mutual coherence function, defined as follows:

$$\gamma^1(\rho_\mathbf{1}, \rho_\mathbf{2}, \tau) = \frac{\Gamma(\rho_\mathbf{1}, \rho_\mathbf{2}, \tau)}{\sqrt{\Gamma(\rho_\mathbf{1}, \rho_\mathbf{1}, 0)\Gamma(\rho_\mathbf{2}, \rho_\mathbf{2}, 0)}} \tag{2.15}$$

If we identify the self correlation function with the intensity distribution at the detector , i.e. $\Gamma(\rho, \rho, t) = \langle I(\rho, t)\rangle$ and substitute in Eq. 2.15, we obtain

$$\gamma^1(\rho_\mathbf{1}, \rho_\mathbf{2}, \tau) = \frac{\left\langle U(\rho_\mathbf{1}, t)U^*(\rho_\mathbf{2}, t+\tau)\right\rangle}{\sqrt{\langle I(\rho_\mathbf{1}, 0)\rangle \langle I(\rho_\mathbf{2}, 0)\rangle}} \tag{2.16}$$

$\gamma^1(\rho_\mathbf{1}, \rho_\mathbf{2}, \tau)$ is a first order complex correlation function in terms of intensities and a second order function in terms of field. Due to the fact that the correlation function $\gamma^1(\rho_\mathbf{1}, \rho_\mathbf{2}, \tau)$ depends on space $(\rho_\mathbf{1}, \rho_\mathbf{2})$ and time t, two coherence lengths are introduced.

The concept of mutual coherence can be also explained through Young's two pinholes experiment [Young, 1804]. Two pinholes are placed in $P_1(\rho_\mathbf{1})$ and $P_2(\rho_\mathbf{2})$; the distance between pinholes and detector is assumed to be large compared to the wavelength of the considered radiation (c.f. Fig. 2.3). Radiations reach the detector at $t = t_0 + \tau$, where τ the time delay simply defined as $\tau = (R_1 - R_2)/c$; c is the speed of light in vacuum and R_1 and R_2 are distances between pinholes at P_1 and P_2 and a generic point Q on the detector surface, respectively. The spatial intensity distribution on the detector is given by the following expression [Lahiri and Wolf, 2010, Mandel and Wolf, 1995]:

$$\begin{aligned}\langle I(\rho, t)\rangle = \quad & \langle I(\rho_\mathbf{1}, t)\rangle + \langle I(\rho_\mathbf{2}, t)\rangle + \\ & 2\sqrt{I(\rho_\mathbf{1}, t)}\sqrt{I(\rho_\mathbf{2}, t)}R\left\{\gamma(\rho_\mathbf{1}, \rho_\mathbf{2}, \tau)\right\}\end{aligned} \tag{2.17}$$

The quantity $R\left\{\gamma(\rho_\mathbf{1}, \rho_\mathbf{2}, \tau)\right\}$ is the real part of the mutual coherence function defined in Eq. 2.16. If intensities in P_1 and P_2 are the same, considering that electromagnetic fields obey to Gaussian statistics, the squared modulus of the complex function $\gamma^1(\rho_\mathbf{1}, \rho_\mathbf{2}, \tau)$ [Oliver et al., 1999]:

$$\left|\gamma^1(\rho_\mathbf{1}, \rho_\mathbf{2}, \tau)\right|^2 = \frac{\left\langle I(\rho_\mathbf{1}, t)I^*(\rho_\mathbf{2}, t+\tau)\right\rangle}{\langle I(\rho_\mathbf{1}, t)\rangle \langle I(\rho_\mathbf{2}, t)\rangle} \tag{2.18}$$

gives the degree of coherence that is directly related to the visibility of the

interference fringes on the detector, so that

$$\nu = \left|\gamma^1(\rho_\mathbf{1}, \rho_\mathbf{2}, \tau)\right|^2 \tag{2.19}$$

2.3 Coherent X-ray Diffraction imaging on strained nano-objects

The particular case of coherent X-rays focused on small objects is treated in this section. Coherent diffraction imaging (CDI) has been developed to be suitable in small-angle experiments, for which small values of $\mathbf{s} = \mathbf{s}_f - \mathbf{s}_i$ are used. The goal of CDI is therefore to allow the reconstruction of single objects, independently on their crystallinity, as biomolecules [Beetz et al., 2005, Miao et al., 2001, Kewish et al., 2010a] and amorphous materials [Barty et al., 2008]. The three-dimensional (3D) reconstruction, in this case, can be obtained from a 3D scattering data (Eq. 2.2) obtained with a tomographic approach [Marchesini et al., 2003a, Yefanov et al., 2009]. The small angle regime is unsuitable when, in a nano-object, crystalline structures and displacement fields have to be determined, as in this regime one is only sensitive to the total electron density and not to the order. To this aim the CDI technique has been developed also in Bragg conditions [Vartanyants et al., 2005, Pfeifer et al., 2006, Williams et al., 2003, Robinson and Harder, 2009, Robinson et al., 2001, Stadler et al., 2007]. The analytical approach that describes scattering from nanocrystals using CDI start from Eq. 2.3 where the position of single scatterers is made explicit. Therefore, in this case, an atomistic formulation is preferred. The intensity recorded during a CDI experiment for a structure is

$$I(\mathbf{s}) = |\mathbf{A}(\mathbf{s})|^2 = \left|\Sigma_i f_i(\mathbf{s}) e^{2i\pi\mathbf{s}\cdot\mathbf{r}_i^{'}}\right|^2 \tag{2.20}$$

$f_i(\mathbf{s})$ and $\mathbf{r}_i^{'}$ are the scattering factor and the position of the atom i, respectively. If we are in presence of strain, the position of the atom i differs from the ideal (unstrained) one according to the following relation:

$$\mathbf{r}_i^{'} = \mathbf{r}_i^0 + \mathbf{u}_i \tag{2.21}$$

$\mathbf{r}_i^0$ is the position in the unstrained structure and $\mathbf{u}_i$ the displacement from that position. Displacement fields, if relatively small within the unit cell, can

be calculated around a Bragg reflection using a block unit cells formalism:

$$\mathbf{r}_{ij} = \mathbf{R}_j^0 + \mathbf{U}_j + \mathbf{r}_i \tag{2.22}$$

where $\mathbf{r}_{ij}$ is the position of the atom i in the cell j and $\mathbf{r}_i$ the position of the atom i relative to the unit cell. $\mathbf{R}_j^0$ and $\mathbf{U}_j$ denote the ideal positions and the displacement of the unit cell j, respectively. Substituting Eq. 2.22 in Eq. 2.21 , the scattering $\mathbf{A}(\mathbf{s})$ can be rewritten as:

$$\mathbf{A}(\mathbf{s}) = \Sigma_i \Sigma_j f_i(\mathbf{s}) e^{2i\pi\mathbf{s}\cdot(\mathbf{R}_j^0+\mathbf{U}_j+\mathbf{r}_i)} = F(\mathbf{s})\Sigma_j e^{2i\pi\mathbf{s}\cdot(\mathbf{R}_j^0+\mathbf{U}_j)} \tag{2.23}$$

and

$$F(\mathbf{s}) = \Sigma_i f_i e^{2i\pi\mathbf{s}\cdot(\mathbf{r}_i)} \tag{2.24}$$

The function $F(\mathbf{s})$ is introduced to denote the structure factor of the undeformed crystal, assuming that the crystallographic components are the same in all the unit cells. If the condition

$$\|\mathbf{s} - \mathbf{s_0}\| \cdot \mathbf{U_j} \ll 1 \tag{2.25}$$

is satisfied, $\mathbf{s} \cdot \mathbf{U_j}$ can be approximated to $\mathbf{s_0} \cdot \mathbf{U_j}$. Here $\mathbf{s_0}$ represents the scattering vector of the chosen Bragg reflection and, using Eq. 2.24 and Eq. 2.25. The scattering amplitude $\mathbf{A}(\mathbf{s})$ becomes

$$\mathbf{A}(\mathbf{s}) = F(\mathbf{s})\Sigma_j f_i(\mathbf{s}) e^{2i\pi\mathbf{s}\cdot(\mathbf{R}_j^0)} e^{2i\pi\mathbf{s}\cdot\mathbf{U}_j} \approx F(\mathbf{s}) FT[e^{2i\pi\mathbf{s_0}\cdot(\mathbf{U}_j)}] \tag{2.26}$$

This last approximation is generally used for the analysis of CDI experiments [Livet, 2007, Chamard et al., 2008, Labat et al., 2007] as it allows a fast Fourier transform computation. However, its validity strongly depends on the size of the object and the amplitude of its deformation [Favre-Nicolin et al., 2010]. This point will be treated in details in Chapter 4. It is important to underline that the sensitivity of CDI technique to displacement fields is limited to the direction parallel to the scattering vector; as shown in Eq. 2.26 only the projection of the displacement onto the scattering vector is accessible. A complete description of the 3D deformation can be achieved if scattering data are collected at least for three linearly independent reflections of the same object [Leake et al., 2009, Newton et al., 2010, Beitra et al., 2010]. With symmetry considerations, the number of independent re-

flections may be reduced. In conclusion, the main innovation of CDI is that this technique is sensitive to the displacement in a crystal and objects can be reconstructed with a resolution even smaller than the d-spacing of the considered reflection. Moreover, due to the penetration depth of x-rays, also buried structure or core-shell structure, inaccessible with other techniques, can be studied without any sample preparation, such as removing the protecting shell, and maintaining unaltered their strain state, contrarily to the case of electron-based microscopy. So far, only small objects ($< 200nm$) have been taken into account for the discussion. However, in the case of larger materials and made of heavy material, the kinematical approximation is not valid anymore. A more appropriate description may be done including also refraction and absorption effects [Stadler et al., 2007].

From an experimental point of view, beside the transverse coherence length one has to consider the aberration of the wavefront which are introduced by optical elements between source and sample. As an example, the wavefield close to the focal point is not a perfect plane wave. The incident wave has generally a characteristic curvature that have to be taken into account when object dimensions are not comparable or even larger than the beam size [Nugent et al., 2005, 2003, Quiney et al., 2005, Williams et al., 2007]. The curvature [Williams et al., 2006] induces relevant variations in both the amplitude and phase of the beam and it influences the diffraction from the illuminated object. However, in the case of a scattering object with a transverse dimension smaller than 200 nm, the wavefield can be approximated to a plane wave only if this object is completely contained in the coherent focal spot which exhibits a constant phase. [Schroer et al., 2008]. This point is discussed in details in Chapter 3.

2.3.1 Phase Retrieval Algorithm

According to Eq. 2.2 and 2.20, only scattering intensities can be recorded during a diffraction experiment and the phase factor (that contains information about the displacement field of the nano-crystal) is lost. CDI offers a suitable method to recover amplitude and phase from the diffraction pattern through dedicated phase retrieval algorithms. No a priori information about the nanostructure is needed. The mechanism of phase retrieval algorithms can be easily understood in the framework of iterative projections onto constraint sets in both direct and reciprocal spaces [Elser, 2003]. Phase retrieval algorithms provide a solution that intersects constraint sets by pro-

jecting the estimation onto each set. The Fourier operator, used to describe relation between an object and its diffraction, is the linear unitary transformation between bases (direct and reciprocal spaces) where constrains are applied. We now consider in N-dimensional Euclidean vector space V_N a discrete object contained in a finite volume S . The vector $f(x_n)$ describes objects as linear transformations in N-dimensional orthogonal bases, with $n \in [1, N]$. Two constraint sets can be introduced: the support C_S and the Fourier amplitude C_F constraints, so that, if y_n is the closest point to x_n that satisfies the given constraint, $F(y_n)$ is the Fourier transform of $f(x_n)$ [Dierolf, 2007].

$$C_S = \begin{cases} 1 & \text{if } x_n \in S \\ 0 & \text{otherwise.} \end{cases} \tag{2.27}$$

$$C_F = \{\mathrm{F} \in V_N \quad | \quad |\tilde{y}_n| = |m_n| \; \forall n \in [1, N]\} \tag{2.28}$$

m_n are measured Fourier amplitudes. The phase retrieval problem can be considered solved if

$$\mathrm{f} \in C_S \cap C_F \tag{2.29}$$

and the intersection of C_S and C_F consists of one single point. A set of constraints-operator is therefore introduced; an operator P so that $P(\mathrm{x}) = \mathrm{y} \mid \|\mathrm{x} - \mathrm{y}\|$ is minimized. In the considered case, two projections operator can be defined, P_S for support constraints and the P_F in the Fourier space, so that:

$$P_S(x_n) = \begin{cases} 1 & \text{if } n \in S \\ 0 & \text{otherwise} \end{cases} \tag{2.30}$$

and

$$\tilde{P}_S(\tilde{x}_n) = \begin{cases} m_n \frac{\tilde{x}_n}{|\tilde{x}_n|}, & \text{if } x_n \neq 0; \\ m_n e^{i\alpha} & \text{otherwise} \end{cases} \tag{2.31}$$

where $\tilde{P}_S = F^{-1} P_S \; F$ is the projector P_S in the Fourier space. For a non-zero component $\tilde{x}_n = |\tilde{x}_n| \, e^{i\Phi_n}$ the amplitude in Fourier space is replaced while the phase is kept. For zero-valued pixels any phase α will work even

if in practice $\alpha = 0$. These projections are applied in n iterations when using iterative phase retrieval algorithms: starting from f_n the next iterated image f_{n+1} is obtained applying a particular combination G_{P_S,P_F} of P_S and P_F :

$$\mathrm{f}_{n+1} = G_{P_S,P_F}(\mathrm{f}_n) \tag{2.32}$$

The convergence is achieved when the iterate does not change anymore. Conventional Phase retrieval algorithms are based on different choices of G_{P_S,P_F}.

Error-Reduction (ER) Algorithm : Presented for the first time by Gerchberg and Saxton [1972], the algorithm was modified by Fienup into the modern ER algorithm. Fienup proposed to use real-space constraints introducing a finite support instead of intensity measurements, allowed only in the reciprocal space [Fienup, 1978, 1987, 1982]. The name Error-Reduction came from the fact that at each projection the closest point satisfying the set of constraints is found and the distance between two sets is minimized. Equation for this algorithm can be written as follows:

$$\mathrm{f}_{n+1} = P_S(P_F(\mathrm{f}_n)) \tag{2.33}$$

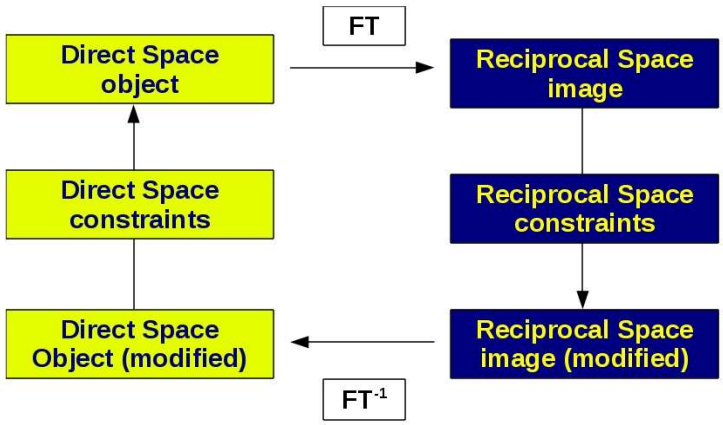

Figure 2.6: Representation of Error-Reduction phase retrieval algorithm. Starting with an arbitrary guess, it consists of several loop between real and reciprocal space by means of Fourier Transformation back and forth and applying in each spaces a set of constrained.

The algorithm starts with an initial guess, corresponding to the measured amplitude, and a first estimation of the real space object is obtained applying a back Fourier Transform to the initial guess to which a random phase is added. In real space a set of constraints is applied: the support constraint according to which all data outside S are set to zero, and, in the case of undeformed objects, the non-negativity, that assures the positivity of the reconstructed real-space density. The constrained object is Fourier transformed and the reconstructed amplitude is replaced by measurements. These steps are repeated until the convergence of the algorithm, that is assured introducing a metric error, usually obtained looking at the autocorrelation of the diffraction pattern [Fienup, 1986]. The schematics of the algorithm is shown in Fig. 2.6 Unfortunately, the ER algorithm easily stacks into local minima and is not sufficient to reconstruction of the object in real space due to the low convergence.

Hybrid Input-Output (HIO) Algorithm : Hybrid Input-Output (HIO) Algorithms: The HIO algorithm, developed by Fienup [Fienup, 1978, 1987, 1982] has been introduced in order to avoid stagnation of the ER algorithm. The schematics of the HIO algorithm is maintained the same of that one illustrated in Fig. 2.6. The innovation is in the modification of the real space set of constraints. The new image is not simply the best estimation that minimized the metric error; the next input is calculated as a combination of objects obtained from the previous (INPUT) and the current (OUTPUT) iterations. The aim of this algorithm is therefore minimizing the error using this combination; a large amount of variations in the next input is produced and at the same time stagnation avoided. Still using the formulation in Eq. 2.32, the HIO algorithm can be summarized as

$$\mathrm{f}_{n+1}(x_n) = P_S(P_F(\mathrm{f}_n(x_n))) = \begin{cases} P_F\mathrm{f'}_n(x_n), & \text{if} x_n \in S; \\ \mathrm{f}_n(x_n) - \beta P_F\mathrm{f'}_n(x_n), & \text{if} x_n \notin S \end{cases} \tag{2.34}$$

S is a support satisfying the support constraints, f_n and $\mathrm{f'}_n$ are the objects from the previous and the current iteration, respectively, β a feedback parameter usually chosen to be slightly smaller than the unity($0.5 < \beta < 1$). It is evident that when $\beta = 1$ HIO algorithm approaches to the case of ER algorithm, replicating the current object with the next iteration. HIO algorithms are the most used in phase retrieval problems in diffractive imaging but other algorithms and a particular combination of them has been devel-

oped to improve the convergence.

Charge Flipping (CF) Algorithm : The CF algorithm, also known as Solvent-Flattening algorithm, combined to HIO and ER algorithms has been fully developed by Oszlányi and Süto [2004] and improved by Wu et al. [2004]. It is analogous to the ER algorithm. The difference lies in the fact the all the density outside the support is not anymore set to zero but forced to be negative:

$$\mathrm{f}_{n+1}(x_n) = P_S(P_F(\mathrm{f}_n(x_n))) = \begin{cases} P_F\mathrm{f}_n(x_n), & \text{if} x_n \in S; \\ -P_F\mathrm{f}_n(x_n), & \text{if} x_n \notin S \end{cases} \tag{2.35}$$

Using the projectors formalism, the algorithm can be simplified as

$$\mathrm{f}_{n+1} = R_S(P_F(\mathrm{f}_n)) \tag{2.36}$$

With respect to the ER, the CF algorithm converges faster to the solution and it is generally used to refine an object reconstructed using a HIO algorithm.

Shrink-Wrap Algorithm : The shrink-wrap algorithm has been introduced by Marchesini [Marchesini et al., 2003b] and is now used in common phase reconstruction in coherent diffraction experiment [van Overveld and Wyvill, 2004]. With respect to HIO and ER, the object support is not fixed but it is updated during the reconstruction; it is therefore determined together with the object itself. The algorithm starts with a support that fits the first estimation of the object in real-space. The first estimate of the support is obviously not accurate, but by selecting the intensity in real-space with a threshold, support is updated until the reconstructed object fits within the autocorrelation function. We state that the support "shrinks" progressively around the object "wrapping" all its volume. This algorithm goes faster to the solutions and only one a priori information is needed, as well as for the other algorithms, that is the object has to be isolated to guarantee a strong contrast between noise and signal (visibility).

Algorithm convergence : The high number of required iterations may also be a limit for certain cases when imaging unknown objects. It is therefore necessary to define a measure of the accuracy of the reconstruction

when iterative algorithms are employed. The question of quantifying the accuracy of reconstruction is essential in order to give meaningful conclusions about the nanostructure that produced the measured diffracted intensities. To this aim, two different approaches can be used: one has the choice to compare the quality of the reconstruction in real or reciprocal space when references in both spaces are available to be compared to the most recent result of the iteration. As in coherent diffraction imaging method the reconstruction is done without the use of a model in real space, no reference intensity map in that space is given and the algorithm accuracy has to be measured in reciprocal space, comparing the latest iterate in reciprocal space with the measured diffracted intensities. In this context, the goodness of a solution is measured in terms of the R-value, i.e. the autocorrelation between the observed and the iterated intensities in reciprocal space. In the case of non-crystalline diffraction measurements, the equivalent R-value can be defined on a two or three-dimensional grids, representative of the number of pixels constituting the diffraction, as

$$R = \frac{\sum_{i,j,m} \left(\left| A^{\mathrm{Recon}}(i,j,m) \right| - \sqrt{I^{\mathrm{Meas}}(i,j,m)} \right)^2}{\sum_{i=1}^{N} I^{\mathrm{Meas}}(i,j,m)} \tag{2.37}$$

where $I^{\mathrm{Meas}}(i,j,m)$ is the observed intensity measured in a discrete array, (i,j,m) are the counters over the pixels and $A^{\mathrm{Recon}}(i,j,m)$ is the calculated diffracted amplitude from the reconstructed structure in real space.

Hovewer, as the topic of this work is motivated by the study of crystallographic objects and the measured intensities are defined at finite lattice positions, the measure of solution quality can be also based on crystallographic parameters. The traditional definition of the R-value and widely used in x-ray crystallography is

$$R = \frac{\sum_{h,k,l} \left(\left| A^{\mathrm{Recon}}(hkl) \right| - \sqrt{I^{\mathrm{Meas}}(hkl)} \right)^2}{\sum_{i=1}^{N} I^{\mathrm{Meas}}(hkl)} \tag{2.38}$$

where h, k and l are the reciprocal lattice vectors, $I^{\mathrm{Meas}}(hkl)$ are the observed intensities at each reciprocal lattice point and $A^{\mathrm{Recon}}(hkl)$ the reconstructed amplitudes at each point of the iteration calculated from the refined model of the sample structure.

2.3.2 Experimental requirements

Phase retrieval algorithms allow the reconstruction of a 3D object (real space) starting from a 3D diffraction pattern (reciprocal space) collected with dedicated detectors. The convergence of these algorithms can be achieved if the 3D image in the reciprocal space responds to particular experimental requirements.

We consider a two dimensional pixels detector of $N = N_x \cdot N_y$ pixels of a certain size $\delta x \delta y$. Being the distance detector-sample and the wavelength λ known, one can calculate the corresponding values of Δs_x and Δs_y. In real space the width L along each Cartesian axis x and y

$$L_x = 2\frac{\pi}{\Delta s_x} \qquad L_y = 2\frac{\pi}{\Delta s_y} \tag{2.39}$$

is therefore fixed by the detector features. The discrete Fourier Transform relates step size Δs in the Fourier space and Δx in direct space by the relationship

$$\Delta x \Delta s = \frac{2\pi}{N} \tag{2.40}$$

where N is the total number of pixels. Moreover, when a discrete Fourier Transform is applied, it is important to define intervals to be used in order to "sample" a continuous function with a discrete grid. If N is even, spatial frequencies (s values) are contained in the range

$$-(\frac{N}{2} - 1)\Delta s < s < (\frac{N}{2})\Delta s \tag{2.41}$$

and, considering Eq. 2.40 and 2.41, the maximum value of s is given by

$$s_{\max} = \frac{N\Delta s}{2} = \frac{\pi}{(\Delta x)} \tag{2.42}$$

Due to the periodicity of a discrete Fourier Transform, if a function in the direct space is sampled with an interval too large, all frequencies higher than $s_{\max}$ results wrapped in the Fourier space; the phenomenon according to which a continuous function is not bandwidth limited is called "aliasing". Aliasing can be avoided if a low limit, known as critical frequency, is introduced. It means that the Fourier Transform of a bandwidth limited

function $f(x, y)$ satisfy the following condition:

$$\tilde{f}(x, y) = 0 \quad \text{for} \quad |s| < s_{\text{Nyq}} \tag{2.43}$$

The critical frequency s_{Nyq} is called Nyquist frequency. Equation 2.40 can be re-written as

$$\Delta x < \frac{2\pi}{2s_{\text{Nyq}}} \tag{2.44}$$

According to Eq. 2.44, a continuous function has to be sampled at intervals at least inversely proportionals to the double of the Nyquist frequency. Condition 2.44 is also known as "the sampling theorem" [Shannon, 1998].

In an diffraction experiment, the total number of points achievable for the reconstruction is limited by the detector. Hence, Eq.2.39 and 2.44 can be combined and the total spatial intervals at the object plane derived

$$L_x = N_x \Delta x \qquad L_y = N_y \Delta y \tag{2.45}$$

If we consider now that the object in the real space is defined by a finite density function $f(x, y)$, a support S can be introduced so that

$$f(x, y) = 0, \qquad \text{for}(x, y) \notin S \tag{2.46}$$

From Eq. 2.42 the maximum size S can be derived for each coordinates

$$\Delta s_x \leq \frac{\pi}{S_x} \qquad \Delta s_y \leq \frac{\pi}{S_y} \tag{2.47}$$

This condition gives the limit at the detector plane not to be exceeded to make reconstruction possible. The frequency sampling satisfying this condition is two times higher than the Shannon condition in Eq. 2.44 (condition 2.47 is known as "oversampling" condition [Sayre, 1952, Miao and Sayre, 2000]). The oversampling ratio, used in case of X-ray diffraction experiments, is defined in direct space as [Miao and Sayre, 2000]

$$\sigma = \frac{N}{N_S} \tag{2.48}$$

where N_S is the number of pixels in the support S. Intensities registered during a CDI experiment are the square modulus of the Fourier Transform (Eq. 2.44) of the object multiplied with the probe. A unique solution $f(x, y)$

which satisfies the relation

$$I = |FT(f(x,y))|^2 \tag{2.49}$$

has to be ensured and to this aim tight constraints have to be imposed. The ambiguity of the solution lies in the fact that a set of direct space functions $f(x,y)$ exists having the identical Fourier modulus. The ambiguity includes a shift in the position of the object $f(x+\Delta x, y+\Delta y)$, the complex conjugate of the electron density $f^*(-x,-y)$ and the presence of a phase factor multiplying the function $e^{i\Phi}f(x,y)$. Different solutions can be found in literature [Bruck and Sodin, 1979, Bates et al., 1984, Baxter and Schmuttenmaer, 2006] to the uniqueness problem, i.e. when $\sigma \geq 2$ [Miao and Sayre, 2000] , so that the number of independent equations is higher than the number N of pixels to reconstruct. As recently proposed [Shapiro et al., 2005, Chapman et al., 2006a],the unique solution is provided by the complex average of independent reconstructions.

2.4 Coherent Diffraction Imaging at ID01: experimental set-up

The main goal of ID01 beamline is to study, with high resolution in real space, deformations and strain at the nanoscale. Up to now most of the research was focused on ensemble of nanostrutures, determining their average properties. But, in recent years, experimental set-up was developed and improved to use micro-focused x-ray beam for the study of individual nanostructures [Mocuta et al., 2008, Scheler et al., 2009]. Recently [Diaz et al., 2009, Biermanns et al., 2009, Favre-Nicolin et al., 2009, Chamard et al., 2010, Favre-Nicolin et al., 2010], submicrofocusing has been combined with the use of coherent beams available on ID01, reaching the ambitious goal of employing Coherent Diffraction and coherent Diffraction Imaging for spatial resolved measurement.

Before reaching the optics hutch, x-rays are produced by accelerated electrons pass through three undulators, two U35 (35 mm period) and one U42 (42 mm period) undulators. The typical bandwidth of a U35 undulator peak is $\Delta E/E = 0.01$. The U35 undulators are used in series to produce a flux 3 times higher than the one achieved with only one U42. A synchrotron radiation between 4 and 50 keV (selecting the first harmonic) can be gen-

erated. The undulator U42 is mainly introduced to reach energies below 3 keV. A front-end shutter separates the optics and the experimental hutches from the storage ring, for safety.

2.4.1 Optics

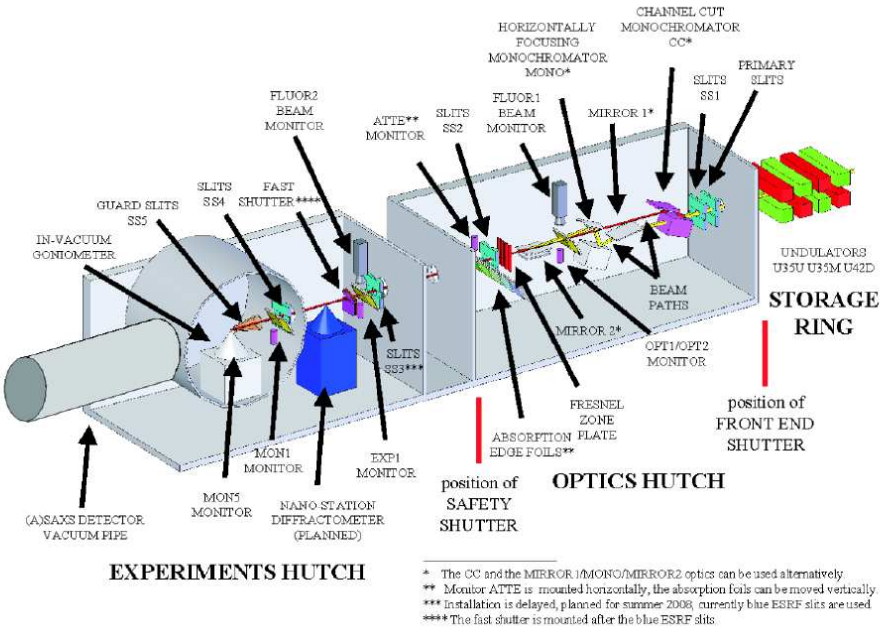

Figure 2.7: Overview of the Optics and Experimental hutches (http://www.esrf.fr)

An overview of beamline ID01 is given in figure 2.18. From the storage ring the unfocused beam pass through optics huch. Here photons are monochromatised by a double bounce Si(111) channel cut monochromator. The channel cut allows the tuning of the desired energy with an energy resolution of $\Delta E/E = 10^{-4}$. The channel cut is set to select an appropriate Bragg reflection of the Si(111) crystal. In reference Diaz et al. [2010], a study of the coherence and wavefront properties of a channel cut monochromator in comparison with a double-crystal monochromator is presented. They showed that the choice of a channel cut monochromator (CCM) is justified by the fact that it can provide a transverse coherence length twice as large as a conventional high-flux double-crystal monochromator (DCM), while not presenting stronger wavefront distortions. They found that the resulting transverse coherence length for the CCM was $\epsilon_v = 53.2$ μm, a factor 2.1 larger than for the DCM, which was $\epsilon_v = 25$ μm (see figure 2.8). Summarizing, the available transverse coherent length on ID01 is $60_v \times 20_h$ μm^2

(vertical x horizontal) for an X-ray wavelength of 1 Angstrom; these values are calculated considering a distance source to sample of 50 m and a source size in the transverse direction of 30 × 125 μm^2. The second crystal of the CC monochromator is motorized and can be tilted with respect to the first one with the aim of suppressing high harmonics contribution. Tilt angle is chosen to be below the critical angle of the first harmonic but above the one of the third harmonic.

2.4.2 Diffractometer

A heavy load 4+2-circles diffractometer is used for scattering experiments in vertical and horizontal scattering planes. The conventional 4-circle diffractometer includes 2θ , θ , Φ and χ circles, used for vertical scattering plane geometry (Fig. 2.19 a)). Two circle γ and μ are added to rotate detector arm and sample in the vertical axis allowing horizontal scattering plane geometry. A heavy duty sample stage is mounted at the centre of the diffractometer. It can hold weight up to 120 kg. Three translations along the direction of propagation (x), perpendicular to it in the horizontal (y) and vertical plane (z) are used to position the sample with a sub-microns accuracy. Adjustment of sample surface is refined with the alignment cradle (Fig. 2.19 b) with a precision of 0.001°. An azimuthal angle gives the possibility of rotating the sample around its axis in the 360° range. At the bottom of the Huber Tower, a tilt angle keep the incident beam angle constant and it is useful in particular for Grazing Incident experiment.

The station ends in a Small angle X-ray scattering (SAXS) tube.

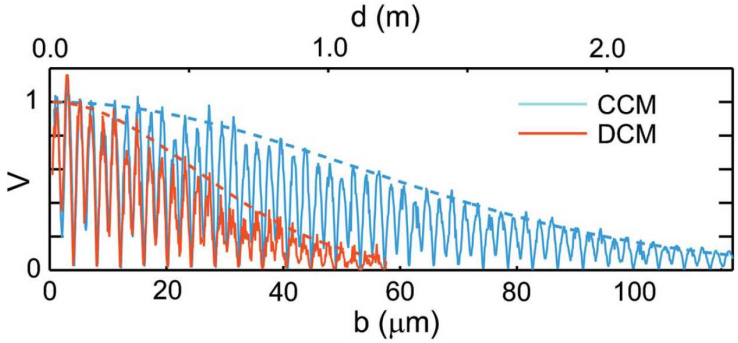

Figure 2.8: Measured visibility of the moiré fringes pattern for the CCM (in blue) and the DCM (in red). The envelope functions were fitted to Gaussian curves (dashed lines) and give a measurement of the complex coherence function in the vertical direction. [Diaz et al., 2010]

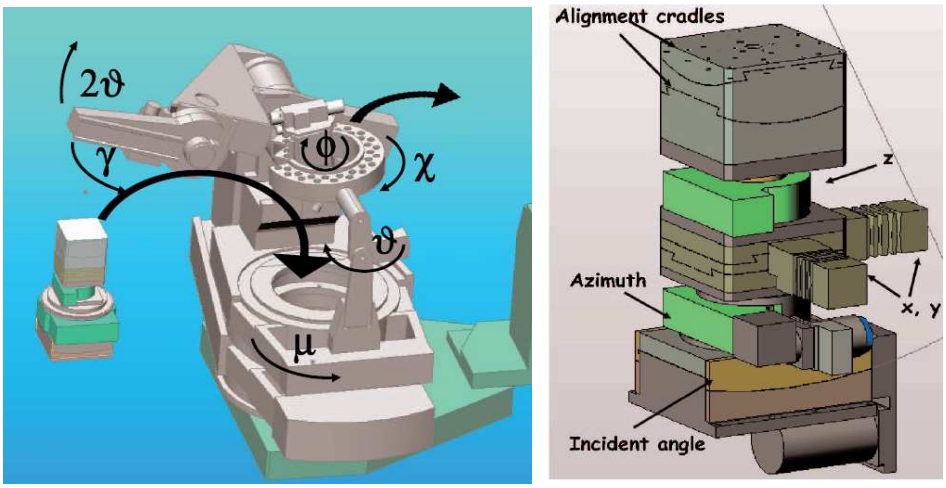

Figure 2.9: (a) The 4+2-circles diffractometer and (b) the Huber Tower [O. Plantevin, 2008].

2.4.3 Focusing optics and nano-positiong stage

The x-ray beam coming from the optics hutch has to be focused to the sample position. On ID01 beamline two different focusing devices are available: Beryllium Compound Refractive Lenses (Be-CRL) and Fresnel Zone Plates (FZP). Be-CRLs [Snigirev et al., 1998] consists of a set of milled Be lenses. They are parabolic shaped and concave with a refractive index smaller than 1 for x-rays. Be lenses can be easily aligned and are often chosen as focusing device despite their high degree of chromaticity (focal distance scales with E^2).

Fresnel Zone Plate [Jefimovs et al., 2007] is a diffractive focusing device. FZP are also chromatic but the focal distance change linearly with photon energy. In this case alignment is not easy but they offers a smaller spot size with respect to Be-CRLs. All the experiments described in this manuscript are carried on using a FZP. The aim of this chapter is not to detail working principle and focusing properties of a FZP. This will be done in chapters 3 and 4.

In figure 2.10 (a,b) a SEM picture of gold FZPs and central stops (CS) chips, both fabricated in the Paul Scherrer Institut (PSI) in Switzerland, are shown. CS is used to block the central part of the direct beam and higher harmonics. FZPs and CS are deposited on a thin SiN membrane (Fig 2.10a); the outermost zone width is 100 nm for all the lenses and the diameter varies from 20 to 200 μm. Stops are produced with diameters ranging from 50 to 100 μm. A specific FZP/CS support (Fig 2.10c) has

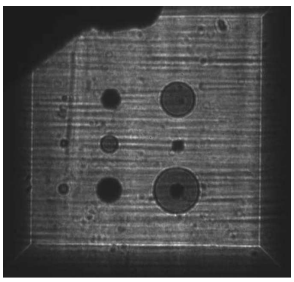

(a) Fresnel zone plate chip

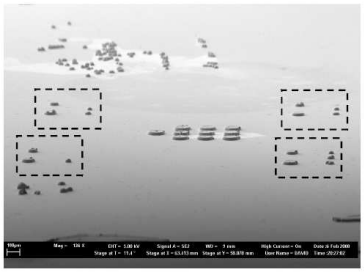

(b) Central stop plate chip

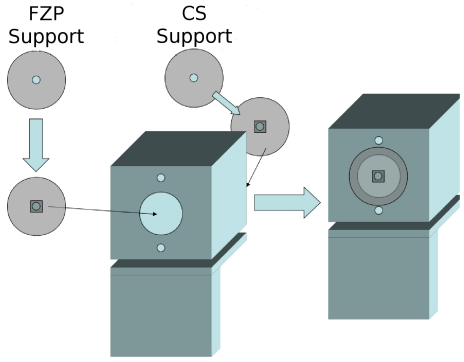

(c) FZP + CS holder

Figure 2.10: Silicon membrane chips with a series of (a) gold Fresnel Zone Plates and (b) gold central stops. The outer most zone is 100 nm for all lenses and diameters varies from 20 to 200 μm. (c) FZP and CS holder designed for ID01.

been designed to install the chips on the diffractometer rail. Recently a new set of FZP has been fabricated with a smaller outermost zone width of 70 nm to obtain a smaller focal spot.

The sample is positioned on the top of the Huber Tower using a special holder designed for ID01. In Fig. 2.10 (c) a sketch of sample holder and stage is shown. A rotating cradle is used to fix the sample holder at the top of the Huber Tower in order to incline the whole holder to the chosen Bragg angle. Sample is aligned with respect to the nanofocused X-ray beam with a stack of piezo stages (Fig. 2.11). Sample stage contains three translation stages a rotation stage, and a nano-positioning scanner. The translation stages have a travel range of 5 mm and the encoder accuracy amounts to 10 nm. The rotation stage has an accuracy of 1 millidegree facilitating the sample alignment in particular for studying asymmetric Bragg reflections. In a coherent diffraction imaging experiment the detector choice is critical. A complex object can be reconstructed according to the CDI approach only

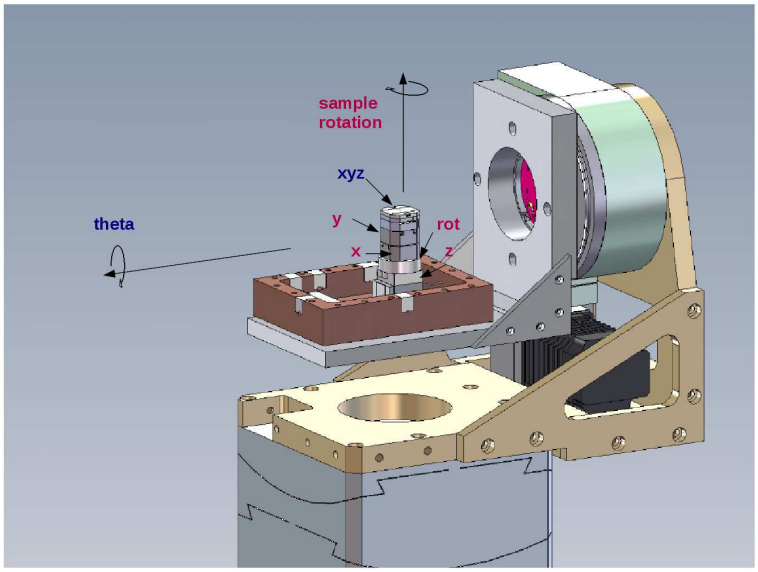

Figure 2.11: Schematic of holder and sample stage implemented in the Huber Tower.

if the coherent oversampled diffraction pattern is properly recorded. The detector dynamic counting rate has to be adapted to the intensity from the sample that we want to measure. Moreover, an appropriate angular resolution is required with respect to the dimension of the system (the larger the sample, the finer the resolution on the detector) to satisfy the oversampling condition.

A Charge-coupled device (CCD) [Boyle and Smith, 2010] (http://princetoninstruments.com) is an indirect illumination detector, with a slow readout of about 1 μsecond/pixel, but it does not offer the adequate dynamical range for this study. The PILATUS detector (PIxeLapparATUs for the Swiss LightSource) [Marchal and Wagner, 2010] (http://pilatus.web.psi.ch/pilatus.htm) is a novel type of detector, developed at the Paul Scherrer Institut (PSI) for the Swiss Light Source (SLS). PILATUS detectors are two-dimensional hybrid pixel array detectors, which operate in single-photon counting mode. The main features include: no readout noise, superior signal-to-noise ratio, read-out time of 5 ms, a dynamic range of 20 bit. These two detectors were not used during the experiments. The Medipix (http://medipix.web.cern.ch/MEDIPIX) is a hybrid silicon pixel detectors for tracking applications in High Energy Physics. It has been developed because of the needs of the Large Hadron Collider experiments at CERN. The Medipix contains 256 x 256 pixels each with a square pixel of 55 X 55 μm. It has a very low noise background

and a counting rate of 1 MHz. The MAXIPIX is a particular Medipix detector developed for the ESRF and it has been employed for the work of this thesis.

Chapter 3

X-rays Propagation and Fresnel Zone Plate

In this chapter, an introduction of Fresnel and Fraunhofer regime in the case of x-ray is given using an experimental approach. The working principles of a Fresnel zone plate are also detailed as the focusing optic of relevance for the presented work. Finally, the mathematical derivation of the paraxial Fresnel free-space approximation is given, which is an essential theoretical tool to explain the propagation of x-ray with a small deviation from a central axis.

3.1 Fresnel and Fraunhofer regime

The understanding of Fresnel and Fraunhofer regime is fundamental in the case of x-ray micro-diffraction experiments and data analysis. The sample is generally placed in the Fresnel regime, while the diffracted beam is detected far from the sample position, i.e. in the Fraunhofer regime. In the following, I describe an experimental method, proposed by Jacques [2009] and used to measure the separation of the Fresnel and Fraunhofer domain. The experimental set-up consisted of a square slit, with lateral aperture a, illuminated by a coherent x-ray wavefront with wavelength λ. When an x-ray beam is diffracted from a slit, the distance d_{FF} identifying the separation between Fresnel and Fraunhofer regions is given by [Born and Wolf, 1999]

$$|d_{FF}| = \frac{(a^2)}{\lambda} \tag{3.1}$$

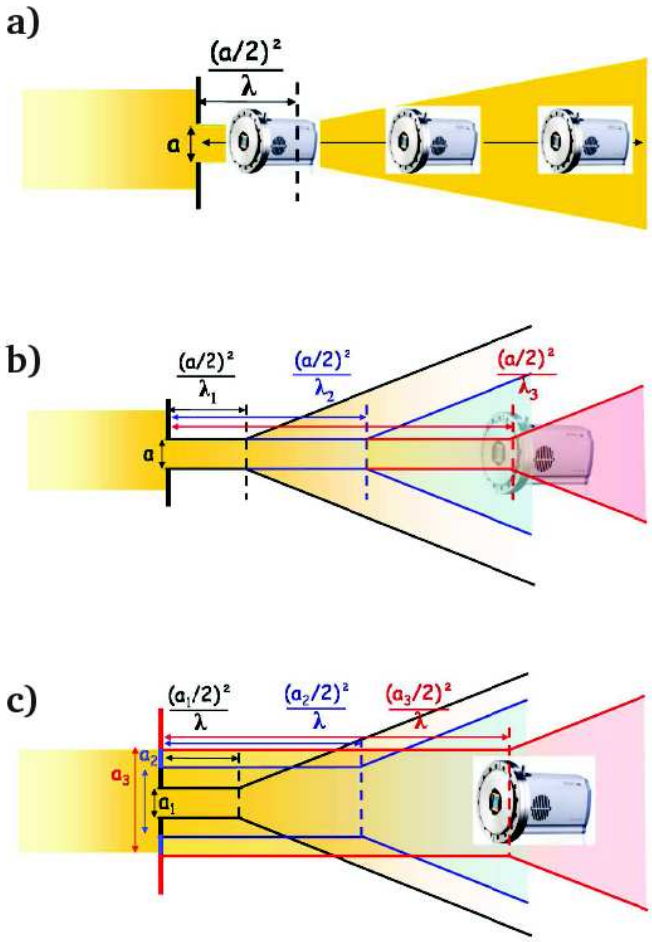

Figure 3.1: Three different methods to probe the separation between Fresnel and Fraunhofer diffraction, changing: a) the position of the detector, b) the wavelength and c) the opening of the slit. ([Jacques, 2009])

According to Eq. 3.1, the separation d_{FF} between these two regimes is proportional to the opening area of the slit and inversely proportional to the wavelength of the incoming beam. Hence, to measure d_{FF}, three different measurements were carried out by Jacques [2009], varying all the parameters involved in Eq. 3.1. The geometries of these three experiments are shown in Fig. 3.1. When x-rays are scattered from a slit, fringes appear in the Fraunhofer region and can be measured only if the dimensions of the slit is comparable or even smaller than the transverse coherent lengths. In these experiments, all parameters and typical distance were chosen with accuracy.

Moving the detector along the horizontal direction, as depicted in Fig. 3.1a, corresponds to scan the x-ray beam at different positions along the

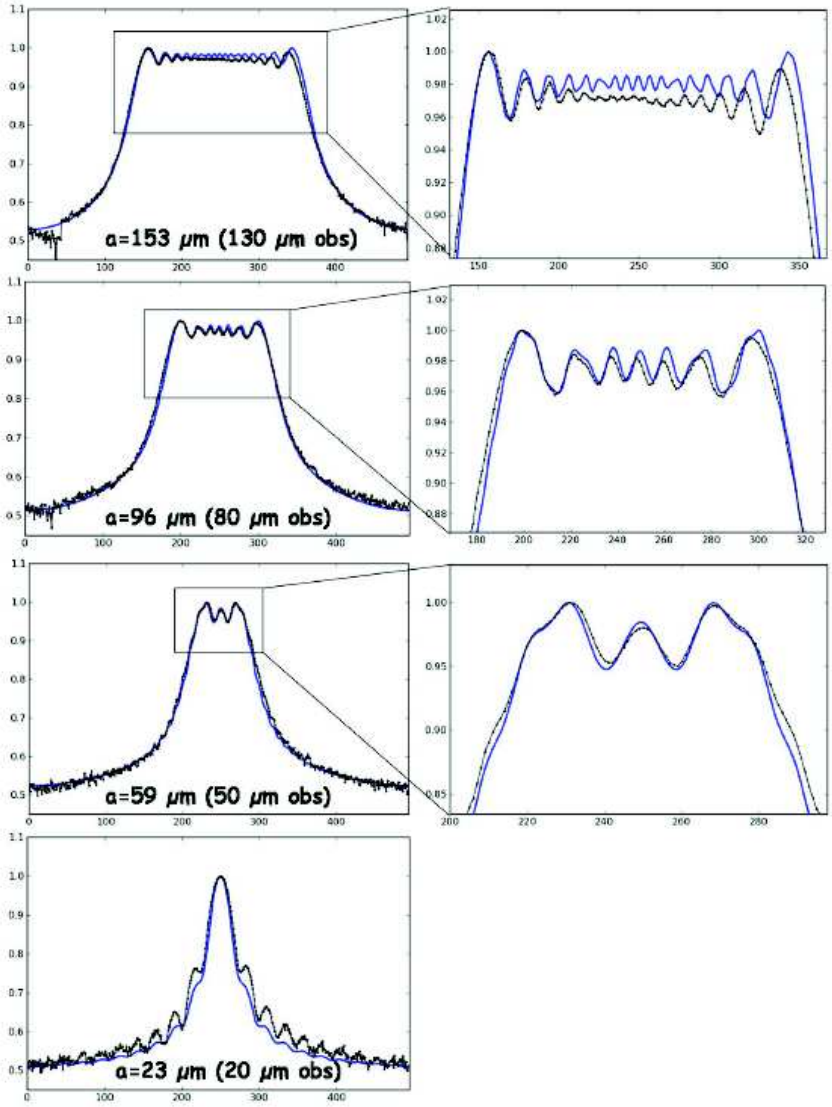

Figure 3.2: Vertical profiles of the calculated (blue line) and the measured (black line) wavefronts using the experimental method in Fig. 3.1c. ([Jacques, 2009])

propagation while maintaining the other parameters unchanged. In this case the separation was found at the theoretical limit $(a^2)/\lambda$.

A second approach is shown in figure 3.1b: the position of the detector is fixed and the wavelength is varied in order to change the value assumed by d_{FF} (for higher energies the distance d_{FF} becomes larger). The detector will be, therefore, at the limit of Fresnel and Fraunhofer regimes only for one specific value of λ satisfying the relation $d_{det} = d_{FF}$.

When the aperture of the slit is varied, as shown in Fig. 3.1c, the detector

stays at the same position and, according to Eq. 3.1, it will be in near-field regime for larger slit openings and in far-field for smaller values of a.

Using the experimental method proposed in Fig. 3.1c, the vertical profiles of the x-ray wavefront with a wavelength of $1\mathring{A}$ and the detector placed at 3 m from the slits were measured for different value of a. Measurements are shown in Fig. 3.2 and compared to the calculations. Fringes similar to the ones expected in the Fraunhofer regime are observed, at the detector position, for the smallest aperture (23 μm). When the slit aperture becomes larger, up to the upper limit of 153 μm, the Fraunhofer fringes completely disappear and interference can be observed only on the central peak.

As expected, when the slit opening approaches the beamline transverse coherence length, in that case 185 μm, the fringes visibility on the central part of the measured wavefront profile becomes smaller. For smaller slit opening we pass from Fresnel to Fraunhofer regime. It is worth noticing that the detector resolution is not adequate to measure the profile of the beam in the Fresnel regime and only Fraunhofer fringes can be solved.

3.2 Theory of Fresnel Zone Plates

In the frame of advanced imaging techniques using coherent beams with the aim of measuring structure at the micro/nonoscale, the key elements are the focusing optics. Among them Fresnel zone plates (FZP), a chromatic diffractive focusing optics, plays an important role in focusing x-ray and extreme UV radiation in several fields of science, such as astronomy [Hettrick et al., 1985, Bowyer et al., 1981, Beuermann et al., 1978, Kastner and Wade, 1978, H. Bruninger and Mozer, 1971, Gursky and Zehnpfennig, 1966], UV spectroscopy [Keating et al., 1972, Pfeifer et al., 1973, Wang et al., 2003], microwave optics [Z., 1999, Hristov and Herben, 1995, Garrett and Wiltse, 1991, Guo et al., 1994, Stout-Grandy et al., 2006, Wiltse, 1999] and x-ray microscopy using synchrotron sources [Kirz, 1974, Howells and Hastings, 1983, Pfeifer et al., 1973, Wang et al., 2003, Chao et al., 2005, Sayre et al., 1998]. In the particular case of coherent x-ray diffraction experiments aimed to characterize strain in single nano-objects, as discussed in Chapter 1, FZP assures high efficiency in a small focal spot, with a transverse size comparable to the illuminated object. Moreover, the phase relation of the coherent wavefront propagating through this lens is preserved (this point will be discussed in details in Chapter 4), assuring the correct interpretation of the

retrieved phase (cf. Chapter 2).

3.2.1 Diffraction from a grating

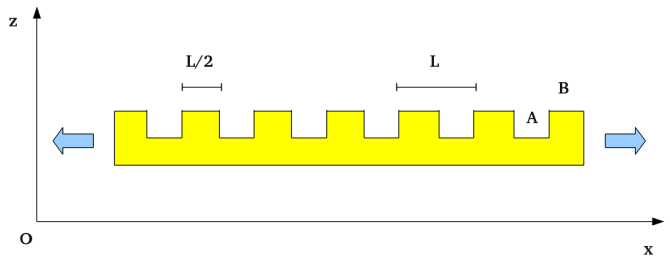

Figure 3.3: Sketch of a binary diffraction grating.

The working principles of a FZP can be easily explained referring to physics of x-ray diffraction from gratings. A diffraction grating is a component of numerous optical devices and generally consists of a surface ruled with close, equidistant, and parallel grooves, with the purpose of resolving light into spectra. A simple two-level binary diffraction grating is shown in Fig. 3.3. Here A and B are used to indicate grooves and lines, respectively. The grating period is L with equal width of grooves and lines.

A diffraction grating acts as a beam splitter, i.e. it is able to disperse a polychromatic beam into a spectrum because of the principle of diffraction. When a polychromatic light is incident on a diffraction grating along its normal, diffraction and interference effects spread the various wavelengths in discrete directions called "orders" or "special orders". This concept is schematically depicted in Fig. 3.4. Here, the normal incident monochromatic wavefield is split upon the passage through the grating. The angles of the various diffraction orders, with respect to the direction of propagation, are [Paganin, 2006]:

$$\theta_m = sign(m)\tan^{-1}\left(\frac{(2|m|-1)\lambda}{\sqrt{L^2-(2|m|-1)^2\lambda^2}}\right), \tag{3.2}$$

where m is the diffraction order, λ the radiation wavelength and L the grating period. The 0^th order passes straight trough the grating. As shown in Eq. 3.2, the diffraction process is wavelength dependent and the grating acts also as spectrometer. Also the angle of a specific diffraction order m measured with respect to the optic axis depends on the wavelength. In this case the diffractive grating is chromatic.

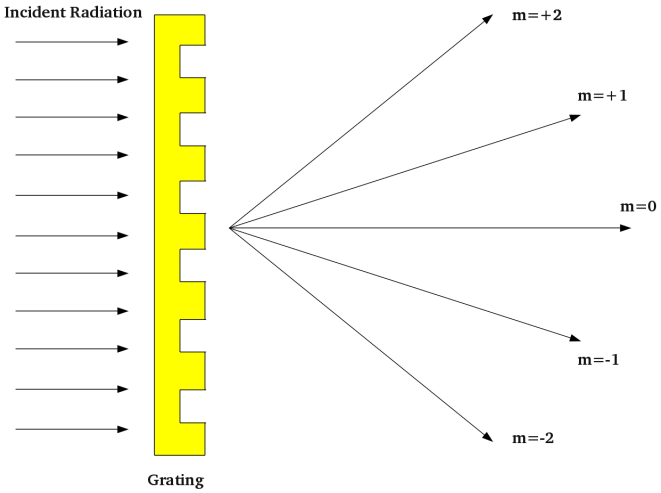

Figure 3.4: Monochromatic plane wave diffracted in a series of diffraction order from a grating.

The efficiency χ_m of such a grating is defined as the ratio of the squared modulus of the amplitude of the diffracted order m^{th} and the squared modulus of the amplitude of the incident beam. To calculate χ_m, one considers a non- absorbing grating, called also *phase grating*. Specifically, x-rays passing through the thin and the thick parts of the grating, are subjected to a phase shift of odd multiple of π. In this condition, for a monochromatic plane wave diffracted by a grating as depicted in Fig. 3.4, the maximal efficiency is [Paganin, 2006]:

$$\chi_m = \frac{4}{\pi^2(2|m|-1)^2}, \quad m = \pm 1, \pm 2, ..., L > (2|m|-1)\lambda. \tag{3.3}$$

The condition $L > (2|m|-1)\lambda$ restricts the above formula to the propagating diffracted orders, i.e. to the case of a period L much longer than the wavelength radiation. For $m = \pm 1$, the efficiency assumes the value of $4/\pi^2$. These calculations have been done considering the case of a single material two-level grating as sketched in Fig. 3.3.

3.2.2 Fresnel zone plate: working principles

In the simplest approximation a Fresnel zone plate (FZP) is a grating consisting of a sequence of many lines and space, placed in a parallel [David et al., 2002, Montiel and Nevi'ere, 1995, Pfeiffer et al., 2006a, Hermannsfeldt et al., 1968] or in a circular geometry [Baez, 1961, Barrett and Horrigan, 1973, New, 1971], as shown in Fig. 3.5. A particular example of

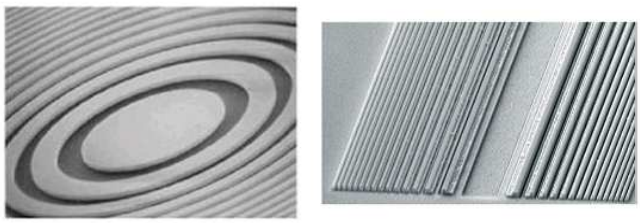

Figure 3.5: Two examples of Fresnel Zone Plate: circular (left) and parallel (right) geometry. [David et al., 2001]

circular zone plate is the Gabor zone plate, based on the concept of radial sinusoidal transmission function in each zone [Beynon et al., 1992, Horman, 1967]. The FZP is employed to focus the x-ray radiation from a source S and generates a positive interference in a specific point P on the FZP axis leading to a strong scattering of the radiation (see Fig.3.6). One says that the image of the source is obtained in P. The period of the zones becomes shorter at increasing radius and decreasing zone width. The nature of this specific periodic structure and the complex refractive index, that is responsible of absorption effects and phase shift, influence the amount of the scattered radiation. Because of the specific periodicity of a FZP, diffraction angles become larger for larger radii. Hence, several triangles can be drawn in the direction of propagation (see Fig.3.6).

The radii r_n, with n=1,2,3,... of each zone can easily derived [Stein, 2002, Michette, 1968] describing the Fresnel zone plate as a tool for point to point imaging (c.f. Fig. 3.6). The optical path length from the source S of the radiation with wavelength λ and its image P, via a generic point on

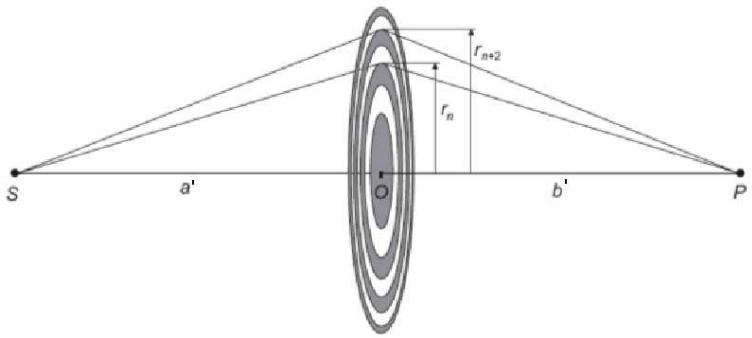

Figure 3.6: Fresnel Zone Plate lenses are used to image an x-ray source S in the image point P; a' and b' are the characteristic distance to the object and the image, respectively. [Attwood, 1999]

the zone plate surface is, according to the Pythagoras' theorem,

$$(a'^2 + r_n^2)^{(1/2)} + (b'^2 + r_n^2)^{(1/2)} \tag{3.4}$$

where, as shown in Fig.3.6, a' is the source distance, b' the image distance from the lens and r_n the radius of the n^{th} zone. Constructive interference occurs when the difference Δ between transmissive and opaque zone. So that

$$\Delta = n\lambda/2 = (a'^2 + r_n^2)^{(1/2)} + (b'^2 + r_n^2)^{(1/2)} - (a' + b') \tag{3.5}$$

Δ is an integer multiple of λ If we impose that $Z = (a' + b')$ and substitute in the previous equation, we obtain the exact expression of the zone positions r_n for a FZP at any wavelength:

$$r_n^2 = \frac{[n\lambda abZ + (n\lambda)^2(Z^2 + ab)/4 + (n\lambda)^3(Z/8) + (n\lambda)^4/4]}{(Z + n\lambda/2)^2} \tag{3.6}$$

If $Z \gg n\lambda/2$, occurring for x-ray wavelengths (0.01 to 10 nanometers), the equation may be rewritten as follows

$$r_n^2 = n\lambda abZ + (n\lambda)^2(a^3 + b^3)/4Z^3 + ... \tag{3.7}$$

If the FZP is considered as a thin lens, the focal length f is defined as

$$\frac{1}{f} = \frac{1}{a} + \frac{1}{b} \tag{3.8}$$

and the magnification M as

$$M = \frac{b}{a}. \tag{3.9}$$

which leads to $Z = f(1 + M)^2/M$. Substituting in the Eq. 3.7, one obtains

$$r_n^2 = n\lambda f + (n\lambda)^2(M + 1)/4(M + 1)^3 + ... \tag{3.10}$$

In our case and for the most application with x-ray $M \gg 1$, when the FZP is used as a magnifier, or $M \to \infty$, when it serves as focusing optics. In both cases $M/(M + 1)^2 \to 0$ and the high order terms can be ignored, so that

$$r_n^2 \simeq n\lambda f + (n\lambda)^2/4 \tag{3.11}$$

The second term of Eq. 3.11 represents the spherical aberration, that is generally significantly smaller than the first term. Therefore, equation 3.11 can be approximated to the first term as follows:

$$r_n \simeq \sqrt{n\lambda f} \tag{3.12}$$

that shows that successive zones increase in radius by $\sqrt{n}$ to get a common focus for first order [Rayleigh, Wave Theory]. It is worth noticing that two successive zones are constructed so as to add $\lambda/2$ to achieve a magnification of M, as defined in Eq. 3.9. This is valid only in case of modest numerical aperture (NA), defined as $NA = \sin\alpha \simeq r_n/f$, where f is the focus. In the same approximation image and object distance are related to the focal length as for light refractive lenses. The term $n^2\lambda^2/4$ is the aberration term; in the case of x-ray wavelength it can be neglected. As Fresnel zone plates are diffractive optics, they have multiple diffractive orders. Figure 3.7 shows schematically the behaviour of the 1^{st}, 3^{rd} and 5^{th} order foci, that are found at

$$f_{(2m+1)} = \frac{f}{2m+1}, \qquad m = 1, 2, 3... \tag{3.13}$$

The 0^{th} order light passes straight through the zone plate.

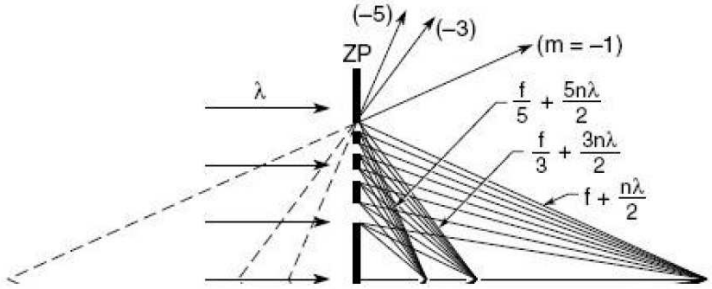

Figure 3.7: Fresnel Zone Plate diffracting focusing for 1st, 3rd, 5th orders.(Modified from http://ast.coe.berkeley.edusxreuv/2005/)

3.2.3 Focusing properties of a FZP and Efficiency Issue

The focusing properties of a FZP can be derived propagating a planar wavefield through the zone plate and calculating the diffraction pattern at the focal position. It has been already demonstrated [Jacobsen et al., 1992] that, as in the case of optical refractive lenses, the focal depth δ_d and the

focal size δ_s (known as Reyleigh resolution) are determined by the NA as follows :

$$\delta_s = 0.61\frac{\lambda}{NA} \qquad \delta_d = 1.22\frac{\lambda}{NA^2}. \tag{3.14}$$

If we take into account that the width of the outermost zone Δr_n is

$$\Delta r_n = \frac{r_n^2 - r_{n-1}^2}{r_n + r_{n-1}} = \frac{r_n^2 - r_{n-1}^2}{2r_n} = \frac{\lambda f}{2r_n} \tag{3.15}$$

and that for $\Delta r_n \ll r_n$, $NA = \sin\alpha \simeq \frac{\lambda}{2\Delta r}$, we can obtain two new relations for δ_s and δ_d

$$\delta_s = 1.22\Delta r_n \qquad \delta_d = 4.88\Delta r_n^2/\lambda \tag{3.16}$$

The size of the central spot, measured at the full width half maximum (FWHM) is therefore independent on the wavelength and it depends only on the outermost zone width. Equation 3.16 should be applied in the case of high order foci, having shorter focal lengths, much higher resolution with the same outermost zone width, but their intensity is much lower. A more useful expression for the focal length can be derived from Eq. 3.15:

$$f = \frac{2r_n\Delta r_n}{\lambda}. \tag{3.17}$$

The diffraction efficiency of a zone plate can be easily calculated according to [Michette, 1968]. One considers the amplitude transmission function of the zone plate as a Fourier series of m terms. The m_{th} coefficient represents the complex amplitude diffracted at the mth focal position (cf. Sect 2.3.1). The efficiencies are therefore given by the square of these coefficients, such as $1/4, 1/\pi^2, 1/(3\pi)^2, ..., 1/(m\pi)^2$ are the diffraction for 0, 1, 3, ... , m orders (Fig. 3.7). Only the $1/(m\pi)^2$ of the total energy contributes to the corresponding focus. Absorption from opaque zones in the X-ray region has also to be taken into account as this effect introduces a phase shift in the diffraction pattern as the wave front passes through both transparent and opaques zones. It is known that for a thin film of thickness t with a refraction index $n = 1 - \delta - i\beta$ the amplitude of the incoming beam, of wavelength lambda, is attenuated by a factor of $T = e^{-2\pi\beta t/\lambda}$ and phase shifted by $\phi = -2\pi\delta t/\lambda$. According to Kirz [Kirz, 1974], the phase shift can

be calculated with the following equation:

$$\eta = \frac{1}{(m\pi)^2}\left(1 + e^{-4\pi\beta t/\lambda} - 2e^{-2\pi\beta t/\lambda}\cos\phi\right) \tag{3.18}$$

Equation 3.18 shows that the efficiency of the m^{th} order of a zone plate is determined by material, thickness and wavelength. Due to the fact that a zone plate is a diffractive optical element, a relevant illumination background is created by both zeroth and higher orders.

3.2.4 A Fresnel Zone Plate with a Central Stop

In a real x-ray diffraction experiment, high harmonics are also generated by the source and are reflected by the monochromatising optics. Therefore, in the experimental set-up, the FZP is always coupled with a central stop, used to eliminate a part of the background coming from the direct beam, as well as the harmonics. Optical properties of a Fresnel zone plate with the implementation of a central stop have been studied by Simpson and Michette [1984] who investigated its properties based on the analogy between the lens and the zone plate with large number of zones. The point spread function of a zone plate with a central stop is given by

$$U(r) = \frac{I_0}{2(1-a^2)}\int_0^R \left[\frac{2J_1 r}{r} - a^2\frac{2J_1(ar)}{ar}\right]^2 r\,dr \tag{3.19}$$

where $U(r)$ represents the electric field of the electromagnetic radiation and J_1 is the Bessel function of the first kind, order one [Watson, 1886]. The intensity in the direction of propagation is obtained from Eq.3.19 as the subtraction of two Airy functions [Born and Wolf, 1999]

$$I(r) = \frac{I_0}{1-a_{CS}^2}\left[\frac{2J_1 r}{r} - a_{CS}^2\frac{2J_1(a_{CS}r)}{a_{CS}r}\right] \tag{3.20}$$

where I_0 is the incoming intensity, a_{CS} is the fraction of area blocked by the stop, $r = 2\pi r_n x/(\lambda z)$ the normalized radial coordinate, x the radial distance in the focal plane, z the image distance. Note that this treatment is valid only in the case of a zone plate with more than 100 zones, for which the difference between its radial intensity distribution at focal plane and the Airy pattern is negligible. The study performed by Simpson and Michette [1984] suggests that in these experimental conditions the central maximum is narrower as bigger is the obstructed area on the lens, leading to a better

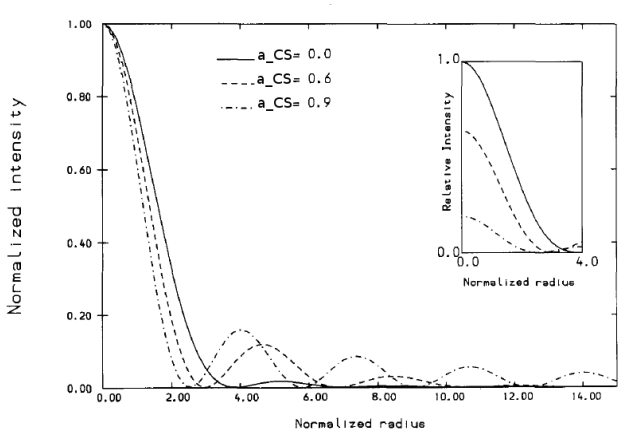

Figure 3.8: Radial intensity distributions for obstruction ratios $a_{CS} = 0$, 0.6 and 0.9. The main plot shows each distribution normalized to its own central peak, while the inset shows the central peaks each normalized to that for a_{CS}=0. (Modified from [Simpson and Michette, 1984])

resolution, while the focal depth increased by $1/(1 - a^2)$. The amount of focused radiation in the side-lobes increases as a_{CS} increases and the total amount of focused energy is obviously reduced by a factor a_{CS}^2. The behaviour of a FZP with a CS is shown in Fig. 3.8, for different obstruction ratios a_{CS}. Therefore the overall effect of the introduction of the central stop is partially good, due to the removal of the background intensity, and partially bad, due to the modified transfer of spatial frequencies ([Michette, 1968], Chapter 8). The spot focused at the first order focus is the one used to illuminate the nanostructure during experiments. To eliminate contributions from the scattering that is not focused at the 1^{st} order

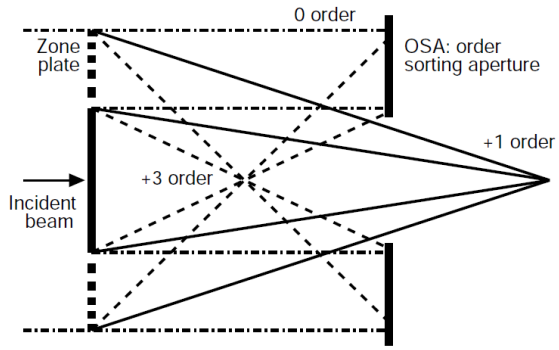

Figure 3.9: Schematic of the zone plate and order sorting aperture setup. (Modified from [Kirz et al., 1995])

focal position (Fig. 3.7), the use of a central stop is generally combined with an order sorting aperture (OSA), that blocks the light diffracted into zero and higher diffraction orders [Kirz et al., 1995]. A schematic of the zone plate and order sorting aperture set-up is shown in Fig. 3.9.

3.3 The Paraxial Fresnel Free-Space Approximation

The free-propagation of an x-ray plane wavefield is treated using the Paraxial Fresnel Free-Space approximation [Sudarshan et al., 1983, Papoulis, 1974]. Specifically, this approximation is useful to treat the x-ray propagation with a small deviation from a central axis of a FZP. Moreover, it will be implemented, as I will show in Chapter 4, in a particular phase retrieval algorithm used to reconstruct the coherent wavefront (amplitude and phase) at the focal plane of a FZP from a single measurement of the direct beam at the detector plane.

3.3.1 Propagation of a Plane WaveFront

One considers a plane monochromatic wavefield with wavelength λ generated at a point source and propagating through an aperture Σ. Let P_1 be a generic point of coordinates (ξ, η) in the aperture Σ. The wavefront propagates to reach a point P_0, lying in the plane (x,y) and distant r_{01} from P_1. The axis z defines the direction of propagation and pierces both planes (x,y) and (ξ, η) in their origins (Fig. 3.10).

According to the Huygens-Fresnel principle, each point of the wavefront in P_1 may be considered as the source of secondary spherical waves that mutually interfere. This principle, that is derived in Appendix A (Eq. A.3) in the specific case of a plane monochromatic wavefield (see Eq. A.3), can be used to calculate the intensity of the wavefront in P_0 resulting from the interference. In rectangular coordinates, the amplitude U(x,y) of the propagating electric field is given by the Huygens-Fresnel principle [Goodman, 2005]:

$$U(x,y) = -\frac{iz}{\lambda}\int\int_{\Sigma} U(\eta,\xi)\frac{e^{ikr_{01}}}{r_{01}^2}d\xi d\eta \tag{3.21}$$

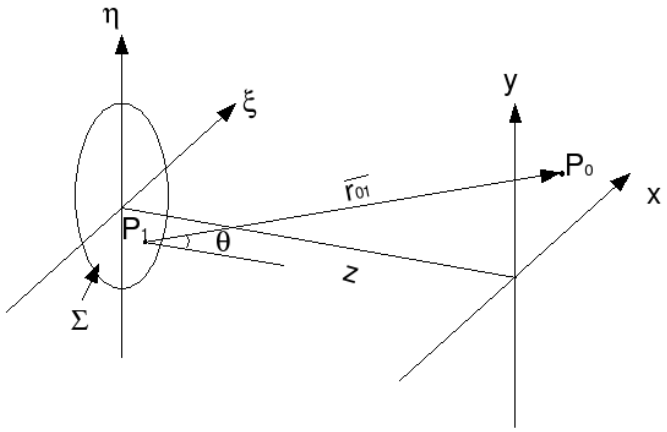

Figure 3.10: Diffraction geometry : P_1 is a generic point of coordinates (ξ, η) and P_0 the source of the wave-front. [http://fourieroptics.org.uk]

Here, the distance r_{01} is given by

$$r_{01} = z\sqrt{1 + \left(\frac{x-\xi}{z}\right)^2 + \left(\frac{y-\eta}{z}\right)^2} \tag{3.22}$$

Equation 3.21 is valid when the condition $r_{01} \gg \lambda$ is satisfied. In addition, if the distance r_{01} between P_1 and P_0 is assumed to tend to ∞, the Huygens-Fresnel principle can be reduced to a simpler expression. In this approximation, the conditions

$$|\frac{x-\xi}{z}|, \quad |\frac{y-\eta}{z}| \ll 1 \tag{3.23}$$

are valid and Eq. 3.22 can be reduced, using the binomial expansion of a square root and neglecting the terms larger than the 4^{th} order:

$$r_{01} \approx z\left[1 + \frac{1}{2}\left(\frac{x-\xi}{z}\right)^2 + \frac{1}{2}\left(\frac{y-\eta}{z}\right)^2\right]. \tag{3.24}$$

Substituting Eq. 3.24 in Eq. 3.21, we easily obtain the expression for the field at the point P of coordinates (x,y), that is

$$\begin{aligned} U(x,y) &= -\frac{ie^{ikz}}{\lambda z}\int\int_{\infty}^{-\infty} U(\eta,\xi) \\ &\quad \exp\left\{\frac{ik}{2z}\left[(x-\xi)^2 + (y-\eta)^2\right]\right\} d\xi d\eta \end{aligned} \tag{3.25}$$

the finite dimensions of the aperture being included in $U(\eta, \xi)$. In Eq. 3.26

it is possible to recognize the convolution between the function $U(\eta, \xi)$ and the kernel $h(x, y)$

$$h(x, y) = -\frac{ie^{ikz}}{\lambda z} \exp\left[\frac{ik}{2z}\left(x^2 + y^2\right)\right] \tag{3.26}$$

Factorising the exponential in the kernel outside the integral sign, a new form for Eq. 3.26 is found

$$\begin{aligned} U(x, y) &= -\frac{ie^{ikz}}{\lambda z} e^{i\frac{k}{2z}(x^2+y^2)} \\ &\int\int_{\infty}^{-\infty} \left(U(\eta, \xi) e^{\frac{ik}{2z}(\xi^2+\eta^2)}\right) e^{\frac{-i2\pi}{\lambda z}(x\xi+y\eta)} d\xi d\eta \end{aligned} \tag{3.27}$$

in which we recognize the Fourier Transform of the product of two functions: the complex field at the exit of the aperture and a quadratic phase exponential. This integral is often referred to as the Paraxial Fresnel Free-Space Propagation, which takes an important place in the treatment of the diffraction theory in particular for focused and coherent beams [Quiney et al., 2006, 2008, Guizar-Sicairos and Fienup, 2009, Williams et al., 2010] that propagate with a small angle of deviation from the axis of the focusing optics.

Chapter 4

Imaging the X-ray beam focused with a Fresnel Zone Plate

Introduction

X-rays provided by a third generation synchrotron source have only partial coherence properties [Vartanyants and Robinson, 2001], with typical transverse coherence lengths in the 10-100 μm range. A lens with a radius small enough to match these lengths can be used to ensure the coherent illumination at the expense of reducing the focal distance, which decreases linearly with the lens diameter. Hence, a good compromise between the preservation of working distances and the loss of photon flux can be obtained reducing the illuminated area on the lens by means of an opening (partial illumination) matching the coherent lengths [Diaz et al., 2009]. This approach, which is at the focus of the present chapter, is particularly interesting for short synchrotron beamlines, i.g. the undulator beamline ID01 at the European synchrotron radiation facility (ESRF, Grenoble) distant of 50 m from the source. The partial illumination necessarily affects the wavefront of the focused x-ray beam with a consequent modification of the exit wavefield. Consequently, the strong contribution of illumination probe in the retrieved exit field has to be demonstrated, as a local wavefront curvature or a change in the phase of the illuminating complex field affects the sample reconstruction [Williams et al., 2006, Nugent et al., 2005, Chamard et al., 2009]. Therefore, an accurate investigation of the sample requires a detailed knowledge of the probe wavefront. Unfortunately, the resolution

of available 2D detectors does not allow to perform direct imaging of the focal spot. One solution to this problem is offered by the ptychography approach, that enables the simultaneous reconstructions of the sample electron density and the illumination function [Thibault et al., 2008, Kewish et al., 2010b]. However, the conditions to perform the experiment as well as the convergence of the inversion process rely on good a priori knowledge of the initial probe estimates. The approach developed in this work aims to solve this problem with the application of iterative phase retrieval algorithm and to retrieve directly from one image of the direct beam at the detector plane, the complex wavefield at the focus of a FZP. This method is based on the suggestion proposed in Ref. [Quiney et al., 2006]. This approach has been adapted according to the experimental conditions used during the experiments, i.e. the partial illumination of the lens. To support and justify the use of the phase retrieval algorithm in partial illumination conditions, numerical simulations of the wavefront propagation have been performed. Most interestingly, these calculations provide very useful information about the variations of the focal spot and focal depth directly related to the change in the lenses numerical aperture (NA) in partial illumination conditions. These simulations demonstrated that the wavefront of the coherent beam is preserved during the focusing process also in our experimental conditions. Moreover, a set of numerical data at the detector plane have been provided to better understand the influence of the slits position along the direction of propagation. In addition numerical calculations have been used to test the validity of phase retrieval algorithm approach. In this chapter, I will show in details by means of numerical simulations the propagation of a coherent plane wave focused with both a full and a partial illuminated zone plate. I will show the results obtained from the *ab-initio* reconstruction of amplitude and phase of the x-ray beam at the focal position of a Fresnel Zone Plate. This is achieved using the intensity pattern in the divergent part of the focused coherent beam as input of a specific phase retrieval algorithm. The results obtained will be also compared with the simulated complex field.

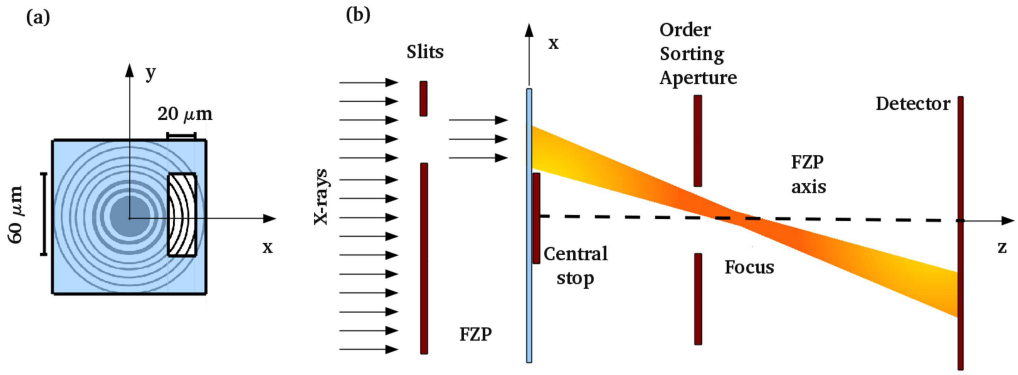

Figure 4.1: (a) Sketch of a partially illuminated Fresnel Zone Plate. A pair of slits defines a rectangular aperture matching the transverse coherence lengths of the x-ray beam. (b) 2D schematic of the propagation of the wavefield produced by a partially illuminated FZP. The slits, placed 1.15 m upstream the lens, used to define the illuminated area, the FZP, the CS and the OSA are represented. The effective direction of propagation is tilted with respect to the FZP axis due to the lateral displacement of the slits.

4.1 Numerical calculations of coherent X-ray propagation

The computational approach for the calculation of a WaveFront propagation when a Fresnel Zone Plate is used as focusing tool is described in this section.

The simulations are based on the set-up used on the ID01 beamline at the European Synchrotron Radiation Facility (ESRF, Grenoble) for coherent diffraction experiments. This undulator beamline has an effective source size, measured after the monochromator, of $125_h \times 30_v$ μm^2 (FWHM) in the horizontal (h) and vertical (v) directions, respectively [Diaz et al., 2010]. At the sample position, 50 m downstream from the source, the measured transverse coherence lengths are $60_v \times 20_h$ μm^2 (FWHM).

Figure 4.1 shows the schematics of the setup. A 200 μm diameter gold FZP with an outermost zone width of 70 nm [Gorelick et al., 2011] is used to focus the (partially) coherent beam. The focal position is defined at 0.09 m for 8 keV energy. The thickness of the zones is equal to 1 μm. This provides an efficiency of 15% in the 6 - 9 keV energy range [David et al., 2001, Gorelick et al., 2011]. The zone plate efficiency measured in Ref. [Gorelick et al., 2011] is plotted in Fig. 4.2.

As the FZP diameter is larger than the coherence lengths, a pair of slits

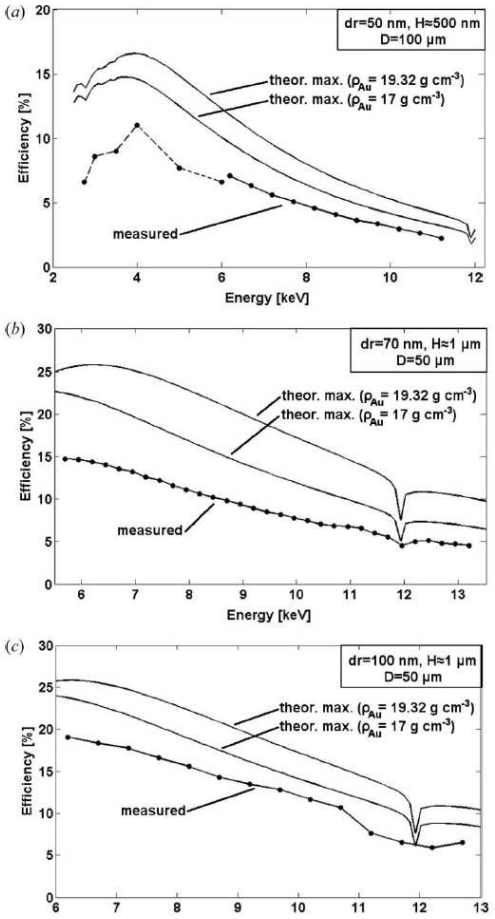

Figure 4.2: Diffraction efficiencies (first order) of various FZPs with an outermost zone width dr, diameter D and zone height H measured over a wide range of X-ray energies and compared with the theoretical maximum values calculated from the tabulated X-ray optical constants. [Gorelick et al., 2011]

located 1.15 m upstream the FZP is used to provide the partial illumination. The slit aperture is laterally shifted (Fig. 4.1a) to avoid the illumination of the central stop (CS). A 65 μm diameter CS and an order sorting aperture (OSA) with a diameter of 50 μm are introduced to avoid direct beam contribution and to block higher diffraction orders (Fig. 4.1b). The measurements of the direct beam in the forward direction are performed in the far-field regime using a Maxipix 2D pixel detector, with 256×256 pixels of 55×55 μm^2 size [Ponchut et al., 2011]. This photon counting detector produces zero read-out noise (Fig. 4.1b, not in scale).

Numerical values used in the calculations are tabulated in Table 4.1. Numerical simulations have been done using the software PYTHON 2.6.5; one and two-dimensional fast Fourier transforms (FFT) have been used.

Fresnel Zone Plate	
Number of Zones (N)	1500
Radius (R_{FZP})	100e(-6) m
Outermost zone width (Δr_N)	70e(-9) m
Phase (ϕ_{FZP})	1.39
X-ray Beam	
Energy (E)	8 KeV
Wavelength (λ)	1.54975e(-10) m
Wave-vector (k)	4.0543e(10) m^{-1}
Central Stop	
Radius (R_{CS})	32.5e(-6) m
Order Selecting Aperture	
Radius (R_{OSA})	25e(-6) m

Table 4.1: Features used for numerical calculations.

In the numerical approach I ideally assume that a monochromatic fully coherent beam is focused by an ideal thin Fresnel Zone Plate for which the transmission function $T(r)$ is :

$$T(r) = \begin{cases} 0, & \text{for } r_{2n-2} < r < r_{2n-1} \\ 1, & \text{for } r_{2n-1} < r < r_{2n} \end{cases} \tag{4.1}$$

with n=1,...,N and N the total number of zones. In the case of a real FZP, $T(r)$ is smaller than 1 as the absorption diminishes the diffraction efficiency, modifying the amplitude of the output field [Kopylov et al., 1995]. For all calculations, I assume that the incoming beam may be approximated to a plane wave; this approximation is valid if we consider that experimentally the dimensions of the illuminated object are small with respect to that of the illumination function. The energy of the incoming beam used for calculations is 8 keV for a wavelength λ of about $1.55 \times 10^{-10} m$ (see Table 4.1).

4.1.1 Fully illuminated Fresnel Zone Plate

The case of a fully illuminated FZP has also been computed to compare the resulting field with the one obtained in the case of partial illumination conditions. As the wavefront propagation in full illumination conditions have been already discussed in Chapter 2, I use those calculations to probe

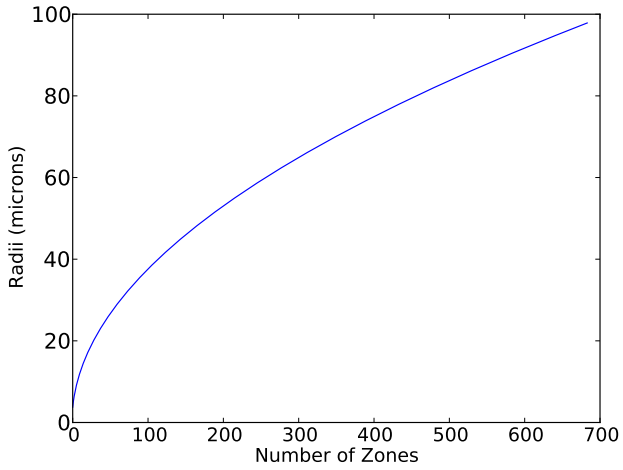

Figure 4.3: Radii dependence on the number of zones.

the validity of the proposed approaches. The propagation of the wavefield produced by a fully illuminated FZP can be computed using two different approaches. The existing cylindrical symmetry of the physical process (due to the intrinsic cylindrical symmetry of the FZP) allows to calculate the propagation starting from a one dimensional FZP. The two-dimensional fields can be therefore obtained at each position of the direction of propagation with a rotation of all calculated profiles. Using this approach, the pixel size used to build the zone plate can be small (i.e. 2 nm corresponding also to the spatial resolution at the focal plane) as the interesting part of the wavefield at the focal plane is limited to 2.6 μm of the computational window. The second approach is to built a 2D FZP and calculate directly the propagation of 2D complex wavefield. In this case, the pixel size is limited to 20 nm, as a compromise between the available computer memory and the resolution required to define the outermost zone width (70 nm). Such a choice implies the use complex matrix with 10^6 elements with a long computational time (even 7 days).

In the (x, y, z) laboratory frame, x (horizontal direction) and y (vertical direction) define the plane perpendicular to the direction of propagation z (FZP axis) (Fig. 4.1). The zone plate profile is built knowing that each radius defining the zone position on the lens surface r_n is given by

$$r_n = \sqrt{\lambda f n}, \qquad n = 1, ..., N \tag{4.2}$$

where λ is the wavelength, $f = d\Delta r_n/\lambda$ the focal position that depends on the outermost zone width Δr_n, the zone plate diameter d and the

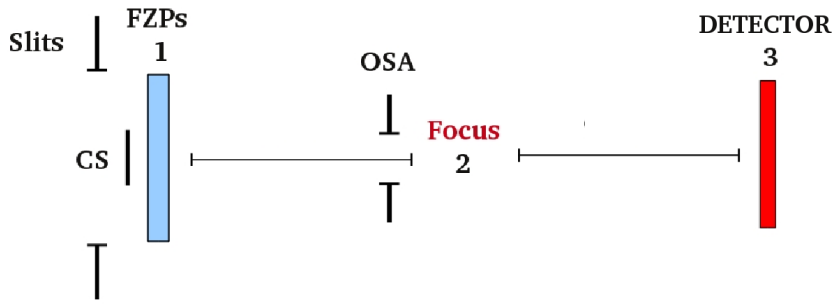

Figure 4.4: One-dimensional sketch of the calculation of a wavefield propagating from the Fresnel zone plate to detector position.

wavelength. N is the total number of zones that can be calculated as $N = d/2\Delta r_n$. The profile radii as a function of the number of zones is shown in Fig. 4.3

The wavefield propagation is computed in three steps:

1. the wavefield is calculated at the FZP position;

2. the wavefield is propagated to the focal plane;

3. the wavefield is propagated at the detector position.

The one-dimensional schematic of the propagation steps is depicted in Fig. 4.4. The 2D complex field calculated at the position z_i along the propagation axis is $\Psi(\rho_i z_i)$. $\rho_i = \sqrt{x^2 + y^2}$ defines positions in the plane transverse to the z-direction. The index $i = 1, 2, 3$ indicates the position corresponding to the three steps along the z-axis. This formulation in which Ψ depends on ρ_i is used to underline the presence of a cylindrical symmetry. The phase factor ϕ_{FZP} defines the phase shift occurring when x-rays propagate through the zones and depends on the structural characteristics of the FZP. In this work ϕ_{FZP} is equal to 1.39 (C. David, personal communication). At step 1 (Fig. 4.4), with $z_i = z_1$, $\Psi(\rho_1 z_1)$ is expressed as:

$$\Psi(\rho_1 z_1) = \exp(-i\phi_{FZP} f_{FZP}(r_n)) \tag{4.3}$$

Here $f_{FZP}(r_n)$ represents a function of zones radii r_n, $n = 1, ..., N$ describing the zone plate profile. At this point the initial complex field is multiplied by a mask function in order to simulate the presence of a central stop (CS) used to block the the high-order harmonics of the incoming field. The mask

function $CS(\rho_1)$ is defined as follows:

$$CS(\rho_1) = \begin{cases} 0 & for|\rho_1| \leqslant R_{CS} \\ 1 & otherwise. \end{cases} \tag{4.4}$$

In Eq. 4.4 R_{CS} is the radius of the chosen central stop. For these calculations, $R_{CS} = 32.5$ μm (see Table 4.1). The thickness of the beam stop is considered infinite as it only affects the intensity and the background at the focal plane. For a more realistic calculation, one should take into account the real FZP thickness, the material and the absorption coefficient at the working energy. The field $\Psi(\rho_1, z_1) \times CS(x, y)$ is propagated in the forward direction according to Bunk et al. [2007]:

$$\Psi(\rho_2, z_2) = FT^{-1}\Big(\mathfrak{P}_z(q, z_{12})FT\big(\Psi(\rho_1, z_1)\big)\Big) \tag{4.5}$$

where $z_{12} = 0.09$ is the distance between the planes 1 and 2, i.e. the focus, and $\mathfrak{P}_z(q, z)$ is the Fresnel propagator in the Fourier space defined by the following expression:

$$\mathfrak{P}_z(q^2, z_{12}) \propto \exp\left(-2\pi i z_{12} q^2/2k\right) \tag{4.6}$$

where $k = 1/\lambda$ is the wavevector FT and FT^{-1} indicates the forth and back Fourier operator, respectively. q represents the transferred momentum calculated as follows:

$$q^2 = q_x^2 + q_y^2 \quad \text{and} \quad |q_x| = |q_y| = 2\pi N_{pxl}/d_{FZP} \tag{4.7}$$

where N_{pxl} is the number of pixel and $d_{FZP} = 2R_{FZP}$ the zone plate diameter. An intermediate step is added before propagating the wavefront at the focal plane. At $z = z_{OSA} = 0.08$ m the propagated field $\Psi(\rho_{OSA} z_{OSA})$ is multiplied with a mask $M_2(x, y)$, modelling the OSA. The OSA is defined as:

$$OSA(\rho_{OSA}) = \begin{cases} 1 & \text{for } |\rho_{OSA}| \leqslant R_{OSA} \\ 0 & \text{otherwise.} \end{cases} \tag{4.8}$$

$R_{OSA} = 25$ μm is the pinhole radius. The resulting field is further propagated to the focal plane according to Eq. 4.6.
In figure 4.5, a and b, the phase and amplitude (expressed in logarithmic

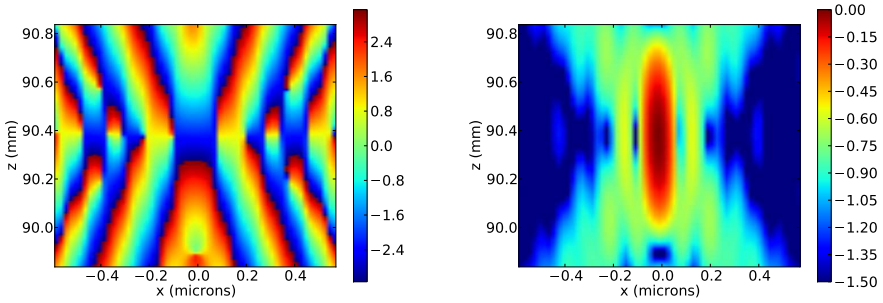

(a) (b)

Figure 4.5: (a) Phase and (b) amplitude in logarithmic scale of the complex field plotted in the plane xz. A central stop and a order sorting aperture with a diameter of 65 μm and 50 μm, respectively, are included in the simulations.

scale) of the calculated complex field in the xz plane in the vicinity of the focal position, are shown respectively. A range of 1 mm along the z-axis has been chosen to measure the focal depth and the phase variation in the direction of propagation. The focal length in the case of a fully illuminated FZP according to Eq. 3.17 in Chapter 3 (page 66) is proportional to the outermost zone width Δr_n. Calculations shows an effective focal length of 0.29 mm (Fig. 4.5b) and phase measured in the focal depth is found to be constant within approximately 0.2 mm (Fig. 4.5a).

The calculated focal spot appears as symmetric in the focal plane (Fig. 4.6), i.e. the plane transverse to the direction of propagation. The calculated phase is constant at the focal spot (Fig. 4.6a). This is also visible in Fig. 4.6c, in which the horizontal cut of the simulated phase at the focal plane is illustrated. In Fig.4.6 d the horizontal cut of the calculated amplitude, expressed in logarithmic scale, is plotted. The focal spot size is 85 nm in both horizontal and vertical directions, in perfect agreement with the expected value (c.f. Eq. 3.16, Chapter 3).

As comparison, I show also the 1D profile of the wavefront at the focus using the 1D FZP and the cylindrical symmetry as previously discussed (see Fig. 4.7). This approach does not influence the calculation of the phase that is always constant at the central peak. On the other hand, the amplitude of the central peak is underestimated. This is because the amplitude of the focal spot in the focal plane is given by the contribution of all the possible 1D profiles covering the FZP surface. The previous approach is therefore preferred.

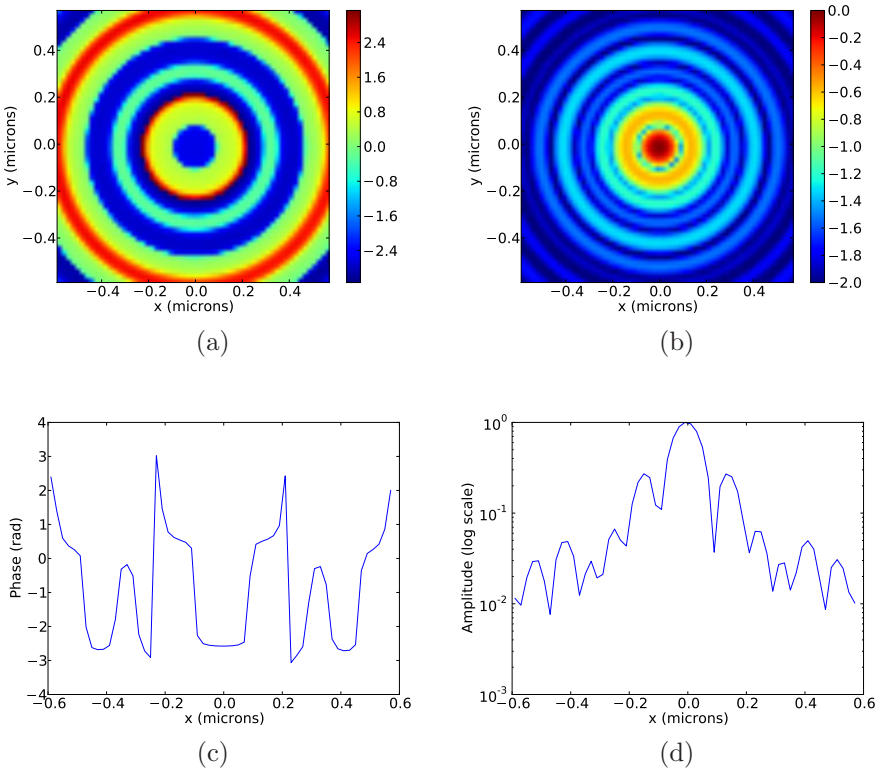

Figure 4.6: (a) Simulated phase and (b) amplitude (logarithmic scale) at the focus of a Fresnel Zone Plate. A central stop and an order sorting aperture with a diameter are included in the simulations. Horizontal cuts of (c) calculated phase and (d) amplitude (logarithmic scale)

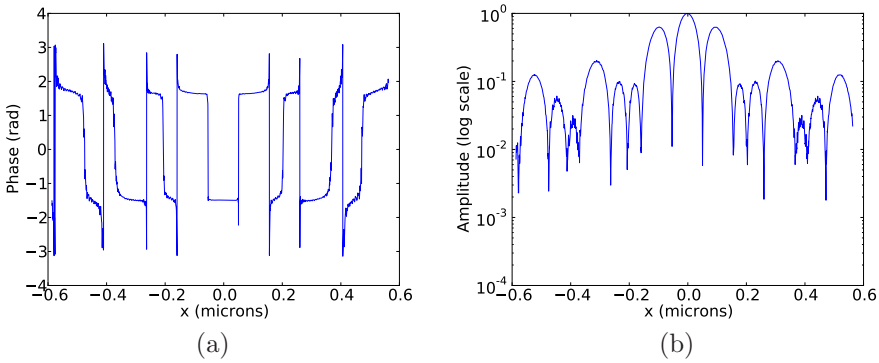

Figure 4.7: Profiles of (a) calculated phase and (b) amplitude (logarithmic scale) using a 1D dimensional FZP.

A constant phase at the sample position is fundamental when a CDI approach is used for nanostructure characterization. The retrieved phase includes information coming from the intrinsic phase of the studied nano-object and the phase of the illumination function. If the latter is constant its contribution can be easily disentangled.

The intensity of the forwarded beam at the detector position, i.e. at step 3, has been calculated according to the paraxial Fresnel free-space approximation [Quiney et al., 2006]:

$$\begin{aligned}\Psi(\rho_3, z_3) &= -\frac{i}{\lambda z_{23}} \exp\left(\frac{2\pi i z_{23}}{\lambda}\right) \exp\left(\frac{\pi i {\rho_3}^2}{\lambda z_{23}}\right) \\ &\times \int\int \Psi(\rho_2, z_2) \exp\left(\frac{\pi i {\rho_2}^2}{\lambda z_{23}}\right) \exp\left(-\frac{2\pi i \boldsymbol{\rho_2} \cdot \boldsymbol{\rho_3}}{\lambda z_{23}}\right) d\rho_2\end{aligned} \tag{4.9}$$

Here $z_{23} = 0.954$ m is the distance between the plane 2 and the plane 3 along the propagation axis. Equation 4.9 can be expressed using the following more practical formula introducing the Fourier Transform (FT) operator [Quiney et al., 2006]:

$$\begin{aligned}\Psi(\rho_3, z_3) &= -i \exp\left(\frac{2\pi i z_{23}}{\lambda}\right) \exp\left(\frac{\pi i \rho_3^2}{\lambda z_{23}}\right) \mathrm{FT}\left[\exp\left(\frac{\pi i \rho_2^2}{\lambda z_{23}}\right) \Psi(\rho_2, z_2)\right] \\ &= A(\rho_3, z_{23}) \mathrm{FT}\left[B(\rho_3, z_{23}) \Psi(\rho_2, z_2)\right]\end{aligned} \tag{4.10}$$

The two oscillatory function $A(\rho_3, z_{23})$ and $B(\rho_3, z_{23})$ and the Fourier Transform are therefore involved in the propagation from a plane 2 to a plane 3. This approximation is equivalent to Eq. 4.5 and it operates in the space of coordinates rather than in the frequencies space. The choice of using Eq. 4.10 rather than Eq. 4.5 allows to handle smaller two-dimensional matrices, reducing both computational memory and time, and to rescale the pixel size of the matrices at each position along the propagation. For our numerical simulations, a range of ≈ 2.6 μm, corresponding to 129 pixels of 20 nm, has been selected at the focal plane to obtain a pixel size d_{pxl} of 57 μm at the detector plane close to the experimental value. The value of d_{pxl} is calculated through the formula:

$$d_{pxl} \approx \frac{\lambda}{2N\Delta\theta}, \tag{4.11}$$

where $\Delta\theta$ is the angular resolution and N the total number of pixels.

All the calculated intensities at the detector plane are used to compare

our theoretical model to the experimental data. Simulated intensity and

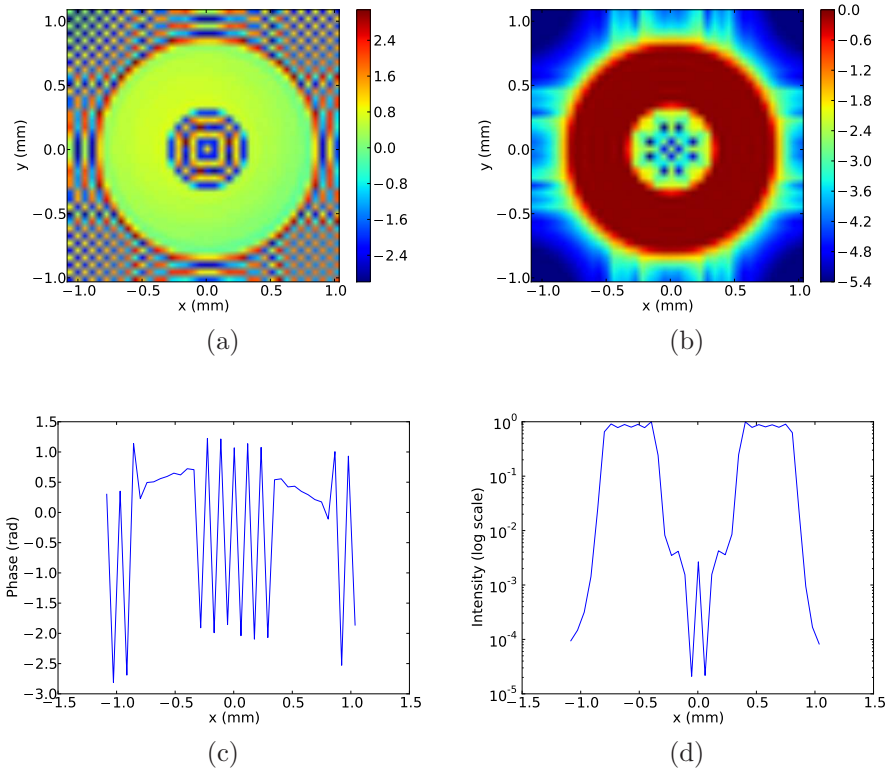

Figure 4.8: (a) Simulated two-dimensional phase (logarithmic scale) and (b) intensity of the calculated complex field at the detector position. The cylindrical symmetry and the constant phase are preserved along the propagation. Horizontal cuts of (c) calculated phase and (d) intensity (logarithmic scale) at the detector plane.

phase at the detector plane are illustrated in Fig. 4.8, having selected a small range in the computational window of ≈ 2.5 mm. The 2-dimensional intensity in Fig. 4.8a, as expected, has the same symmetry as the illuminated object, the FZP. This is also visible in Fig. 4.8c, where a cut of the horizontal axis is plotted. At the detector plane, contributions coming from the zones of the lens are not distinguishable due to the presence of the OSA and the lack of higher order contributions. The intensity is constant in the area corresponding to the illuminated zone plate surface and it drops to zero outside the lens and in the central part, due to the presence of the beam stop. The calculated phase is constant as the FZP is a diffractive optics that preserves the phase of the wavefront along the propagation. The 2D numerical phase and a cut of the horizontal axis are shown in Fig. 4.8 (b) and (d), respectively.

Slit Opening μm^2	Focal Spot Size (FWHM) μm^2	Focal depth (FWHM) mm	Phase rad
$200_v \times 200_h$	$0.085_v \times 0.085_h$	0.29	const.
$120_v \times 40_h$	$0.20_v \times 0.58_h$	0.74	const.
$60_v \times 20_h$	$0.39_v \times 1.20_h$	2.66	const.
$40_v \times 20_h$	$0.60_v \times 1.20_h$	5.68	const.

Table 4.2: Values of beam size and focal depth calculated for different illumination conditions. Calculated phases at the focal spot is also tabulated. The ideal case of a fully illuminated FZP is shown for comparison.

4.1.2 Partially illuminated Fresnel Zone Plate

The propagation of a coherent wavefield produced by a partially illuminated zone plate is detailed in this section. The partial illumination condition is simulated by a mask not centred in the origin and placed at the zone plate plane as shown in Fig. 4.1. The size of the mask corresponds to the slit opening and the lateral shift is necessary to avoid the CS illumination. The scheme of the experimental set-up is shown in figure 4.1. The slits are considered in the following calculations placed at the FZP position and shifted of about 42.5 μm with respect to the zone plate centre. As a consequence of the asymmetric illumination, the direction of the beam propagation is inclined with respect to the FZP axis. The calculated fields in the vicinity of the focal position, i.e. along the FZP axis, are shown in Fig. 4.9. Three different slit openings are used for calculations. In order to simulate our experimental condition, a slit opening of $60_v \times 20_h$ μm^2 has been chosen to match the transverse coherent lengths of the beamline. Two additional illumination conditions have been used for comparison: $40_v \times 20_h$ μm^2 as a lower limit for the slit size and $120_v \times 60_h$ μm^2, which corresponds to the transverse coherence at a double distance from the source. This choice is motivated by the planned upgrade program for the extended ID01 beamline. The values of the simulated focal spot dimensions and focal length are summarized in Table 4.2. The case of a fully illuminated FZP is also reported to show the influence of slits. Both focal depth and transverse dimensions of the focal spot are strongly influenced by the opening. Contrary to the case of a full illuminated FZP (cf. Fig. 4.4 and 4.5), the beam size at the focus is not anymore proportional to the outermost zone width [Jefimovs et al., 2007], but becomes larger for smaller openings and it is defined by the slit opening and by the number of illuminated zones. In Figs. 4.10, the

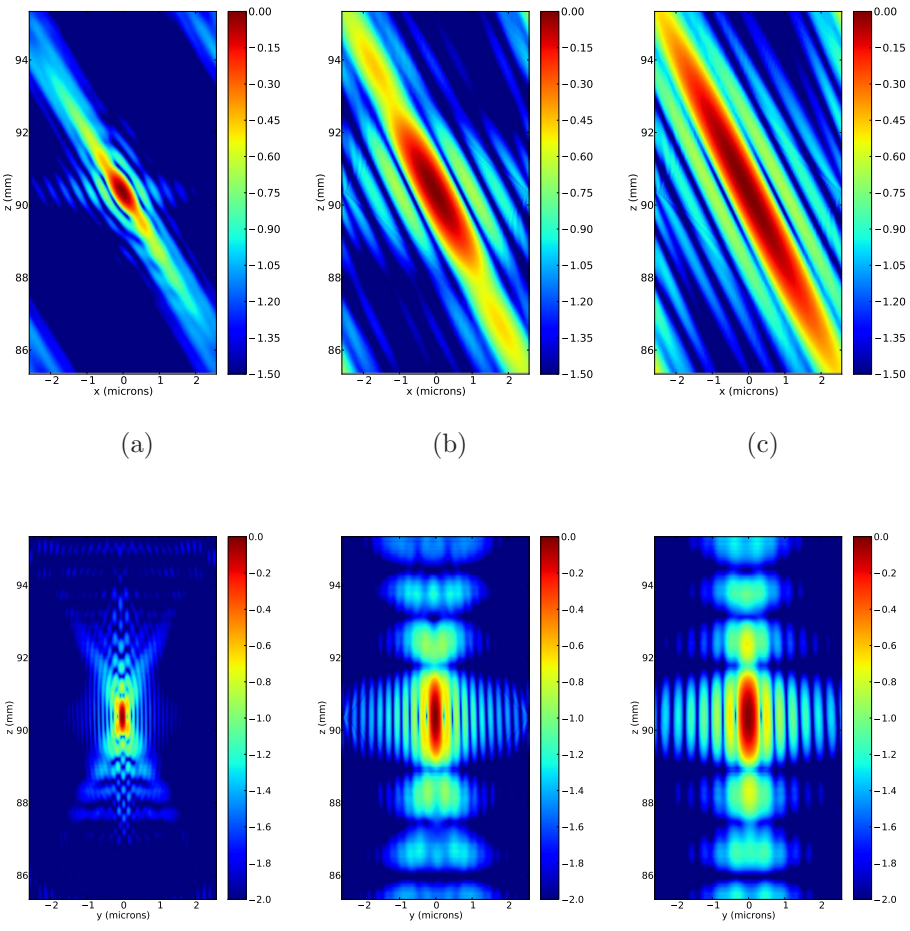

Figure 4.9: Simulated complex field in the vicinity of the focus of a Fresnel Zone Plate. The focal length are strongly influenced by the presence of the slits. Calculations have been computed for three different slits opening: (a,d) $120_v \times 60_h$, (b,e) $60_v \times 20_h$ and (c,f) $40_v \times 20_h$ μm^2. Cuts in (a-c) the horizontal (xz) and (d-f) vertical (yz) planes.

simulated complex fields are shown at the focal plane, perpendicular to the direction of propagation. The amplitude is plotted in logarithmic scale for all three openings (Fig. 4.10, a-c). The shift of the opening also creates a linear phase shift in the xy plane (cf. Fig.4.11) which has been corrected in Fig.4.10(d-f) - i.e. the phase shift plotted in this figure refers to a plane wave along the axis joining the illuminated part of the FZP and the focal spot. The phase correction has been done according to the following formula:

$$\Psi(\rho_2, z_2)_{corr} = \Psi(\rho_2, z_2) \exp\left(2\pi i \frac{\Delta x}{f\lambda}\ \mathbf{x}\right) \tag{4.12}$$

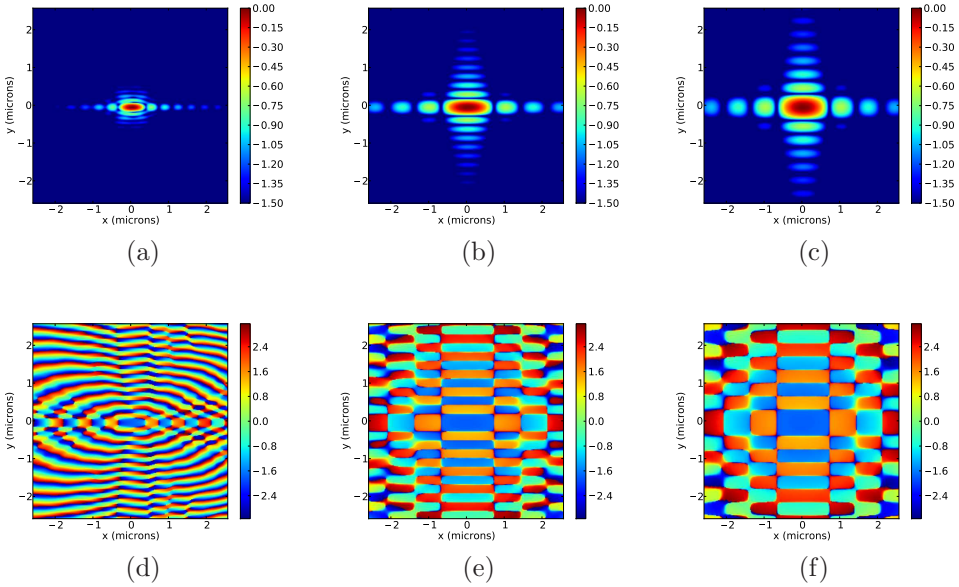

Figure 4.10: Simulated complex field at the focal plane: (a,b,c) amplitude (in logarithm scale) and (d,e,f) phase the focal spot size for three different slits opening: (a,d) $120_v \times 60_h$, (b,e) $60_v \times 20_h$ and (c,f) $40_v \times 20_h$ μm^2. For each opening, the central peak shows a constant phase and focal spot size are found inversely proportional to the slit openings.

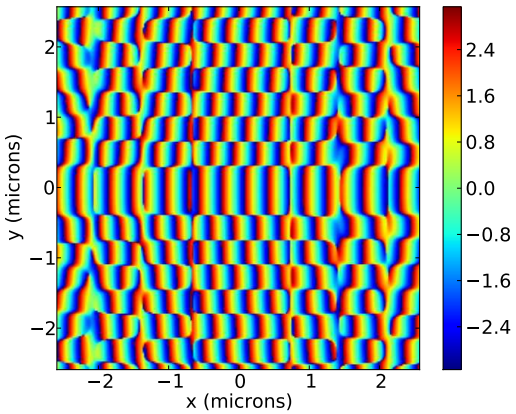

Figure 4.11: Simulated phase at the focal plane without correction for the slit opening $40_v \times 20_h$ μm^2.

where $\Psi(\rho_2, z_2)_{corr}$ and $\Psi(\rho_2, z_2)$ are the corrected and uncorrected fields, Δx the opening shift and $\mathbf{x}$ the axis in the direction of the shift, in this case the horizontal one. λ is the wavelength and f the focal length.

The size of the focal spot is measured at the full width half maximum (FWHM) of the vertical (see Figs. 4.12, a-c) and the horizontal (see Figs. 4.12, d-f) profiles. The asymmetry of the focal spot is the direct con-

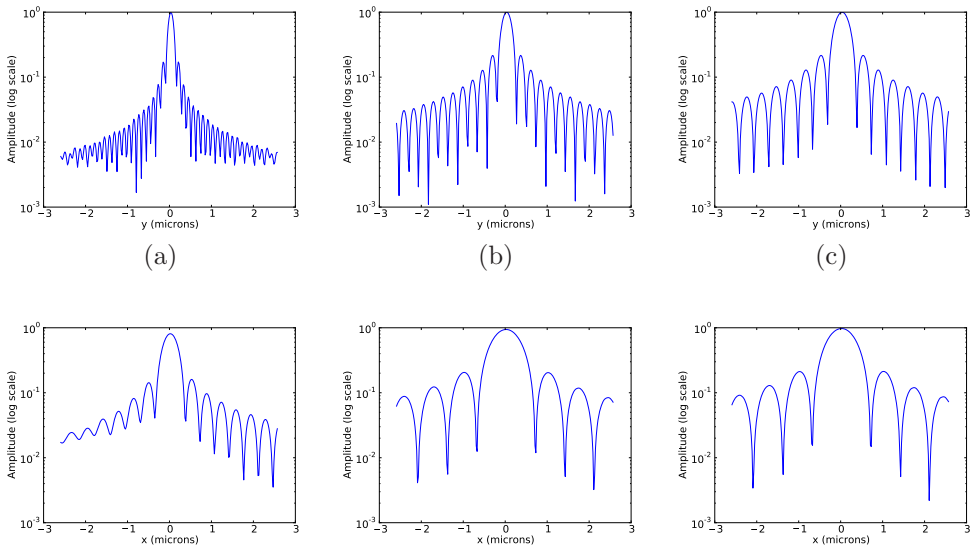

Figure 4.12: Simulated complex field at the focus of a Fresnel Zone Plate: (a,b,c) cuts in the vertical (y) and (d,e,f) in the horizontal directions. Calculations have been computed for three different slits opening: (a,d) $120_v \times 60_h$, (b,e) $60_v \times 20_h$ and (c,f) $40_v \times 20_h$ μm^2.

sequence of the asymmetry of the illumination. The focal depth is also inversely proportional to the slit opening, as shown in Fig. 4.9, and it is found to be significantly larger than the one observed for a fully illuminated FZP (Fig. 4.5]. This effect is attributed to the decreased numerical aperture of the lens, i.e. the smaller divergence of the beam produced with a slit smaller than the transverse FZP dimensions. The effective focal depth can be calculated looking at the xy plane. The cuts in the yz plane (Fig.4.9(d-f)), due to the deviation, give only a portion of the propagated beam. The effective direction of propagation, as expected, is deviated from the Fresnel Zone Plate axis by about 0.37 mrad (Fig.4.9, a-c), due to the lateral shift of the illuminated area with respect to the optical axis (Fig.4.1). The angle is calculated by pure geometrical considerations.

The most interesting result of this study is the confirmation of the constant phase at the focal spot. This indicates that the partial illumination of the FZP does not affect the phase of the focused beam, which enables CDI experiments without complex corrections, as long as the object studied is smaller than the focal spot. The results shown until now are of general applicability. However, in our experimental conditions, slits are not placed at the FZP plane, as in the case of calculations discussed unltil now, but

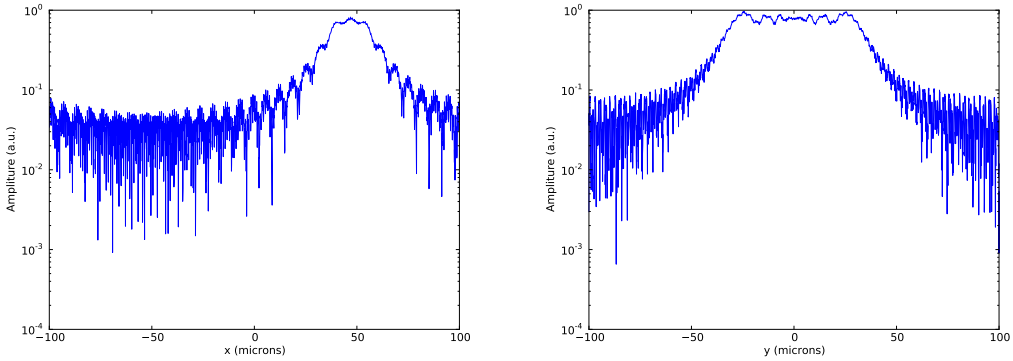

(a) (b)

Figure 4.13: Amplitude (expressed in logarithmic scale) of simulated complex field at the FZP plane considering the propagation from the slits distant 1.15 m: cut in the (a) horizontal and (b) vertical directions. An opening of $72_v \times 28_h \mu m^2$ corresponding to the experimental opening.

they are 1.15 m upstream the FZP. This has to be considered into the numerical simulations of the wavefront propagation in order to check possible influences and compare to experimental data. An additional step in the calculations has been therefore added, i.e. the wavefield propagation from the slit to the zone plate position. That corresponds to calculate the wavefront propagation for 1.15 m in the forward direction. Using the formula given in Eq. 4.5, for an opening of $72_v \times 28_h$ μm^2 corresponding to the actual experimental conditions, the amplitude of the propagated wavefield is shown in Fig. 4.13. Due to the huge dimension of the computational matrix, we decided to plot the horizontal and vertical cuts in Fig. 4.13,a and b, respectively. It is evidenced that for the opening of 20 μm, the distance of 1.15 m is at the limit of the near-field domain. The lateral fringes, typical of the Fraunhofer regime, appear at the side of the central peak (see Fig. 4.13a). This field is then multiplied with the plane wavefield generated at the FZP position and propagated to the focal plane. The results of these calculations are shown in Fig 4.14 for a slit opening of $72_v \times 28_h$ μm^2, corresponding to the experimental opening. The effective direction of propagation is obviously unchanged. An important effect is visible both in the xz plane (a) and the focal plane (c). The X-ray beam is distorted and it becomes asymmetric in the horizontal direction. Looking at the vertical and the horizontal cuts at the focal plane, a spot size of $300_v \times 800_h nm^2$ can be measured at the FWHM (Fig. 4.14, e-f). The phase of the central peak, as illustrated in Fig. (d) for the focal plane, is still constant. Figure 4.15 shows the prop-

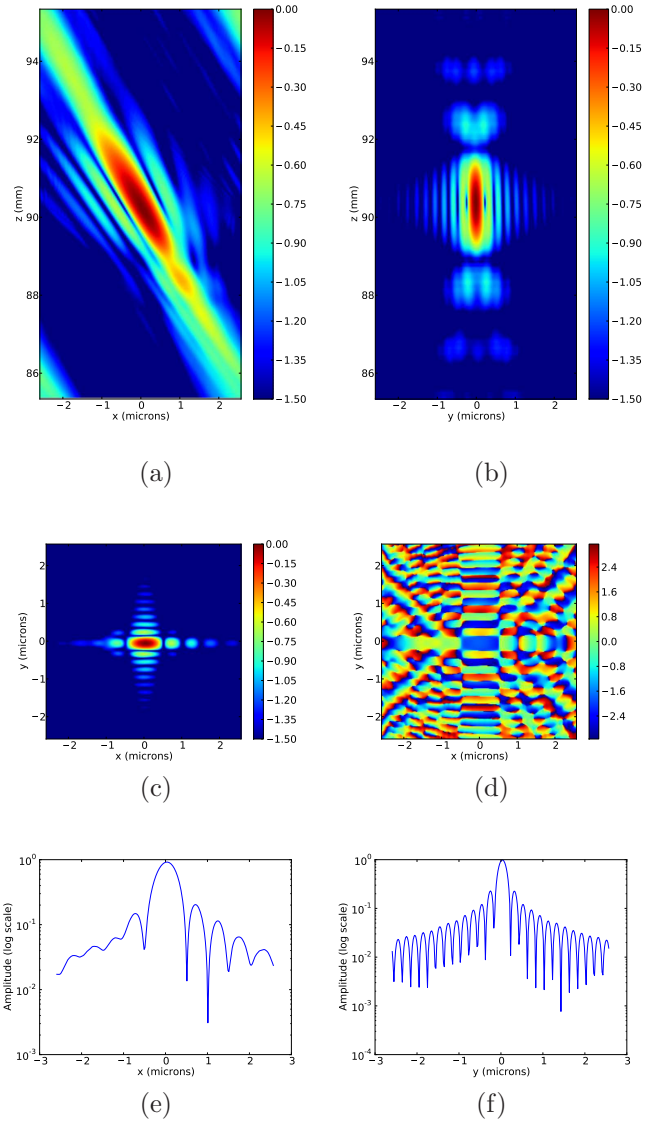

Figure 4.14: Simulated complex field at the focal plane when slits are distant 1.15 m from the FZP plane: calculated amplitudes (in logarithm scale) in the (a) xz, (b) yz and (c) xy planes are shown. (d) Calculated phase in the xy plane is found to be constant. (e,f) Vertical and horizontal cuts of the focal spot show a spot size of $300_v \times 800_h$ nm^2.

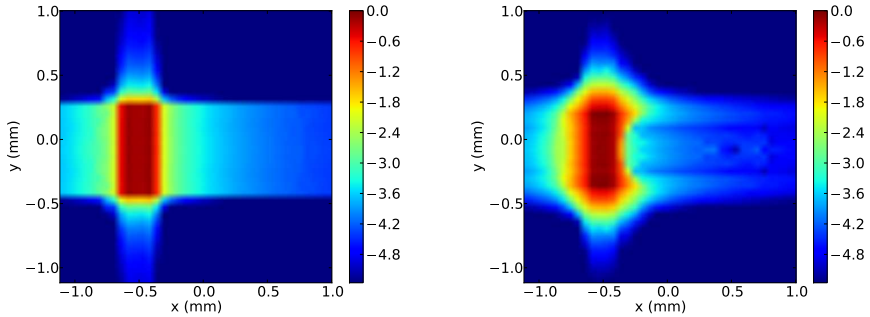

(a) (b)

Figure 4.15: Simulated 2D intensities at the detector plane when (a) slits are at the FZP plane and (b) 1.15 m before the lens.

agated field at the detector position obtained by the procedure described for the case of a full illuminated FZP. The intensity distribution at the detector calculated when the opening is placed at the FZP plane is shown in Fig. 4.15a. The case of an identically open slit located at 1.15 m before the FZP position is shown in Fig. 4.15b as comparison. The slit scattering is responsible of the strong background visible in Fig. 4.15a. Moreover, the interference fringes present in the wavefront at the FZP position illuminate also the central stop, that is partly imaged on the detector. For a sake of completeness, in figure 4.16 the calculated phase at the detector plane is shown for the two cases, i.e. slits close (Fig. 4.16a) and slits far (Fig. 4.16b) for the FZP.

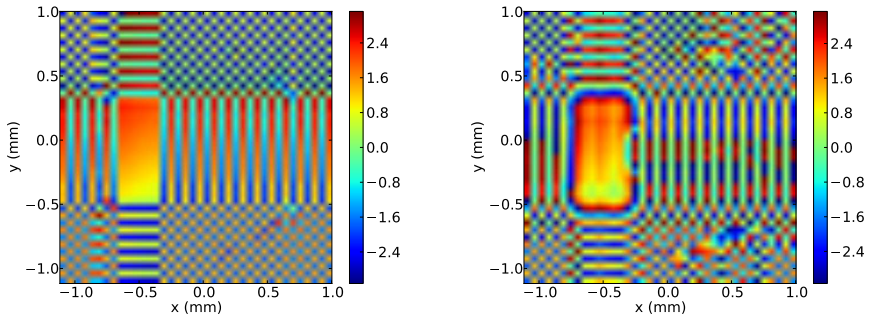

(a) (b)

Figure 4.16: Phases of simulated wavefield at the detector plane for (a) partially illuminated FZP (b) including the propagation of the wavefield from the slits to the lens plane.

4.2 Imaging the focused complex wavefield

In order to reconstruct the focused complex wavefield , we have measured the direct beam produced by a partially illuminated FZP, and used these data to retrieve the wavefield near the focal spot, following the method proposed by Quiney et al. [2006] and Williams et al. [2010]. The experiment was carried out on the undulator beamline ID01. A typical measurement of the direct beam at the detector position is shown in Fig. 4.19a. The Fresnel Zone Plate used for this experiment is made of gold and the thickness of opaque zones is equal to 1 μm. The thickness of the gold central stop is 22 μm [C. David: Personal Communication] that yields a low transmission coefficient, of the order of 5×10^{-4}. Partial illumination is obtained by a set of rectangular slits matching the transverse coherent lengths of the beamline, placed at a distance of 1.15 m before the lens. Using the numerical tools previously described, the x-ray propagation to the detector plane can be simulated using different slits opening until an agreement with experimental data is found. In this way, a model can be provided to de-

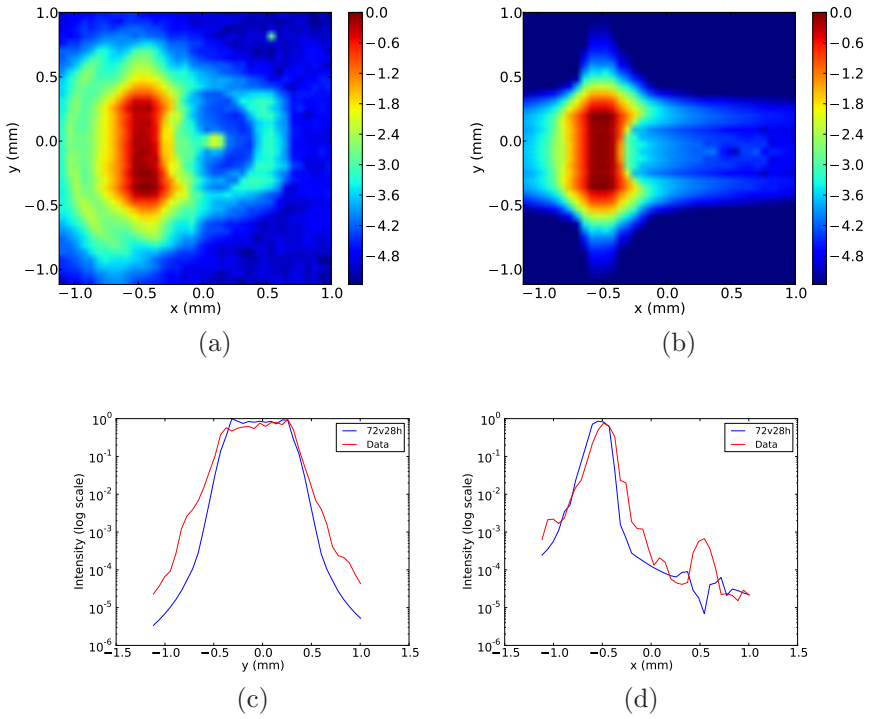

Figure 4.17: (a) Experimental intensity in the divergent part of the focused beam compared to (b) calculations. (c) Horizontal and (d) vertical cuts for experimental intensity and simulated one when slits are 1.15 m distant from the FZP.

velop a phase retrieval algorithm to reconstruct the illumination function at the focal position using experimental data. The slit scattering, which is responsible of the strong background, clearly imposes to introduce in our calculations the propagation between the slit and the FZP (equal to 1.15 m in our set-up). The best agreement of the far-field intensity is obtained for a slit opening of $72_v \times 28_h$ μm^2 (Fig. 4.17, b-c). The discrepancy between these values and the expected ones of $60_v \times 20_h$ μm^2 is attributed to an error in the calibration of the slit. In figure 4.17a, the non-zero intensity pixels in the center of the detector are due to direct beam photons transmitted by the central stop (most likely higher harmonics)

In the next section I describe the modified iterative algorithm and discuss the results obtained from the reconstruction of fully and partially illuminated FZP.

4.2.1 Modified Phase Retrieval Algorithm

The iterative phase retrieval algorithm developed for the reconstruction of the wavefront at the focal position is based on the same principle of iterative retrieval algorithms used in coherent diffraction imaging. This algorithm has been proposed for the first time in Ref. [Quiney et al., 2006]. The paraxial free-space approximation expressed in Eq. 4.9 replaces the back and forth FT in the algorithm to retrieve phase and amplitude of the wavefield at the focal position from the direct beam intensity at the detector plane. According to the proposed method, the wavefront reconstruction is done without employing any sample at the focal position, where no constraints can be applied. Here the wavefield has an extended extension, due to the finite size of the FZP. To make the algorithm converging and the reconstruction successful, the real space constraints, i.e. the support constraints, have to be imposed at the FZP position. The support, whose size is defined by the illuminated area on the lens, is added at the FZP position. Consequently, the employed algorithm consists of 4 steps cycle, from the detector to the focus and from the focus to the FZP and viceversa rather than one as in the typical retrieval algorithm. If we set the FZP plane at z1, the focal plane at z2 and the detector at z3, the algorithm follow the cycle z3-z2-z1-z2-z3. A scheme of the algorithm is shown in Fig. 4.18 to explain the procedure of the reconstruction. In equation 4.9, $z_{ij} = z_j - z_i = -z_{ji}$. The complete cycle can be therefore summarized in 6 steps [Quiney et al., 2006] :

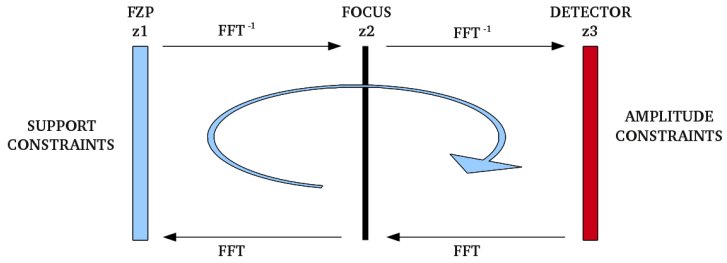

Figure 4.18: Scheme of the two-steps phase retrieval algorithm used to reconstruct the complex wavefield at the focal plane.

1. Propagate the wavefield from z3 to z2 multiplying the measured amplitude by a random phase:
   $\Psi(\rho_2, z_2) = A(\rho_2, z_{32})\mathrm{FT}^{-1}\left[P(\rho_3)\right]$;

2. Propagate the complex field from the focal plane to the lens position defined by z1:
   $P(\rho_1) = -i\exp(2\pi i z_{21}/\lambda)\mathrm{FT}^{-1}\left[B(\rho_2, z_{21})\Psi(\rho_2, z_2)\right]$;

3. Applying finite support constraint to $P(\rho_1)$:
   $P'(\rho_1) = P(\rho_1)S(\rho_1)$;

4. Propagate from z1 to z2:
   $\Psi(\rho_2, z_2) = A(\rho_2, z_{12})\mathrm{FT}\left[P'(\rho_1)\right]$;

5. Propagate from z2 to z3:
   $P(\rho_3) = -i\exp(\frac{2\pi i z_{23}}{\lambda})\mathrm{FT}\left[B(\rho_2, z_{23})\Psi(\rho_2, z_2)\right]$;

6. Imposing constraints on $P(\rho_3)$:
   $|P(\rho_3)| = \sqrt{I^{\mathrm{Meas}}(\rho_3)}$.

In these equations, $S(\rho_1)$ is the support function. At the position z1, corresponding to the lens plane, the complex field is calculated as a complex pupil function that contains also information due to the presence of the OSA and a central stop. The analytical expression for the pupil function at the FZP plane is

$$P(\rho_1) = \Psi(\rho_2, z_2)\exp(\frac{\pi i\rho_1^2}{\lambda z_{12}}) \tag{4.13}$$

and similarly for z3 at the detector plane we have

$$P(\rho_3) = \Psi(\rho_2, z_2)\exp(\frac{\pi i\rho_3^2}{\lambda z_{23}}) \tag{4.14}$$

The algorithm consists of error reduction (ER), hybrid input-output (HIO) and charge flipping (CF) cycles. In addition, a shrink-wrap algorithm [Marchesini et al., 2003b] has been applied as it allows to take into account in the reconstruction the presence of features at the FZP plane due to the propagation from the slit to the lens. At each iteration, the reconstruction is measured by the metric error R, defined as follows:

$$R = \frac{\sum_{i=1}^{N} \left(|P_i(\rho_3)| - \sqrt{I^{\mathrm{Meas}}(\rho_3)} \right)^2}{\sum_{i=1}^{N} I^{\mathrm{Meas}}(\rho_3)} \tag{4.15}$$

4.2.2 Results and Discussion

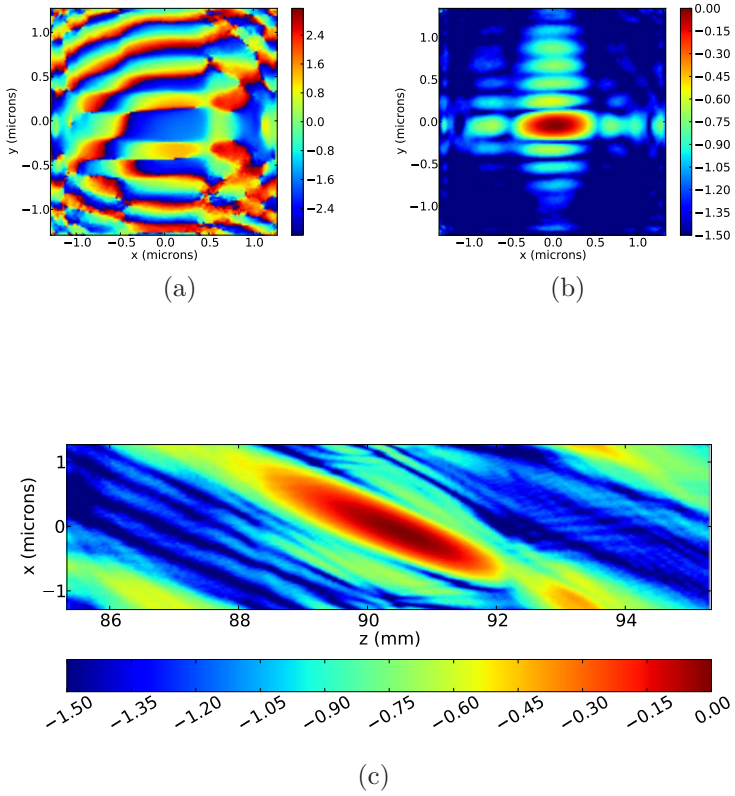

Figure 4.19: (a) Phase and (b) amplitude of the reconstructed complex wavefield at the focus and (c) along the direction of propagation.

The iterative phase retrieval algorithm previously described has been used to reconstruct the wavefront at the focal plane. The algorithm has been first tested using simulated data, shown in Fig. 4.15, a-b, and a set of random phases, varying in a range of 1 rad. The small phase range has been chosen to facilitate the algorithm convergence for the low number of pixels

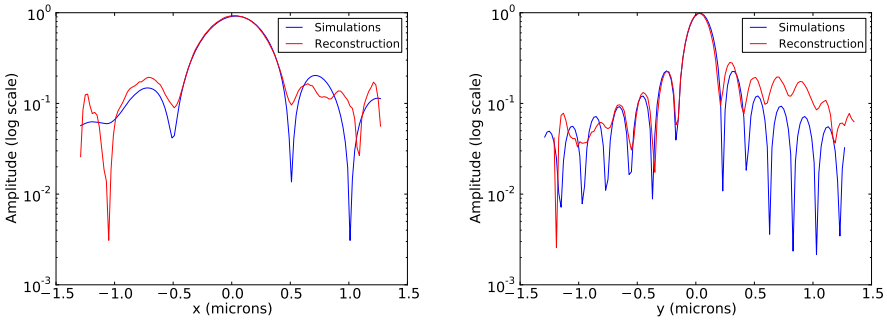

(a) (b)

Figure 4.20: (a) Horizontal and (b) vertical cuts of the reconstructed complex wavefield at the focus compared to the one computed considering a slit opening of $72_v \times 28_h \mu m^2$.

composing the image at the detector plane. The algorithm converges to the correct solution only for a dataset in which the propagation from the slit is not considered. The impossibility of reconstructing the wavefield at the focus when considering the diffraction from the slits is probably due to the important tails and background and, obviously, the limited resolution of the detector. To facilitate the algorithm convergence in the case of real data, corresponding to the case shown in Fig. 4.15b, I have used the simulated phase (cf. Fig. 4.16b) at the detector plane as initial guess in the retrieval algorithm. The reconstruction allows to access the complex wavefield both at the focus and at the FZP.

Results obtained from the inversion are shown in Fig. 4.19. The size of the reconstructed focal spot is $\approx 280_v \times 730_h \ nm^2$ (Fig. 4.19b) and the focal depth is equal to $\approx 4 \ mm$ (Fig. 4.19c and 4.20a,b). The focal spot is asymmetric in the horizontal direction and it compares very well with the calculations (cf. Fig. 4.19a). The fringes in vertical direction are more intense and with an higher background to one side of the focal spot. The asymmetry is highlighted in Fig.4.20b, where the horizontal cut of the amplitude at the focal plane is shown (red color) and compared to the simulations (blue color). This effect is attributed to the peculiar illumination of the FZP obtained with vertical slit blades with an offset in the longitudinal direction [Le Bolloc'h et al., 2002].

The reconstructed pupil function at the FZP plane is shown in Fig. 4.21. As expected, both the resolution and the presence of the OSA does not allow us to retrieve the zone profile of the illuminated area. Finally, I present in Fig. 4.22 the evolution of the metric error R registered during

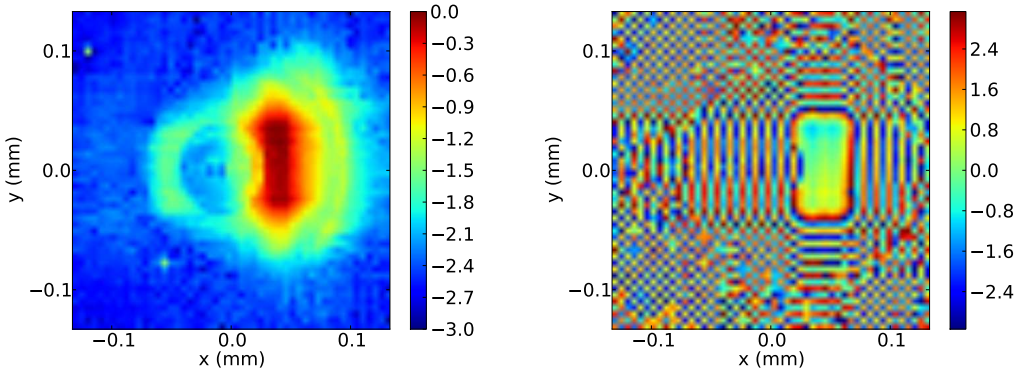

(a) (b)

Figure 4.21: (a) Amplitude (b) and phase of the reconstructed complex wavefield at the zone plate plane.

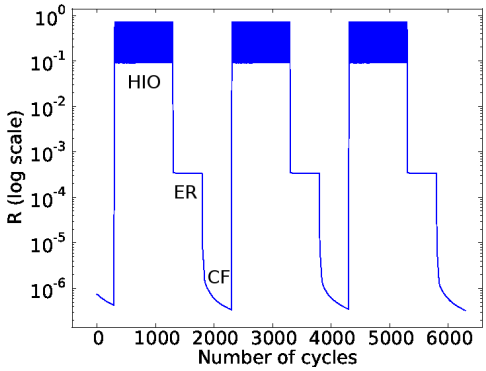

Figure 4.22: Part of the metric error R registered during the reconstruction. Contributions from ER, HIO and CF algorithms are labelled.

the reconstruction process. The different contributions from the employed algorithms (ER, HIO and CF) are labelled in the figure.

For the sake of completeness, the same algorithm described in the previous section has also been used to retrieve the focal plane produced by a fully illuminated FZP from its image of the direct beam at the detector plane (Fig. 4.23a). This reconstruction is similar to the case described by Quiney et al. [2006] and for which the method has been developed. In Fig. 4.23, b and c, the reconstructed amplitude at the focal plane and the retrieved phase of the focal spot are shown, respectively. The reconstruction completely agrees with the simulations in Fig. 4.6 a,b. This reconstruction assumes a fully coherent illumination of the whole FZP. This is not true experimentally and the obtained results do not describe the actual wavefront at the focus. It has been shown from experimental measurements that the

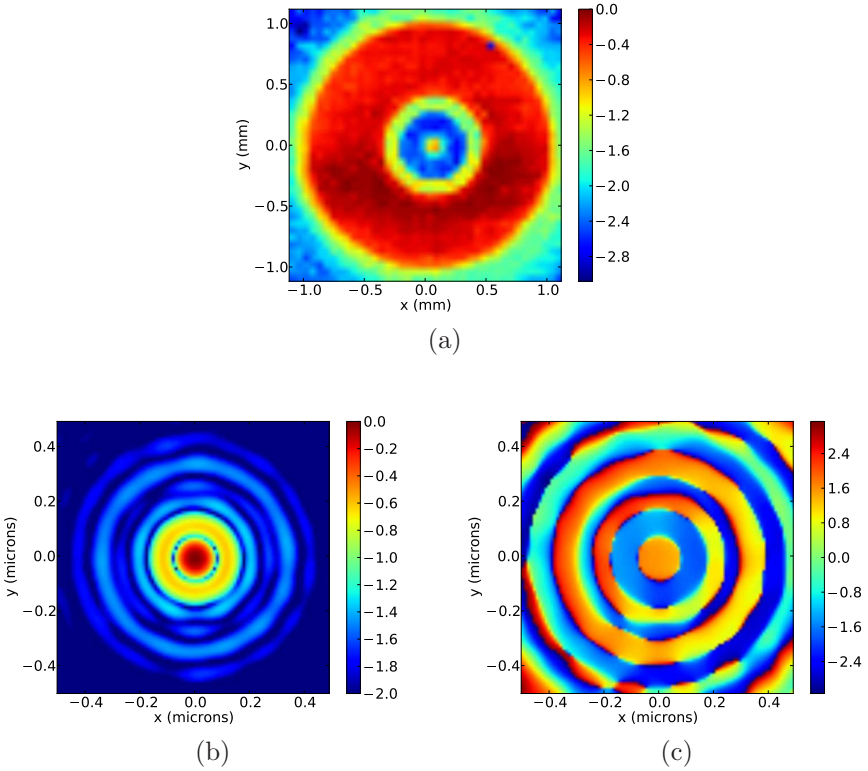

(a) (b) (c)

Figure 4.23: (a) Experimental data used to reconstruct (b) amplitude (logarithmic scale) and (c) phase of the complex wavefield at the focus in the case of a fully illuminated Fresnel zone plate with a fully coherent beam.

focus on ID01 has an asymmetric shape, which reflects directly the different source size and beam divergence in the horizontal and vertical directions. A more appropriate reconstruction should include information on partial coherence effects.

4.3 Imaging the coherent beam using Bragg Ptychography

As suggested in the introduction to this chapter, an alternative approach to retrieve the complex-valued illumination function at the focus of a FZP in the same illumination conditions is the ptychography [Thibault et al., 2008]. This method offers the possibility of reconstructing both the complex fields describing the sample and the probe (i.e. the illumination function) with the use of iterative algorithms. This can be achieved due to the redundancy of information in the diffraction patterns collected from overlapping areas on the sample. A sketch of a typical ptychographic approach is given in

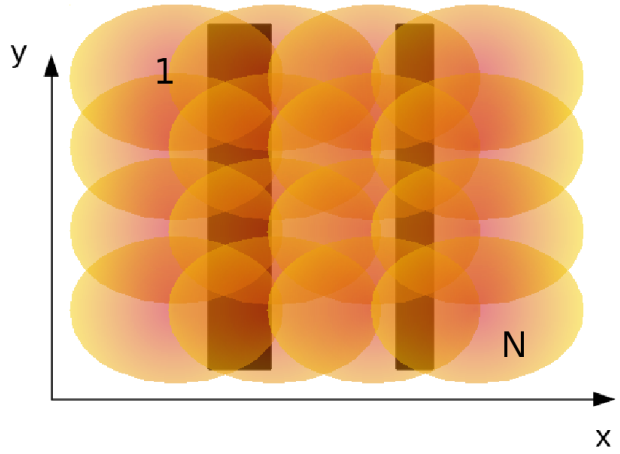

Figure 4.24: Schematic of the ptychographic approach. The beam moves from position 1 to N to cover the surface of the chosen zone on a sample, in that case a schematically depicted double Si lines.

Fig. 4.24.

The experiment described in the following is the first example of ptychography successful applied in Bragg geometry. The Bragg ptychography experiment [Godard et al., 2011] was carried out at the ID01 beamline (ESRF). The monochromatic beam with a wavelength of 0.154 nm was delivered by a Si-111 monolithic channel-cut monochromator. For this experiment a 200 μm diameter Au FZP, with an outermost zone width of 100 nm, was implemented into the set-up. At the working energy of 8 keV, the focal length is 129 mm. A 60 μm diameter central stop and a 50 μm circular order sorting aperture, placed at 10 mm from the FZP plane, complete the set-up. The theoretical focal spot size is approximately 110 nm in both directions. The conditions of partial illumination for this experiment were achieved using an aperture of 80×20 μm^2 and placed 1.15 m before the lens. As previously discussed, the correct illumination of the zone plate was obtained with a lateral shift of the aperture, in the horizontal direction. The sample used for the experiment is a <110>-oriented Si double-line. The line were produced by e-beam lithography from a continuous Si $\langle 001 \rangle$ layer (180 nm thick) covering a SiO_2 film (25 nm thick) onto a Si $\langle 110 \rangle$ substrate. The structures were defined by a positive photo resist with a thickness of 130 nm, using a SF_6 reactive ion etching to transfer the pattern into the Si layer. The two Si lines are about 40 nm high and 520 and 260 nm wide, respectively. The separation between the lines results in a

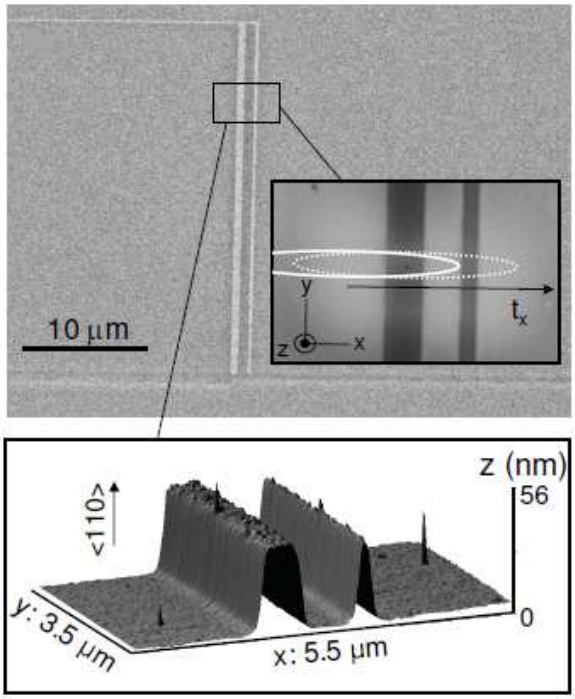

Figure 4.25: Top: Electron microscopy of the <110>-oriented Si double-line. Bottom: Atomic force microscopy of the exploited region.

edge-to-edge distance of 1.7 μm. The line length is about 30 μm, much larger than the beam footprint. The scanning electron microscopy of the lines patterned on the Silicon-on-insulator substrate is shown in Fig. 4.25 (bottom). The zoomed region (inset) emphasizes the area investigated during the ptychography scan. The direction of translation t_x is shown through white ellipses indicating the two first illuminated areas. The same region as seen by atomic force microscopy is in Fig. 4.25 (top). This experiment allowed to investigate in Bragg condition, the (220) reflection of Si, with the line axis lying in the scattering plane (Fig. 4.25).

The phase retrieval algorithm developed in [Godard et al., 2011] is performed in the reciprocal space frame and the conjugated direct space frame. The first step consists in the estimation of the 3D sample scattering function, $\rho(\mathbf{r})$, and the 3D illumination probe, $E(\mathbf{r})$. The algorithm (cPIE), which involves a series of K iterations and N sub-iterations, is summarized in the following:

(i) The exit-field $\psi_{k,j}$ is calculated using the Born approximation. In

the scalar approximation, it is simply given by:

$$\psi_{k,j}(\mathbf{r}) = E_j(\mathbf{r})\rho_{k,j}(\mathbf{r}). \tag{4.16}$$

(*ii*) The far-field distribution $E_{k,j}$ corresponding to the propagation of $\psi_{k,j}$ is obtained from

$$E_{k,j}(\mathbf{q}) = \big(\mathcal{F}\psi_{k,j}\big)(\mathbf{q}) \tag{4.17}$$

where $\mathcal{F}$ denotes the Fourier transform operator.This quantity is corrected so that the calculated intensity matches the experimentally measured data.

(*ii*) The last step allows to update the object estimate, taking into account the probe function and the overlapping condition

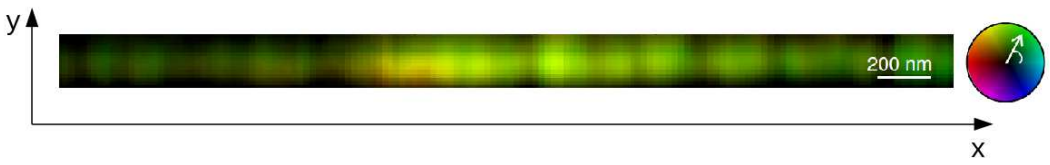

Figure 4.26: Color rendition of the reconstructed probe at the sample position. The retrieved illumination function is shown in the plane perpendicular to the X-ray beam propagation.

In Fig. 4.26 the reconstructed probe at the sample position is shown. The color rendition of the retrieved illumination function is shown in the plane perpendicular to the x-ray beam propagation. On the right, the color code is indicated as a reference: the length of the arrow and the angle correspond to the amplitude (expressed in linear scale) and the phase of the wavefront, respectively. In the same figure, the reference scale of 200 nm is given to estimate the transverse dimensions of the focal spot. The reconstructed phase measured at the focal spot is constant in perfect agreement with our simulations and the results previously discussed. The focal spot is elongated in the horizontal direction, as a consequence of the horizontal aperture of 20 μm and its size is found to be larger than the one expected in the case of a full illuminated FZP. The asymmetry in the horizontal direction is also stronger than the one observed with the CDI approach. These two effects are not due to an ambiguity in the proposed reconstructions but they are attributed to a wrong calibration in the lateral shift of the aperture.

The central stop is directly illuminated by the central part of the beam propagated from the slits position to the FZP plane (that shows an higher intensity with respect to the lateral fringes due to the slits scattering). The amplitude fluctuations within the focal spot are attributed to computational artefacts arising from intensity normalization.

4.4 Conclusions

A numerical approach to characterize the coherent complex field at the focus of a partially illuminated circular FZP has been developed. Systematically varying the illumination conditions, we observe noteworthy changes in the characteristic sizes of the beam at the focal plane. Namely, the focal spot size and the focal depth are found to be diffraction limited, with size increasing by decreasing the illuminated area on the lens. By means of the proposed calculations, the role of the different elements in our set-up, e.g. size and position of the slits defining the illumination of the FZP, can be understood and predicted. In particular, we learned the importance of defining the partial illumination via an aperture placed very close to the FZP. This helps in avoiding the effects due to the wavefront propagation between slits and FZP which induce asymmetric intensity of the focal spot. This has an important impact for a reliable characterization of nanoscale objects using coherent diffraction techniques both in Bragg geometry, where the crystal deformation is encoded in the phase of the reconstructed complex function, and in forward direction. Finally, calculations of the far field amplitude produced by a partially illuminated FZP, have been used to support the reconstruction of the complex illumination function at the focal plane from experimental data. Even in presence of an asymmetry of the focal spot, due to the specific setup used, the reconstructed wavefront has been found to have a constant phase within the central spot, in agreement with our calculations. The use of the new set-up recently developed at the beamline ID01 (see Appendix B) will provide us with new opportunities for a direct wavefront characterisations, through the increased resolution for the measurement of the far field data, and a better control of the illumination conditions of the focussing optics. The use of the ptychography approach on a test sample, for the characterisation of the wavefield produced by FZP in the same illumination conditions presented in this manuscript confirmed the results obtained and presented in this chapter.

Chapter 5

Coherent diffraction imaging on strained nanowires: beyond the ideal case

In this chapter, I report on the application of coherent diffraction imaging technique to recover the strain in nanostructures with the aim of showing how, in reality, experimental cases are compared to the CDI ideal case. In particular, I discuss the radiation damage which occurs when high brilliance radiation are used to illuminate nanosized structure. In addition, through numerical examples, I will show that the reconstructed nanostructure and, in particular, the correct interpretation of its displacement field, requires a precise knowledge of the illumination function. Finally, I show that the strain in nanowires can be retrieved using CDI even in presence of stacking faults (i.e. growth defects), choosing the adequate Bragg reflection that is not affected by these defects.

5.1 Time-dependent analysis on the strain evolution of sSOI lines

When x-ray diffraction techniques and, in particular, high brilliance beams are used to investigate single nanosized objects, radiation damage of the crystalline structure may occur. Radiation damage was already observed when studying macromolecular compounds through multiple isomorphous replacement (MIR) and multiwavelength anomalous dispersion (MAD) phasing methods by Ravelli and McSweeney [2000] and with coher-

ent x-ray diffraction by Marchesini et al. [2003a]. In that case, the dose estimated from the radiation characteristic was 2×10^7 Gy (1Gy = 1 J/kg). As in the case of inorganic compounds there is no knowledge of a dose limit, due to the fact that these compounds do not present specific weak bonds (-CO_2, S-S), they are less likely to break under irradiation. However, it was observed by Favre-Nicolin et al. [2009] that nanowires can also break when illuminated with highly intense x-ray beams. In the particular case of the cited reference, the three-dimensional scattering from a single wire was measured using a rocking scan by rotating the sample over a 0.8° angular range with 0.02° steps. A 50 sec exposure time per image was used to improve the signal to noise ratio. This procedure was repeated four times in order to accumulate more statistics for a successful reconstruction. For these measurements, the photon flux of the experimental radiation was estimated to be ≈ 4 ph/s/$\mathring{A}^2$. Given that the silicon absorption cross-section at E=10 keV is evaluated as $\sigma= 1.5 \times 10^5 \mathring{A}^2$, this results in a absorbed power of 0.6 eV/s per atom, or equivalently 2×10^6 Gy/s, that corresponds to a total dose of 8×10^9 Gy/s per scan. The wire breaking in that case was attributed to the presence of defects in the crystalline structure considered as weak points more sensitive to the irradiation.

In this section, the radiation damage observed during a coherent diffraction experiment is detailed in the case of stressed Silicon-On-Insulator lines (sSOI). A time-dependent analysis revealed that the damage consists in this specific case of a relaxation of the wire structure. Calculations have been performed in order to estimate the variation of the displacement fields during the relaxation of the investigated nanostructure.

5.1.1 Engineered strain in sSOI: sample description

Stressed silicon-on-insulator (sSOI) [Langdo et al., 2004, Ghyselen et al., 2004] layers are widely implemented in Metal Oxide Semiconductors Field-Effect-Transistors (MOSFET) devices mainly because of the presence of strain leads to an enhancement of electron mobility [Fischetti et al., 2002, Baudot et al., 2009]. As example, for the ⟨110⟩ oriented channel the electron mobility improves of 77% and 135%, with respect to the unstrained SOI, due to an initial biaxial stress in sSOI layers of 1.55 GPa and 2.09 GPa, respectively [Baudot et al., 2009].

The schematic of the patterned sSOI lines studied with coherent diffraction imaging is shown in Fig. 5.1. These lines are obtained by lithography

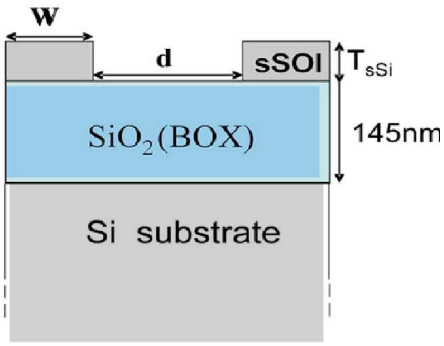

Figure 5.1: Schematic (front view) of the patterned sSOI lines. (Modified from [Baudot et al., 2009])

from a (001) oriented sSOI substrate. They are patterned in the [110] direction, that corresponds to the usual direction of n-MOSFET channels for which electron transport is improved. A misorientation of $\approx 1°$ is achieved between the strained Si lines and the Si substrate. The strained silicon lines have a width W=225 nm and a height of 70 nm and they are deposited on a 145 nm SiO_2 box. The distance d between two consecutive lines is $\approx$ 800 nm.

The strain in the SOI layers is artificially implemented using the top-bottom approach (cf. Chapter 1, pag. 7). A relaxed SiGe layer, free from defects and dislocations, is deposited on a Si substrate. This layer is mechano-chemically polished and a Si layer is epitaxially grown on it. The Si layer is therefore strained with a biaxial tension in the epitaxial planes. The oxide SiO_2 is further deposited on the strained Silicon. Hydrogen or helium implantation in the Si substrate underneath the SiGe layer creates defective layer in which a fracture can propagate. The multilayer structure is reversed and bonded on a new Si layer with deposition of SiO_2 and the upper crystal is removed after an annealing. This develops the fracture in the implemented zone. Hence, a Si-free tensile silicon on insulator (sSOI) substrate is finally obtained after the selective etching of the top SiGe layer. A sketch of the fabrication process of the strained silicon layer to be etched can be found in Fig. 5.2.

The influence of size and thickness on the strain behaviour observed in strained SOI were studied by Baudot et al. [2009] and Moutanabbir et al. [2010]. This last paper evaluates through UV micro-Raman spectroscopy the post-patterning strain for both thin (20 nm) and thick (60 nm) nanos-

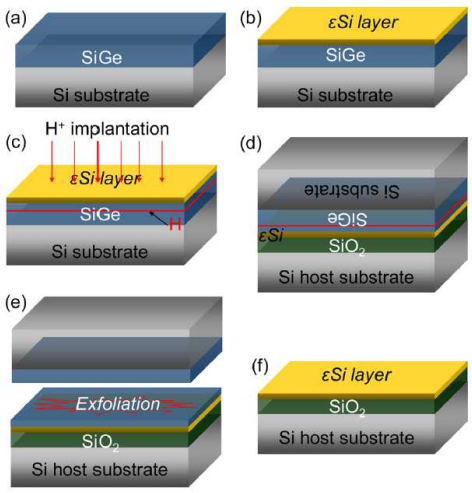

Figure 5.2: Schematic of the fabrication process of strained Si ultrathin layers directly on oxide by using thin layer transfer. (a) Growth of the relaxed $Si_{1x}Ge_x$ virtual substrate; (b) growth of the biaxially tensile strained Si on the $Si_{1x}Ge_x$ virtual substrate;(c) hydrogen ion implantation into the grown heterostructure; (d) bonding of the hydrogen implanted heterostructure to a SiO2/Si substrate; (e) thermal annealing induced layer exfoliation around the hydrogen implantation depth; (f) thin strained Si layer directly on SiO_2/Si obtained after the removal of the residual $Si_{1x}Ge_x$.([Moutanabbir et al., 2010])

tructures with the lateral dimensions W in the range of 80-400 nm. They found that about 40-50% of the initial strain is maintained in the 20 nm thick nanostructures, whereas this fraction drops significantly to $\approx 2-20\%$ for the 60 nm thicker ones.

The average strain of the studied sSOI has been determined during grazing incidence x-ray diffraction (GIXD) experiments performed at the ESRF and reported in Ref. [Baudot et al., 2009]. The average strain calculated along and perpendicular to the line, i.e. along the $(2\bar{2}0)$ direction, is plotted versus the line-width W in Fig. 5.3 for 70 nm high lines. Along the line, patterned along the [110] direction, the strain is maintained for both strained Si thickness even for the narrowest lines. Along the small line dimension, the strain of the thicker lines (70 nm) is fully relaxed whatever the width, but a significant strain is maintained for the thinner lines (10 nm) even for the narrowest lines. Its value decreases from $\epsilon = 0.58\%$ for W=231 nm to $\epsilon = 0.36\%$ for W=77 nm. Such results show that the stress relaxation due to patterning is more critical for thicker strained Si layers, i.e. for smaller aspect ratio. It can be an issue for the use in partially depleted sSOI devices.

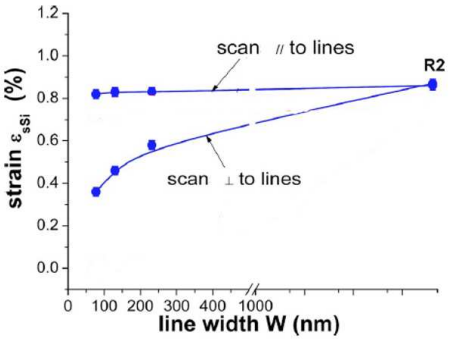

Figure 5.3: Strain calculated from GIXRD in-plane measurements as a function of the sSOI line width with a height of 70 nm along and perpendicular to the lines. R2 is the planar reference before the lines etching. (Modified from [Baudot et al., 2009])

5.1.2 Experiments

Coherent diffraction imaging experiments have been performed at the undulator beamline ID01 at the ESRF. The experimental set-up has been already described in Chapter 2. Due to the fact that silicon is a weak scatterer, the aperture of the slit placed 1.15 m upstream the lens position is set to $80_v \times 30_h\ \mu m^2$, slightly larger than the transverse coherence length, to increase the photon flux. The wavefront characteristics obtained with the employed set-up has been studied in the Chapter 4 of this manuscript.

In figure 5.4 the schematics of the scattering geometry for a given Si Bragg reflection is illustrated. The asymmetric (out-of plane) $(1\bar{1}3)_{Si}$ Bragg reflection has been chosen. This choice is motivated by the necessity of isolating the contribution of the scattering due to the Si-line from the one of the substrate. The separation of these peaks is larger in the reciprocal space for the chosen reflection due to the misorientation of $\approx 1°$ between lines and substrate in the azimutal angle. The incoming radiation (at E=8 keV) is inclined with respect to the sample surface by $\theta_i = 52.3°$ and the diffracted beam is collected with a MAXIPIX detector (for detail see Chapter 2) at $\theta_f = 56.48°$. This configuration is calculated considering the theoretical Bragg angle of the $(1\bar{1}3)$ reflection, $\theta_B = 56.48°$ and the inclination of the corresponding planes with respect to the [110] orientation. The patterned silicon lines are placed parallel to the direction of propagation of the coherent beam. In this geometry the displacement field can be probed in the transverse section of a single strained line from a two-dimensional scattering.

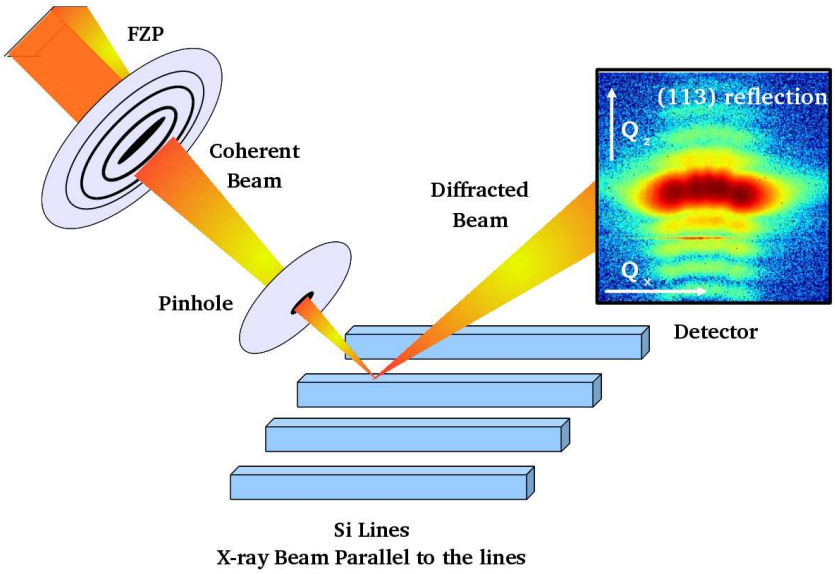

Figure 5.4: Sketch of the experimental set-up. The coherent beam is focused with a FZP. Lines are placed at the focal position parallel to the beam. The typical scattering registered for the $(1\bar{1}3)$ Bragg reflection is also shown.

5.1.3 Finite element method: calculations

In figure 5.4 a typical 2D measurement of the scattered beam at the detector plane is given. As expected [Gailhanou et al., 2007, Minkevich et al., 2008], the diffraction pattern is elongated in the horizontal direction, i.e. k_x direction. The theoretical model based on the geometry of the studied object with different amplitudes of the displacement field is introduced in order to explain this diffraction pattern. The modelled system is a perfect monocrystalline line, infinite in the y direction and with a constant trapezoidal section on the (x, z) plane. In these calculations the line is considered isolated from the substrate and the scattering contribution from the latter is therefore not visible.

The complete displacement fields u_x, u_y and u_z were simulated using finite element methods (FEM) by S. Baudot. In figure 5.5 the effect of u_x and u_z is shown for the section in the (x,z) plane. Arrows are used to depicted the direction of the displacement, both in x and z directions, with respect to the reference positions of an unstrained object. In this case the numerical displacements is relative to the bulk $Si_{1-x}Ge_x$ lattice. The maximum values of displacement along z and x directions are reached at the two edges crossing the x axis of the silicon lines. The effect that the calculated strain produced on the Si-line is a bending of the entire

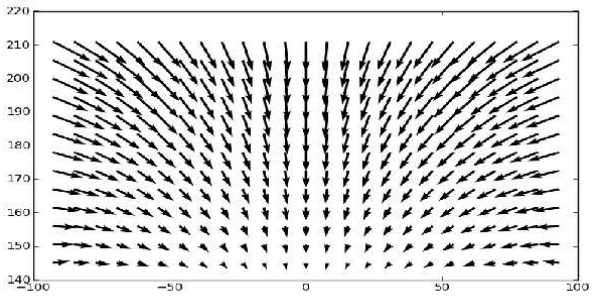

Figure 5.5: Simulated displacement field, using FEM in the trapezoidal section of the line in the (x, z) plane. The calculated displacements is relative to a bulk $Si_{1-x}Ge_x$ lattice. (Courtesy of S. Baudot)

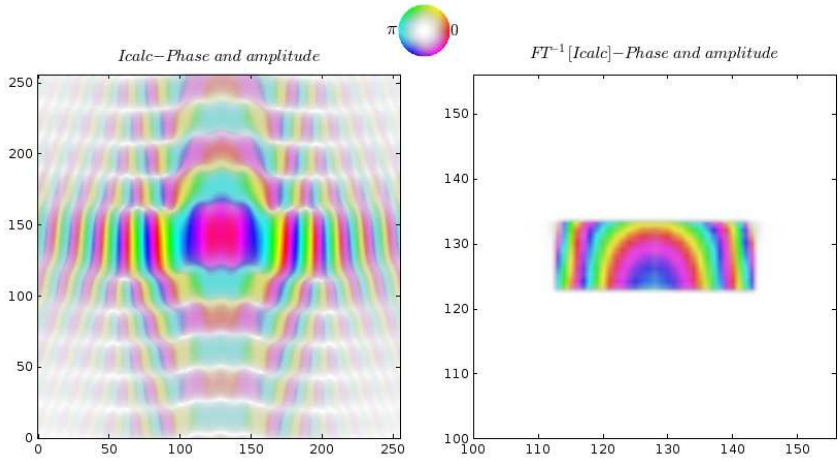

Figure 5.6: Left: Color rendition of the complex-valued 2D diffraction pattern calculated from the displacement field depicted in Fig. 5.5 for the $(1\bar{1}3)$ Bragg reflection. Right: Color rendition of the complex object in the direct space, calculated through the back Fourier transform from scattering to the left.

crystallographic structure. This was also demonstrated by Moutanabbir et al. [2011] by means of TEM measurements on a similar system. The simulated displacement field was calculated using FEM (Ansys softwave) and the resulting trapezoidal section of the line in the (x, z) plane is plotted in Fig. 5.5. The size of the section in the same plane is 200×70 nm^2. The coherent scattering has been calculated from this model in the framework of the kinematical approximation, i.e. using the Fourier transform. This approximation is justified by the low value of the reflectivity and by the fact that the angles of incidence and exit are not in grazing condition. The

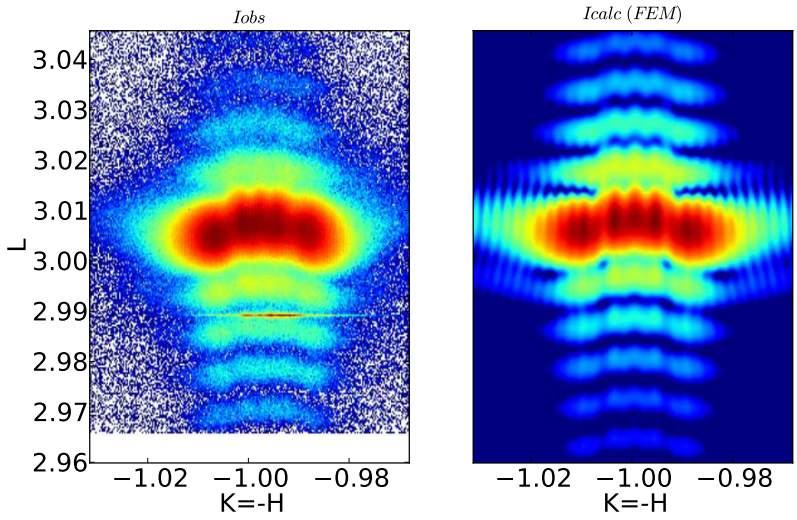

Figure 5.7: a) The measured scattering for a single line is compared to b) the calculated 2D reciprocal space map for the $(1\bar{1}3)$ Bragg reflection.

color rendition of the resulting field in the reciprocal space is shown in Fig. 5.6 (left). Here the phase are represented by color and the amplitude by saturation of colours. The vertical extension of the $(1\ \bar{1}\ 3)$ intensity is also an indication of the maximum value of the ϵ_{zz} strain component. The complex function describing the silicon line, calculated through a back Fourier transform from the scattering, is given Fig. 5.6 (right). The phase Φ in the direct space is used to calculate the displacement field, knowing that:

$$\Phi \approx G_{1\bar{1}3} \cdot \mathbf{u} \approx G_{1\bar{1}3}\ u_z \tag{5.1}$$

In first approximation, in the chosen Bragg reflection we are mostly sensitive to the displacement field in z direction, even if it also contains information on the lateral deformation u_x.

In figure 5.7 the intensity of the registered scattering is shown and compared to the calculated intensity (Fig. 5.7b), on a logarithmic scale. The

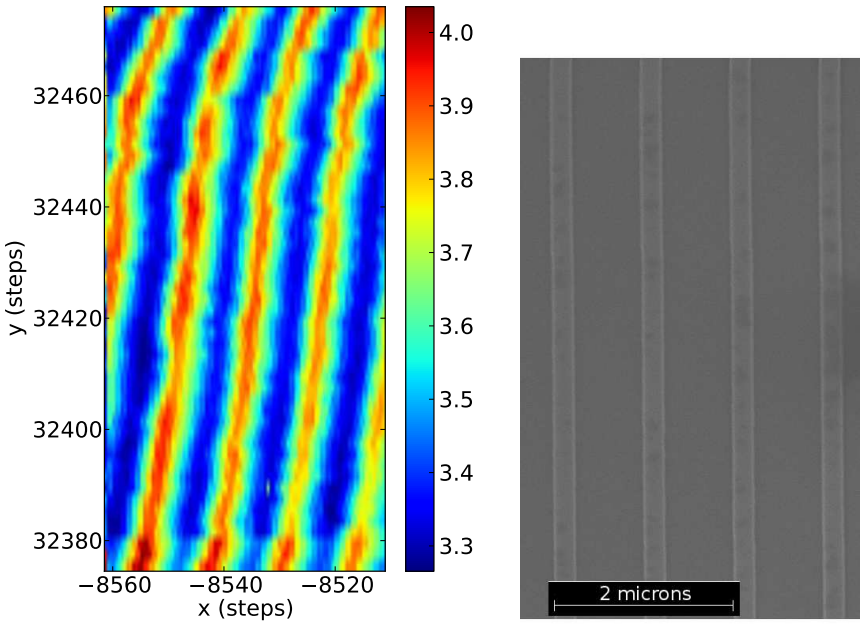

(a) (b)

Figure 5.8: a) Mapping in real space for the $(1\bar{1}3)$ Bragg reflection around different lines. Colours correspond to the total intensity received by the detector at a given sample position. Intensity is expressed in logarithmic scale. b) SEM image of the Si-lines. The irregularity of the lines is due to the mechanical drift of the piezostage during measurements.

diffraction pattern recorded during the experiment for the $(1\ \bar{1}\ 3)$ is mainly due to the contribution from a single silicon line. This is because the transverse dimensions of the available (partially) coherent beam allows to select the contribution of only one line from the pattern. In Fig. 5.8a a real space map of the Si-lines array is shown to demonstrate the sensitivity to the separation of two consecutive lines. Here intensity is plotted using a logarithmic scale. Looking at this figure, lines seem to be not straight. This is the clear effect of the positioning motor used to make the scan that shows low movement repeatability of mechanical drift, as the SEM image of these lines demonstrates (Fig. 5.8b).

The measured reciprocal space map and the calculated diffraction pattern from a single line are compared in Fig. 5.9. They are very similar in particular concerning the $k_z = L$ modulation. In this direction, corresponding in real space to the direction normal to the surface, fringes are directly related to the line thickness ($\approx$ 70 nm). The signal extension observed in the H direction is much larger. This can be explained only as an effect of

the physical bending of the entire structure in the plane (x,z). Therefore, the full reciprocal space image can only be understood considering the total displacement field inside the silicon line.

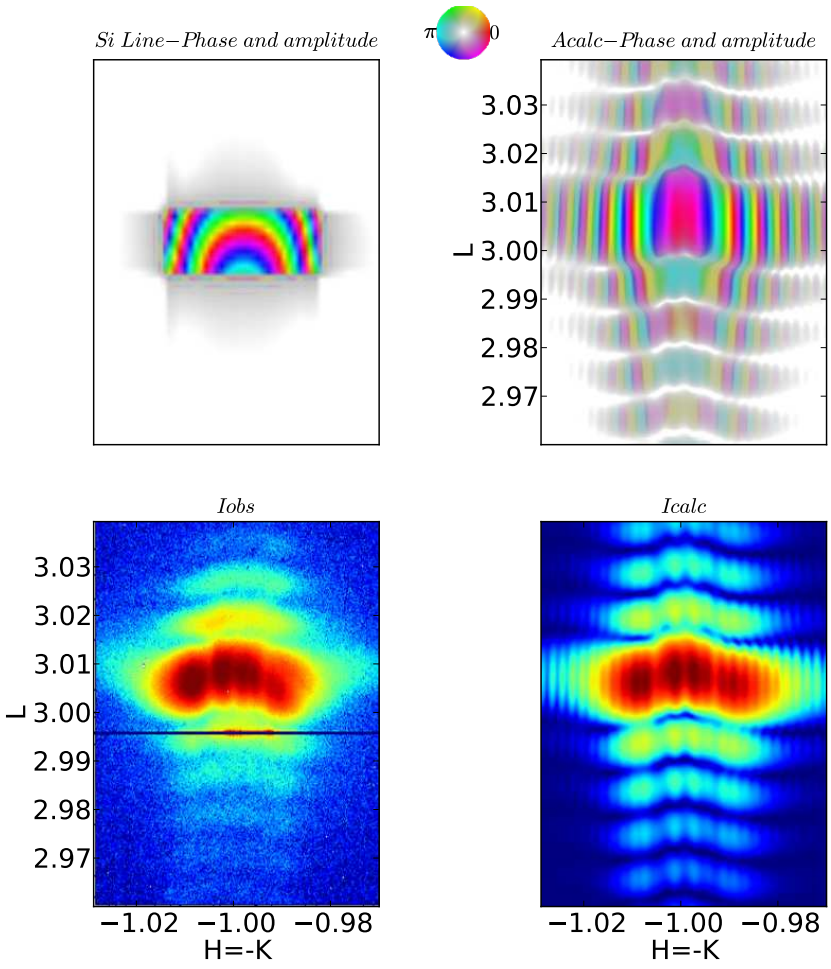

Figure 5.9: Calculated complex-valued function at the sample position from FT of complex scattering (Si line). Calculated complex-valued function at the detector (Acalc) from a FT of the fit using the asymmetric polynomial representation of the displacement u_z. Phase is represented by colours and intensity (expressed in logarithmic scale) by the intensity of the colours. Two dimensional diffraction patterns collected for the chosen silicon line at the time **T=0 sec** (Iobs) compared to the calculated intensity (Icalc). Intensities are expressed using the same logarithmic scale.

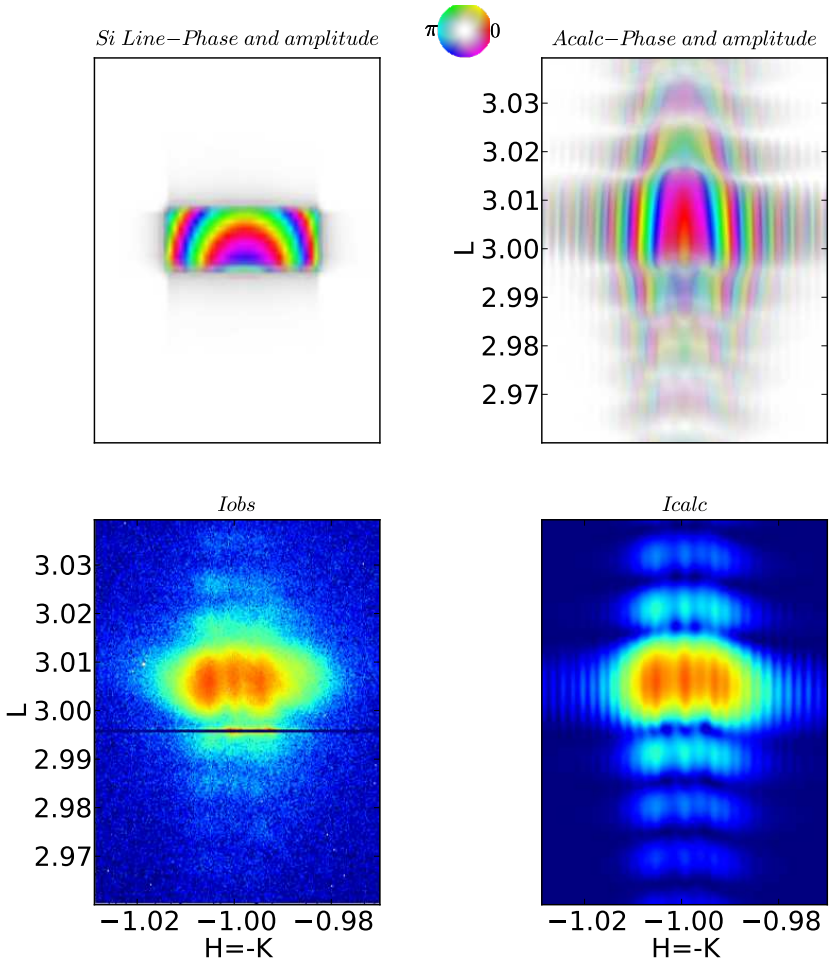

Figure 5.10: Calculated complex-valued function at the sample position from FT of complex scattering (Si line). Calculated complex-valued function at the detector (Acalc) from a FT of the fit using the asymmetric polynomial representation of the displacement u_z. Phase is represented by colours and intensity (expressed in logarithmic scale) by the intensity of the colours. Two dimensional diffraction patterns collected for the chosen silicon line at the time **T=800 sec** (Iobs) compared to the calculated intensity (Icalc). Intensities are expressed using the same logarithmic scale.

5.1.4 Data analysis

A time-dependent characterisation has been performed on a single silicon line. The coherent x-ray beam, focused in a spot with a transverse size of 300×500 nm^2, carries in term of photon flux $10^9/1.5 \times 10^5$ ph/s/nm^2 $\approx 5 \times 10^4$ ph/s/nm^2. As during local strain measurements of nano-semiconductors using monochromatic and high brilliance coherent radiation and depending on the characteristic of the studied nanostructure

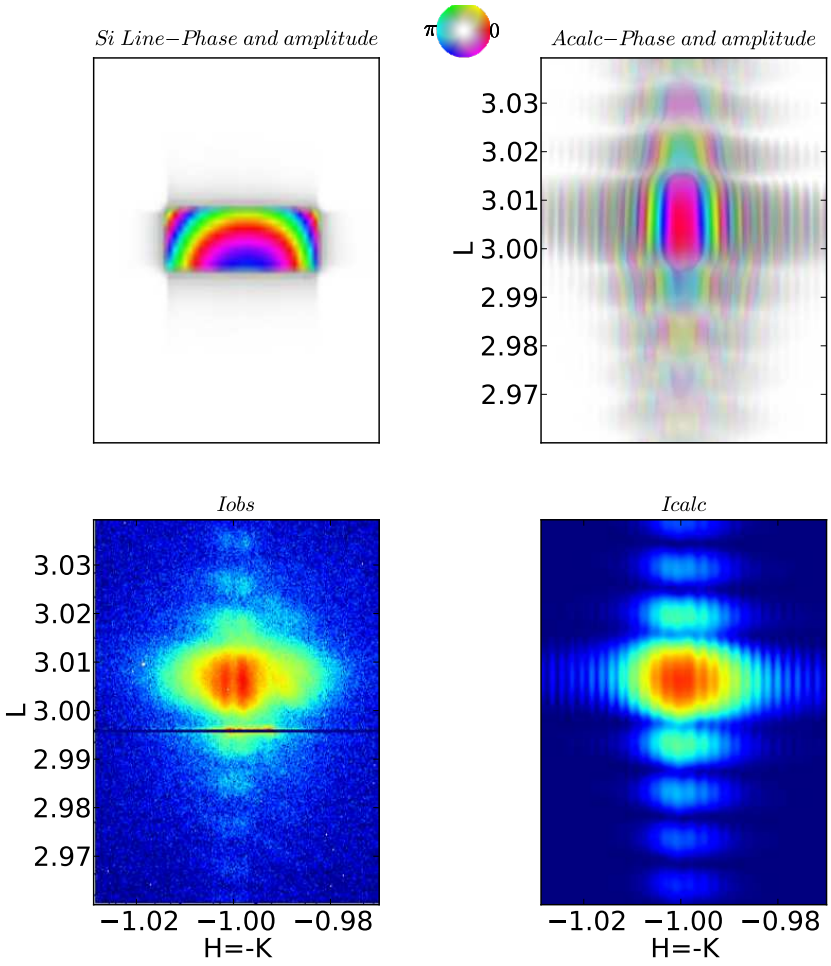

Figure 5.11: Calculated complex-valued function at the sample position from FT of complex scattering (Si line). Calculated complex-valued function at the detector (Acalc) from a FT of the fit using the asymmetric polynomial representation of the displacement u_z. Phase is represented by colours and intensity (expressed in logarithmic scale) by the intensity of the colours. Two dimensional diffraction patterns collected for the chosen silicon line at the time **T=1600 sec** (Iobs) compared to the calculated intensity (Icalc). Intensities are expressed using the same logarithmic scale.

radiation damage may occur, the available x-ray beam has been, therefore, used to illuminate the same portion of a single line with the aim of inducing radiation damage and investigate its nature and its characteristic time of relaxation. Several 2D diffraction patterns of the described Bragg peak, have been collected during the experiment with an acquisition time of 100 sec. The most relevant detector images are shown in Figs. 5.9-5.12 and indicated by (Iobs) at different acquisition time: T= 0 sec (Figs. 5.9a), T= 800

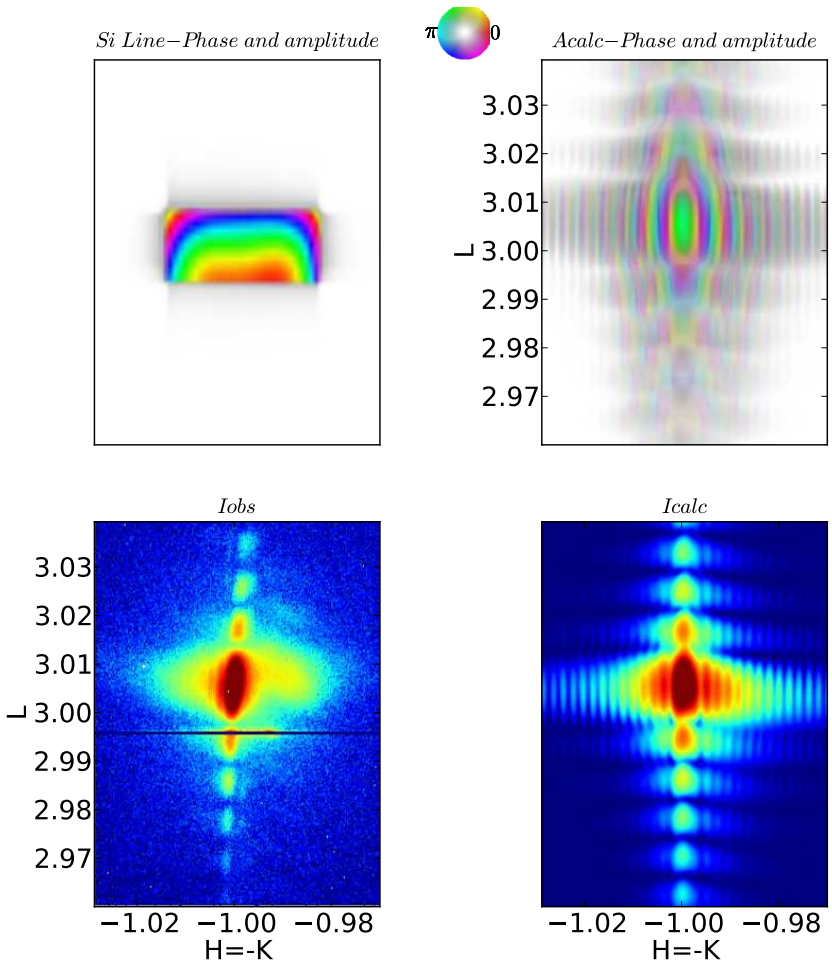

Figure 5.12: Calculated complex-valued function at the sample position from FT of complex scattering (Si line). Calculated complex-valued function at the detector (Acalc) from a FT of the fit using the asymmetric polynomial representation of the displacement u_z. Phase is represented by colours and intensity (expressed in logarithmic scale) by the intensity of the colours. Two dimensional diffraction patterns collected for the chosen silicon line at the time **T=2900 sec** (Iobs) compared to the calculated intensity (Icalc). Intensities are expressed using the same logarithmic scale.

sec (Figs. 5.10a), T= 1600 sec (Figs. 5.11a) and T= 2900 sec (Figs. 5.12a). In each image, the contribution of the Si substrate, visible at L=2.995 has been masked for analysis.

Numerical calculations have been performed to fit these experimental data. In the numerical approach used for this study the displacement field u_z has been approximated with a polynomial depending on both z and x components. In this approach, u_x is not introduced and its changes have

not been studied, as the approximation in Eq. 5.1 have been assumed. As a starting point, we used a symmetric polynomial series in which only even terms for the horizontal component x ($1\bar{1}3$) have been considered. This choice leads to a symmetric diffraction pattern at the detector position as the one shown in Fig. 5.7b. However, in the discussed case, the asymmetry that is visible in the experimental 2D scatterings forces us to introduce at least one odd term in x. The starting polynomial is then minimized using the Powell method [Mathews and Fink, 2003] to calculate the actual displacement fields in the relaxing sSOI line, that generate the diffraction patterns at the time $T_0 + \Delta T$. The minimization process on the asymmetric polynomial series is repeated until an agreement with all the selected scatterings is found. In figures 5.9-5.12, the intensities (indicated by Icalc), calculated from the model, are compared to the experimental data (Iobs) using the same logarithmic scale and they are found to be in good agreement. The complex scattering functions at sample position (Si line) have been calculated through a back FT from the simulated complex-valued fields at the detector plane (Acalc). In a coherent diffraction experiment, these fields are used to calculate from Eq.5.1 the displacement and, consequently, the strain of the investigated nanostructure.

The polynomial displacement fields obtained from the proposed time-dependent study are plotted in Fig. 5.13, for different times T. u_z visibly changed from T=0 sec (Fig. 5.13a) to T=2900 sec (Fig. 5.13d), showing a quite less curved profile. As in the polynomial approximation the displacement field u_z depends on the coordinates x and z, the strain fields ϵ_{zz} and ϵ_{zx} can be easily calculated with a partial derivation of u_z with respect to z and x, respectively. In figure 5.14, ϵ_{zz} (top images) and ϵ_{zx} (bottom images) retrieved from the time-dependent analysis of radiation damage are shown at different times: a) T= 0 sec, b) T= 800 sec, c) T= 1600 sec and d) T= 2900 sec. Looking in particular at the evolution of the strain fields ϵ_{zx} that contains the information concerning the bending of the structure, the silicon line begins to relax already at T=800 sec reaching the maximum relaxation at T= 2900 sec. Moreover, ϵ_{zx} presents a slight asymmetry in the x direction that explains well the asymmetry in intensity distribution of the diffraction pattern registered during the experiment. This effect is attributed to the fact that the structure begins to relax from one side, where probably the damage is occurring, i.e. on the side where the the silicon/oxide bond has been broken.

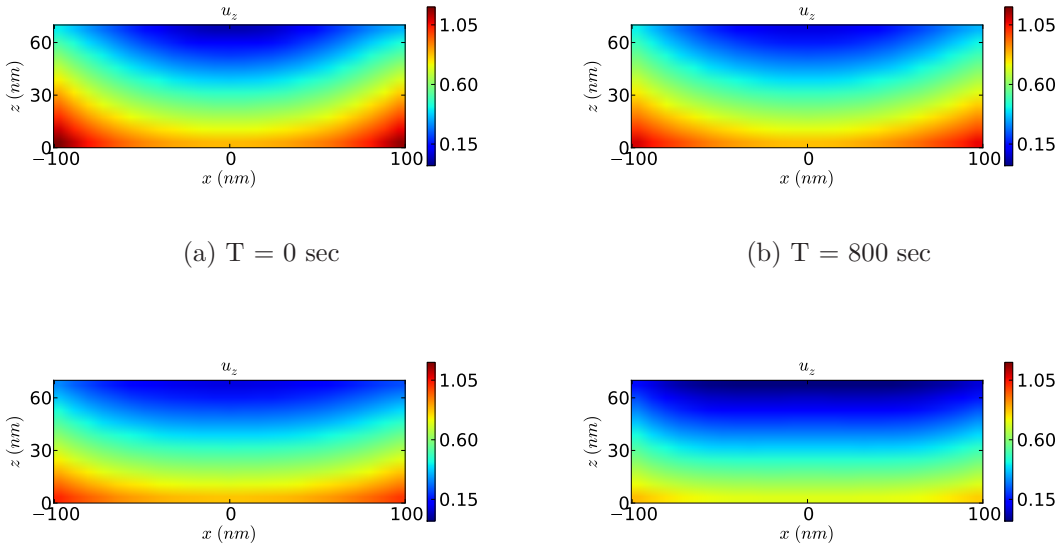

(a) T = 0 sec

(b) T = 800 sec

(c) T = 1600 sec

(d) T = 2900 sec

Figure 5.13: Displacement field u_z obtained from the time-dependent analysis of radiation damage at different time: a) T= 0 sec, b) T= 800 sec, c) T= 1600 sec and d) T= 2900 sec. Colours represent scale units expressed in nanometres.

The relaxation can be also seen if referring to the strain field ϵ_{zz}. Here, its curved shape, evident in Fig. 5.14a (top), is clearly more relaxed in Fig. 5.14c (top) and the structure goes towards the lattice parameter of the bulk Si reference, in this case the silicon. Unfortunately, the refinement process seems to be not correct enough for ϵ_{zz}. The strain variation observed in Fig. 5.14, b-c, has a no logical evolution and reconstructed strain values are incoherent with respect to the variation observed in Fig. 5.14, a-d. This can be attributed to the fact that the position of vertical fringes, that are not clearly visible in the intermediate experimental data, are not correctly reconstructed and it does not allow to solve the strain in the vertical direction. However, from the comparison between the strain retrieved at T=0 sec and T=2900 sec, a logical sequence can be found even if the algorithm did not converge well for the intermediate images (registered at T=800 sec and T=1600).

The mean values of ϵ_{zz} and the square root of the averaged ϵ_{zx}^2 calculated at different times are summarised in Table 5.1. $\langle \epsilon_{zz} \rangle$ varies around an almost constant value when the Si line relaxes while $\sqrt{\langle \epsilon_{zx}^2 \rangle}$ decreases continuously during the relaxation process.

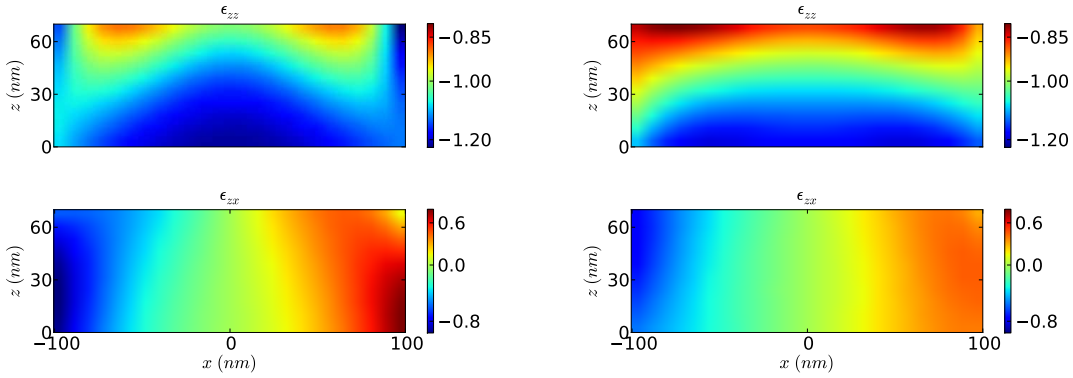

(a) T = 0 sec

(b) T = 800 sec

(c) T = 1600 sec

(d) T = 2900 sec

Figure 5.14: Strain fields ϵ_{zz} and ϵ_{zx} from time-dependent analysis of radiation damage at different time: a) T= 0 sec, b) T= 800 sec, c) T= 1600 sec and d) T= 2900 sec

Strain	0 sec	800 sec	1600	2900
$\langle \epsilon_{zz} \rangle$	-1.089%	-1.026%	-1.053%	-1.053%
$\sqrt{\langle \epsilon_{zx}^2 \rangle}$	0.0436%	0.0332%	0.0283%	0.0200%

Table 5.1: Mean valued calculated for ϵ_{zx} and ϵ_{zx} at t=0, 800, 1600 and 2900 sec.

The origin of the radiation effects induced in strained or unstrained SOI is still object of discussion. Damage in silicon layers irradiated with x-rays also occur, as demonstrated by Polvino et al. [2008], when it is capped with another thin film, both epitaxial or amorphous, as in the considered case.

In the case of SOI wafer, the presence of a thin layer of SiO_2, i.e. a thin layer of a buried thermal oxide, with an amorphous character, may originate oxidation process when illuminated with an x-ray radiation. In this case, we may have a complete mechanical relaxation of the structure. A second possible damage mechanism that may explain changes observed in the displacement field u_z can be attributed to the formation of non radiative defects. Mashkov et al. [1996] observed using an ionization radiation (in that case x-rays) an irreversible creation of defects starting from the network sites in the amorphous insulator and, later, Stevens-Kalceff [2000] reported of near-infrared emission in oxygen deficient electron-irradiated SiO_2 polymorphous. Specifically, they imaged the microscopic spatial distribution of interstistial molecular oxygen, to which the radiation damage was attributed. In addition, it has been already reported by Peled [2003] that synchrotron radiation can reduce SiO_2 to form Si nanocrystals and free oxygen. Thus, the damage mechanism activated by any free oxygen could start at the Si/SiO_2 interface travelling upward thought the crystalline structure. SEM observations are in favour of this interpretation although we are not sure to have clearly localised the beam trace on the sample.

Finally, the asymmetry observed in the experimental diffraction patterns shown in Figs. 5.10-5.12 (a) is attributed to an asymmetric relaxation of the silicon lines. This effect is also confirmed by the numerical analysis. When looking at Figs. 5.14, a-d, a slight asymmetry is observed in the calculated strain field ϵ_{zz} and ϵ_{zx} in real space. Looking at the variation of the diffraction pattern, we can state that the elongated shape in the reciprocal space is due to the bending of the nano-object as the diffraction is less horizontally extended while the silicon line relaxes.

5.2 Strain imaging and illumination function

In chapter 4, the role of the illumination function has been discussed when coherent diffraction imaging techniques are used to investigated the strain in single nanostructures. There, the full characterisation of the coherent wavefront in the case of our experimental conditions has been analysed and will be discussed in details.

In this section, numerical calculations are used to illustrate, by means of two examples, how the displacement fields reconstructed from the coherent scatterings strongly depends on the character of the complex-valued illumi-

nation function, i.e. on its phase. These examples are useful to underline the necessity of disentangling the contributions of the illumination probe and the investigated nanostructure in the reconstructed exit field, at the sample position.

To this aim, we use the simulated strained silicon line, described in the previous section, as numerical sample and we multiply it by a Gaussian function, to simulate the coherent illumination occurring during a CDI experiment. The numerical focal spot size, measured at the FWHM, is ≈ 200 nm. For simplicity only the two-dimensional section in the xz plane has

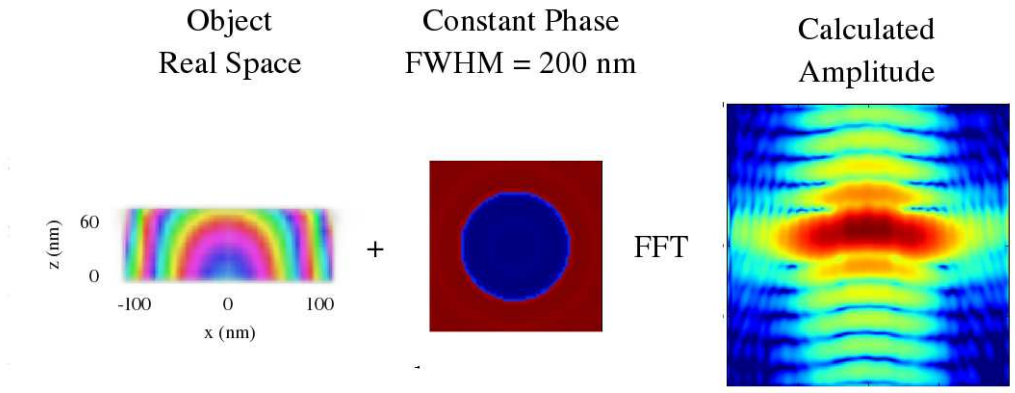

Figure 5.15: Calculated two dimensional diffraction patterns obtained through a FFT of the wire section multiplied by the illumination function with a constant phase within the focal spot.

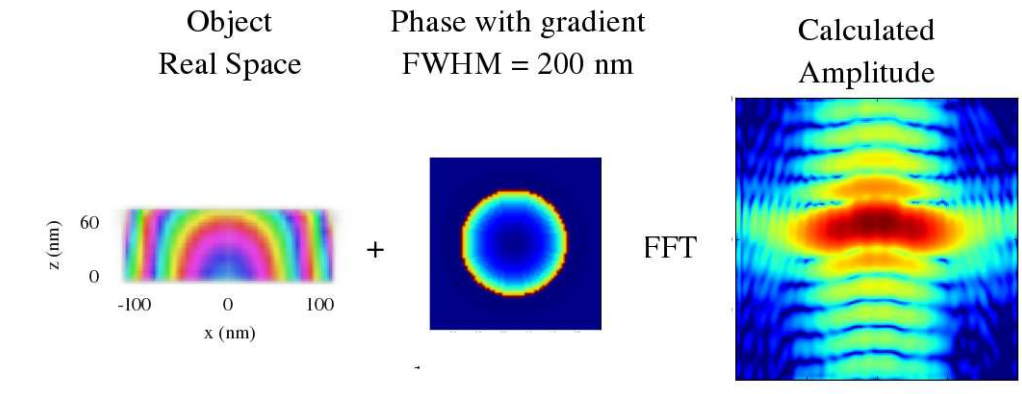

Figure 5.16: Calculated two dimensional diffraction patterns obtained through a FFT of the wire section multiplied by the illumination function with a Gaussian phase within the focal spot.

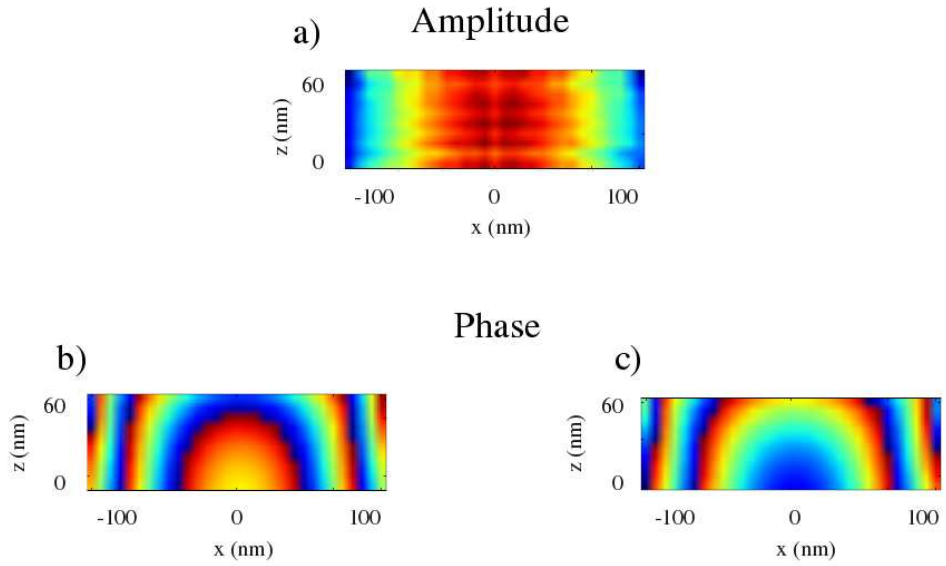

Figure 5.17: Calculated two dimensional a) amplitude and phase in real space. Phases in b) and c) are obtained by Fourier transforming the complex scattering in Figs. 5.15 and 5.16, respectively.

been considered. In the first example, the phase of the focal spot has been chosen constant (see Fig. 5.15). The diffraction pattern, calculated as the square modulus of the Fourier transform of sample multiplied by illumination function, is shown in Fig. 5.15 on the right. The same calculation has been done considering in this case the same illumination function in terms of amplitude and size (FWHM=200 nm) but showing a Gaussian phase within the focal spot Fig. 5.16. In particular the chosen phase varies in the range of $(0, 2\pi)$ from the maximum of the central peak to the tails. Also in this case, the resulting function is obtained multiplying the numerical sample with the probe, is Fourier transformed to obtain the 2D scattering in reciprocal space (Fig. 5.16 on the right).

The calculated reciprocal space complex-valued function, corresponding in this case to the 2D scattering, has been used to calculate, through a back Fourier transform, the real complex-valued exit field at the silicon line position. As shown in Fig. 5.17a, the calculated amplitude is not constant all over the 2D section in the considered plane. This effect can be easily understood considering that the object is illuminated with a Gaussian-like beam with the maximum intensity confined into the FWHM. The amplitude modulations observed in the real space also explain the changes observed in the calculated coherent scattering in Figs. 5.16 and 5.17 with respect

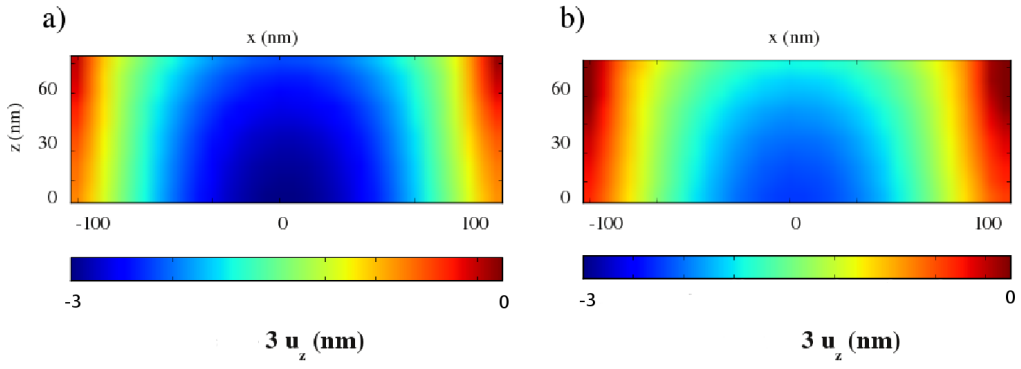

Figure 5.18: Calculated displacement field from the phases shown in Fig. 5.17 obtained for the investigated Bragg reflection $(1\bar{1}3)$. The displacement field $3u_z$ contains the contribution of the illumination function.

to the calculation shown in Fig. 5.7 (see previous section). The two outer lobes in the intensity distribution become smaller and less pronounced. As discussed in the previous section, the maximum of the displacement field in the strained SOI lines along z and x directions are reached at the lateral edges of the silicon lines. Treating the resulting exit field calculated in real space without disentangling the illumination probe contribution corresponds to remove or at least underestimate the contribution of a small slab of crystal at these edges.

The retrieved phases in real space are shown in Fig. 5.17, b and c, for the two considered illumination conditions. They are used to calculate the displacement field **u** that contains, according to Eq. 5.1, the contribution from both u_x and u_z. For $(1\bar{1}3)$ Bragg reflection, the 2D diffraction pattern gives access to $u_x + 3u_z$. Results are shown in Fig. 5.18 in the case of an illumination with a constant phase (Fig. 5.18a) and a Gaussian phase (Fig. 5.18b) within the focal spot . To underline the influence of the illumination probe to the retrieved phases and displacement fields, both are plotted using the same scale (colorbar). Comparing Figs. 5.18, a-b, the displacement fields retrieved from the calculated scattering using different illumination conditions are not in agreement. The displacement assumes different values in the line section, as shown in Fig. 5.18b, with respect to the one obtained from a probe with a constant phase within the focal spot and shown in Fig. 5.18a. In particular, the latter result is similar to the displacement field calculated using FEM without considering the contribution

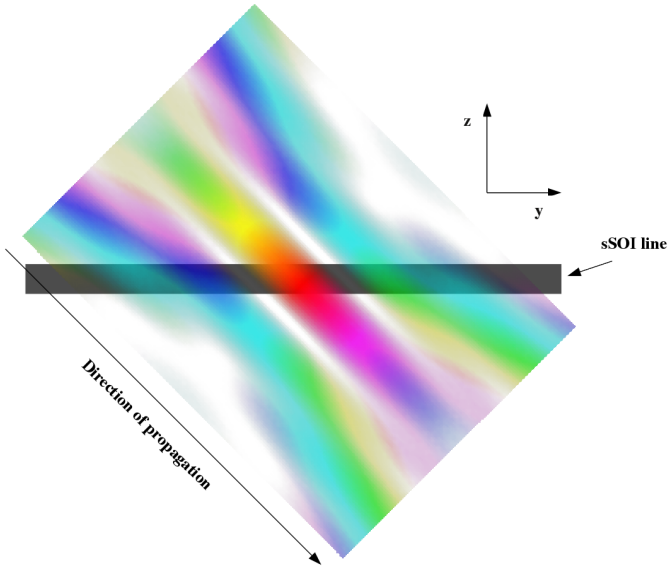

Figure 5.19: Schematics of the contributions (amplitude and phase) of the coherent probe along the sSOI lines. In this direction, the phase variation of the probe has to be taken into account to study the influences of the illumination when a CDI approach is used to investigate the nanostructure.

the wavefront at the focal plane.

This example confirms again that the wavefront at the focal position strongly influences the investigation of the single nano-object, in particular when coherent x-ray diffraction techniques are used to image the displacement fields and consequently the strain in the probed crystalline structure. As discussed in the case of a single strained silicon line, if the complex-valued illumination function is unknown, its contribution cannot be disentangled from the phase of the retrieved complex exit field at the sample position. As result, this phase cannot be used to describe correctly the actual displacement in the nanostructure. From these examples, it is evident that the imaging of strained nano-object has to be coupled with an accurate characterisation of the illumination function. A more precise study may also include the third dimension, i.e. the coherent wavefield and the size of the crystalline structure in the direction of propagation. However, this calculation is more complicated with respect to the two dimensional cases discussed in this section as, in a three dimensional study, the phase variation in the direction of propagation typical of the illumination probe must be considered (see Fig. 5.19), together with the absorption effects.

5.3 Nanowires with stacking faults

Homogeneous nanowires without any external stress only present strain on the atomic layers that are closer to the surface due to the free-boundary relaxation as discussed in Chapter 1. Given the limited real-space resolution obtained by CDI (5-20 nm, see Chapter 2, section 2.3), this outer layer contraction cannot be measured and, in this case, coherent scattering around a Bragg reflection will be dominated by the Fourier transform of the shape of the nanowire. As by definition nanowires have a large aspect ratio, i.e. their length is much larger than their diameter (that is generally smaller than the illumination probe), the scattering signal can be considered as a quasi-2D signal corresponding to the 2D FT of the nanowire cross-section.

In the case of an heterogeneous nanowire, CDI is sensitive to the displacement and the chemical nature of all atoms. In this section, as example, the case of a numerical $[001]_{WZ}$-oriented hexagonal InAs nanowire, with an InP insertion, is considered. Figure 5.20 shows the numerical calculations of the strain field inside the nanowire as obtained by atomistic simulations. The InP insertion has a lower bulk lattice parameter than InAs (a_{WZ}^{InP}= 0.415 nm, a_{WZ}^{Inas}= 0.4268 nm), so that the insertion contracts the lattice. In this calculations, the InAs part of the nanowire has a wurtzite structure. The radius of the regular hexagon, corresponding to the wire section and without any compression or expansion, is R = 60 nm. Several wire lengths and insertion thicknesses were simulated to test the sensitivity of the CDI approach. In particular the cases of two different insertion heights, 3 and 15 nm, are discussed. The relaxed atomic positions are computed using Keating's valence force field (VFF model) [Keating, 1966].

The amplitude of the displacement field in the nanowire due to the presence of the insertion (computed relatively to a perfect InAs lattice) has a maximum value of 1-2 unit cells in the horizontal direction (u_x), depending on the thickness of the insertion; in the vertical direction (u_z), the maximum displacement varies with the InP thickness t, ranging from 0.16 (t = 1.5 nm) to 0.6 unit cells (t = 15 nm). The contraction of the InAs crystal is due to the presence of InP. the calculated intensities are shown in Fig. 5.20, a-d, for a 3 nm insertion and in Fig. 5.20, e-h, for a 15 nm InP insertion. Some differences can be observed comparing the scattering calculated with the two insertions. In particular, the scattering calculated from the larger insertion of t = 15 nm (Fig 5.20 (g) and (h)) shows a well-separated and a more intense peak with respect to the case of 3 nm insertion appears due to

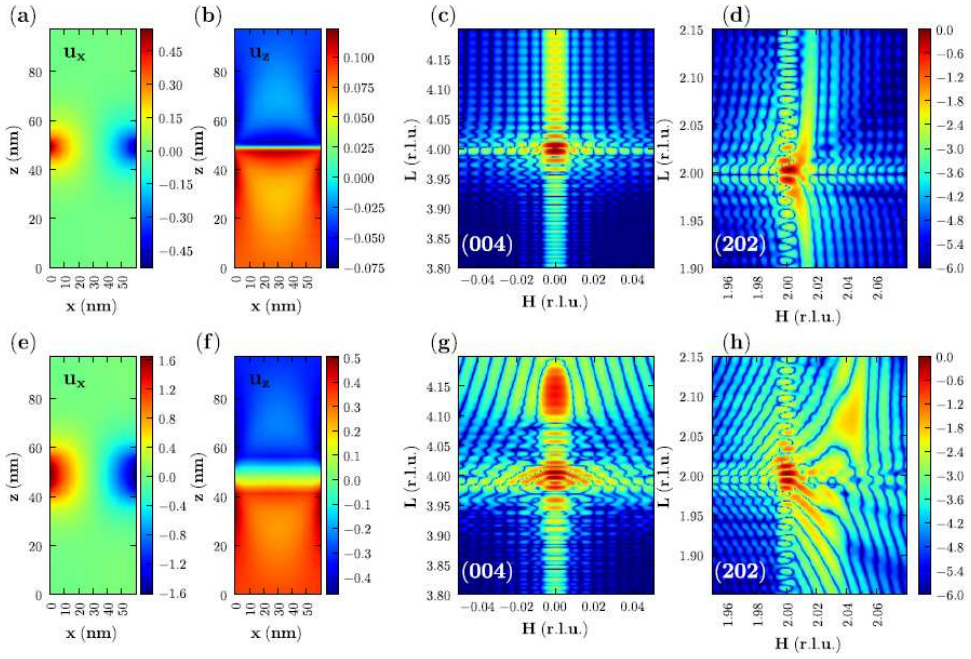

Figure 5.20: Atomistic simulations of an InAs wurtzite nanowire (diameter = 60 nm, height = 100 nm) with (a)-(d) a 3 nm and (e)-(h) a 15 nm InP insertion: (a, e) the radial displacement (along [110], expressed relatively to the perfect InAs lattice, in unit cells), (b, f) the axial displacement (along [001]), the calculated intensities around the (c, g) (004) and (d, h) (202) reflections, with a logarithmic colour scale. The map coordinates are given in reciprocal lattice units (r.l.u.) relative to InAs.

the InP contribution. Is is worth noticing that this second peak is roughly two orders of magnitude less intense than the main InAs peak. Due to the smaller lattice parameter, the scattering from the InP insertion occurs at higher angles. The asymmetry in the diffraction pattern in presence of an insertion is a clear sign of the strain field.

From these simulations it can be deduced that it should be possible to measure a scattering signal specific to a small (a few nm) insertion, assuming at least three or four orders of magnitude in the measured intensities of the experimental data.

This can be experimentally achieved when using CDI technique to image the strain at the nanoscale. However, a successful experiment in term of the diffracted intensity is a compromise between the incoming photon flux and the scattering power of the investigated nanowire, the latter being roughly proportional to the electron density of the material.

The numerical calculations presented until now assume a perfect InAs/InP nanowire, without any structural faults and demonstrate that

during a coherent diffraction experiment, the scattering around a chosen Bragg peak is sensitive to the displacement from a perfect periodic lattice even if this is due to an insertion smaller than the achieved resolution. This is possible as this insertion produces a shift of the crystalline plane into the crystal.

In reality, nanowires without defects are difficult to achieve. It is, therefore, important to evaluate, via numerical calculations, the influence of faults on the coherent scattering. In addition, calculations discussed in the following will be used to check if stacking faults, i.e. faults occurred during growth via bottom-up techniques, can hide the scattering signal due to a strained lattice and, consequently affect the retrieved phase.

Stacking faults commonly occur in nanowires grown by epitaxy and sometimes may lead to a periodic twinning structures. This is especially true for III-V nanowires grown by VLS, as the geometry of the wire and growth kinetics may stabilize the metastable wurtzite structure instead of the zincblende bulk phase. In the following, I present a theoretical study on the influence of stacking faults when a nanowire with defects is probed with a coherent diffraction technique. In addition, an experimental example is also offered in the case of heterogeneous InSb/InP nanowires, presenting stacking faults in the InSb section.

In the case of a nanowire showing a wurtzite crystalline structure, a simple stacking fault can be described according to the following sequence:

$$AB|AB|AB|AB|CB|CB|CB|CB|CB, \tag{5.2}$$

where the first part represents the unfaulted 'AB' sequence. In this example, the unfaulted series is followed by a 'CB' sequence, due to the fact that all atoms are shifted by

$$\mathbf{v} = \frac{1}{3}(1\bar{1}0)_{WZ} \tag{5.3}$$

from their position in the normal sequence. This abrupt shift produces a specific interference pattern around some specific reflections; the scattering vector corresponding to these Bragg reflection is not orthogonal to $\mathbf{v}$ and all the interferences produced in the diffraction pattern generated by a faulted structure cumulate with the contributions coming from the deformation induced by the strain, when it is present.

To show the influence of defects in the diffraction patterns, the scattering from InAs/InP nanowires, epitaxially grown on the InP substrate, has

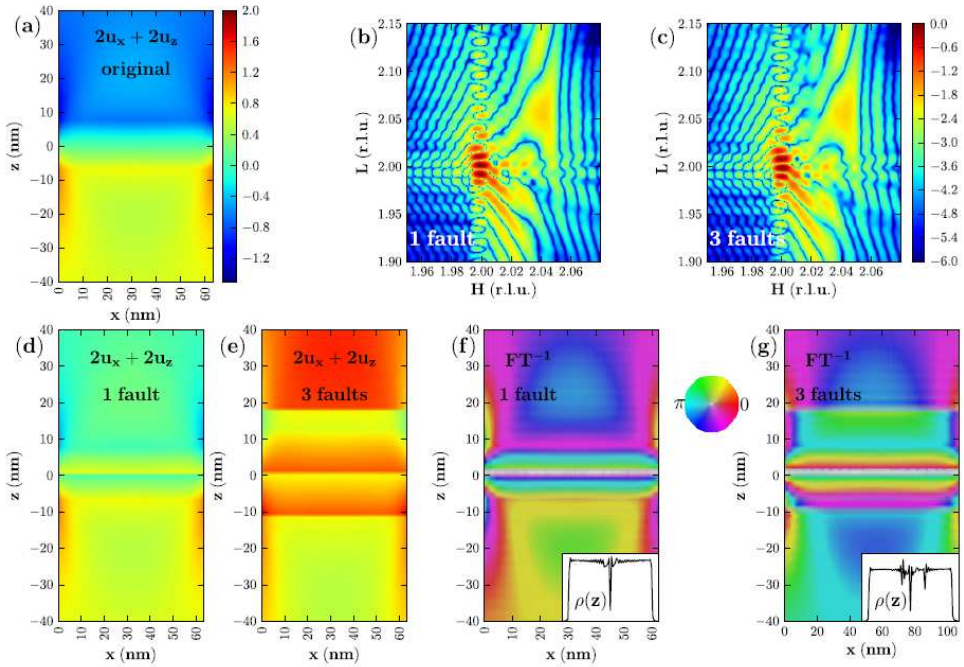

Figure 5.21: Simulation of the influence of stacking faults on the coherent scattering from InAs/InP nanowires (diameter = 60 nm, height = 100 nm) around a $(202)_{WZ}$ reflection. 2ux + 2uz for (a) the original InAs/InP nanowire obtained using atomistic simulations, and in the case of (d) one and (e) three stacking faults. The colour scale is expressed in unit cells (u.c.) and is the same for (a, d, e). The resulting scattered intensity is shown in (b) (one fault) and (c) (three faults). Complex recovered density (see text for details) is shown in the case of one (f) and three (g) faults. In these images the phase is given by the colour (as indicated by the colour wheel), while the amplitude is given by the saturation of the colour.

been calculated in the presence of one and three stacking faults, around the (202) Bragg reflection. The calculations are illustrated in Fig. 5.21. In Figure 5.21a, the unfaulted InAs/InP nanowire is shown. The diameter is 60 nm and the height of the wire portion selected for the calculations is 100 nm. The strain relaxation at the InAs/InP interface is calculated according the atomistic method described in Chapter 2. Along the wire height, stacking faults are added and the diffraction pattern is directly calculated from the faulted structure. The oscillation fringes of the scatterings are clearly affected by the faults, when one or three stacking faults are inserted along the wire portion (Fig. 5.21, b and c, respectively). The scattering can be compared to the one calculated for the unfaulted case and shown in Fig. 5.20. These calculations have been performed using the exact atomic positions of each scatterers in real space. This corresponds in reciprocal

space to the scatterings computed at the following reciprocal lattice unit coordinates: $h\epsilon[1.76, 2.4[, k\epsilon[-0.24, 0.24[, l\epsilon[1.76, 2.4[$ with a step of 0.004.

Due to the presence of these stacking faults the reconstruction of the density and the correct value of the phases shift in the wire can be achieved only using as input the theoretical phase values.

On the other hand, from an experimental point of view, the reconstruction obtained by means of iterative phase retrieval algorithm may be inhibited as the resolution achieved during CDI experiments is limited (5-20 nm corresponds to ≈10-40 unit cells in the case of InAs) and the stacking faults may occur, in the direct space, in a smaller number of unit cells (e.g. for the $\mathbf{s}$= (202) reflection and if $\mathbf{v} = \frac{1}{3}(\mathbf{a} - \mathbf{b})$, the phase shift is $2\pi\mathbf{s} \cdot \mathbf{v} = 4\pi/3$). In addition, iterative retrieval algorithms converge more slowly for strained objects than in the case of unstrained objects. This is due to the fact that, in presence of strain, the real-space constraints are limited to the finite support and cannot include the positivity, as in the case of unstrained nano-objects. A solution to the algorithm convergence in the discussed case is the continuity of the phase field of the reconstructed object, as recently proposed by Minkevich et al. [2007]. However, in the case of faulted wire this strategy is not of help. Moreover, as already pointed out by Chamard et al. [2008], the scattering around a given reflection depends on the domains (zincblende or wurtzite) that are illuminated with the beam along the wire height. Obviously, the contribution from each domain is observed only if the chosen reflection is allowed by its crystalline structure [Favre-Nicolin et al., 2010].

With the aim of evaluating quantitatively the influence of the stacking faults on the reconstruction from CDI data, simulated intensities, illustrated in Figs. 5.21, b and c, can be used as input to compute the inverse fast Fourier transform in order to obtain the complex-valued exit field at the sample position. The 3D diffraction patterns have been calculated from the 3D simulated data in direct space around the $(202)_{WZ}$ reflections. The results are presented in Figs. 5.21, f and g in the case of one and three growth faults, respectively. The phase of the sample exit function is recovered from both the scattering in Figs. 5.21, b and c, i.e. with one and three stacking faults. The displacement fields can be therefore extracted from the retrieved phases, knowing that, for the chosen scattering geometry, we have $2\pi(2u_x+2u_z)$. As expected, in each reconstructed amplitude holes are found at the faults position. This effect is due to the fact that defects introduce an additional sequence of layers (ABC) in the middle of the $(AB|AB|AB)$,

and this leads to a zero intensity for the probed reflection [Beitra et al., 2010] as explained in the following. If the layer A is used as a reference, B and C are shifted by

$$\mathbf{v_B} = \mathbf{v} + \left(00\frac{1}{2}\right) = \left(\frac{1}{3}\frac{\bar{1}}{3}\frac{1}{2}\right), \quad \mathbf{v_C} = 2\mathbf{v} + (001) = \left(\frac{2}{3}\frac{\bar{2}}{3}1\right) \tag{5.4}$$

Their scattered amplitudes around the $(202)_{WZ}$ reflection are then equal to

$$1 + e^{2i\pi\mathbf{s}\cdot\mathbf{v_B}} + e^{2i\pi\mathbf{s}\cdot\mathbf{v_C}} = 1 + e^{4i\pi/3} + e^{8i\pi/3} = 0 \tag{5.5}$$

As a consequence, this sequence does not contribute to the intensity in the reciprocal space, and it is recovered as a zero electronic density. The correct intensity near the faults can be reconstructed only if the direct space resolution is sufficient to resolve individual layers, i.e. half a wurtzite unit cell along the (001) direction. As already discussed, the available resolution is larger and it is indeed preferable to select a reflection insensitive to the faults to overcome this problem.

5.3.1 CDI on InSb/InP nanowires with stacking faults

In this section, the experimental evidence of a CDI scattering influenced by the presence of stacking faults is discussed in the case of a single InSb/InP nanowire. The theoretical model of the stacking faults is offered in order to calculate and reproduce the experimental diffraction pattern.

Sample description

InSb is one of the most promising material for application in high-frequency and low-power electron devices. In particular, InSb, with its large lattice parameter, is found to be under strong compressive strain when combined with other group, such as groups III-V, due to the lattice mismatch [Caroff et al., 2009]. These InSb/InP nanowires have been grown on InP (111)B substrate, on which Au aerosols, with a diameter in the range of 10-60 nm, have been deposited. The aerosols have been randomly disposed, obtaining a mean surface coverage of 1-5 droplets/μm^2. The nanowire growth has been performed at the University of Lund (Sweden) using the standard metal-organic vapor phase epitaxy (MOVPE) technique. The InP section has been annealed at 420° using trimethylindium (TMIn) and phosphine (PH_3) as nominal precursors. Te InSb wire has

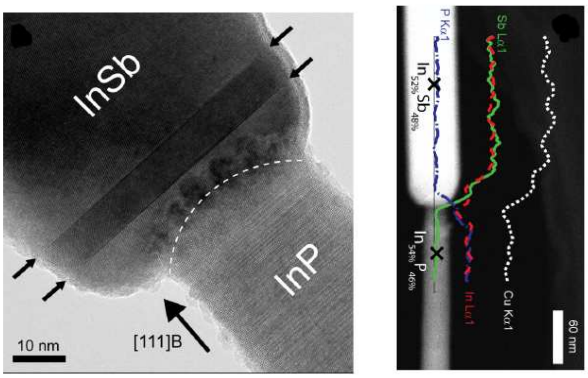

Figure 5.22: Left: HRTEM image in the [110] direction of the InSb-InP interface. The stacking faults is present in the InSb part close to the interface. Right: X-ray energy dispersive measurements of the heterostructure. (Modified from [Borg et al., 2009])

been obtained with the standard precursors TMIn and trimethylantimony (TMSb) at 450°.

Figure 5.22 (left) shows the HRTEM image of a single InSb/InP nanowire. Multiple stacking faults are present in the InP part that has a wurtzite structure. The investigated InSb segment of the nanowire, as expected, has a zinc-blende crystalline structure throughout. However, the InSb nanowire contains twin planes within a 10 nm section (Fig. 5.22, left), changing the structure to wurtzite. This is comfirmed by the results obtained from x-ray energy dispersive measurements [Caroff et al., 2009], shown in Fig. 5.22 (right), performed at the interface. An indication of a curved heterointerface has been found due to the P interdiffusion within 15 nm length.

The ensemble of nanowires has been also studied during a GIXRD experiment performed on the bending magnet beamline BM32 at the ESRF using 30.4 keV photon energy. The reciprocal space map (h0l) in shown in Fig. 5.23 (top). Here, the contribution coming from the InP and InSb sections, indexed on the figure, are well separated due to the different crystalline structures. Figure 5.23 (bottom) shows the measurements of the (10l) crystal truncation rod (CTR) at different grazing incidence angle α_c: 0.00°, 0.05° and 0.10° for the InP, present both in the substrate and in the wire, and InSb, whose contribution is only due to the wires sections. The choice of α_c: 0.00° is motivated by the fact that also in transmission the contribution of the wires in the diffraction can be measured. In figure intensities are expressed in logarithmic scale and positions in reciprocal lattice

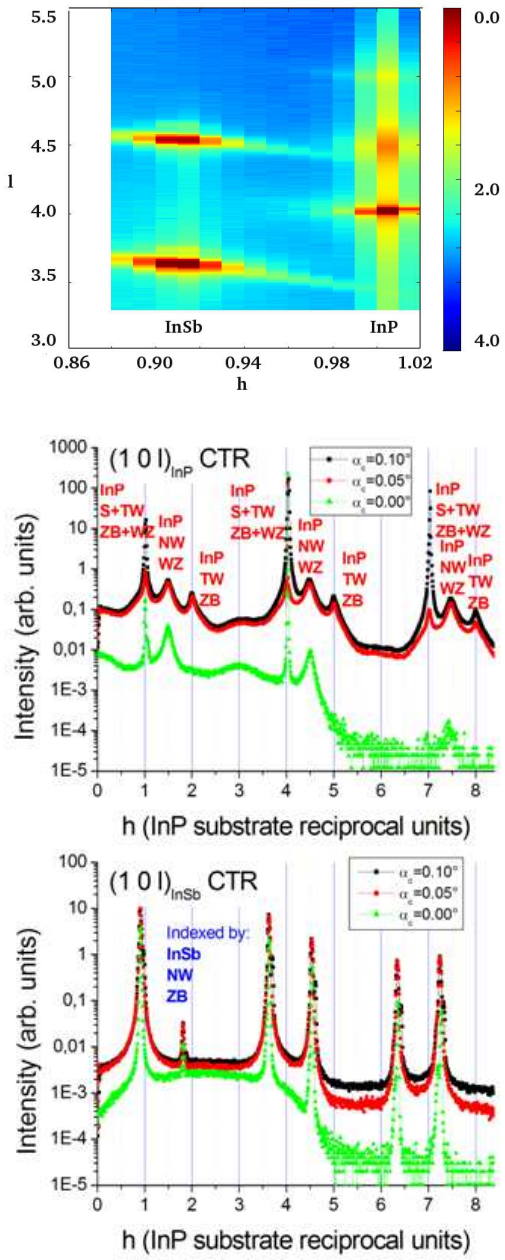

Figure 5.23: Top: Reciprocal space map (h0l) collected on an assembly of InSb/InP nanowires during a GIDX experiment on BM32 (ESRF). Bottom: (10l) truncation rods for InP and InSb. Measurements have been done on the same beamlines at three different incident angles α_c: 0.00°, 0.05° and 0.10°.

units (with respect to InP). The strain distribution in these nanowires is directly related to the width of the measured Bragg peaks.

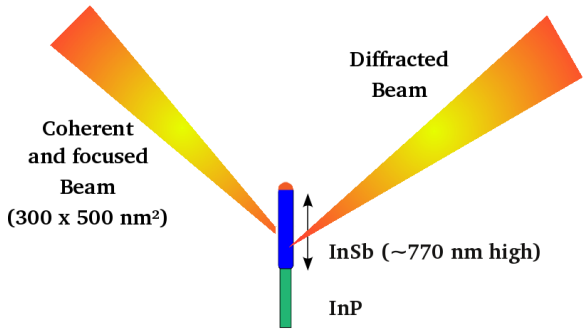

Figure 5.24: CXDI set up used to probe a single InSb/InP nanowire.

Experiment and data analysis

The coherent scattering from single InSb/InP nanowires has been recorded on the undulator beamline ID01 at the ESRF using the microdiffraction set-up already described in Chapter 2. During this experiment, the beam has been focused with a FZP with an outermost zone width of 100 nm. This implies, as explained in Chapter 4, a larger focal spot size with respect to the case of a 70 nm outermost zone width, i.e. $300_v \times 800_h$ nm^2 (FWHM). Slits in front of FZP were closed down to 80×30 μm^2 rather than 60×20 μm^2 as a compromise between coherence and photon flux. All data were collected using a MAXIPIX camera to ensure the best resolution and the lowest background. Due to the particular experimental conditions and to the very small diameter of the wires ($\approx$60 nm), the experiment has been limited to the measurements of 2D diffraction patterns. To analyse the InSb section of the wire, still standing on the substrate, the detector has been placed at the Bragg angle of (111) reflection of InSb, as no interference between InSb (wire) and InP (substrate) are expected. The scattering from InSb could be easily recorded taking advantage of the large difference in the lattice parameters. The schematic of the experimental geometry is shown in Fig. 5.24. During the experiment, due to the beam size, it has been possible to select a single nanowire and perform a profile along the growth direction. The 2D diffractions collected for the (111) reflection are shown in Fig. 5.25 for both the InP (left) and InSb (right) sections of the same nanowire. To measure the InP section, wires have been detached from the substrate and dispersed randomly on it, avoiding the substrate contribution.

The size of the available x-ray beam is small enough to select different part of the InSb section, whose length is 0.68 ± 0.15 μm, simply moving from

the top to the bottom, close to the interface with the InP, by means of the accurate nanopositiong motors of the experimental set-up. To avoid the contribution of the stacking faults, we chose the $(3\bar{3}3)_{ZB}$ Bragg reflection because it is not affected by them. In general, for a displacement vector $\mathbf{v}$, any reflection for which $\mathbf{s} \cdot \mathbf{v}$ is an integer is unaffected by these faults. Diffractions from the top and the bottom of the InSb wire are shown in Fig. 5.26. They have been registered translating the selected nanowire by 250 nm in the growth direction. The scattering from the top shows a small asymmetry in the $s_{\langle 111 \rangle}$ direction (Fig. 5.26, left) while, surprisingly, fringes appears at larger $s_{\langle 111 \rangle}$ (Fig. 5.26, right).

To reproduce the asymmetry observed in the intensity of the fringes at larger $s_{\langle 111 \rangle}$, the strain of an InSb nanowire, with a height of 250 nm and a width of 54 nm, has been simulated. The model used consists of successive

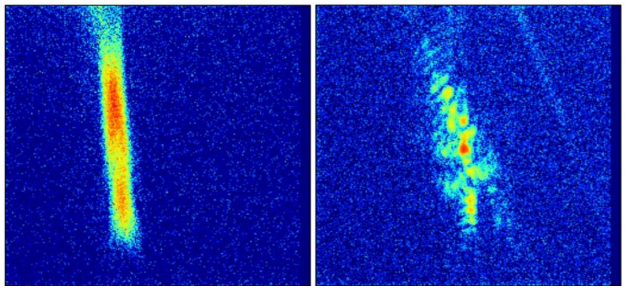

Figure 5.25: 2D coherent diffraction images of a single InSb/InP nanowire . Scattering from (111) reflection has been collected for the InSb (right) and the InP (left) sections of the same nanowire. The illuminated InSb section is certainly faulted as the strain asymmetry in the intensity distribution shows.

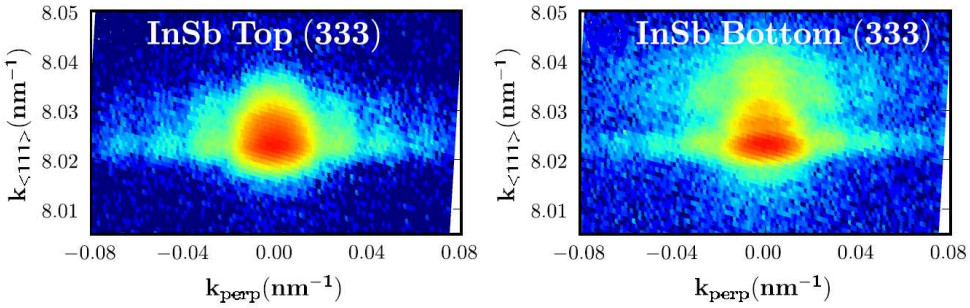

Figure 5.26: Experimental diffraction image from an InSb/InP nanowire at $(3\bar{3}3)_Z B$ Bragg reflection, measured at the top (left) and bottom (right) (near the InSb/InP interface) of the InSb section.

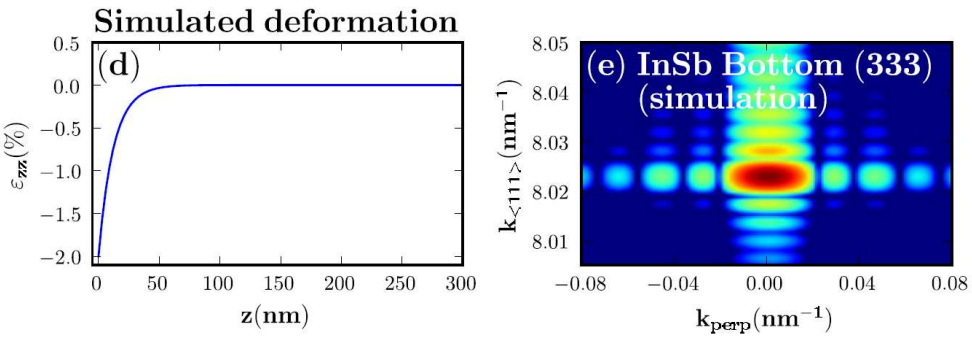

Figure 5.27: Left: Simulated deformation as a function of the height near the base of the InSb section (height = 250 nm). Right: Calculated scattering corresponding to the deformation depicted to the left.

layers added with a different spacing, according to the following relation:

$$\epsilon_{zz} = \epsilon^0_{zz} e^{-z/\Delta} \tag{5.6}$$

where ϵ^0_{zz} is the starting value of the strain 2%, z represents the vertical direction and Δ the unknown section along z-axis in which the strain relaxation occurs. In the proposed model, the strain relaxation which occurs through more complex mechanisms (as in the case of dislocations) is not considered. The best agreement with the experimental pattern, shown in Fig. 5.27 right, obtained for Δ = 10 nm (c.f. Fig. 5.27, left), reproduces well the fringes observed during the experiment. In the horizontal direction, fringes are due to the width of the wire while the asymmetric fringes in the vertical direction are the direct effect of a combination of the height of the wire and the deformation. The shorter $d_{111}-$spacing at the bottom of InSb (relatively to bulk InSb) is probably due to interdiffusion during the deposition, with an $InSb_xP_{1x}$ chemical composition varying in the first 10-20 nm of InSb. It is evident that the combined presence of strain and defects in a structure remains a complicated problem to be solved. However, the most important development of this study is probably the ability to use the very small size of the beam to study different parts of a given heterostructure.

Conclusions

The development of Bragg CDI is particularly important as it gives access to the deformation in the volume of objects at the nanoscale, which is essential for the understanding of their structural properties. In prac-

tice, the experimental case does not fully correspond to the ideal one and different issues have to be faced. Radiation damage can occur when the nanostructure is investigated with high brilliance radiation. In the case of sSOI line, a time-dependent analysis has been proposed to study the strain evolution during the relaxation observed for this crystalline structure and to obtain the strain profiles. This study has been limited to a 2D analysis, because the acquisition time is larger than the characteristic time at which radiation damage occurs.

The contribution of the complex illumination function is an important issue when studying strained nanostructures with coherent imaging techniques. As demonstrated through numerical examples, the retrieved phase and, consequently, the recovered displacement field are influenced by the phase of the experimental coherent wavefront. For a quantitative study, these contribution have to be separated. The possibility suggested in Chapter 4 is the reconstruction of the illumination probe at the sample position can be reconstructed using a CDI approach representing the solution of the discussed case.

The last section of this Chapter has been dedicated to the analysis of faulted structures. As shown with numerical calculations for InAs/InP nanowires, information about the strain state can be hindered by the presence of structural faults. However, the careful selection of measured reflections allows to be insensitive to the stacking order and recover the strain profile. This method could be of course improved by studying several reflections on the same object, which is still difficult to perform for nanoscale materials smaller than 100 nm, as the mechanical precision (confusion sphere) of existing goniometers is much larger than this value. A solution to this problem has been proposed in Chapter 6, in which the feasibility of energy scans with a FZP as focusing optics has been demonstrated.

Chapter 6

Imaging the strain in single GaAs nanowires with InAs Quantum Dots and Quantum Well

In this Chapter, I report on preliminary results obtained from single GaAs nanowires with an insertion of either a InAs quantum well (QW) or a monolayer of InAs QDs with the aim of locating the insertion. The lattice displacements due to the presence of these insertions have been imaged using coherent imaging techniques. In particular, an innovative method has been proposed to collect the 3D diffraction pattern using the energy scan when focusing the coherent beam with a FZP. In addition, a preliminary 2D ptychographic analysis on single GaAs nanowires with QW and QDs is discussed in the last section of this chapter.

6.1 Introduction

The electronic and structural properties of quantum wells and dots such as GaAs/InAs/GaAs(100) have been studied already at the beginning of the Nineties [Giannini et al., 1993]. The information on the atomic structure of the interface, i.e. between GaAs bulk-InAs insertion-GaAs cap, is the essential issue to fully understand the electronic properties of such heterostructures. Quantum dots can be interpreted as a model system for the realisation of a truly three-dimensionally quantum confined structure. When these characteristic dimensions are smaller than the de Broglie wavelength of the

carriers, the energy levels become discrete. With the improvement of growth techniques, controlled assemblies of quantum dots are today fabricated and, thus, applications based on quantum dots become more practical. Nevertheless, the optical properties of quantum dots are strongly influenced by the shape, size, density and strain distribution determined by the growth conditions [Schmidt, 2007].

As already discussed in Chapter 1, in the general case of thin layers epitaxially grown on a bulk crystal, the elastic model describes well the strain and the atomic relaxation. In the case of the structure of interest, Brandt et al. [1992] postulated, using high-resolution transmission electron microscopy (HRTEM), that the elastic theory, that can be used to describe the strain relaxation, breaks down in the limit of one monolayer (ML) of InAs. This work has been the subject of a debate and contradicted by many other studies (see as example [Bernard and Zunger, 1994]). Other experimental results, that were obtained using x-ray beams, indicated the elastic behaviour of InAs QW in a GaAs structure. Among them, Lee et al. [1996] by x-ray standing waves (XSW) technique found that the measured perpendicular strain within the InAs layer was in good agreement with macroscopic elasticity theory. Woicik et al. [1995] and Zheng et al. [1998] also observed the same behaviour by XSW and extended x-ray absorption fine structure (EXAFS) experiments and high-resolution x-ray diffraction (HRXRD), respectively.

6.2 Numerical calculations

In this section, I present the numerical calculations performed both in real (the complex-valued function describing the nanowire) and reciprocal space (the diffraction pattern). For these calculations, a GaAs nanowire with an insertion of one QW is used for simplicity to check numerically the sensitivity of the CDI approach to the presence of the well.

In figure 6.1 the schematics of the projected side view of an InAs QW inserted between the GaAs cap layer and buffer layer is shown. Here, Ga, In and As atoms are represented using different colours, green, red and blue, respectively. A phase shift occurs between the GaAs bulk and cap due to the presence of the InAs ML. The GaAs substrate, that is considered at the origin of the calculated phase shift, is $\langle 001 \rangle$ oriented. The (004) diffraction planes of the GaAs substrate are indicated by bold lines while the dashed

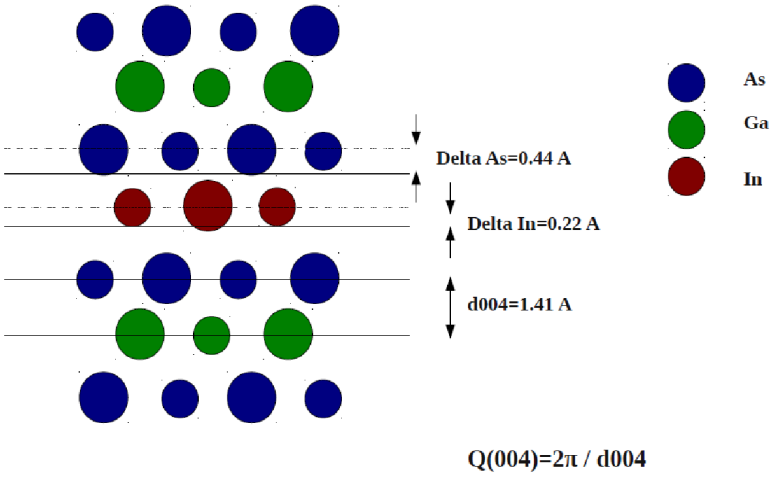

Figure 6.1: The projected side view along the [001] direction of 1 ML InAs buried between the GaAs cap layer and buffer layer. The substrate GaAs diffraction planes are indicated by bold lines while the dashed lines indicate the indium position and the position for the arsenic in the cap. The displacements of the In atoms and the cap As atoms are also represented with respect to the (004) diffraction planes [Lee et al., 1996].

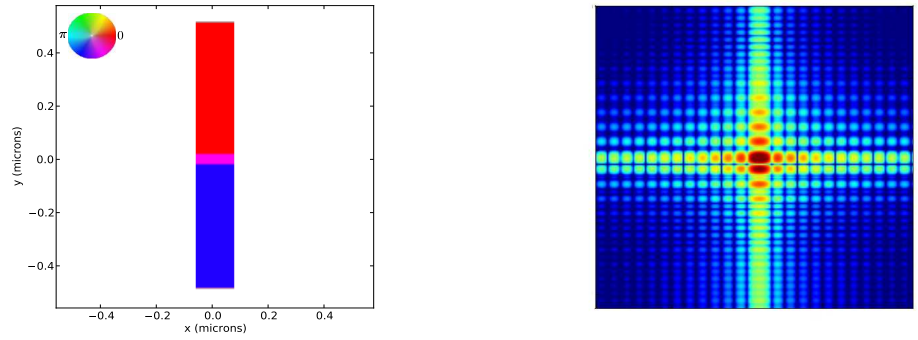

(a) (b)

Figure 6.2: a) Color rendition of the calculated 2-dimensional GaAs nanowire with a monolayer of InAs QDs for the $(004)_{InAs}$ Bragg reflection. Phase is represented by colours. b) 2-dimensional intensity in reciprocal space calculated with a FT of the complex object in real space shown in a).

lines indicate the indium position and the arsenic position in the cap.

The theoretical values of the inter-atomic distance between Ga and As in the bulk is $d_{004} = 1.41$ $\mathring{A}$. Indium atoms are displaced with respect to the Ga layer in the cap of $\Delta_{In} = 0.22$ $\mathring{A}$ [Lee et al., 1996]. This creates

a shift of the Arsenic planes in the cap of approximately $\Delta_{As} = 0.44$ $\mathring{A}$. From these values, the phase of the complex scattering function in a single GaAs/InAs nanowire can be estimated as suggested in Fig. 6.1:

$$\phi = Q(004) \times \Delta_{GaAs} \tag{6.1}$$

where Φ is the phase shift in real space and Δ_{GaAs} is the planes shift in the GaAs cap. The corresponding calculation is shown in Fig. 6.2a for the $(004)_{GaAs}$ Bragg reflection. In this figure, phase is represented by colours and amplitude by the intensity of colours (the amplitude is considered in first approximation constant all over the wire section due to the experimental resolution). The intensity in reciprocal space has been calculated from the complex object in Fig. 6.2a using a FT and it is shown in Fig. 6.2b. This phase profile (corresponding to a phase shift of ≈ 1 rad) produces a split in the central peak of the scattering, which should be measurable in the experimental data.

6.3 Experiment

The 3D diffraction pattern of single nanowires (both QW and QDs) has been collected at the undulator beamline ID01 of the ESRF with the aim of determining the position of InAs monolayer. A 10 keV coherent beam has been focused with a FZP in the partial illumination conditions (cf. Chapter 4). The $(004)_{GaAs}$ Bragg reflection reflection has been selected, setting the θ angle (i.e. the angle between the sample surface and the direction of the incoming beam) at $\approx 26°$. The four chips MAXIPIX detector, with a total of 516×516 pixels, has been placed at the 2θ Bragg angle of the $(004)_{GaAs}$ reflection at $\approx 52°$ and at approximately 1.35 m from the sample position.

Due to the small size of nanowires, generally with a 600 nm diameter and 2 μm long, and considering, as in the case of heterostructures, the presence of strain distribution, they exhibit extended three dimensional diffraction patterns in reciprocal space. When coherent diffraction techniques are applied in the small angle regime, the 3D intensity can be easily collected with a rotation with respect to its vertical axis of the probed nano-object , which is continuously illuminated by the beam. The 3D scattering in Bragg condition can be collected either using a rocking scan, i.e. angular rotation of the sample with respect to the direction of the incoming beam, or by an energy scan, i.e. changing the energy of the incoming beam (cf. section 6.3.1).

This scan is generally performed with achromatic focusing optics, as the KB mirrors, as it benefits from the fact that focal length is independent on the energy. The issue of performing an energy scan with a chromatic optics, as the FZP, has also been overcome in this work, in an elegant and original way, exploiting the specific properties of the focused beam. As discussed in Chapter 4, the partial illumination conditions of a FZP implies important changes in the propagation of the coherent beam. In particular, focal depth and focal spot size increase with decreasing the slit aperture, while the phase remains flat within the focal spot. The outcome of the calculation of the wavefront propagation in the partial illumination conditions, achieved in this thesis work, has allowed to prove the feasibility of an energy scan when using a FZP. If the displacement of the focal point is small during the energy scan, the sample can be maintained in the focal spot even without moving the optics. The advantage of this experimental approach is strong as any sample movement is avoided eliminating any vibration induced by the movement of the diffractometer.

The use of chromatic optics for the energy scan has been probed in the ID01 group by [Cornelius et al., 2011]. In that case Beryllium compound reflective lenses were moved at each energy value during the scan in order to compensate the variation in the focal length and to keep the sample in the focus during the measurements. In the case of a FZP, the energy scan was considered until now unfeasible due to the short focal depth.

6.3.1 Collecting 3D scatterings in Bragg geometry

The three scans used to register the three dimensional coherent scattering with 2D detectors are schematically illustrated in Fig. 6.3. Each scan corresponds to specific movements of the detector scanning the reciprocal space. For each scan, the bold line (green) is used to indicate the initial Bragg configuration and the the dashed (blue) and dotted (orange) lines indicate the variation of the incident and diffracted beams, with wavevectors $\mathbf{k}_i$ and $\mathbf{k}_f$, respectively. The angle 2θ represents the Bragg angle of the chosen Bragg reflection.

As depicted in Fig. 6.3a, the three-dimensional intensity distributions is obtained by performing a rocking scan through the selected Bragg peak and simultaneously recording two-dimensional intensity cuts (Fewster, 1997). This corresponds to the mechanical rotation of few degrees of the sample with respect to the direction of the beam. The 2θ Bragg angle is fixed;

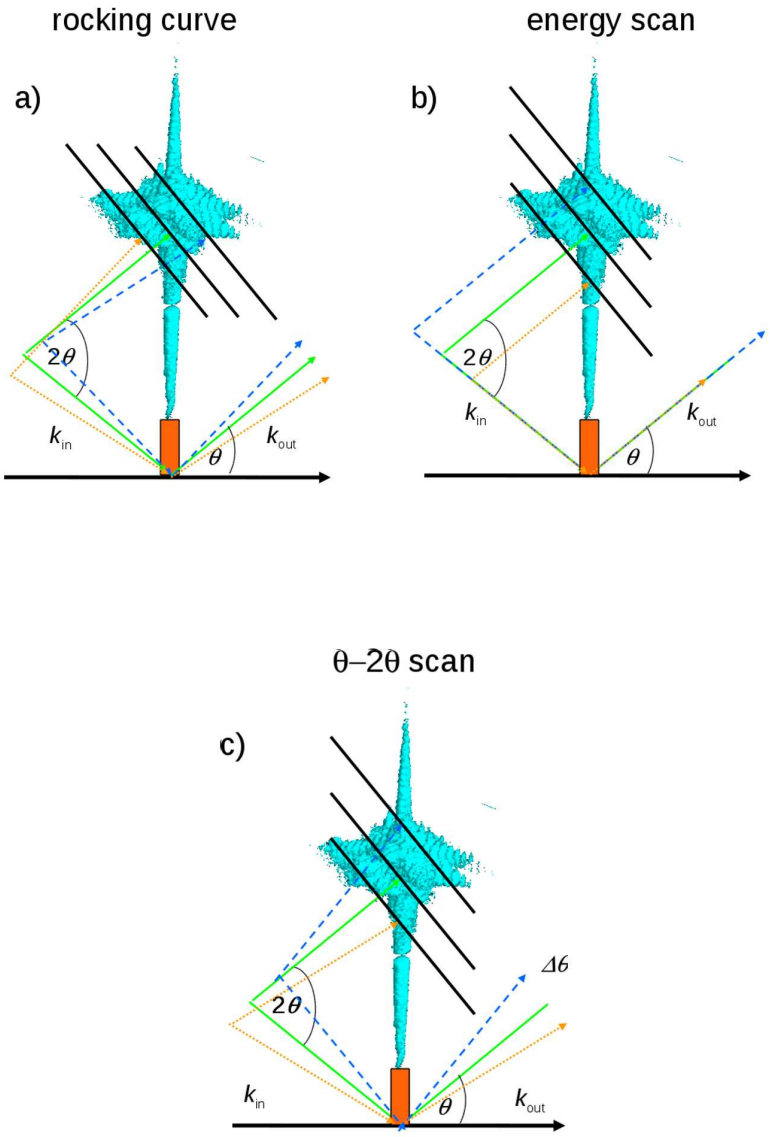

Figure 6.3: Simplified schematics in reciprocal space for (a) a rocking-curve scan, (b) an energy scan and (c) a $\theta - 2\theta$ scan. The dashed and dotted lines indicate the variation of the incident and diffracted beams. The movement of the detector (as projected on the Ewald's sphere) is also illustrated.

hence, the detector scans horizontally the 3D scattering in the reciprocal space. In practice the detector doesn't move but the 2D patterns move along the detector. The collected data have to be orthonormalised to be displayed in the reciprocal space.

One main issue concerning the collection of three-dimensional data is the sphere of confusion of the existing diffractometers that could be quite

large (typically a few tens of micrometers over a 360° rotation). If it is compared to the sample and beam size (a few hundreds of nanometers), the investigated nanostructures can easily move out of the beam, even though a rocking curve is taken over typically 1°. Therefore, the acquisition through a rocking-curve scan requires the re-alignment of the structure with translations into the nanobeam for every rocking angle, resulting in an increase of the acquisition time.

The $\theta - 2\theta$ scan (Fig. 6.3c) is equivalent to the energy scan, both the sample and the detector have to be rotated of few degree to cover all the reciprocal space. This approach is unsuitable when very tiny nanostructures are investigated due to the vibrations produced by the detector arm movements.

The energy scan can be used to avoid any movement of both the object and the diffractometer (Fig. 6.3b). In this case, the energy is varied by only few eV in order to record the 3D reciprocal space map , keeping all the angles at the values imposed by the Bragg conditions. The undulators gaps adjustment is required while scanning the energy to stay at the maximum of the undulator emission peak and the incident intensity remains constant. As a consequence, the 3D scattering in the reciprocal space is scanned vertically by the detector. As in the case of a rocking-curve scan, data has to be orthonormalised. The orthonormalisation process is more complex when 3D scattering is collected using the energy scan, as different crystalline planes will diffract on the detector due to the change in energy, according to Bragg's law:

$$2d_{hkl} = \frac{n\lambda}{\sin\theta}, \quad n\epsilon\mathbb{N}. \tag{6.2}$$

Here d_{hkl} is the distance between crystalline plane expressed in reciprocal lattice unit (hkl). Looking at Eq. 6.2, for a fixed detector position θ, different crystalline planes defined by (hkl) will diffract while changing the energy E values (or, equivalently the wavelength λ) of the incident radiation.

6.3.2 Sample description

The samples (GaAs nanowire with InAs QW and QDs insertions) investigated during the CDI experiment were prepared by Malik and Claudon at the CEA/Grenoble. The GaAs wires are $\approx$2 μm high with a diameter in the 200-600 nm range. The photonic nanowires were defined from a planar structure grown by molecular beam epitaxy. This planar structure

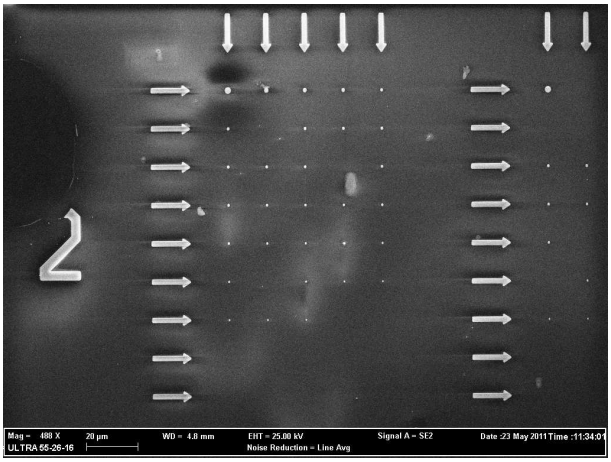

Figure 6.4: Scanning electron microscopy of the investigated array.

consisted of a Stranski-Krastanov InAs QDs array or a QW buried under 2.5 μm thick GaAs layer. The GaAs layer laid on a 500-nm-thick sacrificial layer of $Al_{0.8}Ga_{0.2}$. A mirror structure, consisting of 11 nm of SiO_2 and 250 nm of gold, was deposited on top of the epitaxial layer and further glued in a flip-chip step on a GaAs host wafer using epoxy. A mechanical and selective wet etching was used to remove the growth wafer and the sacrificial layer, creating a mirror-flat surface. Finally, after deposition of a 400-nm-thick Si3N4 hard mask, several identical arrays of aluminium disks of various diameters were defined by electron-beam lithography. After dry etching of the hard mask (SF6 plasma), these nanowires were etched using optimized plasma etching on a SiCl4 and argon gas mixture.

Interesting photonic properties were obtained in the case of GaAs nanowire with one monolayer of QDs and reported in [Claudon et al., 2010]. The physical properties and the optical emission response of pho-

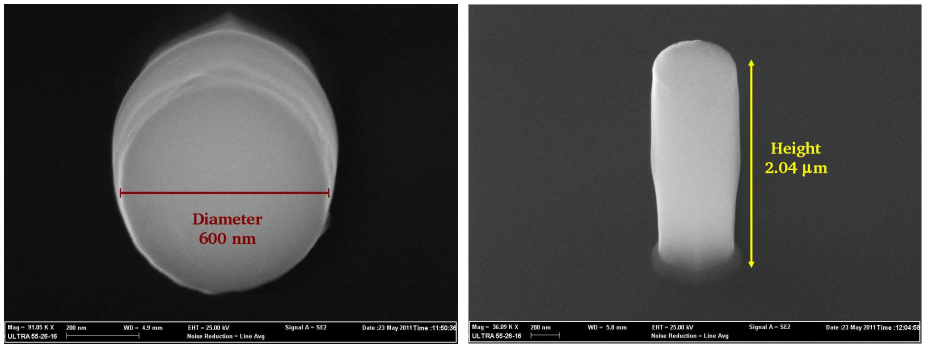

Figure 6.5: Scanning electron microscopy images of the investigated nanowire with InAs QDs. Left: Top view. Right: Side view (with an angle of 51°) of the same wire.

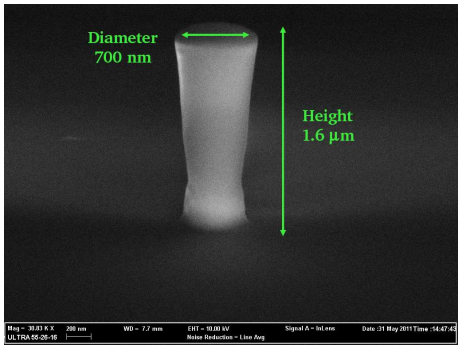

Figure 6.6: Scanning electron microscopy images of the investigated nanowire with InAs QW.

tonic nanowires, similar to the one studied during the CDI experiment, were measured and exhibit a nearly perfect radiative performance with single photon emission. This property can be explained only considering that a single QD is buried in the considered nanowire. This fabrication method was demonstrated to be a promising approach for the growth of vertical semiconductor photonic nanowires in the context of quantum communication with an electrical injection. A coherent diffraction experiment, as the one performed in this work, would allow to locate and characterise the QDs and QW and correlate optical properties and structure.

The GaAs nanowires are arranged on the sample surface in 5×9 rectangular array marked with arrows (Fig. 6.4). The exact position of each wire is given by crossing these arrows with the x-ray beam. The diameter of these nanowires varies and depends on the specific position in the array, from the largest (left corner of the top side) to the smallest one (right corner on the bottom). Due to some problems during the sample etching or bonding, some of the wires with smaller radii (in the range of 300-100 nm) did not remain on the substrate. One of the investigated wire with QDs insertion has been selected in the array is shown in Fig. 6.5 and the quantum wire with the InAs QW insertion is also shown in Fig. 6.6. The vertical profiles of these wire are different due to a different etching process in order to enhance photonic properties.

6.3.3 Experimental data

A combination of the high magnification microscope implemented on the diffractometer, the knowledge of the structure design of the sample combined to x-ray microdiffraction mapping [Mocuta et al., 2008] helped

to select a single nanowire for CDI measurements. The scanning electron microscope images of the top and side view of the nanowire investigated during the experiment is shown in Fig. 6.5. The wire exhibits a diameter of ≈ 600 nm and a height of ≈2.0 μm, calculated considering the angle of 51° between the electron gun and the sample. Once the quantum wire, in the diffraction conditions under the x-ray radiation, has been identified, a vertical scan along the wire height has been performed to check the experimental sensitivity to the insertion of one monolayer of QDs. A range of 3 μm has been covered in order to scan the total height of the nanowire, from the bottom to the top, until losing the diffraction signal. In figure 6.7, six selected diffraction pattern are shown, corresponding to the scattering from the bottom (Fig. 6.7a) to the top of the wire (Fig. 6.7f), collected with a step size of 200 nm. In this figure experimental data are not treated and the images are obtained selecting 150×150 pixels on the detector. The split of the central peak is clearly visible in Fig. 6.7c, corresponding to the scattering registered at ≈1.2 μm from the bottom of the wire. This effect has been predicted by the numerical calculation discussed in section 6.2. This shows that the monolayer of QDs is inserted at the middle of the wire total height as expected. Some differences can be also noticed between the 2D diffraction patterns collected below and above the QDs position. The central peak shifts from the bottom side (Figs. 6.7,a-b) to the top side (Figs. 6.7,d-f) of the splitting. This is therefore due to presence of a phase shift in the complex valued object in real space (cf. Fig. 6.2a), in this specific case between the GaAs bulk and cap. The splitting is the direct consequence of the presence of QDs layer insertion (i.e. of the phase shift in the complex-valued function describing the object in real space (see Fig. 6.2a)), when illuminated with a coherent x-ray beam.

The three dimensional reciprocal space map has been registered using both an energy scan and a rocking scan, whose feasibility has been recently assured by the new diffractometer available on ID01 (see Appendix B) having improved stability. The energy scan has been performed in a range of ±50 eV with a step of 1 eV, around the central values of 10 keV, with an acquisition time of 20 s/step. At each value of the scan, the three undulator gaps have been re-adjusted to insure the maximum intensity of the incoming radiation. Figure 6.8 shows three different views of the raw 3D coherent scattering collected around the $(004)_{InAs}$ Bragg reflection of a single nanowire at the QDs position. Figure 6.8a, which corresponds to

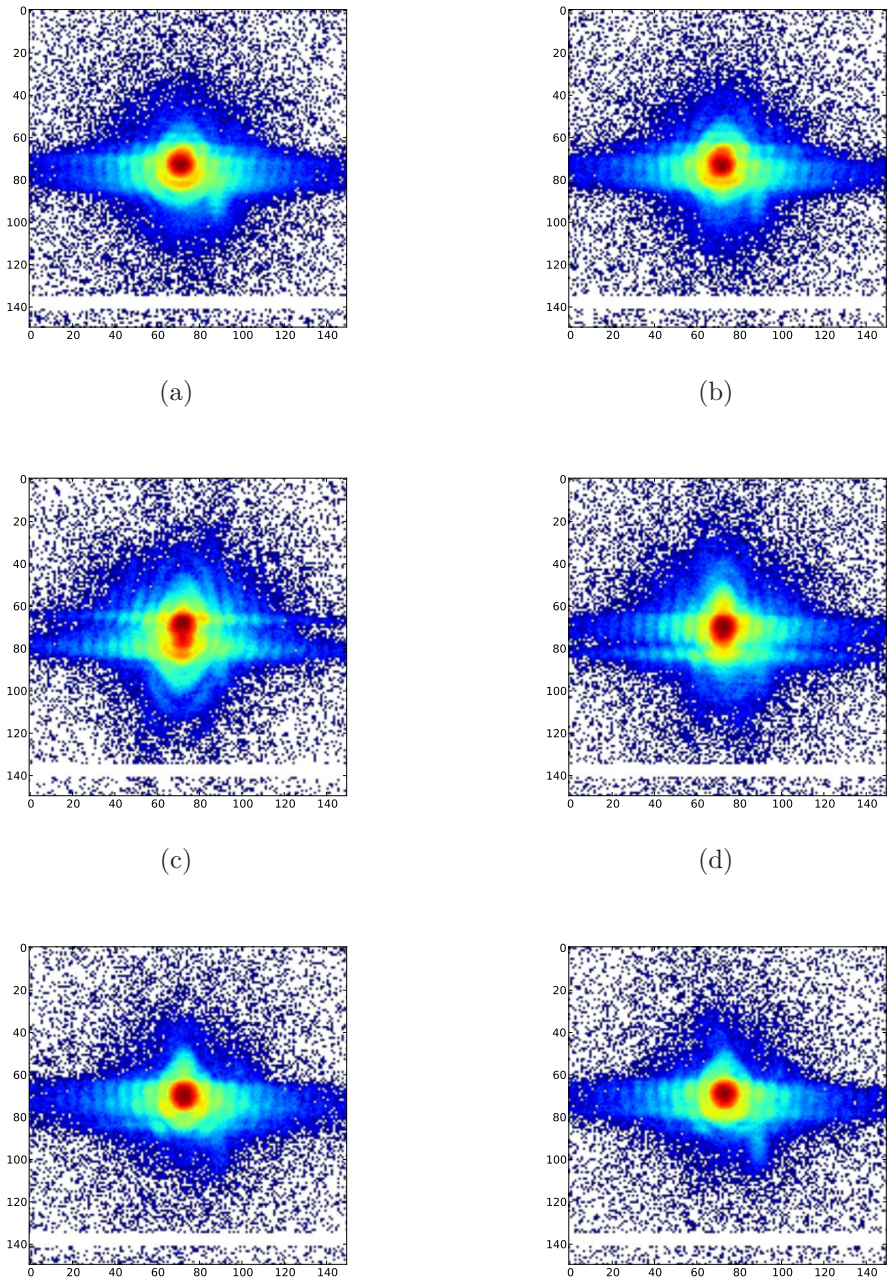

Figure 6.7: Vertical scan along the nanowire from a) the bottom to f) the top. Each raw image has been collected using 200 nm motor step and acquisition time of 20 s. The QDs are inserted at a position between the scatterings depicted in c) and d). A selection of 150×150 pixels on the detector is shown.

the top view, exhibit circular oscillations that are produced by the circular finite size of the wire. The streaks of intensity are also coming from the

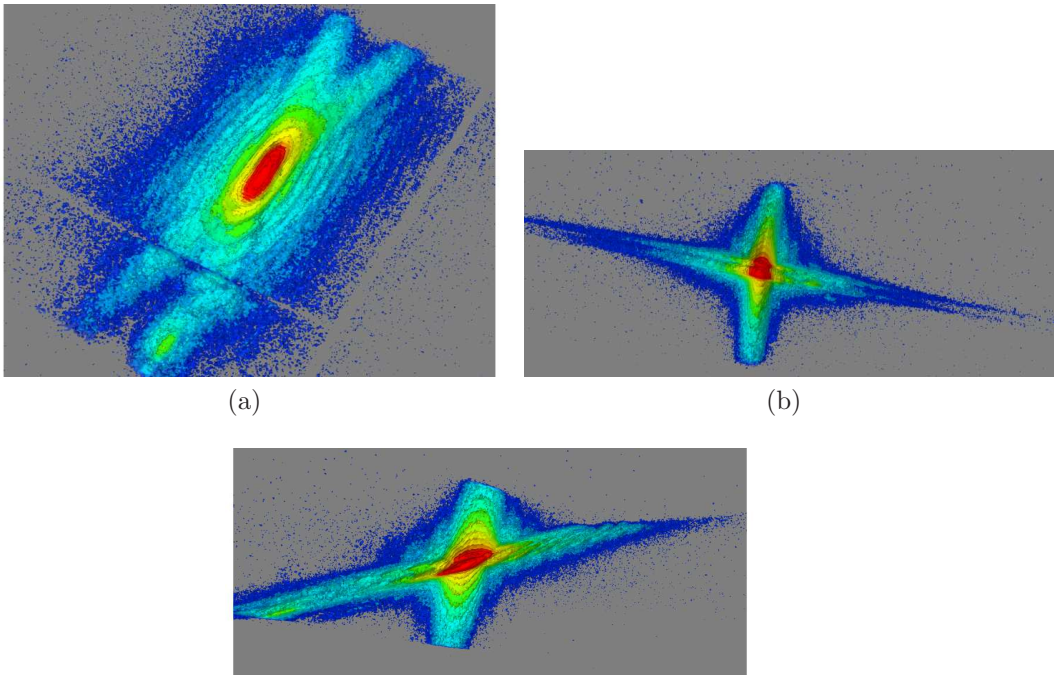

(a) (b)

(c)

Figure 6.8: 3-dimensional diffraction pattern (not orthonormalised) collected at the QDs position for the $(004)_{GaAs}$ Bragg reflection using the energy scan in a range of ± 50 eV with a step of 1 eV and acquisition time of 5 s. The splitting of the central peak close to 10 keV is evident in figures b) and c).

shape of the illuminated nanowire, which may present facets due to crystallographic etching. As expected, the peak splitting is clearly visible on the 3D scattering in particular looking at the figure 6.8 b and c. A cut of the 3D coherent scattering in the vertical plane should correspond to the calculated diffraction in Fig. 6.2b. As comparison, the 3D scattering (not orthonormalised) collected from the same nanowire at the insertion with a rocking scan is shown in Fig. 6.9.

6.3.4 Data treatment

Experimental data has to be treated before starting the phasing analysis. An important step required by the properties of the FFT is to centre experimental data into the computational array. This preliminary treatment helps in the convergence of phasing process. Moreover, this prevent the introduction of an asymmetry into the reconstruction that could lead to a gradient in the retrieved phase. Depending on the number of pixels and the computing memory, experimental data may be binned with the aim of

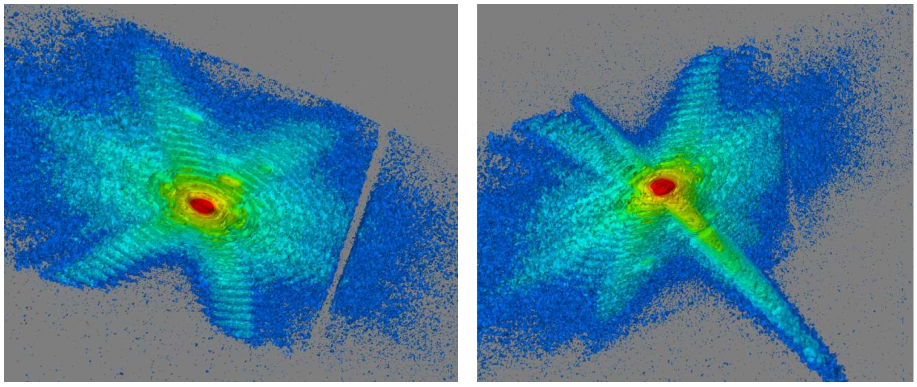

(a) (b)

Figure 6.9: 3-dimensional diffraction pattern (not orthonormalised) collected at the QDs position for the $(004)_{GaAs}$ Bragg reflection using the rocking scan in the angular range of 0.60° with a step of 0.005° and acquisition time of 20 s/step.

saving time during data processing and analysis. This strategy is generally used to improve the statistics but is limited by the required oversampling ratio. In addition, after the collection, raw data must be checked for "aliens", i.e. contributions coming from overgrowth or substrate, erroneous intensity measurements due to cosmic rays or air scattering; they must be masked as they may introduce asymmetry into the reconstructed object. Finally, an orthonormalisation process is required to correct the movement of the detector during the collection of the 3D scattering, that depends on the chosen scan mode (cf. Fig. 6.3). The orthonormalisation process when the energy scan is employed to register the 3D scattering is detailed in Appendix C.

The quantitative analysis of the 3D coherent diffraction patterns collected in the case of the GaAs nanowire with QW and QDs will be used to retrieve the complex-valued object in real space and locate the QDs layer along the wire height and determine the phase shift into the crystalline structure. However, this analysis is still in progress and will not be detailed in this manuscript.

6.4 Two-dimensional Ptychography in Bragg geometry

As discussed in Section 6.3.3, during the experiment several vertical scans have been performed along the height of selected nanowires in order to locate the InAs insertion. This has been possible due to the proven sensitivity of CDI technique to the presence of QW and QDs. Images of the 2D scattering have been collected at different position along the wire using a step size of 200 nm. As the 10 keV energy focal spot size obtained with a FZP with a 70 nm outermost zone width and in partial illumination conditions is $\approx$ 400 nm (FWHM) in the vertical direction, data collected with the vertical scan can be analysed through a ptychographic approach (see Chapter 4, last section). In this particular case, the registered overlapping corresponds to approximately 50% of the illumination probe.

The vertical scan collected in the case of 1ML of QDs is shown in Fig. 6.10 while the one registered for the InAs QW is presented in Fig. 6.11. They consist of 11 images of the scattering collected at the $(004)_{GaAs}$ Bragg reflection at different height of the wires (also labelled on the different images of Fig. 6.10), from the bottom (positive z values) to the top (negative z values). The splitting of the central peak in the case of 1ML of QDs is visible looking at the scattering collected at z=-6.4 nm (Fig. 6.10). This splitting is less clearly seen in the case of the InAs QW even if a shift of the central peak with respect to the centre of the selected computational window has been registered (comparing scatterings at z=-197 nm and z=200.8 nm) which corresponds to the phase shift in real space.

As starting guess for the illumination function, a Gaussian probe has been used with a focal spot size of approximately 407×526 nm^2, measured at the FWHM (Figs. 6.12 and 6.13). An iterative phase retrieval algorithm, as the one proposed by Thibault et al. [2009], has been used to reconstruct the exit field at the sample position and, at the same time, the complex coherent wavefront used during the experiment. With the ptychography approach, the contribution of the illumination function in the retrieved exit field can therefore be disentangled, allowing the correct interpretation of the strain in the investigated nanostructure. The achieved spatial resolution for the reconstruction in real space at the sample position is $\approx$8 nm and depends on the number of selected pixels at the detector plane.

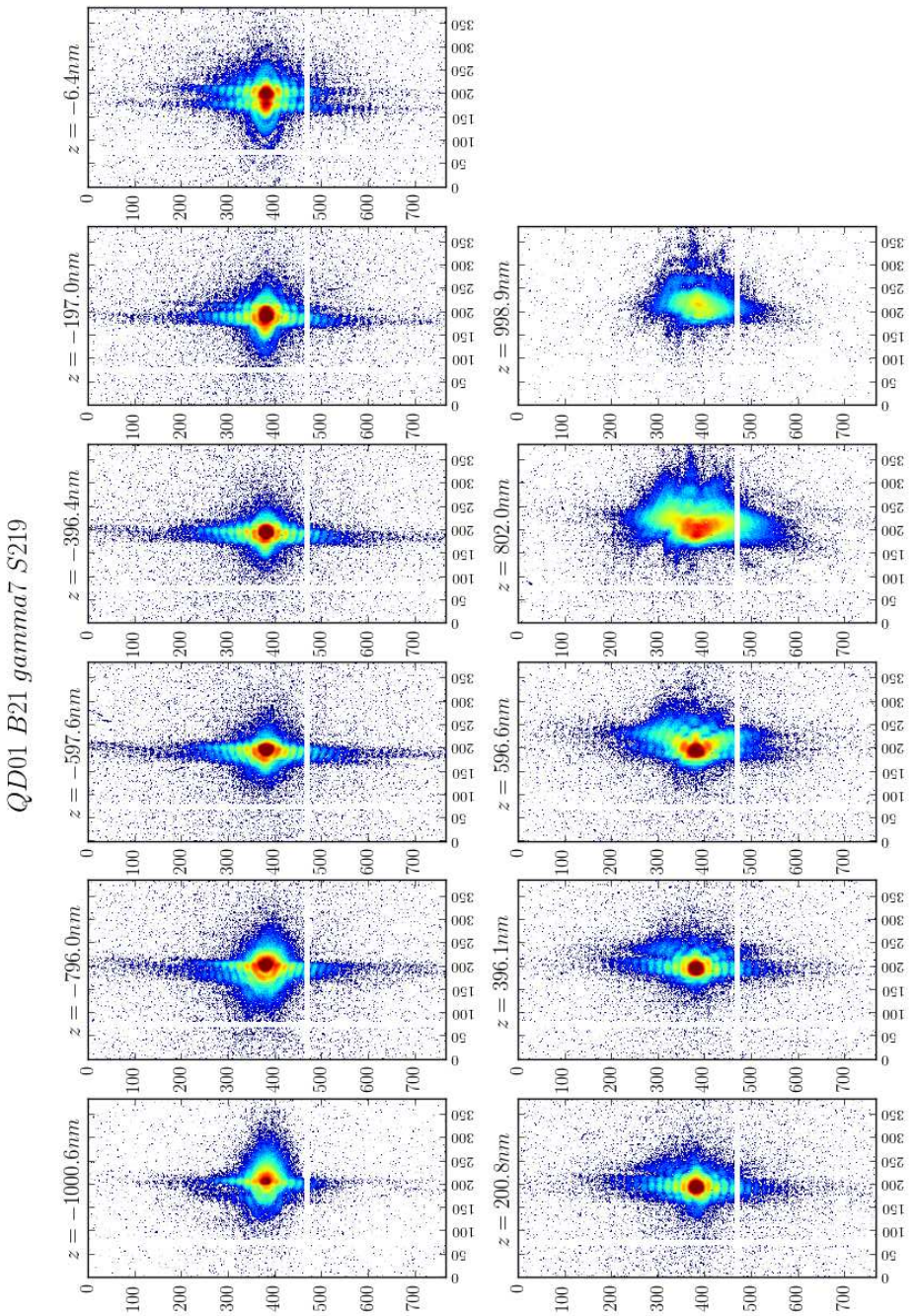

Figure 6.10: 2D scatterings (raw data) from a vertical scan along the GaAs wire with InAs QDs insertion plane shown in Fig. 6.5 and used for ptychography. On the horizontal and vertical axis the number of selected pixels at the detector plane.

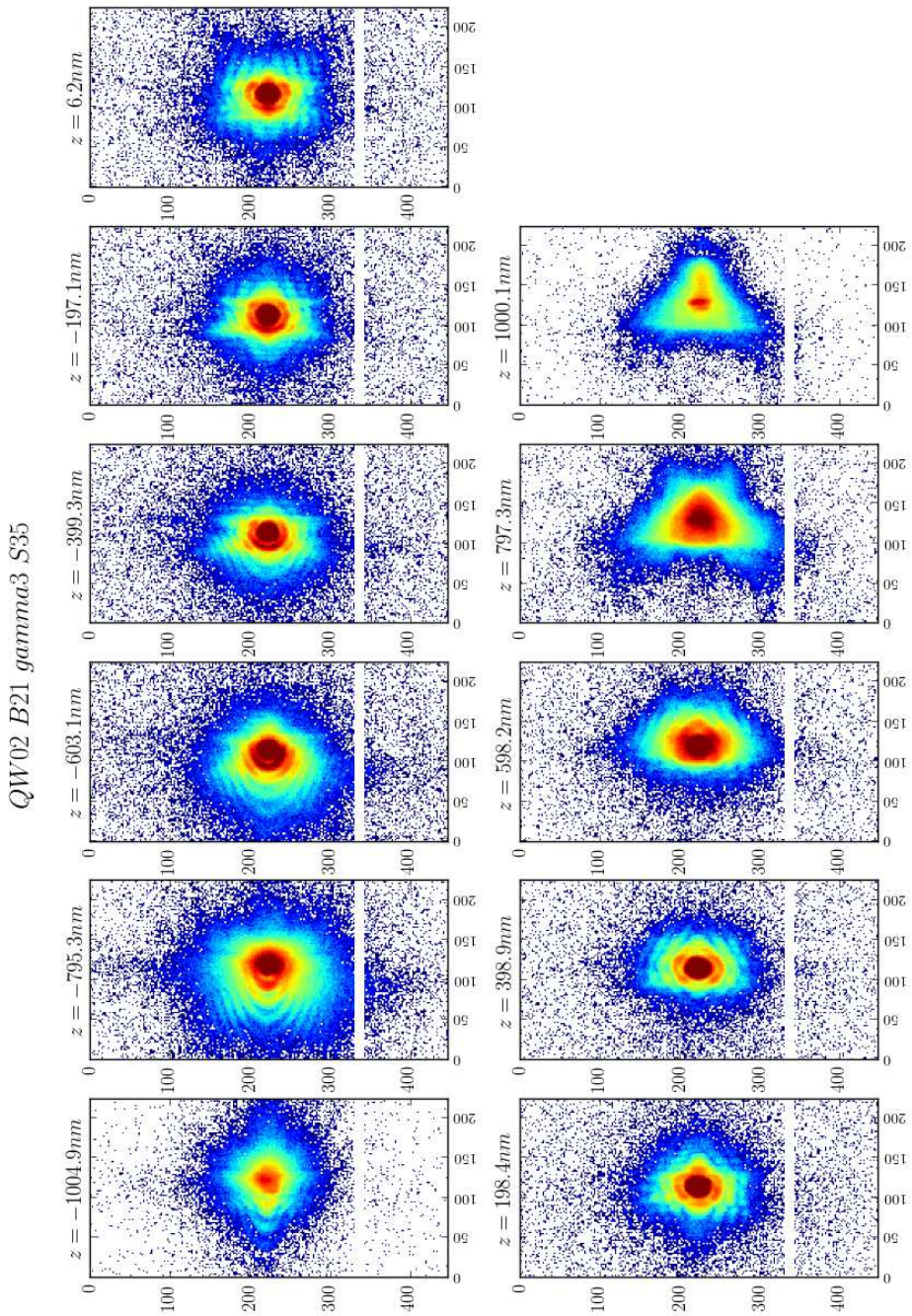

Figure 6.11: 2D scatterings (raw data) from the vertical scan along the GaAs wire with InAs QW insertion shown in Fig. 6.6 and used for ptychography. On the horizontal and vertical axis the number of selected pixels at the detector plane.

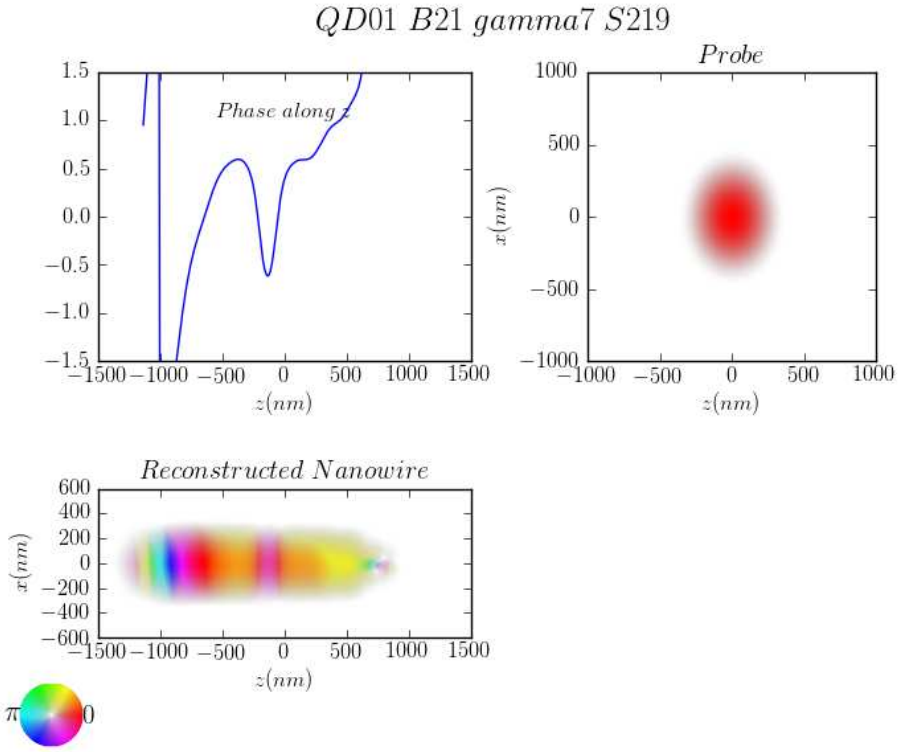

Figure 6.12: Preliminary results from ptychography analysis of the diffraction patterns shown in Fig. 6.10. The phase shift occurs at z ≈ −100 nm. Phase is expressed in radians. The reconstructed shape is in agreement with the one shown in Fig. 6.5b.

The complex-valued function describing in real space the nanowire with 1ML of InAs QDs has been reconstructed and it is presented in Fig.6.12. As expected, we can observe the phase shift at the z value corresponding to the insertion position. In addition, we can notice a second phase shift (at z≈-250) which is probably due to the strain relaxation of the crystalline structure above the quantum dots position.

The results obtained for the QW (Fig.6.13) are in agreement with the calculations shown in Section 6.2 (cf. Fig.6.2) even if the reconstructed phase shift is smaller than the calculated one. As the resolution achieved in the reconstruction is too large with respect to the width of the QW/1ML QDs insertion, the electron density of the insertion cannot be reconstructed. However, the technique has been demonstrated to be sensitive to the phase shift caused at the insertion position in the nanowire structure.

The supplementary phase variations reconstructed at the bottom of the nanowire with QW and at the top of the one with QDs are attributed to defects induced by the fabrication process (lithography and gluing of

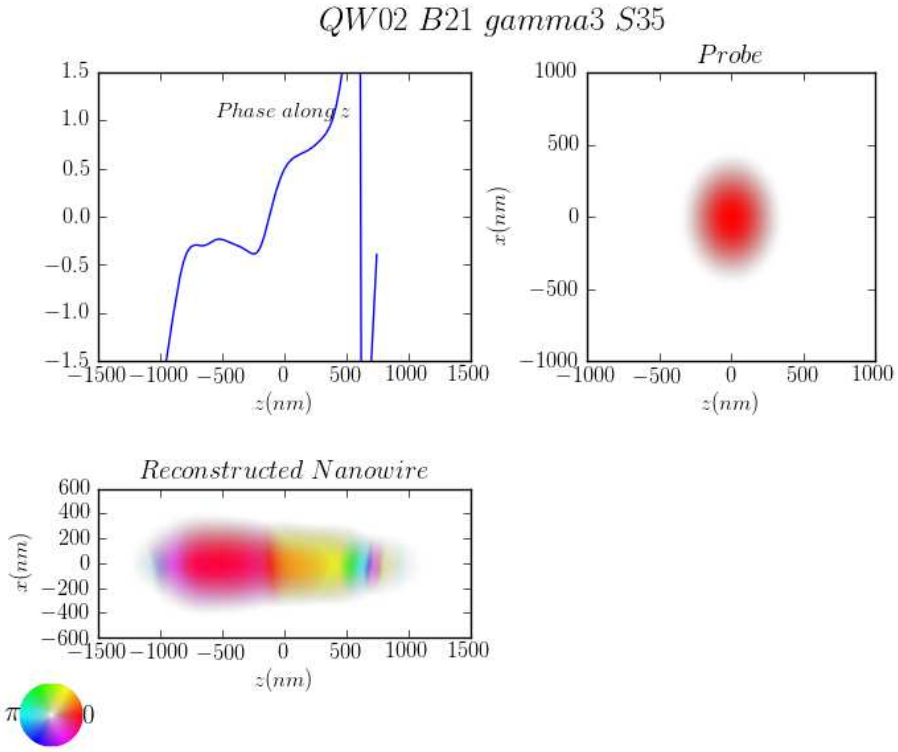

Figure 6.13: Preliminary results from ptychography analysis of the diffraction patterns shown in Fig. 6.11. The phase shift occurs at z ≈ -100 nm. Phase is expressed in radians. The reconstructed shape is in agreement with the one shown in Fig. 6.6.

nanowires on the sample surface).

6.5 Conclusions

In this chapter I reported on the preliminary results obtained from the application of CDI in Bragg geometry on single GaAs quantum wires with either InAs QDs or QW insertion. As previously discussed, important contributions to coherent imaging technique have been offered. First, the sensitivity of coherent diffraction technique to the presence of the insertion of one monolayer InAs quantum well or InAs quantum dots embedded in single GaAs nanowire has been discussed, demonstrating that it was possible to locate very small lattice displacements in heterostructures. This may open new possibilities for the application of the CDI technique for the strain determination. In addition, we have demonstrated the possibility of collecting the 3D reciprocal space map (RSM) from a single nanowire using the energy scan even when chromatic optics (in the discussed case a FZP)

are used to focus the coherent beam to the sample position. This approach exploits specific properties of the focused beam in the case of a partially illuminated FZP, discussed in details in Chapter 4 of this manuscript. As the focal depth was found to increase while decreasing the aperture of the slits, the energy scan can be therefore performed without any re-adjustment of the optics as the sample is kept in the focus. The phasing analysis is still in progress and the 3D RSM registered during the experiment at the insertion position using an energy scan will allow measuring the strain relaxation in the wire at the insertion from the retrieved phase in the real space. As ultimate goal, the possibility of localising the single QDs will be also explored. Finally, 2D coherent scatterings collected at different positions along the wire height have been treated and preliminarily analysed using the ptychographic approach. Due to the vertical size of the coherent focal spot combined with the step size of the performed vertical scans, an overlapping of approximately 50% has been obtained. The preliminary reconstructions of investigated nanowires, obtained with a Gaussian probe with a focal spot size of $\approx 407 \times 526$ nm^2 (FWHM) as initial guess, exhibit the expected phase shift due to the presence of the QW/QDs insertion and they are in good agreement with calculations. This analysis will be improved in the future and the more realistic wavefront at the focal plane, as the one obtained with a FZP in partial illumination conditions (see Chapter 4), will be employed as initial probe for the reconstruction.

Conclusions and outlook

Coherent x-ray diffraction imaging is a technique used to image the strain at the nanoscale. However, the application of CDI to real systems often requires the proposition of *ad-hoc* solution to overcome specific experimental issues representing intrinsic limits of the technique.

The main objective of the work presented in this manuscript has been the exploitation of coherent x-ray diffraction imaging in Bragg condition to recover the strain in the particular case of heterogeneous or highly strained homogeneous nanowires. Special attention has been devoted to the detailed strain analysis of nanowires in presence of radiation damage, stacking faults and limited strain sensitivity. In these cases, experimental results have been supported by numerical calculations. An important issue when strain is imaged with the CDI approach is the influence of the wavefront on the reconstructed phase. This has been investigated and discussed in the presented work and represents one of the most important contribution to the CDI technique.

In the case of InSb/InP nanowires with stacking faults, the use of carefully selected reflections has allowed to be insensitive to the stacking order and image the strain in the InSb section as a consequence of the InP interdiffusion.

We demonstrated that the imaging of strain in presence of radiation damage can be used to understand the relaxation of a crystalline structure and the mechanism through which the damage occurs. Specifically, a time-dependent analysis has been performed on sSOI lines to recover the modification in the displacement field due to the effects of the induced strain relaxation. The recovered displacements u_z have been used to calculated two components of the strain fields, ϵ_{zz} and ϵ_{zx}. In particular, ϵ_{zx}, which contains the information about the bending of the line, exhibits a clear relaxation effects passing from the average initial value of 0.0436% to 0.0200%.

Through numerical examples, we also showed that the wavefront at the

focal position strongly influences the quantitative analysis of the displacement in single nano-objects when coherent imaging techniques are employed. As discussed in the case of the numerical strained silicon line, the retrieved phase cannot be used to describe correctly the actual displacement into the nanostructure if the complex-valued illumination function is unknown. This has motivated, in this work, the accurate wavefront characterisation for the ID01 experimental conditions proposed as a solution to this particular issue.

The propagation of a coherent complex field focused with a partially illuminated circular FZP has been provided through numerical calculations and experimental reconstructions. The focal spot size and the focal depth are found to be diffraction limited, with size increasing by decreasing the illuminated area on the lens. The proposed calculations has allowed to understand and predict the role of the optical element in the experimental set-up. One of the most important results of this study is that the reconstructed phase has been found to be flat near the focal spot centre allowing a simple analysis for CDI experiments. These results have been also confirmed by the first experimental evidence of ptychography in Bragg geometry on a test sample.

The application of CDI requires the ability to study the 3D profile of at least one reflection of the investigated object. Unfortunately, this is still difficult when a rocking scan is employed to collect the 3D scattering in particular for objects smaller than 100 nm. This is due to the limited mechanical precision of existing goniometers which does not allow to maintain the sample in the centre of rotation during the scan. As shown in this work, any sample movement during the 3D scattering collection can be bypassed by using the energy scan rather than a rocking scan even when a FZP is employed as focusing optics. This method has been applied in the case of a single GaAs nanowire with an insertion of InAs quantum dots or quantum well. The strain relaxation occurring in these nanowires due to the presence of the insertion has been imaged using CDI. In addition, we demonstrated the possibility of treating data collected at different positions along the wire height with a ptychographic approach. The preliminary results obtained with these two approaches have demonstrated the sensitivity of CDI to insertions smaller than the achievable resolution.

The future steps of this research project include the refinement of the analysis of experimental data collected from the GaAs quantum wires. In the case of 3D scatterings collected with the energy scan, a preliminary

orthonormalisation process has been already proposed. An adequate iterative phase retrieval algorithm has to be developed to recover the full 3D phase map in real space in order to calculate the strain relaxation due to the buried structures. The main issue of the reconstruction is the choice of real space constraints (i.e. the support). An adequate choice may be represented by the three dimensional coherent wavefront that has been fully characterised during this work. This would allow the improvement of the algorithm convergence and the disentanglement of the contribution of the probe in the retrieved phase. In addition, the two dimensional reconstruction discussed in this manuscript using the ptychographic approach needs to be improved. The quality of the reconstructed object depends also on the starting guess for the illumination function. In the discussed case, the coherent wavefront corresponding to our particular experimental conditions can be used as starting probe for a successful reconstruction.

Appendix A

The Huygens-Fresnel principle

According to the Huygens' principle [Huygens, 1920], each point of a wavefront may be considered at the initial time t_0 as the source of secondary spherical waves. At the generic time t, the wave-front may be seen as the envelope of these waves. Later on, Fresnel extended the Huygens's construction postulating that the secondary waves interfere mutually. The Huygens-Fresnel principle took a fundamental place in the theory of the diffraction. A mathematical derivation of the Huygens-Fresnel principle is provided for a strictly monochromatic plane wave [Born and Wolf, 1999].

Let consider a monochromatic plane wave, generated at the point source P_0, propagating through an opening A in an opaque screen of radius R. The interference has to be determined in P. The distances r and s define the position in A of a generic point Q with respect to P_0 and P, respectively. Supposing that the linear dimension of the opening is much smaller than the distance between P_0 and P from the screen, the amplitude U_P of the waves superposition in P (the contribution of the only electric field is considered) is given by the Kirchhoff integral

$$4\pi U_P = \int\int_{S_{TOT}} \left\{ U \frac{\partial}{\partial n} \left(\frac{e^{iks}}{(r+s)} \right) - \frac{e^{iks}}{(r+s)} \frac{\partial U}{\partial n} \right\} dS. \tag{A.1}$$

Here S_{TOT}, as shown in Fig A.1, left, is the sum of the opening A, the portion of non illuminated side B of the screen and a portion C of a sphere centred in P. $\mathbf{k}$ is the scattering vector. Assuming that in B U and $\partial U/\partial n$ are approximately zero [Born and Wolf, 1999], Eq. A.1 can be rewritten as follows:

$$U_P = -\frac{iA_0}{2\lambda} \int\int_A \frac{e^{ik(s+r)}}{rs} \left\{ \cos(n,r) - \cos(n,s) \right\} dS \tag{A.2}$$

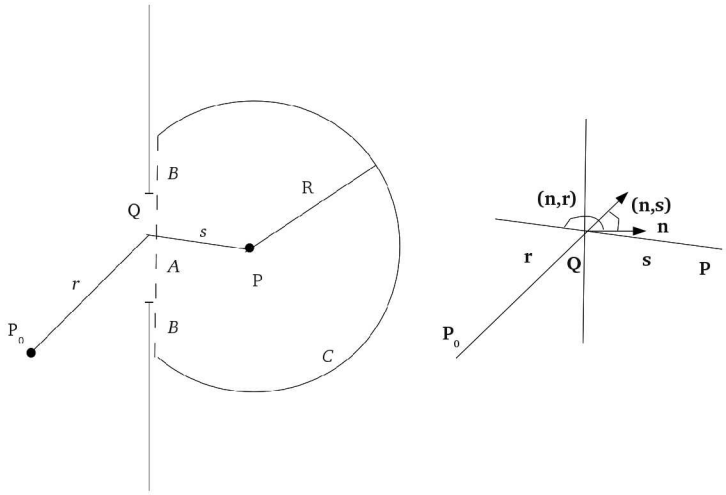

Figure A.1: Illustration of the Fresnel-Kirchhoff diffraction integral (geometry of a single slit) using boundary values problem proposed by Kirchhoff.

In Eq. A.2 (n,r) and (n,s) are the angles between the normal **n** to the screen and the directions **r** and **s**, respectively (c.f. Fig. A.1, right) and A_0 is a constant. Equation A.2 has known as the Fresnel-Kirchhoff diffraction formula. The contribution from C may be neglected in the limit of $R \to \infty$. In reference [Marchand and Wolf, 1966], the superposition of secondary waves has been treated using different boundary conditions that the one proposed by Kirchhoff, avoiding in the specific the use of the screen C and the boundary values problem on B. One considers any point Q of an aperture A having generic coordinates (ξ, η). Let be r and s the distance of P_0 and P, respectively, from this point in the aperture. If P_0 and P are far enough, r and s can be replaced by r' and s' (Fig.A.2) and the contribution of $\{\cos(n,r) - \cos(n,s)\}$ can be neglected. Therefore, Equation A.2

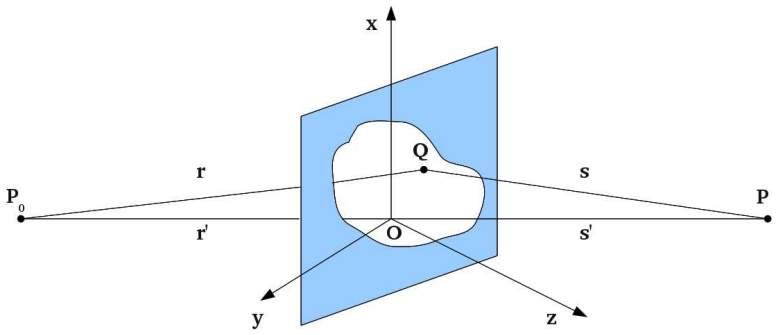

Figure A.2: Schematics of the Huygens-Fresnel principle using the boundary conditions in [Marchand and Wolf, 1966].

becomes [Born and Wolf, 1999]:

$$U_P = -\frac{i\cos\delta}{2\lambda}\frac{A_0 e^{ik(r'+s')}}{r's'}\int\int_A e^{ikf(\xi,\eta)}d\xi d\eta \tag{A.3}$$

where the function $f(\xi,\eta)$ is

$$\begin{aligned} f(\xi,\eta) &= (l_0-l)\xi+(m_0-m)\eta+ \\ &+\frac{1}{2}\left[\left(\frac{1}{r'}+\frac{1}{s'}\right)(\xi^2+\eta^2)-\frac{(l_0\xi+m_0\eta)^2}{r'}-\frac{(l\xi+m\eta)^2}{s'}\right]\ldots \end{aligned} \tag{A.4}$$

In the previous equation, (x,y,z) and (x_0,y_0,z_0) are the coordinates of the source and the point of observation, respectively, and (l_0,m_0) and (l,m), defined as

$$\begin{aligned} l_0 &= -\frac{x_0}{r'}, \quad m_0 = -\frac{y_0}{r'} \\ l &= \frac{x}{s'}, \qquad m = -\frac{y}{s'}, \end{aligned} \tag{A.5}$$

represent the two direction cosines $\cos(n,r)$ and $\cos(n,s)$. The determination of the interference in P is reduced to the evaluation of the integral in Eq. A.3. High-order terms in η and ξ may be neglected when $r'\to\infty$, $s'\to\infty$. These terms do not contribute to the integral if the following condition

$$\frac{1}{2}k\left[\left(\frac{1}{r'}+\frac{1}{s'}\right)(\xi^2+\eta^2)-\frac{(l_0\xi+m_0\eta)^2}{r'}-\frac{(l\xi+m\eta)^2}{s'}\right]\ll 2\pi \tag{A.6}$$

is satisfied, that corresponds to

$$|r'|\gg\frac{(\xi^2+\eta^2)_{max}}{\lambda}, \qquad |s'|\gg\frac{(\xi^2+\eta^2)_{max}}{\lambda} \tag{A.7}$$

Appendix B

New diffractometer at the undulator beamline ID01

The European synchrotron radiation facility is planning a major upgrade that will be developed in the next 5 years. The upgrade focuses on five areas of applied and fundamental research, among which we find nanoscience and nanotechnology and x-ray imaging. Within this project, the upgrade of the undulator beamline ID01 aims to offer the possibility of combining x-ray diffraction with coherent nano-beams together with various scanning probe microscopy methods. The beamline length will double from 50 m to 100 m and this will improve the transverse coherence length, as well as the the demagnification factors for focusing optics. The transverse coherence lengths, today equal to $\approx 20 \times 60$ μm^2, will reach the values of 40×120 μm^2. This new beamline will deliver a high performing instrument for nano-diffraction experiments across a wide x-ray energy range (6-30 keV). In particular coherent imaging techniques will be improved both in forward direction and in Bragg condition. X-ray scattering will continue to be combined with microscopy technique to locate nanostructures under investigation, as in-situ atomic force microscopy, already exploited today, and a scanning electron microscope that should be integrated on a second nano endstation. To this aim, two endstations will be mounted in different experimental hutches at different distances from the source.

According to the upgrade program, a (3+2 circles) diffractometer specifically designed for nano-beam diffraction will be placed in the first experimental hutch. This diffractometer has been recently commissioned and it can be already used for experiments. The schematic of the new diffractometer is shown in Fig. B.1 and the sample stage depicted in Fig. B.2. Table B.1

and B.2 summarise the specifications of the diffractometer. The main conceptual improvements of this diffractometer are the decoupling of the sample goniometer from the detector arm and placement of sample goniometer and focusing optics on the same support. The first solution avoids vibrations of the sample stage due to the heavy detector arm improvements. The use of one unique support for optics and sample suppresses mutual vibrations and/or drift. The stability obtained with this solution is surprisingly good and goes ever many tens of hours.

The decoupling of goniometer and detector and the suppression of the circle χ has as direct consequence the reduction of the sphere of confusion of the goniometer: in a rotation of $\pm 1^\circ$ the value is < 0.1 μm and in the range of a total rotation, i.e. 360°, 15 μm.

Micrometric precision translation stages under the detector table and the goniometer allow the precise alignment of these two parts. The nanopositioning of the sample is assured with an HexaPOD (Symmetrie) and a PI piezo stage (Physik Instrumente). The HexaPOD has a stroke of $\pm$ 12 mm in the horizontal plane and it has the same value for both x an y directions. A stroke of $\pm$ 5 mm is achieved in the vertical direction. The typical step size is 100 nm. The PI stage is generally used for particular applications requiring high repeatability. It provides travel ranges close to 100 μm with a very small step of only 20 nm.

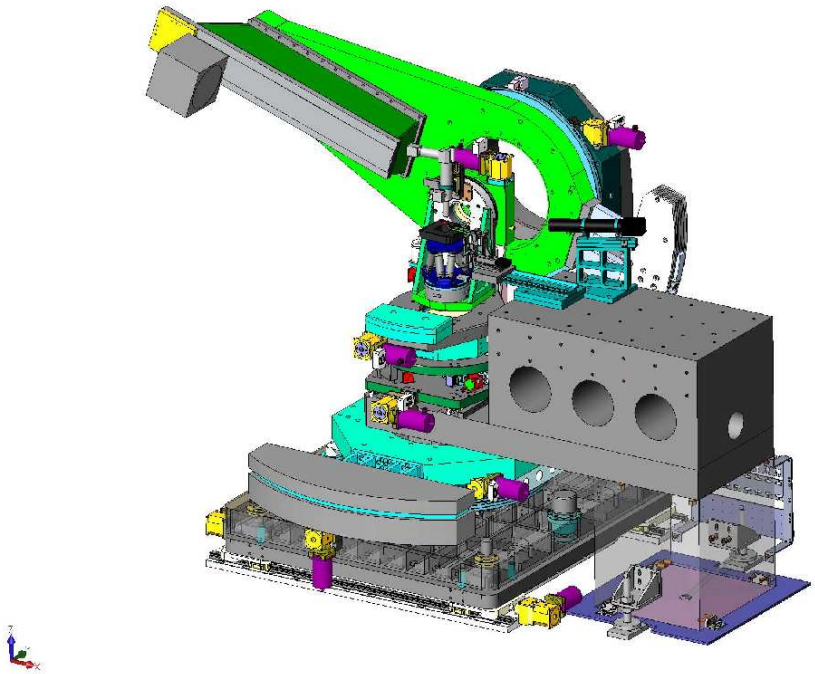

Figure B.1: Schematic view of the new diffractometer.

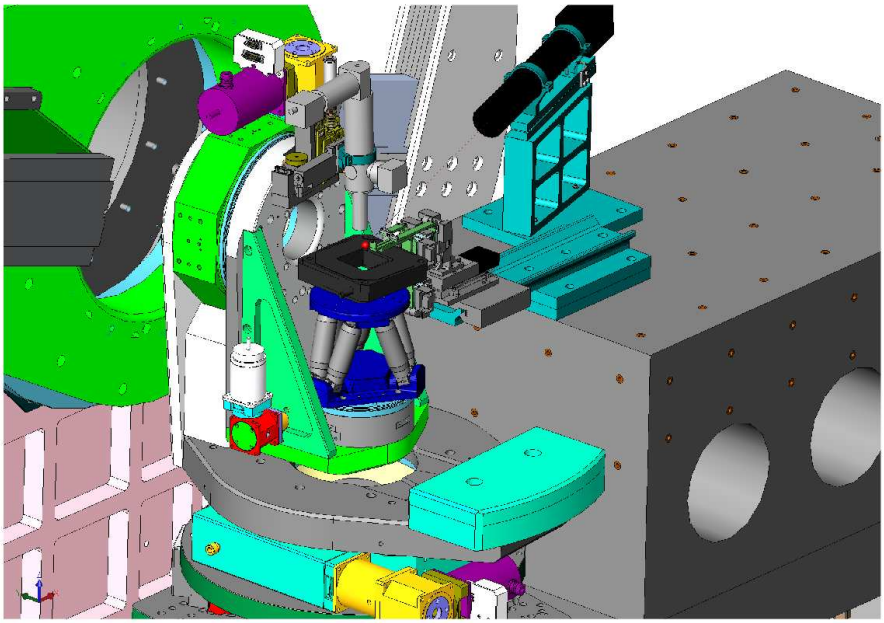

Figure B.2: Zoom view on the sample stage.

Stage	Stroke	Resolution
RSz	$\pm 100^\circ$	$< 0.001^\circ$
RSy	$+5^\circ - 95^\circ$	$< 0.001^\circ$
Ty	$+30\ -10$ mm	$< 2\ \mu$m
Tz	$+30\ -10$ mm	$< 2\ \mu$m

Table B.1: Specifications for the new diffractometer.

Stage	Stroke	Resolution
Rz	$+95^\circ\ -5^\circ$	$< 0.0002^\circ$
Ry	$+5^\circ - 120^\circ$	$< 0.0002^\circ$
Tx	± 10 mm	$0.2\ \mu$m
Ty	$+30\ -10$ mm	$0.2\ \mu$m
Tz	$+32\ -10$ mm	$0.2\ \mu$m

Table B.2: Specifications for the detector arm.

Appendix C

Orthonormalisation process for energy scan

In the following, the orthonormalisation process when the energy scan is used during experiments is detailed. The process provided to orthonormalise 3D diffraction pattern collected with an energy scan is based on the method proposed by Favre-Nicolin et al. [2000]. An integration procedure was developed in the case of dispersive anomalous diffraction (DAD), for the collection and analysis of the raw images, to yield data in the form I(h, k, l, λ) for all reflections. This procedure has been adapted to the case of a coherent diffraction experiment, assuming a low divergence of the incident beam and a non-oscillating sample. The starting equations, in the experimental conditions of relevance for this work, are defined as follows:

$$\begin{cases} x^* = \frac{1}{\lambda D}\big[-\cos\delta(X - X_0) \times \mathrm{pxl_{size}} + D\sin\delta\big] \\ y^* = \frac{1}{\lambda D}\big[\cos\nu(\sin\delta(X - X_0) \times \mathrm{pxl_{size}} + D\cos\delta) + \\ \qquad -\sin\nu(Y - Y_0) \times \mathrm{pxl_{size}}\big] - \frac{1}{\lambda} \\ z^* = \frac{1}{\lambda D}\big[\sin\nu(\sin\delta(X - X_0) \times \mathrm{pxl_{size}} + D\cos\delta) - \cos\nu(Y - Y_0) \times \mathrm{pxl_{size}}\big] \end{cases}$$

where δ, ν define positions on the detector placed at sample-detector distance D , and X_0, Y_0, the coordinate system on the detector. The pixel size is indicated by pxl_{size}. The experimental geometry is shown in Fig. C.1. This set of equations can be used to transform raw data in the reference frame (x^*, y^*, z^*) of the sample. Let impose that $\lambda = \beta/E$, where $\beta = 12398.4$ eV $\mathring{A}$. This relation can be substituted in the previous set of equations to make explicit the dependence on the energy E. The equations for x^*, y^* and z^* can be partially derived with respect to the three indepen-

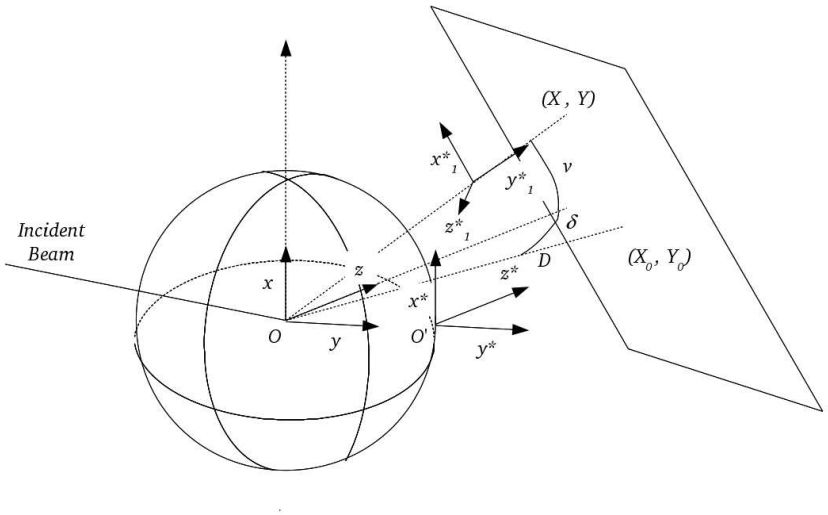

Figure C.1: Description of a monochromatic wavefield impinging on a sample, that is placed at the centre of the Ewald sphere, with all orientational parameters needed to describe the experiment: δ, ν define positions on the detector placed at the sample-detector distance D, and X_0, Y_0, the coordinate system on the detector. The pixel size is indicated by pxl_{size}

dent variables X, Y and E. The total derivatives dx^*, dy^* and dz^* can be easily obtained as:

$$\begin{cases} dx^* = -\frac{E\times \mathrm{pxl_{size}}}{D\beta}\cos\delta dX + \frac{1}{D\beta}\big[\cos\delta(X-X_0)\times \mathrm{pxl_{size}} + D\sin\delta\big] \\ dy^* = \frac{E\times \mathrm{pxl_{size}}}{D\beta}\big[\cos\nu\sin\delta dX + \sin\nu dY)\big] + \\ \qquad + \Big[\frac{\cos\nu(\sin\delta(X-X_0))+\sin\nu(Y-Y_0)\times \mathrm{pxl_{size}}}{D\beta} - \frac{1}{\beta}\Big] dE \\ dz^* = \frac{E\times \mathrm{pxl_{size}}}{D\beta}\big[\sin\nu\sin\delta dX - \cos\nu dY\big] + \\ \qquad + \frac{\sin\nu\Big(\sin\delta(X-X_0)\times \mathrm{pxl_{size}} + D\cos\delta\Big) - \cos\nu(Y-Y_0)\mathrm{pxl_{size}}}{D\beta} dE \end{cases}$$

If one considers that the 3D scattering is centred in the detector plane, i.e.

$$\begin{cases} \nu \simeq 0 \\ X = X_0 \\ Y = Y_0 \end{cases}$$

it results that:

$$\begin{cases} dx^* = -\frac{E\times \mathrm{pxl_{size}}}{D\beta}\cos\delta dX + \frac{\sin\delta}{\beta} dE \\ dy^* = -\frac{E\times \mathrm{pxl_{size}}}{D\beta}\sin\delta dX + \frac{\cos\delta}{\beta} dE \\ dz^* = \frac{E\times \mathrm{pxl_{size}}}{D\beta} dY \end{cases}$$

Considering the reference frame (x_1^*,y_1^*,z_1^*) perpendicular to the final wavevector $\mathbf{k_f}$(cf. Fig. C.1) and using the transformation matrix (rotation around the z-axis of an angle δ)

$$\begin{pmatrix} \cos\delta & -\sin\delta & 0 \\ \sin\delta & \cos\delta & 0 \\ 0 & 0 & 1 \end{pmatrix} \tag{C.1}$$

the following three relationships are obtained:

$$\begin{cases} dx_1^* = -\frac{E\times \mathrm{pxl_{size}}}{D\beta} dX + \frac{\sin\delta}{\beta} dE \\ dy_1^* = (1-\cos\delta)\frac{dE}{\beta} \\ dz_1^* = \frac{E\times \mathrm{pxl_{size}}}{D\beta} dY \end{cases}$$

These equations can be used top compensate the shift in x direction due to the detector movement and orthonormalise experimental data.

Bibliography

A. Armigliato, R. Balboni, G. P. Carnevale, G. Pavia, D. Piccolo, S. Frabboni, A. Benedetti, and A. G. Cullis. Application of convergent beam electron diffraction to two-dimensional strain mapping in silicon devices. *Applied Physics Letters*, 82 (13):2172, 2003.

D. Attwood, G. Sommargren, R. Beguiristain, K. Nguyen, J. Bokor, N. Ceglio, K. Jackson, M. Koike, and J. Underwood. Undulator radiation for at-wavelength interferometry of optics for extreme-ultraviolet lithography. *Applied Optics*, 32(34):7022–7031, December 1993.

D. T. Attwood. *Soft X Rays and Extreme Ultraviolet Radiation: Principles and Applications*. Cambridge University Press (Cambridge), 1999.

A. V. Baez. Fresnel zone plate for optical image formation using extreme ultraviolet and soft x radiation. *Journal of the Optical Society of America*, 51(4):405–412, April 1961.

H. H. Barrett and F. A. Horrigan. Fresnel zone plate imaging of gamma rays; theory. *Applied Optics*, 12(11):2686–2702, November 1973.

A. Barty, S. Marchesini, H. N. Chapman, C. Cui, M. R. Howells, D. A. Shapiro, A. M. Minor, J. C. H. Spence, U. Weierstall, J. Ilavsky, A. Noy, S. P. Hau-Riege, A. B. Artyukhin, T. Baumann, T. Willey, J. Stolken, T. van Buuren, and J. H. Kinney. Three-Dimensional coherent X-Ray diffraction imaging of a ceramic nanofoam: Determination of structural deformation mechanisms. *Physical Review Letters*, 101(5): 055501, 2008.

J. K. Bates, M. G. Seitz, and M. J. Steindler. The relevance of vapor phase hydration aging to nuclear waste isolation. *Nuclear and Chemical Waste Management*, 5(1): 63–73, 1984.

S. Baudot, F. Andrieu, F. Rieutord, and J. Eymery. Elastic relaxation in patterned and implanted strained silicon on insulator. *Journal of Applied Physics*, 105(11):114302, 2009.

J. B. Baxter and C. A. Schmuttenmaer. Conductivity of ZnO nanowires, nanoparticles, and thin films using Time-Resolved terahertz spectroscopy. *The Journal of Physical Chemistry B*, 110(50):25229–25239, December 2006.

A. Béché, J. L. Rouviére, L. Clément, and J. M. Hartmann. Improved precision in strain measurement using nanobeam electron diffraction. *Applied Physics Letters*, 95(12): 123114, 2009.

T. Beetz, M.R. Howells, C. Jacobsen, C.-C. Kao, J. Kirz, E. Lima, T.O. Mentes, H. Miao, C. Sanchez-Hanke, D. Sayre, and D. Shapiro. Apparatus for xray diffraction microscopy and tomography of cryo specimens. *Nuclear Instruments and Methods in Physics Research Section A: Accelerators, Spectrometers, Detectors and Associated Equipment*, 545(1-2):459–468, 2005.

L. Beitra, M. Watari, T. Matsuura, N. Shimamoto, R. Harder, and I. Robinson. Confocal microscope alignment of nanocrystals for coherent diffraction imaging. *AIP Conference Proceedings*, 1234(1):57–60, 2010.

J. E. Bernard and A. Zunger. Is there an elastic anomaly for (001) monolayer of InAs embedded in GaAs? *Applied Physics Letters*, 65:165–167, July 1994.

K. P. Beuermann, H. Bruninger, and J. Trmper. Aberrations of a facet-type transmission grating for cosmic x-ray and XUV spectroscopy. *Applied Optics*, 17(15):2304–2309, 1978.

T. D. Beynon, I. Kirk, and T. R. Mathews. Gabor zone plate with binary transmittance values. *Optics Letters*, 17(7):544–546, April 1992.

A. Biermanns, A. Davydok, H. Paetzelt, A. Diaz, V. Gottschalch, T. H. Metzger, and U. Pietsch. Individual GaAs nanorods imaged by coherent x-ray diffraction. *Journal of Synchrotron Radiation*, 16(6):796–802, 2009.

G. Binnig, C. F. Quate, and Ch. Gerber. Atomic force microscope. *Physical Review Letters*, 56(9):930–933, Mar 1986.

M. Borg, M. Messing, P. Caroff, K. Dick Thelander, K. Deppert, and L.-E. Wernersson. Movpe growth and structural characterization of extremely lattice-mismatched inp-insb nanowire heter... *2009 IEEE 21st International Conference On Indium Phosphide & Related Materials (IPRM)*, s. 249-252, 2009.

M. Born and E. Wolf. *Principles of Optics*. Cambridge university Press (Cambridge), 1999. 7th expanded edition.

S. Bowyer, R. Kimble, F. Paresce, M. Lampton, and G. Penegor. Continuous-readout extreme-ultraviolet airglow spectrometer. *Applied Optics*, 20(3):477–486, February 1981.

W. S. Boyle and G. E. Smith. Charge coupled semiconductor devices. *Bell Syst. Tech. J*, 49, 2010.

O. Brandt, K. Ploog, R. Bierwolf, and M. Hohenstein. Breakdown of continuum elasticity theory in the limit of monatomic films. *Physical Review Letters*, 68(9):1339–1342, 1992.

Y. M. Bruck and L. G. Sodin. On the ambiguity of the image reconstruction problem. *Optics Communications*, 30(3):304–308, September 1979.

O. Bunk, A. Diaz, F. Pfeiffer, C. David, B. Schmitt, D. K. Satapathy, and J. Friso van der Veen. Diffractive imaging for periodic samples: retrieving one-dimensional concentration profiles across microfluidic channels. *Acta Crystallographica Section A Foundations of Crystallography*, 63(4):306–314, 2007.

D. Camacho. *Modeling of the structural, electronic and optical properties of GaN/AlN nitride nanowires*. PhD thesis, 2010.

P. Caroff, K. Dick A., J. Johansson, M. E. Messing, K. Deppert, and L. Samuelson. Controlled polytypic and twin-plane superlattices in iii-v nanowires. *Nat Nano*, 4(1): 50–55, January 2009.

P. Caroff, M. E; Messing, B. M. Borg, K. A. Dick, K. Deppert, and L.-E. Wernersson. InSb heterostructure nanowires: MOVPE growth under extreme lattice mismatch. *Nanotechnology*, 20(49):495606, 2009. ISSN 0957-4484.

V. Chamard, J. Stangl, S. Labat, B. Mandl, R. T. Lechner, and T. H. Metzger. Evidence of stacking-fault distribution along an InAs nanowire using micro-focused coherent x-ray diffraction. *Journal of Applied Crystallography*, 41(2):272–280, 2008.

V. Chamard, A. Diaz, J. Stangl, and S. Labat. Structural investigation of InAs nanowires with coherent x-rays. *The Journal of Strain Analysis for Engineering Design*, 44(7): 533–542, 2009.

V. Chamard, J. Stangl, G. Carbone, A. Diaz, G. Chen, C. Alfonso, C. Mocuta, , and T. H. Metzger. Three-Dimensional X-Ray fourier transform holography: The bragg case. *Physical Review Letters*, 104(16), 2010.

W. Chao, B. D. Harteneck, J. Alexander Liddle, E. H. Anderson, and D. T. Attwood. Soft x-ray microscopy at a spatial resolution better than 15[thinsp]nm. *Nature*, 435 (7046):1210–1213, 2005.

H. N. Chapman, A. Barty, M. J. Bogan, S. Boutet, M. Frank, S. P. Hau-Riege, S. Marchesini, B. W. Woods, S. Bajt, W. H. Benner, R. A. London, E. Plonjes, M. Kuhlmann, R. Treusch, S. Dusterer, T. Tschentscher, J. R. Schneider, E. Spiller, T. Moller, C. Bostedt, M. Hoener, D. A. Shapiro, K. O. Hodgson, D. van der Spoel, F. Burmeister, M. Bergh, C. Caleman, G. Huldt, M. M. Seibert, F. R. N. C. Maia, R. W. Lee, A. Szoke, N. Timneanu, and J. Hajdu. Femtosecond diffractive imaging with a soft-X-ray free-electron laser. *Nature Physics*, 2(12):839–843, December 2006a.

H. N. Chapman, A. Barty, S. Marchesini, A. Noy, S. P. Hau-Riege, C. Cui, M. R. Howells, R. Rosen, H. He, J. C. H. Spence, U. Weierstall, T. Beetz, C. Jacobsen, and D. Shapiro. High-resolution ab initio three-dimensional x-ray diffraction microscopy. *Journal of the Optical Society of America A*, 23(5):1179–1200, May 2006b.

J. Claudon, J. Bleuse, N. Singh Malik, M. Bazin, P. Jaffrennou, N. Gregersen, C. Sauvan, P. Lalanne, and J.-M. Gérard. A highly efficient single-photon source based on a quantum dot in a photonic nanowire. *Nature Photonics*, 4(3):174–177, 2010.

T. W. Cornelius, D. Carbone, V. L. R. Jacques, T. U. Schülli, and T. H. Metzger. Three-dimensional diffraction mapping by tuning the X-ray energy. *Journal of Synchrotron Radiation*, 18(3):413–417, May 2011.

Y. Cui, Q. Wei, H. Park, and C. M. Lieber. Nanowire nanosensors for highly sensitive and selective detection of biological and chemical species. *Science*, 293(5533):1289 –1292, 2001.

C. David, B. Noehammer, E. Ziegler, and O. Hignette. Tunable diffractive optical elements for hard x-rays. In *Proceedings of SPIE*, pages 96–104, San Diego, CA, USA, 2001.

C. David, B. Nöhammer, and E. Ziegler. Wet etching of linear fresnel zone plates for hard x-rays. *Microelectronic Engineering*, 61-62:987–992, 2002.

L. De Caro and L. Tapfer. Elastic lattice deformation of semiconductor heterostructures grown on arbitrarily oriented substrate surfaces. *Phys. Rev. B*, 48(4):2298–2303, Jul 1993.

L. De Caro and L. Tapfer. Elastic lattice deformation in quantum-wire heterostructures. *Physical Review B*, 49(16):11127–11133, Apr 1994.

L. De Caro, E. Carlino, G. Caputo, P. D. Cozzoli, and C. Giannini. Electron diffractive imaging of oxygen atoms in nanocrystals at sub-angström resolution. *Nature Nanotechnology*, 5(5):360–365, 2010.

I. De Wolf, V. Senez, R. Balboni, A. Armigliato, S. Frabboni, A. Cedola, and S. Lagomarsino. Techniques for mechanical strain analysis in sub-micrometer structures: Tem/cbed, micro-raman spectroscopy, x-ray micro-diffraction and modeling. *Microelectronic Engineering*, 70(2-4):425 – 435, 2003.

E. Di Fabrizio, F. Romanato, M. Gentili, S Cabrini, B. Kaulich, J. Susini, and R. Barrett. High-efficiency multilevel zone plates for keV x-rays. *Nature*, 401(6756):895–898, October 1999.

A. Diaz, C. Mocuta, J. Stangl, B. Mandl, C. David, J. Vila-Comamala, V. Chamard, T. H. Metzger, and G. Bauer. Coherent diffraction imaging of a single epitaxial InAs nanowire using a focused x-ray beam. *Physical Review B*, 79(12):125324, March 2009.

A. Diaz, C. Mocuta, J. Stangl, M. Keplinger, T. Weitkamp, F Pfeiffer, C. David, T. H. Metzger, and G. Bauer. Coherence and wavefront characterization of Si-111 monochromators using double-grating interferometry. *Journal of Synchrotron Radiation*, 17(3): 299–307, May 2010.

M. Dierolf. *Development of a Lensless Microscopy Technique for Imaging Cellular Structures*. PhD thesis, 2007.

V. Elser. Phase retrieval by iterated projections. *Journal of the Optical Society of America A*, 20(1):40–55, January 2003.

Elsevier. *Stress and strain in epitaxy: theoretical concepts, measurements and application.* Elsevier (Netherlands), 1920.

E. Ertekin, P. A. Greaney, D. C. Chrzan, and T. D. Sands. Equilibrium limits of coherency in strained nanowire heterostructures. *Journal of Applied Physics*, 97(11): 114325, 2005.

J. Eymery, F. Rieutord, V. Favre-Nicolin, O. Robach, Y.-M. Niquet, L. Fröberg, T. Martensson, and L. Samuelson. Strain and shape of epitaxial inas/inp nanowire superlattice measured by grazing incidence x-ray techniques. *Nano Letters*, 7(9):2596–2601, 2007.

V. Favre-Nicolin, S. Bos, J. E. Lorenzo, P. Bordet, W. Shepard, and J.-L. Hodeau. Integration procedure for the quantitative analysis of dispersive anomalous diffraction. *Journal of Applied Crystallography*, 33(1):52–63, Feb 2000.

V. Favre-Nicolin, J. Eymery, R. Koester, and P. Gentile. Coherent-diffraction imaging of single nanowires of diameter 95 nanometers. *Physical Review B*, 79(19):195401, May 2009.

V. Favre-Nicolin, F. Mastropietro, J. Eymery, D. Camacho, Y. M. Niquet, B. M. Borg, M. E. Messing, L.-E. Wernersson, R. E. Algra, E. P. A. M. Bakkers, T. H. Metzger, R. Harder, and I. K. Robinson. Analysis of strain and stacking faults in single nanowires using bragg coherent diffraction imaging. *New Journal of Physics*, 12(3): 035013, 2010.

J. R. Fienup. Reconstruction of an object from the modulus of its fourier transform. *Optics Letters*, 3(1):27–29, 1978.

J. R. Fienup. Phase retrieval algorithms: a comparison. *Applied Optics*, 21(15):2758–2769, 1982.

J. R. Fienup. Phase retrieval using boundary conditions. *Journal of the Optical Society of America A*, 3(2):284–288, February 1986.

J. R. Fienup. Reconstruction of a complex-valued object from the modulus of its fourier transform using a support constraint. *Journal of the Optical Society of America A*, 4 (1):118, 1987.

M. V. Fischetti, F. Gamiz, and W. Hansch. On the enhanced electron mobility in strained-silicon inversion layers. *Journal of Applied Physics*, 92(12):7320, 2002.

M. Gailhanou, A. Loubens, J.-S. Micha, B. Charlet, A. A. Minkevich, R. Fortunier, and O. Thomas. Strain field in silicon on insulator lines using high resolution x-ray diffraction. *Applied Physics Letters*, 90(11):111914, 2007.

J. E. Garrett and J. C. Wiltse. Fresnel zone plate antennas at millimeter wavelengths. *International Journal of Infrared and Millimeter Waves*, 12:195–220, 1991. 10.1007/BF01010296.

R. W. Gerchberg and W. O. Saxton. A practical algorithm for the determination of the phase from image and diffraction plane pictures. *Optik*, 35(237), 1972.

B. Ghyselen, J. M. Hartmann, T. Ernst, C. Aulnette, B. Osternaud, Y. Bogumilowicz, A. Abbadie, P. Besson, O. Rayssac, A. Tiberj, N. Daval, I. Cayrefourq, F. Fournel, H. Moriceau, C. Di Nardo, F. Andrieu, V. Paillard, M. Cabié, L. Vincent, E. Snoeck, F. Cristiano, A. Rocher, A. Ponchet, A. Claverie, P. Boucaud, M. N. Semeria, D. Bensahel, N. Kernevez, and C. Mazure. Engineering strained silicon on insulator wafers with the smart cuttm technology. *Solid-State Electronics*, 48(8):1285 – 1296, 2004. Strained-Si Heterostructures and Devices.

C. Giannini, L. Tapfer, S. Lagomarsino, J. C. Boulliard, A. Taccoenand B. Capelle, M. Ilg, O. Brandt, and K. H. Ploog. X-ray standing wave and high-resolution x-ray diffraction study of the GaAs/InAs/GaAs(100) heterointerface. *Phys. Rev. B*, 48: 11496–11499, Oct 1993.

P. Godard, D. Carbone, M. Allain, F. Mastropietro, G. Chen, A. Diaz, T. H. Metzger, J. Stangl, and V. Chamard. Three-dimensional high-resolution quantitative microscopy of extended crystals. *Nature Communications*, 2(568), 2011.

J. W. Goodman. *Introduction to Fourier optics*. Roberts and Company Publishers, 2005.

S. Gorelick, J. Vila-Comamala, V. A. Guzenko, R. Barrett, M. Salomé, and C. David. High-efficiency fresnel zone plates for hard x-rays by 100keV e-beam lithography and electroplating. *Journal of Synchrotron Radiation*, 18(3), 2011.

M. Guizar-Sicairos and J. R. Fienup. Measurement of coherent x-ray focusedbeams by phase retrieval with transversetranslation diversity. *Optics Express*, 17(4):2670–2685, February 2009.

Y. J. Guo, I. H. Sassi, and S. K. Barton. Multilayer offset fresnel zone plate reflector. *IEEE Microwave and Guided Wave Letters*, 4(6), 1994.

H. Gursky and T. Zehnpfennig. An image-forming slitless spectrometer for soft x-ray astronomy. *Applied Optics*, 5(5), May 1966.

J. V. Feitzinger H. H. Fink D. H. Hohn H. Koops G. Kramer U. Mayer G. Mollenstedt H. Bruninger, H. J. Einighammer and M. Mozer. Euv and soft x-ray images of the sun. *Solar Physics*, 20(81), 1971.

O. Hayden, R. Agarwal, and W. Lu. Semiconductor nanowire devices. *Nano Today*, 3 (5-6):12 – 22, 2008.

R. F. S. Hearmon. The elastic constants of anisotropic materials. *Reviews of Modern Physics*, 18(3):409–440, Jul 1946.

W. B. Herrmannsfeldt, M. J. Lee, J. J. Spranza, and K. R. Trigger. Precision alignment using a system of large rectangular fresnel lenses. *Applied Optics*, 7(6):995–1005, 1968.

M. C. Hettrick, S. Bowyer, R. F. Malina, C. Martin, and S. Mrowka. Extreme ultraviolet explorer spectrometer. *Applied Optics*, 24(12):1737–1756, 1985.

M. H. Horman. Efficiences of zone plates and phase zone plates. *Applied Optics*, 6(11): 2011–2013, November 1967.

M. Howells and J. Hastings. Design considerations for an x-ray microprobe. *Nuclear Instruments and Methods in Physics Research*, 208(1-3):379–386, 1983.

H. D. Hristov and M. H. A. J. Herben. Millimeterwave fresnel zone plate lens and antenna. *IEEE Transaction on microwaves theory and techniques*, 42(12), 1995.

W. J. Huang, R. Sun, J. Tao, L. D. Menard, R. G. Nuzzo, and J. M. Zuo. Coordination-dependent surface atomic contraction in nanocrystals revealed by coherent diffraction. *Nature Materials*, 7(4):308–313, April 2008.

F. Hüe, M. Hÿtch, H. Bender, F. Houdellier, and A. Claverie. Direct mapping of strain in a strained silicon transistor by high-resolution electron microscopy. *Physical Review Letters*, 100(15):156602, Apr 2008.

C. Huygens. *Traitéde la lumière*. Gauthier-Villars (Paris), 1920.

M. Hytch, F. Houdellier, F. Hue, and E. Snoeck. Nanoscale holographic interferometry for strain measurements in electronic devices. *Nature*, 453(7198):1086–1089, 2008.

C. Jacobsen, J. Kirz, and S. Williams. Resolution in soft x-ray microscopy. *Ultramicroscopy*, 47:55–79, 1992.

V. Jacques. Application de la diffraction cohérente des rayons x à l'étude de défauts topologiques dans les structures atomiques et électroniques, December 2009. (PhD thesis).

S. C. Jain and W. Hayes. Structure, properties and applications of Ge_xSi_{1-x} strained layers and superlattices. *Semiconductor Science and Technology*, 6(7):547–576, 1991.

K. Jefimovs, O. Bunk, F. Pfeiffer, D. Grolimund, J.F. van der Veen, and C. David. Fabrication of fresnel zone plates for hard x-rays. *Microelectronic Engineering*, 84 (5-8), May 2007.

S. O. Kastner and Jr. Wade. Aspheric grating for extreme ultraviolet astronomy. *Applied Optics*, 17(8):1252–1258, April 1978.

U. Kaufmann, M. Kunzer, K. Köhler, H. Obloh, W. Pletschen, P. Schlotter, R. Schmidt, J. Wagner, A. Ellens, W. Rossner, and M.Kobusch. Ultraviolet pumped tricolor phosphor blend white emitting leds. *physica status solidi (a)*, 188(1):143–146, 2001.

P. N. Keating. Effect of invariance requirements on the elastic strain energy of crystals with application to the diamond structure. *Phys. Rev.*, 145(2):637–645, May 1966.

P. N. Keating, R. K. Mueller, and T. Savatari. Fresnel-Zone-Plate spectrometer with central stop. *Journal of the Optical Society of America*, 62(8):945–948, 1972.

C. M. Kewish, P. Thibault, O. Bunk, and F. Pfeiffer. The potential for two-dimensional crystallography of membrane proteins at future x-ray free-electron laser sources. *New Journal of Physics*, 12(3):035005, 2010a.

C. M. Kewish, P. Thibault, M. Dierolf, O. Bunk, A. Menzel, J. Vila-Comamala, K. Jefimovs, and F. Pfeiffer. Ptychographic characterization of the wavefield in the focus of reflective hard x-ray optics. *Ultramicroscopy*, 110(4):325–329, March 2010b.

P. Kirkpatrick and A. V. Baez. Formation of optical images by X-Rays. *Journal of the Optical Society of America*, 38(9):766–773, 1948.

J. Kirz. Phase zone plates for x rays and the extreme uv. *Journal of the Optical Society of America*, 64(3):301–309, March 1974.

J. Kirz, C. Jacobsen, and M. Howells. Soft X-Ray microscopes and their biological applications. *Quarterly Reviews of Biophysics*, 28(01):33–130, 1995.

Y. V. Kopylov, A. V. Popov, and A. V. Vinogradov. Application of the parabolic wave equation to x-ray diffraction optics. *Optics Communications*, 118(5-6):619 – 636, 1995.

S. Labat, V. Chamard, and O. Thomas. Local strain in a 3D nano-crystal revealed by 2D coherent x-ray diffraction imaging. *Thin Solid Films*, 515(14):5557–5562, May 2007.

M. Lahiri and E. Wolf. Quantum theory of optical coherence of nonstationary light in the space-frequency domain. *Physical Review A*, 82(4):043837, October 2010.

L. D. Landau, E. M. Lifshitz, A. Markovich Kosevich, and L. Petrovich Pitaevski. *Theory of elasticity*. Elsevier, 1986. ISBN 9780750626330.

T. A. Langdo, M. T. Currie, Z. Y. Cheng, J. G. Fiorenza, M. Erdtmann, G. Braithwaite, C. W. Leitz, C. J. Vineis, J. A. Carlin, A. Lochtefeld, M. T. Bulsara, I. Lauer, D. A. Antoniadis, and M. Somerville. Strained si on insulator technology: from materials to devices. *Solid-State Electronics*, 48(8):1357 – 1367, 2004. Strained-Si Heterostructures and Devices.

D. Le Bolloc'h, F. Livet, F. Bley, T. Schulli, M. Veron, and T. H. Metzger. X-ray diffraction from rectangular slits. *Journal of Synchrotron Radiation*, 9(4):258–265, 2002.

S. J. Leake. *Coherent x-ray diffraction imaging of zinc oxide crystals*. PhD thesis, 2010.

S. J. Leake, M. C. Newton, R. Harder, and I. K. Robinson. Longitudinal coherence function in x-ray imaging of crystals. *Optics Express*, 17(18):15853–15859, 2009.

T.-L. Lee, Y. Qian, P.F. Lyman, J.C. Woicik, J.G. Pellegrino, and M.J. Bedzyk. The use of x-ray standing waves and evanescent-wave emission to study buried strained-layer heterostructures. *Physica B: Condensed Matter*, 221(1-4):437–444, April 1996.

P.-A. Lemieux and D. J. Durian. Investigating non-Gaussian scattering processes by using nth-order intensity correlation functions. *Journal of the Optical Society of America A*, 16(7):1651–1664, 1999.

Yat Li, Fang Qian, Jie Xiang, and C. M. Lieber. Nanowire electronic and optoelectronic devices. *Materials Today*, 9(10):18 – 27, 2006.

F. Livet. Diffraction with a coherent x-ray beam: dynamics and imaging. *Acta Crystallographica Section A Foundations of Crystallography*, 63(2):87–107, 2007.

J. G. Lu, P. Chang, and Z. Fan. Quasi-one-dimensional metal oxide materials–synthesis, properties and applications. *Materials Science and Engineering: R: Reports*, 52(1-3): 49 – 91, 2006.

A. Malachias. *X-ray Study of Strain, Composition, Elastic energy and Atomic ordering in Ge islands on Si(001)*. PhD thesis, 2005.

L. Mandel and E. Wolf. *Optical coherence and quantum optics*. Cambridge University Press, September 1995.

J. Marchal and A. Wagner. Performance of pilatus detector technology for long-wavelength macromolecular crystallography. *Nuclear Instruments and Methods in Physics Research Section A: Accelerators, Spectrometers, Detectors and Associated Equipment*, In Press, 2010.

E. W. Marchand and E. Wolf. Consistent formulation of kirchhoffs diffraction theory. *Journal of the Optical Society of America*, 56(12):1712–1721, December 1966.

S. Marchesini, H. Chapman, S. Hau-Riege, R. London, A. Szoke, H. He, M. Howells, H. Padmore, R. Rosen, J. Spence, and U. Weierstall. Coherent x-ray diffractive imaging: applications and limitations. *Optics Express*, 11(19):2344–2353, 2003a.

S. Marchesini, H. He, H. N. Chapman, S. P. Hau-Riege, A. Noy, M. R. Howells, U. Weierstall, and J. C. H. Spence. X-ray image reconstruction from a diffraction pattern alone. *Physical Review B*, 68(14):140101, October 2003b.

V. A. Mashkov, Wm. R. Austin, Lin Zhang, and R. G. Leisure. Fundamental role of creation and activation in Radiation-Induced defect production in High-Purity amorphous SiO_2. *Physical Review Letters*, 76(16):2926, April 1996.

J. H. Mathews J.H. Mathews and K.K. Fink. *Numerical methods using Matlab*. Pearson Education, 2003. 4^th Edition.

A. McPherson, Y. G. Kuznetsov, A. J. Malkin, and M. Plomp. Macromolecular crystal growth investigations using atomic force microscopy. *Journal of Synchrotron Radiation*, 11(1):21–23, Jan 2004.

J. Miao and D. Sayre. On possible extensions of x-ray crystallography through diffraction-pattern oversampling. *Acta Crystallographica Section A Foundations of Crystallography*, 56(6):596–605, 2000.

J. Miao, P. Charalambous, J. Kirz, and D. Sayre. Extending the methodology of x-ray crystallography to allow imaging of micrometre-sized non-crystalline specimens. *Nature*, 400(6742):342–344, 1999.

J. Miao, K. O. Hodgson, and D. Sayre. An approach to three-dimensional structures of biomolecules by using single-molecule diffraction images. *Proceedings of the National Academy of Sciences of the United States of America*, 98(12):6641 –6645, 2001.

A. G. Michette. *Optical Syctems for Soft X-rays*. Plenum (New York), 1968.

Hidekazu Mimura, Soichiro Handa, Takashi Kimura, Hirokatsu Yumoto, Daisuke Yamakawa, Hikaru Yokoyama, Satoshi Matsuyama, Kouji Inagaki, Kazuya Yamamura, Yasuhisa Sano, Kenji Tamasaku, Yoshinori Nishino, Makina Yabashi, Tetsuya Ishikawa, and Kazuto Yamauchi. Breaking the 10nm barrier in hard-X-ray focusing. *Nature Physics*, 6(2):122–125, 2009.

A. A. Minkevich, M. Gailhanou, J.-S. Micha, B. Charlet, V. Chamard, and O. Thomas. Inversion of the diffraction pattern from an inhomogeneously strained crystal using an iterative algorithm. *Physical Review B*, 76(10):104106, 2007.

A. A. Minkevich, T. Baumbach, M. Gailhanou, and O. Thomas. Applicability of an iterative inversion algorithm to the diffraction patterns from inhomogeneously strained crystals. *Physical Review B*, 78(17):174110, Nov 2008.

A. A Minkevich, E. Fohtung, T. Slobodskyy, M. Riotte, D. Grigoriev, M. Schmidbauer, A. C Irvine, V. Novak, V. Holy, and T. Baumbach. Selective coherent x-ray diffractive imaging of displacement fields in (Ga,Mn)As/GaAs periodical wires. *Physical Review B*, 84:054113, 2011.

C. Mocuta, J. Stangl, K. Mundboth, T. H. Metzger, G. Bauer, I. A. Vartanyants, M. Schmidbauer, and T. Boeck. Beyond the ensemble average: X-ray microdiffraction analysis of single SiGe islands. *Physical Review B*, 77(24):245425, 2008.

S. Mokkapati and C. Jagadish. III-V compound SC for optoelectronic devices. *Materials Today*, 12(4):22 – 32, 2009.

F. Montiel and M. Nevi'ere. Electromagnetic theory of braggfresnel linear zone plates. *Optical Society of America A*, 12(12), 1995.

V. J. Morris, A. R. Kirby, and A. P. Gunning. Using atomic force microscopy to probe food biopolymer functionality. *Scanning*, 21(5):287–292, 1999.

O. Moutanabbir, M. Reiche, A. Hähnel, W. Erfurth, U. Gösele, M. Motohashi, A. Tarun, N. Hayazawa, and S. Kawata. Nanoscale patterning induced strain redistribution in ultrathin strained Si layers on oxide. *Nanotechnology*, 21(13):134013, 2010.

O. Moutanabbir, M. Reiche, F. Naumann N. Zakharov, and M. Petzold. Observation of free surface-induced bending upon nanopatterning of ultrathin strained silicon layer. *Nanotechnology*, 22:045701, 2011.

B. M. New. Design, production and performance of circular fresnel zone plates. *Applied Optics*, 10(3):498–503, March 1971.

M. C. Newton, Steven J. L., R. Harder, and I. K. Robinson. Three-dimensional imaging of strain in a single ZnO nanorod. *Nat Mater*, 9(2):120–124, February 2010.

Y. Niquet. Electronic and optical properties of InAsGaAs nanowire superlattices. *Physical Review B*, 74(15), 2006.

K. A. Nugent. Coherent methods in the x-ray sciences. *Advances in Physics*, 59(1):1, 2010.

K. A. Nugent, A. G. Peele, H. N. Chapman, and A. P. Mancuso. Unique phase recovery for nonperiodic objects. *Phys. Rev. Lett.*, 91(20):203902, Nov 2003.

K. A. Nugent, A. G. Peele, H. M. Quiney, and H. N. Chapman. Diffraction with wavefront curvature: a path to unique phase recovery. *Acta Crystallographica Section A*, 61(3): 373–381, May 2005.

D. Carbone O. Plantevin. Versatile vacuum chamber for in situ surface x-ray scattering studies. *Journal of synchrotron radiation*, 15(Pt 4):414–9, 2008.

W. D. Oliver, J. Kim, R. C. Liu, and Y. Yamamoto. Hanbury brown and Twiss-Type experiment with electrons. *Science*, 284(5412):299 –301, April 1999.

Gábor Oszlányi and András Süto. *Ab initio* structure solution by charge flipping. *Acta Crystallographica Section A*, 60(2):134–141, Mar 2004.

M. Ouyang, J.-L. Huang, and C. M. Lieber. Fundamental electronic properties and applications of single-walled carbon nanotubes. *Accounts of Chemical Research*, 35 (12):1018–1025, 2002.

D.d M. Paganin. *coherent x-ray optics*. Oxford University Press, 2006.

A. Papoulis. Ambiguity function in fourier optics. *J. Opt. Soc. Am.*, 64(6):779–788, Jun 1974.

P. Pauzauskie and P. Yang. Nanowire photonics. *Materials Today*, 9(10):36–45, 2006.

A. Peled. *Photo-Exited Process, Diagnostic and Applications*. Kluwer Academic Publisher (Boston), 2003.

C. D. Pfeifer, L. D. Ferris, and W. M. Yen. Optical image formation with a fresnel zone plate using vacuum-ultraviolet radiation. *Journal of the Optical Society of America*, 63(1):91–95, January 1973.

M. A. Pfeifer, G. J. Williams, I. A. Vartanyants, R. Harder, and I. K. Robinson. Three-dimensional mapping of a deformation field inside a nanocrystal. *Nature*, 442(7098): 63–66, 2006.

F. Pfeiffer, C. David, J. F. van der Veen, and C. Bergemann. Nanometer focusing properties of fresnel zone plates described by dynamical diffraction theory. *Physical Review B*, 73(24):245331, 2006a.

F. Pfeiffer, T. Weitkamp, O. Bunk, and C. David. Phase retrieval and differential phase-contrast imaging with low-brilliance x-ray sources. *Nature Physics*, 2(4):258–261, April 2006b.

S. M. Polvino, C. E. Murray, Ö. Kalenci, I. C. Noyan, B. Lai, and Z. Cai. Synchrotron microbeam x-ray radiation damage in semiconductor layers. *Applied Physics Letters*, 92(22):224105, 2008.

C. Ponchut, J. M. Rigal, J. Clément, E. Papillon, A. Homs, and S. Petitdemange. Maxipix, a fast readout photon-counting x-ray area detector for synchrotron applications. *Journal of Instrumentation*, 6(01):C01069, 2011.

H. M. Quiney, K. A. Nugent, and A. G. Peele. Iterative image reconstruction algorithms using wave-front intensity and phase variation. *Optics Letters*, 30(13), 2005.

H. M. Quiney, A. G. Peele, Z. Cai, D. Paterson, and K. A. Nugent. Diffractive imaging of highly focused x-ray fields. *Nat Phys*, 2(2):101–104, February 2006.

H. M. Quiney, G. J. Williams, and K. A. Nugent. Non-iterative solution of the phase retrieval problem using a single diffraction measurement. *Optics Express*, 16(10):6896, 2008.

R. B. G. Ravelli and S. M. McSweeney. The fingerprint that x-rays can leave on structures. *Structure*, 8:315–328, 2000.

G. Renaud, R. Lazzari, and F. Leroy. Probing surface and interface morphology with grazing incidence small angle x-ray scattering. *Surface Science Reports*, 64(8):255 – 380, 2009.

I. Robinson and R. Harder. Coherent x-ray diffraction imaging of strain at the nanoscale. *Nature Materials*, 8(4):291–298, April 2009.

I. K. Robinson, I. A. Vartanyants, G. J. Williams, M. A. Pfeifer, and J. A. Pitney. Reconstruction of the shapes of gold nanocrystals using coherent X-Ray diffraction. *Physical Review Letters*, 87(19):195505, October 2001.

A. Sakdinawat and D. Attwood. Nanoscale x-ray imaging. *Nature Photonics*, 4(12): 840–848, December 2010.

L. Samuelson. Self-forming nanoscale devices. *Materials Today*, 6(10):22 – 31, 2003.

L. Samuelson. Semiconductor nanowires for 0D and 1D physics and applications. *Physica E: Low-dimensional Systems and Nanostructures*, 25(2-3):313–318, 2004.

D. Sander, R. Skomski, A. Enders, C. Schmidthals, D. Reuter, and J. Kirschner. The correlation between mechanical stress and magnetic properties of ultrathin films. *Journal of Physics D: Applied Physics*, 31(6):663, 1998.

D. Sayre. The squaring method: a new method for phase determination. *Acta Crystallographica*, 5(1):60–65, January 1952.

D. Sayre, H. N. Chapman, and J. Miao. On the extendibility of x-ray crystallography to noncrystals. *Acta Crystallographica Section A Foundations of Crystallography*, 54(2): 232–239, 1998.

T. Scheler, M. Rodrigues, T. W. Cornelius, C. Mocuta, A. Malachias, R. Magalhaes-Paniago, F. Comin, J. Chevrier, and T. H. Metzger. Probing the elastic properties of individual nanostructures by combining in situ atomic force microscopy and micro-x-ray diffraction. *Applied Physics Letters*, 94(2):023109, 2009.

O. G. Schmidt. *Lateral alignment of etitaxial quantum dots.* Springer (Berlin), 2007.

C. G. Schroer, P. Boye, J. M. Feldkamp, J. Patommel, A. Schropp, A. Schwab, S. Stephan, M. Burghammer, S. Schöder, and C. Riekel. Coherent xray diffraction imaging with nanofocused illumination. *Phys. Rev. Lett.*, 101(9):090801, Aug 2008.

C. E. Shannon. Communication in the presence of noise. *PROCEEDINGS OF THE IEEE,*, 86(2):447–457, 1998.

D. Shapiro, P. Thibault, T. Beetz, V. Elser, M. Howells, C. Jacobsen, J. Kirz, E. Lima, H. Miao, A. M. Neiman, and D. Sayre. Biological imaging by soft x-ray diffraction microscopy. *Proceedings of the National Academy of Sciences of the United States of America*, 102(43):15343 –15346, October 2005.

M. J. Simpson and A. G. Michette. Imaging properties of modified fresnel zone plates. *Optica Acta: International Journal of Optics*, 31(4):403, 1984.

R. A. Smith. *Semiconductors.* London, 1979.

A. Snigirev, V. Kohn, I. Snigireva, A. Souvorov, and B. Lengeler. Focusing High-Energy x rays by compound refractive lenses. *Applied Optics*, 37(4):653–662, February 1998.

L.-M. Stadler, R. Harder, I. K. Robinson, C. Rentenberger, H.-P. Karnthaler, B. Sepiol, and G. Vogl. Coherent x-ray diffraction imaging of grown-in antiphase boundaries in Fe_65Al_35. *Physical Review B*, 76(1):014204, 2007.

A. G. Stein. Focusing optics for soft and hard x-rays: Fabrication, replication and simulation, 2002. PhD thesis.

M. A. Stevens-Kalceff. Electron-Irradiation-Induced radiolytic oxygen generation and microsegregation in silicon dioxide polymorphs. *Physical Review Letters*, 84(14):3137, April 2000.

S. M. Stout-Grandy, A. Petosa, I. V. Minin, O. V. Minin, and J. Wight. A systematic study of varying reference phase in the design of circular fresnel zone plate antennas. *Antennas and Propagation, IEEE Transactions on*, 54(12):3629 –3637, 2006.

E. C. G. Sudarshan, R. Simon, and N. Mukunda. Paraxial-wave optics and relativistic front description. i. the scalar theory. *Phys. Rev. A*, 28(5):2921–2932, Nov 1983.

S. Takagi. A dynamical theory of diffraction for a distorted crystal. *Journal of the Physical Society of Japan*, 26:1239–1253, 1969.

C. Thelander, P. Agarwal, S. Brongersma, J. Eymery, L. F. Feiner, A. Forchel, M. Scheffler, W. Riess, B. J. Ohlsson, U. Gösele, and L. Samuelson. Nanowire-based one-dimensional electronics. *Materials Today*, 9(10):28 – 35, 2006.

P. Thibault, M. Dierolf, A. Menzel, O. Bunk, C. David, and F. Pfeiffer. High-Resolution scanning x-ray diffraction microscopy. *Science*, 321(5887):379 –382, 2008.

P. Thibault, M. Dierolf, O. Bunk, A. Menzel, and F. Pfeiffer. Probe retrieval in ptychographic coherent diffractive imaging. *Ultramicroscopy*, 109(4):338 – 343, 2009.

O. Thomas. Diffraction analysis of elastic strains in micro and nanostructures. *Zeitschrift für Kristallographie*, 223(9):569–574, 2008.

O. Thomas, A. Loubens, P. Gergaud, and S. Labat. X-ray scattering: A powerful probe of lattice strain in materials with small dimensions. *Applied Surface Science*, 253(1):182 – 187, 2006. Proceedings of the E-MRS 2005 Spring Meeting Symposium P: Current trends in optical and X-ray metrology of advanced materials for nanoscale devices - EMRS 2005 - P.

Katsuhiro Tomioka, Junichi Motohisa, Shinjiroh Hara, and Takashi Fukui. Control of InAs nanowire growth directions on Si. *Nano Letters*, 8(10):3475–3480, October 2008.

J. Y. Tsao. *Materials fundamentals of molecular beam epitaxy.* Academic Press, INC., 1992.

F. van der Veen and F. Pfeiffer. Coherent x-ray scattering. *Journal of Physics: Condensed Matter*, 16(28):5003–5030, 2004.

K. van Overveld and B. Wyvill. Shrinkwrap: An efficient adaptive algorithm for triangulating an iso-surface. *The Visual Computer*, 20:362–379, 2004. 10.1007/s00371-002-0197-4.

I. A. Vartanyants and I. K. Robinson. Partial coherence effects on the imaging of small crystals using coherent x-ray diffraction. *Journal of Physics: Condensed Matter*, 13 (47):10593, 2001.

I. A. Vartanyants, I. K. Robinson, J. D. Onken, M. A. Pfeifer, G. J. Williams, F. Pfeiffer, H. Metzger, Z. Zhong, and G. Bauer. Coherent x-ray diffraction from quantum dots. *Physical Review B*, 71(24):245302, 2005.

N. Vaxelaire. *Etude des inhomogénéités de déformation dans les film minces polycristallins par diffraction x cohérents.* PhD thesis, 2011.

R. S. Wagner and W. C. Ellis. The vapor-liquid-solid mechanism of crystal growth and its application to silicon. *Transaction of the Metallurgic Society of AIME*, 233:725–783, June 1964.

X. Wang, J. Zhuang, Q. Peng, and Y. Li. A general strategy for nanocrystal synthesis. *Nature*, 437(7055):121–124, 2005.

Yuxin Wang, Wenbing Yun, and C. Jacobsen. Achromatic fresnel optics for wideband extreme-ultraviolet and x-ray imaging. *Nature*, 424(6944):50–53, 2003.

B. E. Warren. *Xray diffraction*. Courier Dover Publications, 1990.

G. N. Watson. *A treatise on the theory of Bessel functions*. 1886.

G. J. Williams, M. A. Pfeifer, I. A. Vartanyants, and I. K. Robinson. Three-Dimensional imaging of microstructure in au nanocrystals. *Physical Review Letters*, 90(17):175501, April 2003.

G. J. Williams, H. M. Quiney, B. B. Dhal, C. Q. Tran, K. A. Nugent, A. G. Peele, D. Paterson, and M. D. de Jonge. Fresnel coherent diffractive imaging. *Physical Review Letters*, 97(2):025506, July 2006.

G. J. Williams, H. M. Quiney, A. G. Peele, and K. A. Nugent. Coherent diffractive imaging and partial coherence. *Physical Review B*, 75(10):104102, March 2007.

G. J. Williams, H. M. Quiney, A. G. Peele, and K. A. Nugent. Fresnel coherent diffractive imaging: treatment and analysis of data. *New Journal of Physics*, 12(3):035020, 2010.

J. C. Wiltse. History and evolution of fresnel zone plate antennas for microwaves and millimetre waves. *Antennas and Propagation Society International Symposium, 1999. IEEE*, 2:722 –725 vol.2, August 1999.

J. C. Woicik, J. G. Pellegrino, S. H. Southworth, P. S. Shaw, B. A. Karlin, C. E. Bouldin, and K. E. Miyano. Accommodation of strain in ultrathin InAs/GaAs films. *Physical Review B*, 52(4):R2281, 1995.

J. S. Wu, J. C. H; Spence, M. O'Keeffe, and T. L. Groy. Application of a modified oszlnyi and süto ab initio charge-flipping algorithm to experimental data. *Acta Crystallographica. Section A, Foundations of Crystallography*, 60(Pt 4):326–330, July 2004.

Y. Wu and P. Yang. Direct observation of vaporliquidsolid nanowire growth. *Journal of the American Chemical Society*, 123(13):3165–3166, 2001.

O. M. Yefanov, A. V. Zozulya, I. A. Vartanyants, J. Stangl, C. Mocuta, T. H. Metzger, G. Bauer, T. Boeck, and M. Schmidbauer. Coherent diffraction tomography of nanoislands from grazing-incidence small-angle x-ray scattering. *Applied Physics Letters*, 94 (12):123104, 2009.

T. Young. The bakerian lecture: Experiments and calculations relative to physical optics. *Philosophical Transactions of the Royal Society of London*, 94:1–16, January 1804. Article Type: research-article / Full publication date: 1804 / Copyright 1804 The Royal Society.

Wen-Xun Z. An improved zoning rule of the fresnel zone plate. *Microwave and Optical Technology Letters*, 23(2):69–73, 1999.

Y. Zheng, J. C. Boulliard, B. Capelle, A. Lifchitz, and S. Lagomarsino. Strain state in single quantum well GaAs/1ML-InAs/GaAs(100) analysed by high-resolution x-ray diffraction. *Europhysics Letters (EPL)*, 41(6):623–628, 1998.

Author's Publications

This project has resulted in scientific articles that have been published or in preparation for publication.

- Godard, P., Carbone, D., Allain, M., **Mastropietro F.**, Chen, G., Diaz, A., Metzger, T. H., Stangl, J., Chamard, V., *Three-dimensional high-resolution quantitative microscopy of extended crystals*, Nature Communications, Vol. 2, 568 (2011).

- **Mastropietro F.**, Carbone, D., Diaz, A., Eymery, J., Sentenac, A., Metzger T. H., Chamard V., Favre-Nicolin, V., *Coherent x-ray wavefront reconstruction of a partially illuminated Fresnel Zone Plate*, Optics Express, , Vol. 19, Issue 20, pp. 1922319232 (2011).

- Favre-Nicolin, V., **Mastropietro F.**, Eymery, J., Camacho, D., Niquet, Y.M., Borg, B.M., Messing, M.E., Wernersson, L.E., Algra, R.E.,Bakkers, E.P.A.M., Metzger, T.H., Robinson, I.K., *Analysis of strain and stacking faults in single nanowires using Bragg Coherent Diffraction Imaging* , 2010 New Journal of Physics, Vol. 12 035013.

Papers in preparation.

- Favre-Nicolin, V., **Mastropietro F.**, Eymery, J., Carbone, D., Claudon, J., Gérard, J.M., *X-ray Coherent Bragg Imaging of a Single InAs Bilayer in a 200 nm diameter GaAs nanowire*, in preparation.

- **Mastropietro F.**, Favre-Nicolin, V. Eymery, J., Baudot, S., Carbone, D., Andrieu, F., *In-situ study of the relaxation of strained silicon-on-insulator lines using x-ray coherent diffraction imaging.*, in preparation.

Coherent x-ray diffraction imaging on single nanowires

Francesca Mastropietro[1,2]

The coherent diffraction imaging technique (CDI) in Bragg condition can be used to study strain in single nanowires. This is possible due to the recent development of dedicated focusing optics, e.g. Fresnel Zone Plate (FZP), offering the possibility of focusing x-ray beams to sub-micron sizes while preserving a coherent beam. This technique allows to reconstruct (using phase retrieval algorithms) the studied nanostructure as a complex-valued density map, where the amplitude corresponds to the electronic density and the phase to the displacement of the atoms with respect to a perfect crystalline lattice projected onto the scattering vector. The application of CDI to image the strain into heterogeneous (GaAs nanowire with an insertion of 1 monolayer of quantum dots and InSb nanowire with and insertion of InP) and homogeneous highly stressed nano-structures (strained Silicon-on-Insulator lines) has been studied in this work. When using focused X-ray beams, both the amplitude and of the incoming wavefield must be known for a quantitative reconstruction. CDI has been used to reconstruct the coherent wavefield used during experiments and the effects of this illumination function for the imaging of strained nanowires have been also studied.

Keywords: Coherent x-ray diffraction imaging, strain, nanowires, wavefront, phase retrieval algorithms

Imagerie de nanofils uniques par diffraction cohérente des rayons x

L'imagerie par diffraction des rayons X cohérents (CDI) en condition de Bragg est utilisée pour étudier la déformation de nano-objets uniques. Ceci est possible grâce au développement d'optiques focalisantes, comme les lentilles de Fresnel (FZP), produisant un faisceau sub-micronique cohérent. Les nanostructure étudiées sont reconstruites avec des algorithmes d'inversion à partir de données de diffraction, sous la forme d'un objet complexe, où l'amplitude correspond à la densité électronique 3D et la phase correspond à la projection de la déformation de l'objet (par rapport à un réseau cristallin parfait) dans la direction du vecteur de diffraction. Dans ce travail, nous avons étudié la déformation dans des nanofils hétérogènes (nanofil de GaAs avec une mono-couche de boîtes quantiques de InAs) et homogènes (silicium fortement contraint sur isolant (sSOI)). Lorsqu'un faisceau focalisé de rayons X est utilisé, à la fois l'amplitude et la phase de l'onde incidente doivent être connues pour une étude quantitative. Le faisceau focalisé utilisé pendant les expériences a été recontruit avec la technique CDI, et les effets de cette fonction d'illumination sur l'imagerie de nanofils contraints ont été étudiés.

Mots-clés: Imagerie par diffraction x cohérente, contrainte, nanofils, algorithms d'inversion

[1] : SP2M / UMR-E CEA / UJF-Grenoble 1, INAC, Grenoble, F-38054, France
[2] : European Synchrotron Radiation Facility, Grenoble, France